Development of a vacuum arc thruster for nanosatellite propulsion

by

Jonathan Lun

Thesis presented at Stellenbosch University
in partial fulfilment of the requirements for the degree of

Master of Science in Mechanical Engineering
Department of Mechanical and Mechatronic Engineering

Supervisor: Mr R. T. Dobson
Co-Supervisor: Prof. W. H. Steyn

December 2008

Declaration

By submitting this thesis electronically, I declare that the entirety of the work contained therein is my own, original work, that I am the owner of the copyright thereof (unless to the extent explicitly otherwise stated) and that I have not previously in its entirety or in part submitted it for obtaining any qualification.

Date: 15 December 2008

Abstract

This thesis describes the development of a vacuum arc thruster (VAT) to be used as a potential low mass ($<$ 500 g), low power ($<$ 5–10 W) propulsion system for nanosatellites. The thruster uses a high voltage capacitive circuit to initiate and power the arc process with a 400 ns high current (150–800 A) pulse. A one-dimensional steady state analytical model describing the cathode region of the vacuum arc was developed. The model made use of mass and energy balances at the sheath region and cathode surface respectively to predict key quantities such as thrust, ion velocity, ion-to-arc current ratio and erosion rate. Predicted results were shown to be within the limits of reported literature ($\sim$63 μN/A, 26.12 km/s, 0.077 and 110 μg/C respectively). A sensitivity analysis of the analytical model found that a high electric field in the cathode region impedes and decelerates ion flow, which is used for thrust. This was confirmed experimentally for thrust values at arc voltages greater than 2000 V.

Both direct and indirect means of measuring thrust were achieved by using a deflecting cantilever beam and an ion collector system, respectively. The transient response of the cantilever beam to impulsive thrust was analytically modeled, whilst the ion current was found by measuring the current induced on a plate subject to ion bombardment. Knowledge of the ion current density distribution was successfully used to approximate the effective normal thrust vector. Direct and indirect thrust levels were roughly 140 and 82 μN/A of average arc current, respectively. Measured thrust was found to be higher than predicted thrust due to thrust contributions from the ablation of Teflon insulation. The discrepancy is also due to the uncertainty in quantifying free parameters in the analytical model such as the fraction of generated ions flowing away from the cathode region. The thrust-to-power ratio, specific impulse and efficiency of the vacuum arc thruster at an average arc current of 200 A was measured to be 0.6 μN/W, 160 s and 0.05 %, respectively.

A thruster performance analysis and specification showed that the VAT is capable of achieving specific orbital and slew manoeuvres within a constant 5–10 W average power. It was concluded that thruster performance could be improved by using a two-stage arc circuit consisting of a high voltage, low current, short pulse trigger and a low voltage, high current, long pulse driver.

Uittreksel

Hierdie tesis beskryf die ontwikkeling/ontwerp van 'n vakuum boogvonkstuwer vir die potensiële toepassing as 'n lae massa ($<$ 500 g), lae drywing ($<$ 5–10 W) aandrywingstelsel vir 'n nanosatelliet. Die stuwer maak van 'n hoë spanning kapasitorstroombaan gebruik, om die boogvonkstuwer te begin en met 'n 400 ns lange hoë stroompuls (150–800A) aan te dryf. 'n Eendimensionele gestadigde toestand analitiese model was ook ontwikkel om die vakuum boogvonk aan die katode se kant te beskryf. Hierdie model maak van die wet van behoud van massa en energie gebruik, om onderskeidelik die wolk van gelaaide partikels voor die katode en katode-oppervlakte te beskyf, sodat belangrike parameters soos stukrag, ioonsnelheid, ioon-tot-boogvonkstroom-verhouding en erosietempo voorspel kan word. Dit is gewys dat hierdie voorspelde waardes ver binne die perke, wat in die literatuur voorgegee word, lê (onderskeidelik, $\sim$63 μN/A, 26.12 km/s, 0.077 en 110 μg/C). 'n Sensitiwiteitsanalise van die analitiese model het gevind dat 'n hoë elektriese veldsterkte in die omgewing van die katode die vloei van ione, wat die stukrag produseer, belemmer. Hierdie was eksperimenteel bevestig vir stukragte as gevolg van boogvonkspannings hoër as 2000V.

Die geproduseerde stukrag is gemeet deur gebruik te maak van beide direkte en indirekte metodes. Direkte metings is met behulp van 'n deflekterende vrydraearm gedoen, terwyl indirekte metings deur 'n ioon opvangstelsel gedoen is. Die gestadigde toestand uittree van die vrydraearm is analities gemodelleer terwyl die ioonstroom gemeet is deur die stroom te meet wat op 'n plaat, wat deur die ione gebombardeer word, geïnduseer word. Kennis van die ioonstroomdigtheidverspreiding was gebruik om die effektiewe, loodregte stukrag suksesvol te voorspel. Direkte en indirekte stukragvlakke was ongeveer 140 en 82 μN/A van gemiddelde boogvonkstroom. Die gemete stukrag was hoër as die voorspelde stukrag. Hierdie afwyking word toegeskryf aan die bydrae van die Teflon wat wegbreek. Die afwyking kan verder toegeskryf word aan die onsekerhede in die keuse van die vryveranderlikes se waardes in die analitiese model soos byvoorbeeld die breukdeel van gevormde ione wat vanaf die katode wegbeweeg. Die stukrag-tot-drywingsverhouding, spesifieke impuls en effektiwiteit van die stuwer, by n gemiddelde boogvonkstroom van 200 A, was onderskeidelik as 0.6 μN/W, 160 s en 0.05 %, gemeet.

Stuwer werkverrigtingspesifikasies het gewys dat die vakuum boogvonkstuwer in staat is om spesifieke orbitale en rolbewegings uit te voer, terwyl n gemiddelde drywing van 5–10 W gehandhaaf word. Daar is tot die gevolgtrekking gekom dat die stuwer se werkverrigting verbeter kan word

deur gebruik te maak van ’n dubbele-stadium boogvonkbaan bestaande uit ’n hoë spanning, lae stroomsnellerbaan en lae spanning, hoë stroomaandrywingsbaan.

Acknowledgments

Thanks goes to a number of people who helped make this project possible:

- To my supervisors, Mr Robert Dobson and Prof. Herman Steyn, for their guidance, support and wisdom. A special thanks to Prof. Steyn for securing funding for this thesis.
- To all ESL staff, especially Arno Barnard, A. J. Van der Westhuizen, Quintis Brandt and Willie Van Rooyen for their practical advice and help on electrical matters. Special thanks to Willie Van Rooyen for making the pulse circuit.
- To the Electrical Engineering staff, Petrus, Ulrich Buttner and Mr WJ Croukamp, for their willingness to lend their energy, time and costly equipment.
- To those at the Mechanical department and workshop, Mr K Van der Westhuizen, Ferdi and Cobus Zietsmann, Calvin Hamerse and Tony Lumbwe, for their help with mechanical work, advice and support equipment.
- To my ESL colleagues, for their audacious company. A special thanks to my office colleague, Dewald Mienie, for being a good person to bounce ideas off, a listening ear and supplier of soldering wire.
- To Andrew Gill, for his advice and ideas on the thruster design, experimental work and for offering to proof-read this thesis.
- To the NACoE and Francois Denner, for providing me with this opportunity to study such an interesting topic.
- To my friends, for their prayers, support and love.
- To my family, for always supporting what I do.
- To Maryke Sher, your love and promise has kept me going.
- To my Lord God, your mercy knows no bounds.

Dedication

To Maryke, for patiently waiting.

Contents

List of Figures

List of Tables

Nomenclature

Roman Letters

A	Area (m^2)
a	Atom, beam impact point (m)
B_T	Ion collector correction factor
b	Beam width (m)
C	Capacitance (F)
C_G	Center of gravity
C_T	Thrust correction factor
C_{Ta}	Anode correction factor
C_{Tb}	Thruster plume distribution correction factor
c	Exhaust velocity (m/s)
c_1, c_2	Deflector length (m) and width (m) respectively
c_3	Collector plate length (m)
D	Resultant parameter
D_T	Deflector correction factor
D_{Ta}	Deflector intercepting correction factor
D_{Tb}	Deflector plume distribution correction factor
d_1	Ion collector drift length (m)
d_2	Deflector ion drift length (m)
E	Electric field (V/m)
E_b	Young's modulus (Pa)
E_k	Kinetic energy (eV)
E_r	Erosion rate by vapourisation (μg/C)
e	Electron, electron charge (C)
F	Thrust (N), Force (N)
f	Fractional ion charge state
G	Degeneracy
g	Gravitational acceleration (m/s^2)
H	Thrust-to-power ratio (N/W)

h	Planck's constant (Js), beam thickness (m)
I	Current (A)
I^*	Average spot current (A)
I_b	Area moment of inertia (m^4)
I_i'	Ion current per unit of ion cathode current
I_m	Mass moment of inertia (kgm^2)
I_{sp}	Specific impulse (s)
I_0	Impulse (Ns)
i	Ion
J	Current density (A/m^2)
J_i'	Ion current density per unit of ion cathode current (m^{-2})
K_1, K_2	Vapour pressure constants
K_b	Boltzmann constant (J/K)
k	Exponential distribution spread factor
L	Lorenz number ($W\Omega K^{-2}$), beam length (m)
L_m	Satellite side length (m)
l	Inductance (H)
M	Constant
M_f	Ion mass fraction
m	Mass (kg)
m_o	Spacecraft mass (kg)
m_p	Propellant, cathode mass (kg)
$\dot{m}_i$	Ion mass flow rate ($\mu g/s$)
$\dot{m}_s$	Cathode erosion rate ($\mu g/s$)
N	Number of cathode spots
N_s	Pulse number
n	Particle density (m^{-3}), integer
P	Power (W)
p	Pressure (Pa)
Q	Charge (C)
q	Power density (W/m^2)
R	Resistance (Ω)
r	Radius (m)
r_o	Orbit altitude (km)
S	Pulse frequency (Hz)
S_Y	Spin number
T	Temperature (eV or K)
T_b	Boiling point (K)
t	Time (s)
t_D	Time between two consecutive pulses (s)
t_m	Sampling time (s)

U	Ionisation energy (eV)
u	Atomic mass unit (kg)
V	Voltage, potential drop (V)
v	Velocity (m/s)
W	Energy potential (eV)
w_1, w_2, w_3	Length (m), width (m) and breadth (m) respectively
X	Independent variable
x	X-axis co-ordinate on cathode surface, satellite body or along beam length (m)
Y	Energy level, dimensionless deflection parameter
y	Y-axis co-ordinate on cathode surface, satellite body or beam deflection (m)
Z	Ion charge state
z	Z-axis co-ordinate on satellite body, distance away from thruster (m)

Greek Symbols

α	Backflow coefficient
α_n	Trigonometric function of the frequency equation roots
β	Field-enhancement factor
$\beta_n L$	Roots of the frequency equation
Γ	Flux density ($m^{-2}s^{-1}$)
γ	Degree of ionisation
γ_n	Ratio of frequency equation roots
γ_{se}	Secondary electron emission coefficient
Δ	Difference in conduction heat flux terms (W/m^2)
Δm_p	Propellant mass loss (kg)
Δm_s	Cathode mass loss (kg)
Δt	Manoeuvre time (s)
ΔV	Strain gauge voltage signal (V)
Δv	Velocity change (m/s)
$\Delta\theta$	Orbital manoeuvre separating angle (rad)
δ	Error
ϵ_o	Permittivity of free space (C^2/Nm^2)
ϵ_x	Strain (mm/mm)
ζ	Ion-to-arc current ratio
η_T	Thruster efficiency
θ	Angle (rad)
θ_1, θ_3	Anode interference angle in the X and Y plane respectively (rad)
θ_2, θ_4	Deflector edge angle in the X and Y plane respectively (rad)

Λ	Partition function
λ	Thermal conductivity of cathode (W/mK)
μ	Beam mass per unit length (kg/m)
μ_o	Standard gravitational parameter ($km^3\ s^{-2}$)
ν	Ion condensation ($m^{-2}s^{-1}$)
ρ	Density (kg/m^3)
σ_x	Stress (Pa)
σ	Electric conductivity of cathode (S/m)
σ_{sb}	Stefan-Boltzmann constant (W/K)
τ	Time constant (s)
ϕ	Work function (eV)
ϕ_n	nth normal modal function or mode shape
Ω	Orbital angular velocity (rad/s)
ω_1	First modal/natural frequency (Hz)

Subscripts

b	Beam
c	Collector, collected
con	Conduction
$cool$	Cooling
cs	Cathode-sheath region
d	Total discharge
e	Electron
eff	Effective field-enhanced
em	Emitted electrons
er	Returning electrons
f	Far from the cathode surface
$heat$	Heating
i	Ion, ionisation
J	Joule heating
k	Ion species
max	Maximum
n	Neutral
o	Thruster operating time
P	Power supply
p	Plasma, plasma region near the cathode
rad	Radiation
s	Cathode, cathode spot, cathode surface
sh	At the sheath

T	Thrust
t	Total
vap	Vapourised from the cathode
Y	Energy level
z	In the normal direction
∞	Far distance from imaginary surface

Abbreviations

AASC	Alameda Applied Sciences Corporation
CSD	Charge State Distribution
DC	Direct Current
DTMS	Direct Thrust Measurement System
EMI	Electromagnetic Interference
EP	Electric Propulsion
ESL	Electronic Systems Laboratory
FEEP	Field Emission Electric Propulsion
GD	Gas Dynamic
HV	High Voltage
ICDD	Ion Current Density Distribution
ITMS	Indirect Thrust Measurement System
IT	Ion Thruster
JPL	Jet Propulsion Laboratory
KGD	Kharkov-modified Gas Dynamic
LAT	Laser Ablation Thruster
LEO	Low Earth Orbit
LTE	Local Thermal Equilibrium
MEMS	Microelectromechanical Systems
PH	Potential Hump
PFN	Pulse Forming Network
PPT	Pulsed Plasma Thruster
PPU	Power Processing Unit
R/VLT	Resistojet/Vaporizing Liquid Thruster
S/C	Spacecraft
SCR	Silicon-Controlled Rectifier
SG	Strain Gauge
TLHB	Thermal Lowering Heat Barrier
TOF	Time Of Flight
TVS	Transient Voltage Suppressors
VAT	Vacuum Arc Thruster

Chapter 1

Introduction

1.1 Background and Motivation

1.1.1 Growth of the Nanosatellite Industry

Traditionally, the satellite industry has been dominated by satellites of large size/mass and high-power consumption, funded primarily by governments, large corporations and institutions. In recent years, however, there has been an increased trend in the deployment of micro- and nano-class satellites as a result of universities developing student space programs (Lewin 2004). An important aspect of small satellites is their potential to form constellations of satellites, each serving an individual part of a larger entity. For example, a constellation of nanosatellites may each carry one or two scientific instruments to collectively perform the research of a single large satellite (Esper et al. 2003). This inherently reduces the risk of the entire mission failing by separating the payload into smaller segments. In addition, nanosatellites may be launched over an extended period of time, thereby allowing greater flexibility in mission capability, cost and lifetime. One possibility of small satellite constellations is their potential to manoeuvre into, maintain or disperse desired formations (Jilla & Miller 1997). The ability to spread or concentrate, wholly or partially, over a planet, moon, asteroid or any sufficiently large body likens the constellation's behaviour to that of a flock of birds or swarm of insects. A spread network of satellites can collect data and perform experiments on a much larger scale than any single satellite could achieve. Constellations can also converge at a point of interest to study a particular region of the earth's surface. Some examples of satellite formation flying are shown in Figure 1.1.

Previously limited to theoretical exercises, in recent years there has been a number of university nanosatellite programs emerging such as QuakeSat (Long et al. 2002), ION-F (Martin et al. 1999a), SNAP-2 (Baker et al. 2005) and CanX-2 (Rankin et al. 2004) to demonstrate the potential of nanosatel-

lite technology. The Stellenbosch University (SU) ESL Nanosat Project is an example of a conceptual nanosatellite formation flying demonstration mission (Steyn 2007).

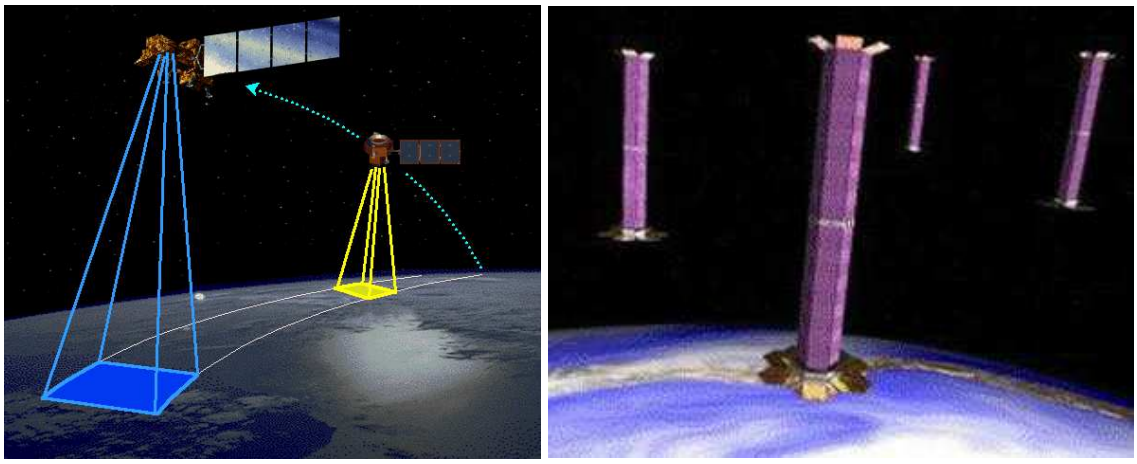

Figure 1.1: Formation flying concepts (NASA 2007a, NASA 2007b)

1.1.2 The Role of Micropropulsion

Nanosatellites are typically launched into Low Earth Orbit (LEO) and therefore suffer from a relatively short operating lifetime due to atmospheric drag. A micropropulsion system may, in addition to formation-oriented functions, serve the purpose of providing drag compensation, significantly increasing a nanosatellite's operating lifetime and consequently, its usefulness and cost effectiveness. Nanosatellites bring new challenges to propulsion systems: accurate low thrust in the milli- and micro-Newton range, low operating power (< 20 W), low mass (< 500 g) and compact size.

Micropropulsion has traditionally been the downward scaling of their larger counterparts such as cold-gas propulsion and resistojets both of which are low-cost and have relatively high reliability. However, there are many efforts to develop new as well as improve on current forms of micropropulsion, increasingly toward the level of microelectromechanical systems (MEMS) technology (Schein 2006). The use of electric propulsion (EP) has also been on the rise, given the potential of greater performance and lower system mass than chemical propulsion. Low-power electric propulsion systems such as Pulsed Plasma Thrusters (PPT), Field Emission Electric Propulsion (FEEP) and Vacuum Arc Thrusters (VAT) have shown promise as micropropulsion for nanosatellites. Attempts at scaling ion engines for micropropulsion, however, have been more difficult to achieve due to physical limitations, increased complexity and high-power consumption of these devices. However, NASA's Jet Propulsion Laboratory continues to develop a competitive micro-ion thruster (Schein 2006).

Thus, the reality of small satellite constellations cannot be achieved without the development of micropropulsion technologies. More specifically, nanosatellites require innovative micropropulsion systems to fully utilize their strengths as small, cheap and potentially mobile entities.

1.1.3 Vacuum Arc Thrusters

Appendix A contains a literature survey used to determine which type of propulsion technology would best accomplish the objectives of a conceptual nanosatellite formation flying demonstration. The vacuum arc thruster was ultimately chosen for study due to its novelty of using solid metal propellant, low power usage, variable-thrust capability and low system mass. The vacuum arc thruster consists of anode and cathode electrodes separated by a thin layer of insulation. An arc is generated between the two electrodes in a gap at the thruster's end, producing ions from the cathode metal that accelerates outward creating thrust. The arc originates from small localised spots formed on the cathode surface known as *cathode spots*.

1.2 Objectives

This work aims to study and develop an electric propulsion thruster for potential use on board a conceptual nanosatellite (5 kg, 20 cm cubic) within an average power limit of 5 W to perform orbital or attitude control manoeuvres. A vacuum arc thruster, powered by a capacitive discharge power circuit, was designed, built and tested at the Electronic Systems Laboratory and Semiconductor Laboratory, Department of Electrical and Electronic Engineering, Stellenbosch University. An analytical model of the vacuum arc thruster was developed to predict and characterise thruster behaviour and performance. Thrust measurements were performed to validate the thruster's analytical model and design. It is the intention of this work to develop a predictive theory of vacuum arc thruster performance and aspects of vacuum arc thruster design.

Chapter 2

Literature Survey

This chapter provides a brief outline of vacuum arc thruster operation, design and general performance. An introduction to basic vacuum arc phenomena is presented as well as a brief summary of vacuum arc theoretical models. A number of thrust measurement techniques that have been used to measure thrust in the micro-Newton range are also outlined.

2.1 An Introduction to Vacuum Arc Thrusters

The vacuum arc thruster (VAT) was originally studied in the 1960–70's, but has acquired renewed attention in recent years by Alameda Applied Science Corporation (AASC) in San Leandro, California since circa 1998 (Qi et al. 1998, Keidar et al. 2005). Patents on the VAT were lodged as recently as March 2007 (Schein et al. 2007). The main proponents for its development was to provide a more efficient, higher thrust-to-weight ratio thruster alternative to 'prior art' pulsed plasma thrusters (PPTs) (Schein et al. 2007). The thruster is capable of operating within a wide range of average power levels (1-100 W), making the technology highly desirable and flexible for low-power micro- and nano-satellite missions (Schein et al. 2002). Since the VAT has only recently been developed, a limited amount of literature is available on its design and performance. The current majority of VAT literature originates from the researchers working with or for AASC. Some designs by AASC are shown in Figure 2.1.

2.1.1 Basic VAT Theory and Performance

The VAT relies on a pulsed high current vacuum arc to vapourise and ionise cathode material, which accelerates outward as a plasma jet for thrust. Charged liquid droplets/macroparticles and some

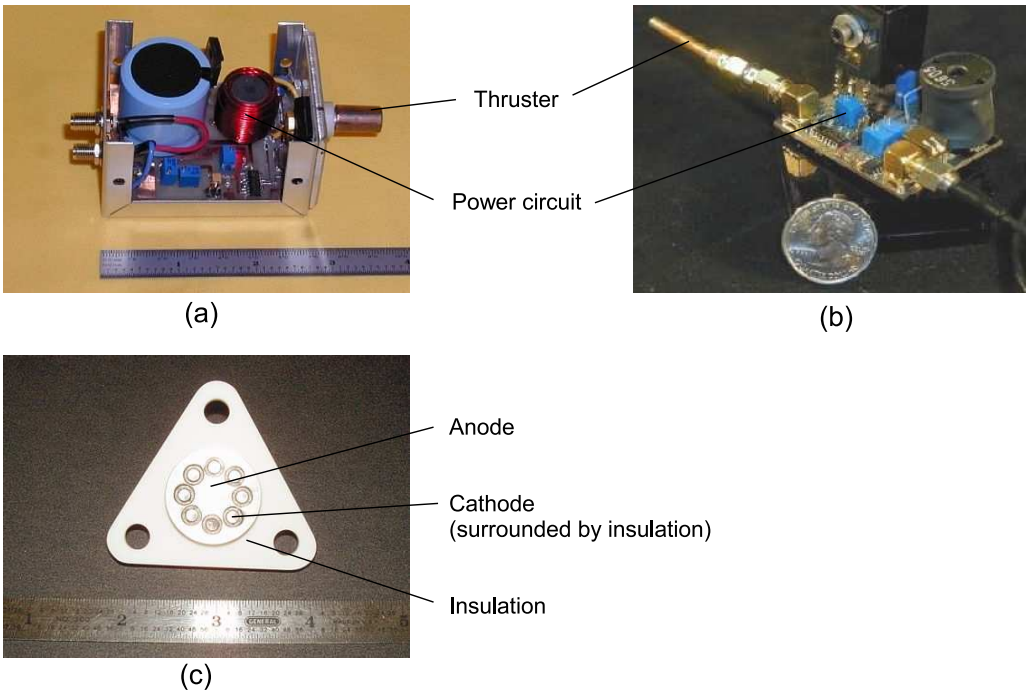

Figure 2.1: Examples of AASC vacuum arc thrusters: (a) (Keidar et al. 2005), (b) HuskySat, (c) (Optical Energy Technologies Inc. 2008)

neutral particles are also present in the thrust plume, but most of the thrust is produced by ion flow. A basic VAT theory makes use of several experimentally-attained values to obtain estimates of thrust, specific impulse and efficiency. The only VAT theoretical model that could be found was a semi-empirical model by Polk et al. (2001) that predicted thruster performance for a large number of cathode materials based on experimental data of cathode erosion rate (17–620 μg/C), ion velocity (5–30 km/s), ion current (about 10% of the arc current) and average ion charge states (1^+–3^+). Their model also included the effects of electrode interference and plume distribution. Typical VAT operation (Schein et al. 2002, Schein 2006) and predicted VAT performance (Polk et al. 2001) is summaried in Table 2.1.

Table 2.1: Typical VAT thruster operating conditions and performance

Arc current	10–300 A
Avg. input power	1–100 W
Pulse rate	20–200 Hz
Thrust per pulse	1–100 mN
Specific Impulse	100–1500 s
Thruster efficiency	1–12%
Thrust-to-power ratio	0.1–20 μN/W
Thruster mass	$<$ 100 g
PPU mass	$<$ 500 g

A notable quality of the vacuum arc thruster is its ability to throttle power and thrust levels without effect on efficiency or specific impulse (Schein et al. 2002, Polk et al. 2001). This is because the thrust mechanism originates from microscopically-sized cathode spots. As a result, increasing power levels would merely spawn additional spots, producing plasma jets separate from one another and collectively produce more thrust. In other words, the effectiveness of the thruster to convert propellant mass into useful thrust (i.e. specific impulse) is robust due to the self-regulating nature of the vacuum arc. The efficiency of the thruster, however, is largely limited by losses from converting the cathode material into plasma (Schein et al. 2002). The VAT has also been adapted as an ion source for ion thrusters, which use accelerating grids at large voltage potentials to accelerate the ions in the form of a beam (Polk et al. 2001). Ion thrusters have been shown to operate with much higher specific impulse (∼5000 s) and efficiency (∼40 %) than normal VATs, but are required to operate at much higher power levels (∼100 W).

2.1.2 Geometry

The vacuum arc thruster can take the form of a planar, coaxial or tubular configuration (see Figure 2.2). Most designs that were found specified an inner cathode electrode surrounded by an outer anode electrode. Polk et al. (2001) tested a coaxial geometry and found that flush electrode faces give the best thrust because the cathode plasma flow is not intercepted by the anode surface. However, it was also noted that a recessed cathode may be more practical in terms of reducing spacecraft contamination from thruster exhaust. Rysanek et al. (2002) initially used a coaxial design, but later opted for a planar or sandwich design for simplicity and ease of manufacture (Figure 2.2). A variation of the design was to reverse the locations of the electrodes such that the cathode surrounds the anode. This novel feature allows the use of the spacecraft metal frame as the cathode. Schein et al. (2007) proposed a tubular geometry where hollow rings of anode, cathode and insulation were placed together to form a tube. They also presented a coaxial geometry with a hollow cathode, which allows for the attachment of a spring feed mechanism (see Figure 2.3). This geometry was seen to be more reliable due to the easier deposition of metal onto the insulator for arc triggering (Rysanek 2007b). A cathode comprised of a rack of metal balls was also proposed by Schein et al. (2007) to ensure uniform erosion.

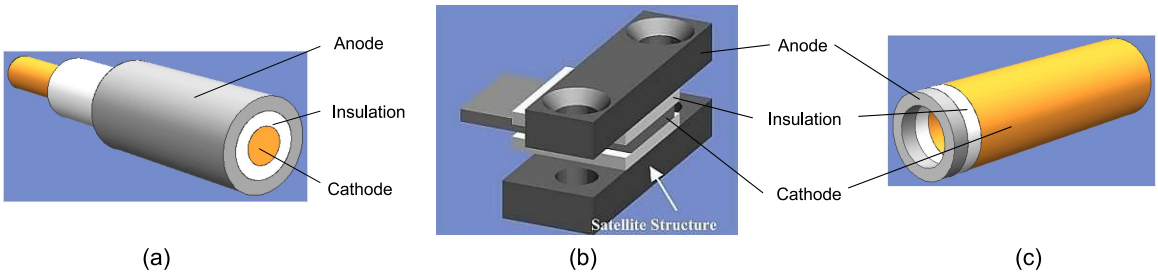

Figure 2.2: Illustration of various VAT geometries: (a) coaxial, (b) planar and (c) ring designs (Rysanek 2007b)

2.1.3 Electrode and Insulator Materials

Generally, any conducting material can be used to form the electrodes, whilst any material with high electrical resistance (100 Ω–1 MΩ) can form the insulator (Schein et al. 2007). Polk et al. (2001) tested a wide range of cathodic materials and found that the highest performing materials were magnesium, chromium, yttrium, tantalum and tungsten due to a combination of high ion velocity and high ion fraction in the plasma. Schein et al. (2002) also performed tests with titanium cathodes. Rysanek et al. (2002) used the aluminum structural frame of the spacecraft as cathodic material. Polk et al. (2001) made use of a molybdenum anode, whilst Schein et al. (2002) and Rysanek et al. (2002) employed a copper anode. Rysanek et al. (2002) made use of ceramic alumina as an insulator.

2.1.4 Feed Mechanism

Some designs make use of a feed mechanism to increase the amount of cathodic propellant for use, whilst others appear to omit the feature entirely. For example, Schein et al. (2007) used a helical spring to displace a hollow cathode tube (Figure 2.3). The mechanism is light, simple and effective since no other moving parts apart from the spring are required and the feed mechanism is self-regulating. On the other hand, one may omit the use of a feed mechanism by surrounding the anode with the cathodic aluminium structure instead.

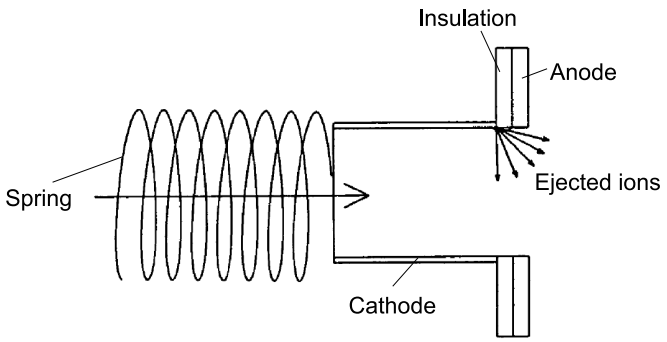

Figure 2.3: Helical spring feed mechanism (adapted from Schein et al. (2007))

2.1.5 Arc Power Circuit

A power source capable of high voltage and high current capacity is needed to initiate and sustain arc conditions at the electrodes. To reduce the thruster's average power consumption, the VAT is operated in pulse mode. Most VAT designs found used an inductive energy storage driver compared to the 'prior art' PPT, which uses a capacitive energy storage driver (Figure 2.4) (Schein et al. 2002, Schein et al. 2007). Inductive drivers have the advantage of lower voltages, better control over the current and higher pulse rates, but require greater heat dissipation than capacitor drivers.

Figure 2.5 illustrates the inductive driver's operation: an inductor increases the current level in the circuit (charge-up phase). Once the desired current level has been reached, an arc is initiated and the current decreases (discharge phase). A switch is used to control the pulse rate of the thruster. Arc operating voltages were found to be around 20 V for most metals, whilst a wide range of arc currents (6–100 A) can be used (Polk et al. 2001, Schein et al. 2002). A Pulse Forming Network (PFN), comprised of a series of inductors and capacitors, is also commonly used to help provide a longer and relatively flat arc pulse, i.e. a rectangular pulse.

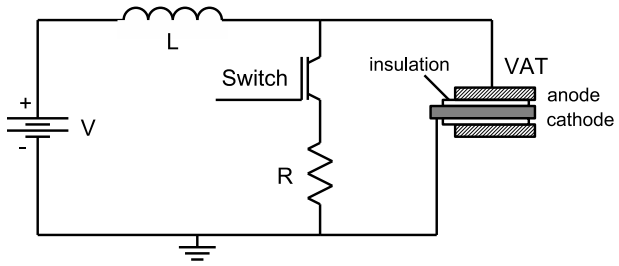

Figure 2.4: Schematic of IES driven VAT (adapted from Schein et al. (2002))

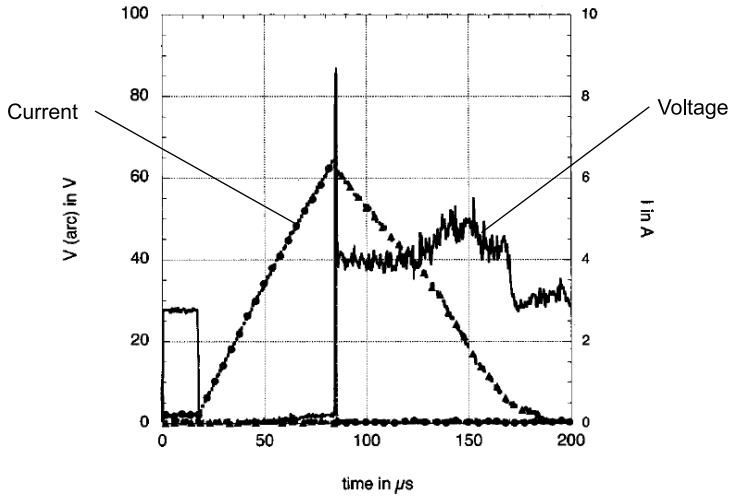

Figure 2.5: Voltage and current passing through the switch in Schein et al.'s (2002) VAT design

2.1.6 Arc Initiation/Triggering

Arc initiation can be done in a variety of ways such as high-voltage breakdown, fuse wire explosion, contact separation, mechanical triggering, plasma/gas injection, laser triggering and many others (Anders et al. 1998). However, many of these methods require high voltages (up to a few kV), complex equipment and/or low repetition rates. Studies done by Anders et al. (1998, 2000) compared various arc initiation techniques and presented a new form of 'triggerless' vacuum arc initiation.

In 'triggerless' arc initiation, a thin film of conducting material is applied to the exposed area of in-

sulation between the two electrodes in order to reduce the spatial gap for the arc to travel. It was found that even short circuiting slightly initiated the arc more reliably. The conducting film material is preferentially graphite, which is may be easily applied as graphite pencil marks. When the circuit discharges energy into the thruster, the conducting layer is heated up from the high power density present in the layer and is evaporated and ionised, which provides an electrically conducting medium for the arc to travel through and thus overcoming the high dielectric strength of vacuum (Figure 2.6). Initiating voltages may be as low as 100 V (Schein et al. 2002), but is more reliable at a few hundred volts. Arc initiation was possible over a wide range of gap resistances between 1 Ω–100 kΩ, demonstrating the robustness of the trigger mechanism. An important consequence of the arc process is the ejection of cathode ions, neutrals and macroparticles that condense onto the surrounding insulator where the conducting layer has just vapourised. Therefore, the total desired effect is to achieve a relatively steady layer of conducting material to initiate subsequent arcs. However, this balance is upset by the eventual excess deposition of cathode metal, which short-circuits the thruster. The thruster must be operated in a pulsed fashion to limit the amount of deposition and power usage. Pulse numbers of up to 10^6 have been demonstrated (Anders et al. 1998).

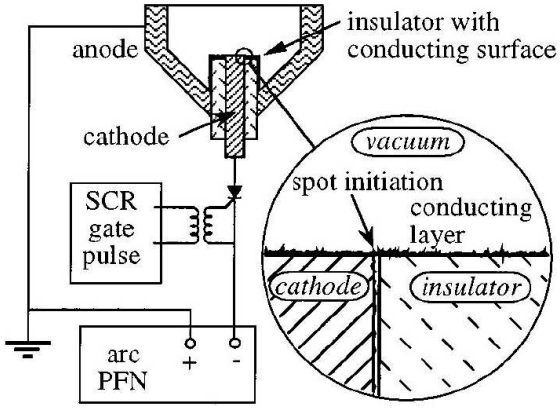

Figure 2.6: Illustration of the 'triggerless' arc initiation method (Polk et al. 2001)

2.1.7 Technical Challenges and the Effect of Macroparticle Production and Ejection

Polk et al. (2001) regards initiation reliability, cathode erosion, a reliable feed mechanism and minimal satellite contamination from exhausted propellant as important design factors. Engine lifetime of the VAT may be determined by understanding failure modes such as short circuiting. Rysanek (2007a) found no difficulty in initiation reliability and cathode erosion when using a trigger electrode for initiating the arc. Daalder (1976) studied the behaviour of macroparticle ejection from vacuum arcs and reported that the majority of these droplets are ejected at low angles to the plane of the cathode surface. Rysanek (2007b) also studied the charged nature of the ejected macroparticles in vacuum arc thrusters. The presence of charged macroparticles and liquid droplets is highly disadvantageous,

since the surrounding spacecraft components can be contaminated with metal droplets. Recently, Keidar et al. (2005) developed a magnetically enhanced vacuum arc thruster that reduced contamination and increased thrust by confining the expanding plasma with the magnetic field produced by the inductive driver (see Figure 2.1 above). In addition, gross melting makes the thruster inefficient, since less mass is being ionised to produce useful thrust. Methods of measuring the cathode erosion rate include the weight loss method, measuring changes in cathode geometry and measuring crater volumes (Boxman et al. 1995). The weight loss method appears to be the most common of all methods due to it's relative simplicity and fundamental accuracy over other methods, since it measures the net erosion rate of the entire cathode structure (Shalev et al. 1985, Polk et al. 2001). Boxman et al., Shalev et al. and Polk et al. also indicated that although the erosion rate is generally found to be constant for relatively low levels of arc current and short arc pulse durations, the erosion rate increased strongly for high currents and long pulse durations. This is because the presence of a large number of spots tend to produce overlapping temperature profiles of adjacent cathode spot surfaces, resulting in gross melting.

2.2 Thrust Measurement Techniques

There exist a variety of thrust measurement techniques developed for microthrusters. The choice of thrust measurement is limited to systems that can measure small impulses, either individually or accumulated over time. Various types of thrust balances were studied. Cubbin et al. (1997) designed an optical interferometric proximeter system that measures the deflection of a swinging arm supported by flexural pivots (frictionless pivots) by detecting the phase difference between two laser beams reflected off the arm (see Figure 2.7). Their system was capable of measuring a wide range of thrust impulses (100 μNs–10 Ns) and steady state thrust as low as 20 μN. Cubbin et al. (1997) also mentions other thrust measurement displacement sensors such as inductive and capacitive proximetry probes, accelerometers, linear voltage differential transformers (LVDTs) or an optical angular reading. Gamero-Castaño (2003) developed a torsional balance to measure steady state and impulsive thrust with a resolution as low as 0.03 μN. The balance consists of two horizontal arms with the thruster on one side and a counterweight on the other. The entire balance is supported at the top and bottom by flexural pivots. Deflection of the structure is measured with a linear displacement sensor. Xiong et al. (2005) developed a thrust stand comprised of a thin cantilever beam and a LVDT to measure steady state thrust levels in the micro-Newton range.

The use of an indirect thrust measurement system (ITMS) was also explored. This approach required measurement of the two parameters that define thrust, namely, the propellant mass flow rate and propellant velocity. Byon & Anders (2003), Anders & Yushkov (2002) and Oks et al. (2006) developed ion collector systems that captured the amount of ions ejected by vacuum arc sources (see Figure 2.8). Usually a large collector plate or faraday cup is used to absorb the ions, which induce a measurable

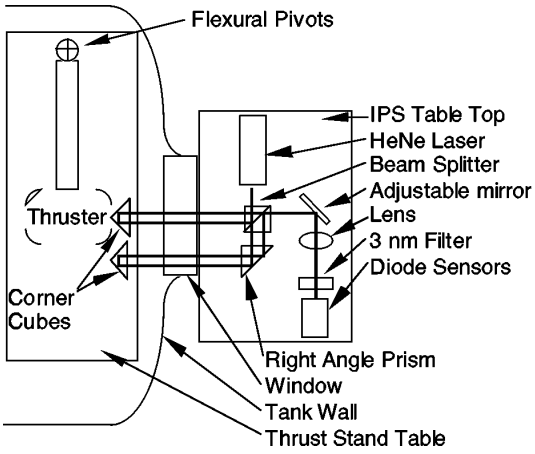

Figure 2.7: Schematic of Cubbin et al.'s (1997) thrust stand

current flow through a circuit. Bias voltages are typically used to attract the ions and repel the electrons in the incoming plasma. Oks et al. (2006) and Anders & Yushkov (2002) also developed systems that were capable of measuring ion velocities using the Time-of-Flight (TOF) method. The TOF method measures the time for ions to travel over a certain distance known as the *drift length*, which is the distance between the ion source and an ion collector or faraday cup. This technique is valid for vacuum arc ion sources as the ion velocity was observed to be constant soon after being accelerated out of the arc region (< 1 mm) (Byon & Anders 2003). Drift lengths in previous studies vary from 0.3–2 m (Byon & Anders 2003). A collection of extractor grids, additional anode walls/grids, timed gates and even magnetic field coils are sometimes used to filter out plasma electrons, separate ions of different charge states and focus ion beams (Byon & Anders 2003, Oks et al. 2006). Byon & Anders (2003) performed experiments to determine the ion velocity distributions of a number of cathode materials. However, for simplicity this work shall only be concerned with the average ion velocity of the ejected ions. Another approach to finding ion velocities is by measuring the ion energy distribution function using a retarding field analyzer. However, this method is complex and require sophisticated equipment (Byon & Anders 2003). Figure 2.9 illustrates an example of the measured ion current and the time delay in the TOF method.

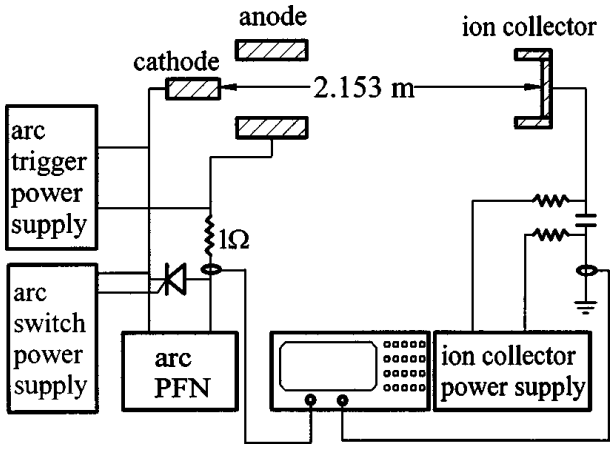

Figure 2.8: Schematic of Byon & Anders's (2003) experimental setup

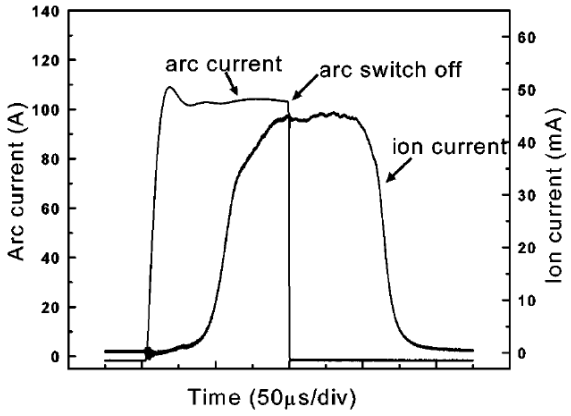

Figure 2.9: Example result of measured ion current and the TOF method (Byon & Anders 2003)

The direct thrust measurement system (DTMS) is seen as the more accurate form of measuring thrust compared to the ITMS since a direct energy transfer to the measurement system occurs. The ITMS will tend to measure a smaller portion of the thrust and only considers the contribution of the ions to thrust.

2.3 An Introduction to Vacuum Arc Theory

There is a large body of literature produced over the last 200 years on the subject of vacuum arcs. The modern study of vacuum arcs was motivated mainly by its presence in vacuum tubes and switches in the early-to-mid twentieth century (Lafferty 1980). Later on, importance was seen in its use as ion sources for a variety of applications such as film deposition technology (Brown et al. 1999) and now, more recently as a form of electric propulsion technology.

The vacuum arc is an electrical discharge occurring in the region between two electrodes in a vacuum environment. Actually, the term *vacuum arc* is a misnomer because the arc cannot exist without a medium in which to travel in. This medium is provided by material from the cathode electrode, which evaporates and is ionised to form a localised plasma region (Lafferty 1980). The anode plays the role of collecting the electrons to complete the closed circuit, and only contributes to the arc discharge at high current levels (on the order of kA). The self-sustaining arc requires a minimum of a few amperes (typically 0.1–6 A) and a few tens of volts (typically around 20–30 V) depending on the type of cathode material (Boxman et al. 1995).

The arc originates from small cathode spots (1–10 μm) (Polk et al. 2001), which appear to move rapidly in an apparently random fashion along the cathode surface (barring any influence from an external magnetic field). Figure 2.10 (a) was taken with a high resolution microscope and depicts the formation of craters created by these cathode spots. Figure 2.10 (b) shows the formation of cathode spots from a 2 kA pulsed vacuum arc source (Boxman et al. 1995). Cathode spots are roughly

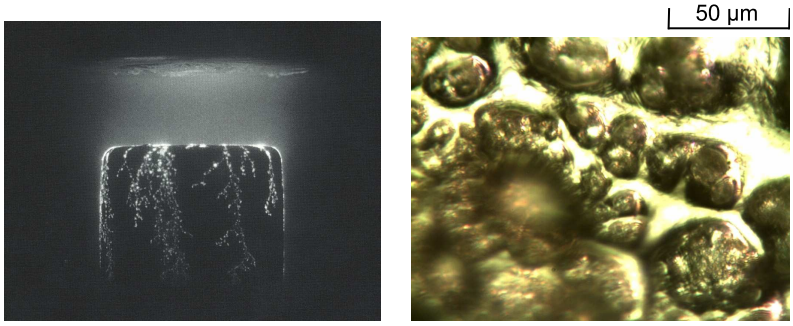

Figure 2.10: (a) Cathode spots (Boxman et al. 1995), (b) Craters formed by cathode spots

classified as follows (Boxman et al. 1995):

1. Type I - fast moving spots: (a) Type 1 - oxidized or contaminated surfaces; (b) Type 2 - clean surfaces
2. Type II - slow moving spots
3. Type III - grouped spots

The majority of vacuum arc studies focus on the cathode spot region because of their pivotal role in the existence of the arc: their formation, life-cycle, appearance, macro- and micro-structure, behavior/motion and action upon the cathode surface. Yet, a large part of vacuum arc phenomena remains unexplained and unaccounted for (Hantzsche 2003). The rapid life-cycle (order of ns), microscopic scale (μm) and extreme conditions of the cathode spot make experimentation difficult to obtain clear and accurate results, resulting in many decades of debate on quantities such as the total current density (Hantzsche & Jüttner 1985). Ultimately, knowledge of the vacuum arc is limited by the spatial and temporal resolution of available experimental test equipment, which is constantly improving over time (Beilis 2001b).

Arguably, the most well-known and excellent sources of collective knowledge on the subject of vacuum arcs are the works of Lafferty (1980) and Boxman et al. (1995). Both texts consolidate the main ideas and concepts of vacuum arcs developed over the last century and provide guidance on the strengths and limitations of current models. Lafferty (1980) is viewed more as a reference to detailed and (then) ongoing work, whilst Boxman et al. (1995), which may be seen as an update to Lafferty's work, includes the finer workings of vacuum arc theory with the advantageous perspective of more recent discoveries.

2.3.1 Physical Description of the Cathode Spot Region

The vacuum arc is generally separated into a number of regions or zones, each defined by a specific activity or state. Many physical properties of vacuum arcs are often linked to one another, resulting

in feedback processes. Figure 2.11 illustrates the active processes of the vacuum arc in the cathode region. Four general zones are presented: the cathode spot surface, a positive sheath region, a pre-sheath or ionisation zone and an arc plasma region. Each zone is characterised by specific energy processes or interactions/general behaviour of atoms (a), ions (i) and electrons (e).

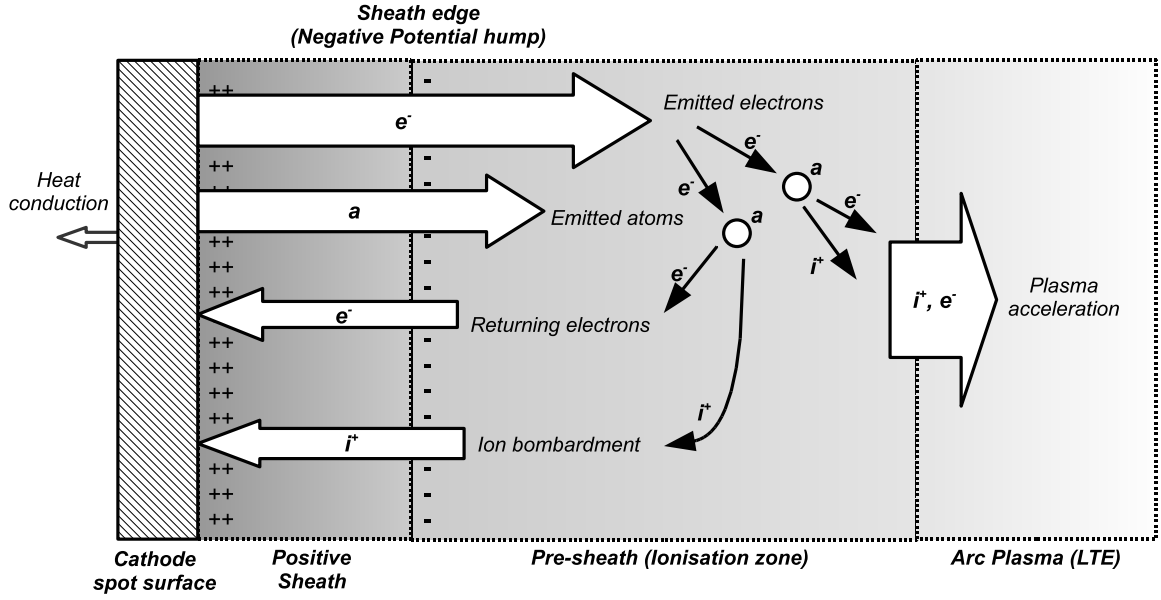

Figure 2.11: Illustration of the vacuum arc in the vicinity of a cathode spot region

Joule heating and ion bombardment form high temperature cathode spots at surface microprotrusions, ejecting cathode atoms. There are two fields of thought concerning the source of the metal atoms: tiny explosions or vapourisation. Tiny craters are thus formed by the loss of cathode material. Over the spot lifetime, growth of these craters decreases Joule heating and the temperature drops below the point of sustaining vapour and electron emission and the site extinguishes. A new site at a nearby microprotrusion is ignited by the molten flow of the previous site. Erosion of the cathode (7–620 μg/C) (Polk et al. 2001) is generally described in μg/C to allow quantitative comparison between materials independently of the arc current used.

In the vacuum arc, a large potential difference exists between the electrodes, which produces an electric field ($\sim 10^9$ V/m) (Rossignol et al. 2003), causing electron field emission at the cathode (Mackeown 1929). The high temperature of the cathode surface also causes electron thermionic emission. Hantzsche (2003) views the field strength as critical to achieving arc conditions. He explains that both thermionic and field emission are needed to produce the electron emission density required for arc conditions to occur. Since the electrons travel faster than the atoms, a 'potential hump' is formed in front of the cathode surface, forming a sheath potential drop between the surface and the sheath edge. The accelerated electrons have sufficient kinetic energy to ionise nearly all the metal atoms near or within the potential hump in a region known as the Pre-sheath or Ionisation zone. The escaping ions have been shown to be multiply-charged depending on the arc discharge time (Anders 2001). Some of the generated ions are attracted back to the cathode surface, accelerated by the potential drop caused by the

potential hump, and produce a sheath of positive ions over the cathode surface. The bombardment of returning ions is the main cause of cathode heating. Liquid metal droplets or macroparticles are also ejected from the cathode spot, but travel much slower ($\sim 10^2$ m/s) than the ejected ions ($\sim 10^4$ m/s) (Anders et al. 1993, Polk et al. 2001). Typical ion current densities and heat fluxes are roughly on the order of 10^{10}–10^{12} A/m^2 and 10^9–10^{13} W/m^2 respectively (Polk et al. 2001).

The quasi-neutral plasma is accelerated outwards against the direction of the electric field, producing thrust. Plasma acceleration is generally complex since more than one mechanism is involved. Three main ion-accelerating mechanisms have been identified: a high pressure gradient produced from the plasma cloud in front of the cathode, electrostatic attraction of the negative 'potential hump' and electron-ion friction (electrons imparting momentum to ions by collision). Minor mechanisms such as Joule heating and electromagnetic forces have also been identified as possible accelerating mechanisms (Rysanek & Burton 2003, Hantzsche 1991). Typical plasma densities are roughly on the order of 10^{24} m^{-3} and the escaping ion current is about 7–10% of the arc current (Polk et al. 2001).

2.3.2 Summary of Vacuum Arc Theoretical Models

Vacuum arc theory is rich with various theories concerning the cathode spot and the surrounding region. Overviews of these theories are published by Hantzsche (1983) and Beilis (2001b). A unified vacuum arc theory is still in progress, due to the complex behaviour of the vacuum arc. The most early analytical models are those of one-dimensionality and a steady state nature. A number of authors (Hantzsche 1991, Rethfeld et al. 1996, Mitterauer & Till 1987) employ numerical methods of solution that are required to solve conservation equations of mass, momentum and energy. Others such as Riemann (1989) follow Ecker's example of defining arc existence regions to account for uncertainty in vacuum arc analysis. These regions are defined by irrefutable physical inequalities based on energy and mass conservation. Two types of arc regions, namely mode (0) and (1), as defined by Ecker, were discovered at which the arc could exist (Lafferty 1980). Mode (1) is characterised by more intense arc properties such as surface temperatures of $\sim$5000 K, electric fields strengths of $\sim 10^{10}$ V/m and total current densities of $\sim 10^{12}$ A/m^2 compared to mode (0) (3500 K, 10^9 V/m, 10^{10} A/m^2). Non-refractory metals, such as aluminium and copper possess both modes as possible arcs existence areas, but prefer to operate in mode (0) for stability reasons (Lafferty 1980). On the other hand, refractory metals such as tungsten and magnesium only occur in mode (1) (Lafferty 1980). To improve the accuracy of vacuum arc analysis, Hantzsche (1983) realized the importance of developing dynamic multi-dimensional models of the cathode spot region. However, these models are highly complex and have yet to completely describe the interaction of the many processes in vacuum arcs, discouraging their use in this work.

Concerning acceleration of the plasma, Weickert (1987) developed a model of the plasma jet taking into account all main accelerating mechanisms. However, his theoretical model is quite complex and beyond the scope of this work. Plasma jet simulations by Keidar et al. (2005) and Mitterauer & Till

(1987) are also beyond the scope of this work. The *Zero Order Model*, which assumes a quasi-neutral plasma in local thermodynamic equilibrium (LTE) is the most simple of plasma models (Boxman et al. 1995). Kutzner & Miller (1989) discussed the earliest two main theories concerning the acceleration of the plasma, namely Potential Hump (PH) and Gas Dynamic (GD) theory. PH theory attributes the potential drop as the primary accelerating mechanism and assumes that all ions are formed at the same potential, whilst GD theory attributes the plasma pressure as the primary accelerating mechanism and assumes that all the ions are formed at the same velocity. While both theories given reasonably good results compared to experiments for mean ion charge states and energies, neither performs well for describing the charge states and energies of individual ions. Both accelerating mechanisms are extremes of each other, and are actually dependent on one another, suggesting the need for a 'middle-ground' theory (Rysanek 2007b). Kutzner & Miller highlighted a modified version of the GD theory, called the Kharkov-modified Gas Dynamic (KGD) theory, which attempts to account for the effect of the ion charge state on its kinetic energy by means of a simple power law. Kutzner & Miller concluded that the KGD theory predicted the best average ion velocity results when compared to experiments. However, the ion velocity distribution implied by the theory, which suggests that individual ions with higher charge states travel faster, is debatable amongst researchers. Studies by Yushkov et al. (2001) and Byon & Anders (2003) revealed that this is not the case even though higher *average* charge states produce greater velocities and that the velocity distribution itself is dictated by effects currently unaccounted for. For physical correctness and simplicity, this work shall use the explanation of the gas-dynamic acceleration mechanism by Yushkov et al. (2001) to ascertain the mean ion velocity.

2.4 Summary

Preliminary design aspects of VATs were studied and thrust measurement techniques identified. The vacuum arc thruster can operate over a wide power range, provides an elegant means of generating plasma and can adopt a variety of design configurations. However, predicting and measuring the low thrust generated by the VAT is a challenging task. Both direct and indirect methods of thrust measurement can be used for experimental testing of the VAT. The vacuum arc model most commonly studied is that of describing the cathode spot region in a one-dimensional steady state model, although increasingly more dynamic spots models are being pursued.

Chapter 3

Thruster and Power Circuit Design

This chapter describes the design process in choosing a suitable VAT and pulsed power circuit. A number of conceptual designs are presented. A product requirement specification was created to enable the designer to make a suitable design choice of thruster geometry and basic functioning (See Appendix B). A final VAT and pulse circuit design is presented in detail and basic thruster operation is explained.

3.1 Conceptual Design

3.1.1 VAT Power Circuit

The only VAT pulse circuit found in literature was the inductive driver. However, a capacitive driver can also be used by placing a capacitor in parallel with the thruster and charging it to the breakdown voltage of the electrode gap. Capacitive drivers are simple to produce and can produce high currents at short pulses and thus have low heat dissipation during the charge-up phase. However, charge-up times are longer, which limits the pulse rate of the VAT and arc pulses have a 'spike' shaped profile. A PFN may be used to flatten the profile. However, for electrical simplicity, this work only considered pure capacitively-produced arcs.

3.1.2 VAT Concepts

Several design concepts were explored to address key areas such as the thruster head, use and viability of a feed mechanism and mounting/fastening options (Figure 3.1). The features of each concept are described below.

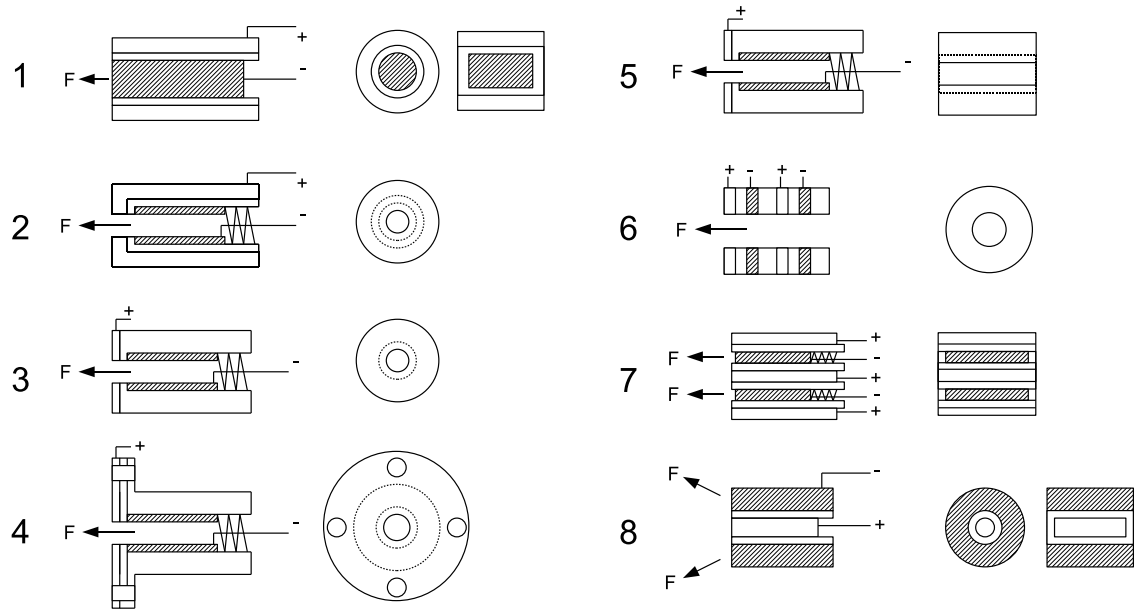

Figure 3.1: VAT concepts

Concept 1: Simple Electrodes, No Feed Mechanism

The first concept is the simple assembly of two coaxial/planar electrodes separated by insulator. The electrode and insulator faces are flush to one another. No feed mechanism is available. Most concepts described below are derived from this one.

Concept 2: Coaxial, Hollow Cathode with Feed Mechanism

Based on concept 1, the thruster has a spring feed mechanism that pushes the hollow cathode against a layer of insulation. Both are fixed by the anode. The recessed cathode minimises spacecraft contamination at the expense of lower thrust and possible anode erosion.

Concept 3: Variation of Concept 2

This concept variation is designed to reduce the amount of surrounding anode, but risks exposure of insulator material to the space environment

Concept 4: Head Variation of Concept 3

This concept includes a bolt mounting scheme and insulator separator ring.

Concept 5: A Planar Variation of Concept 3

Concept 6: Tubular Geometry

Electrodes and insulator rings are layered to form a tube. No feed mechanism is present. The thruster may be extended with additional layers of material to increase thruster capacity.

Concept 7: Planar Cluster

Rectangular wafers of electrode and insulator are fastened together with bolts. A spring mechanism feeds the cathode wafer. The cathodes are guided by shaped intermediate insulator layers. This concept has high potential for scaling, cluster formation and component modification.

Concept 8: Inverse Sandwich

The locations of the anode and cathode are reversed so that the anode is surrounded by bulk cathode material. No feed mechanism is present. This concept carries the same advantages as concept 7. Whilst simple, the contamination from the exhaust plume is likely to be great and the thrust vector not as straightforward to control since the arc may initiate at any point on the surrounding bulk cathode material.

3.1.3 Concept Evaluation

As an example, to accomplish the goal of providing a velocity change Δv of say, 5 m/s, a suitable amount of propellant must be available for consumption. Using the classic rocket equation

$$\frac{m_p}{m_o} = 1 - \exp\left(-\frac{\Delta v}{I_{sp} g}\right) \tag{3.1}$$

where m_p is the propellant mass, m_o is the satellite mass, I_{sp} is the specific impulse and g is the gravitational acceleration constant. For example, assuming a typical VAT specific impulse of I_{sp} = 1100 s and m_o = 5 kg, a propellant mass of m_p = 2.32 g results. As an preliminary design, aluminium (ρ = 2.7 g/cm^3 (Hatch 1984)) was used as cathode material, given its high specific impulse and thrust-to-weight ratio performance in vacuum arc thruster tests (Polk et al. 2001, Schein et al. 2002). Thus, a cathode material volume of m_p/ρ = 2.32/2.71 = 0.855 cm^3 is required. This translates roughly to a 30 $\times$ 30 mm plate of 1 mm thickness, a 10 mm diameter tube of 1 mm wall thickness and 30 mm length, a 2 mm diameter rod of 270 mm length or a 0.5 mm diameter wire of 4350 mm. Using thin cathode wire is only feasible if a reliable feed mechanism is available to insert the wire at the same rate as the erosion rate. Wire would most likely be wrapped as a coil rotated by an electric motor.

Both the thin rod and wire shapes are impractical to store on-board. The thin rod and flat plate designs also require feed mechanisms. A tubular design would also require many layers of cathode material, which may become impractical without increasing the tube diameters. There are some perceived weaknesses with the coaxial configuration: (a) although a rotating motor may be used to feed cathode wire into the thruster, electronic control would be needed to monitor the erosion rate in real-time; (b) it is foreseeable that the long rod design would experience bending loads during launch, which is an added risk. The planar design was thus deemed the most compact form for carrying propellant.

Thus, it was also recognised that a feed mechanism was necessary to achieve the required Δv. This eliminated concepts 1, 6 and 8. (It was also argued that concept 8's exhaust would cause too much contamination). It was also concluded that the cathode must either be in a plate or hollow tube form to satisfy compact propellant storage and simplicity in the feed mechanism. Exposure of the insulator to the space environment was of some concern, especially the effects of outgassing and atomic erosion. Since the insulator would require some form of protection, it seemed simpler to use the anode for that purpose. Thus concepts 3–5, which expose a significant proportion of insulation, were eliminated. Each VAT geometry (coaxial, tubular and planar) has various strengths and weaknesses as shown below in Table 3.1. Coaxial and planar concepts 2 and 7 are compared in Table 3.2 below.

Table 3.1: Comparison of thruster geometries

Geometry	**Strengths**	**Weaknesses**
Coaxial	Well-directed thrust Allows for feed mechanism	Difficult to scale and modify Smaller cathode cross-section
Tubular	Minimal spacecraft contamination Scalable	No feed mechanism, limited propellant Mounting difficulties
Planar	Modifiable, scalable Greater cathode cross-section Feed mechanism Easy manufacture and replacement	Less accurate thrust vector Greater spacecraft contamination Less accurate thrust vector

Table 3.2: VAT concept evaluation (1–low, 2–med, 3–high, more points represents a better choice)

Evaluation criteria	**Planar**	**Coaxial**
Minimising Spacecraft contamination	2	3
Simplicity	3	3
Ease of Manufacture	3	1
Flexibility	3	2
Compactness	2	2
Low mass	2	2
Total	**15**	**13**

3.1.4 Conclusions

VAT concept 7 (planar) was the concept of choice. It allowed for a large amount of propellant, inclusion of a spring feed mechanism and minimised insulation exposure to the space environment. A capacitive discharge power circuit was used because of its relative simplicity of operation.

3.2 Preliminary Designs

It was envisaged that the thruster position on a cubic satellite would be on the outside edges to allow for translational and rotational motion. Thus, a thruster is placed in each corner of the satellite, facing away from one another. Nominal operation consists of a minimum of two, and a maximum of four thrusters to operate at any given time during a translational or rotational manoeuvre. It was calculated earlier that the volume of propellant needed was 0.855 cm^3. Since a maximum of four thrusters can be used to achieve the manoeuvre, the propellant volume shall be quartered to 0.214 cm^3. Commercially pure aluminium was used as the cathode for good performance (Polk et al. 2001), low cost and ease of machinability/manufacture. The cathode dimensions were $10 \times 16 \times 2$ mm for a conservative approach. The anode was made of low cost 25 mm square aluminium plates of 1 mm thickness placed on the top and bottom of the cathode-insulation piece. Two 1 mm thick alumina ceramic layers separate the electrodes and a two additional pieces were made to guide and fix the cathode in place. A flush electrode gap in the front of the thruster allows for arcing to occur. The electrode and insulator materials were found to be suitable for the space vacuum environment (William A. Campbell & Scialdone 1993). The entire thruster was designed such that it could be fastened with bolts to a circuit board which could also hold the electronic components powering and controlling the thruster. Figure 3.2 illustrates the VAT design.

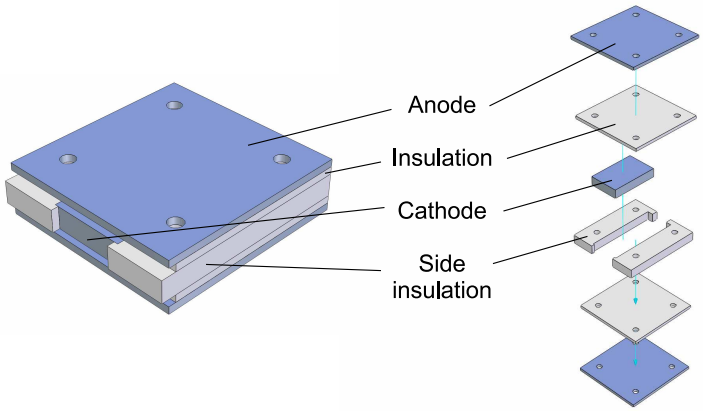

Figure 3.2: Illustration of VAT design

An initial power circuit was designed to use a high voltage (HV) regulator to convert the voltage from 12 V to 500 V at 2 mA (see Figures 3.3 and 3.4). Two 0.47μF 630 V capacitors in parallel were used to

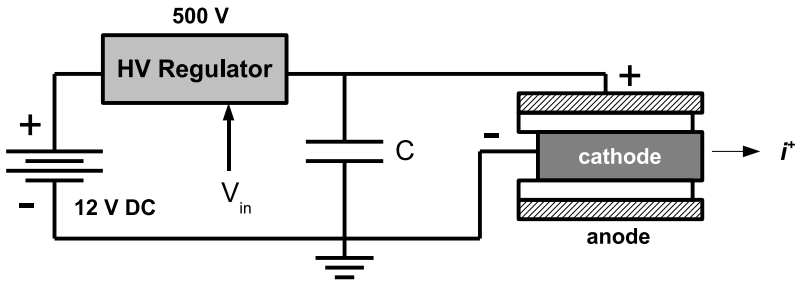

Figure 3.3: Schematic of preliminary VAT power circuit design

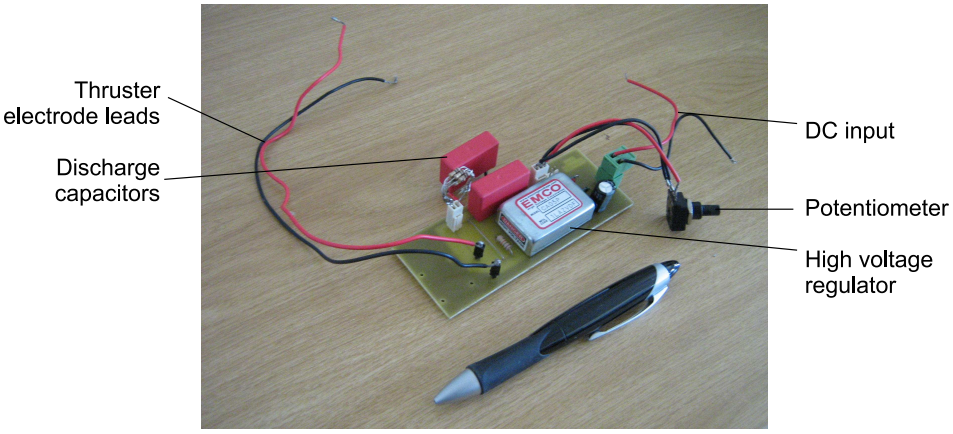

Figure 3.4: Figure of preliminary VAT power circuit design

store energy. The pulse cycle was controlled by the charge time of the capacitors. A potentiometer was used to control the voltage output of the regulator. Initially, graphite (by means of pencil marks) was applied on the interelectrode insulation based on the recommendations of Anders et al. (1998) and Anders et al. (2000). Initial tests showed that although 500 V may have been sufficient for an initial arc triggering, the pre-arc current flowing through the thruster was too low to allow the conducting layer on the insulator to heat up and dissipate to form the initial plasma for continuous and reliable arc triggering. Hence, a more powerful version of the initial circuit was made to produce larger voltages (see the final design in the next section). It was felt that due to the nature of the short, high current arc pulse of the capacitive driver, a combination of the triggerless and HV flashover method should be utilized. HV breakdown (a few kV) of the gap would also be more suitable to improve triggering reliability over the thruster's lifetime. However, the thruster was shown to be highly sensitive to the size of the conducting layer on the insulator. Repeated tests showed that with subsequent pulses, the graphite dissipated easily (despite application of a thick layer) and the gap increased in size for several pulses, resulting in an increasingly higher breakdown voltage. Scratching aluminium onto the insulator faired slightly better, but only for slightly more pulses than graphite. Alternatively, electrically conductive silver paint was applied across the insulator to provide a much thicker conductive layer than the previously applied graphite and aluminium. In so doing, the silver layer will not be overcome by Joule heating and instead remain on the insulator until it is eventually replaced by cathode material. In addition, silver and aluminium have similar boiling points (2435 K

vs. 2792 K) and vapour pressure curves. Thus, it is expected that similar evaporation rates of the conductive layer and cathode will prolong the thruster's potential operation. However, it was extremely difficult to repeatedly apply a thin layer of silver to form a small (10–100 μm) gap to the cathode and this approach was eventually abandoned also.

Using only HV breakdown of the 1 mm insulator gap was shown to be require very high ($>$ 4–5 kV), which was deemed undesirable. Thus, efforts were made to shorten the insulator gap between the electrodes using a ceramic coating as opposed to a ceramic sheet. A 10 μm TLHB ceramic coating from Powerkote was applied to the anode plates. However, the breakdown voltage of the coating was found to be very low ($<$ 100 V) and therefore insufficient for use. The use of micanite sheets as another form of insulation was successfully employed. Mica proved to be highly resilient to HV breakdown and high temperatures. Thin layers ($\leq$ 0.2 mm) of mica could be used and easily shaped due to their flexibility and more suitable breakdown voltages of 1–2 kV could be achieved. Care was taken that the thruster gap was not made too thin such that short circuiting occurs. A suitable mica sheet thickness was found to be in the region of 0.1 mm.

To form side insulation on either side of the cathode, alumina ceramic sheets had to be cut with an ultrasonic milling machine to create holes for the screws. Although somewhat successful, it was found that the ceramic suffered cracking after some time possibly from microcracks formed during manufacturing. Instead, Teflon (PTFE) pieces were formed as side insulators because they could be easily formed and replaced. However, Teflon has a tendency to fail more easily since it has a much lower dielectric strength than alumina and a burning temperature of $\sim$250 °C.

3.3 Final Design

The final VAT design is comprised of 25 mm square 1 mm thick aluminium anodes, a 10 $\times$ 16 $\times$ 2 mm aluminium cathode, 24 $\times$ 25 mm $\times$ 0.1 mm micanite sheets as the main electrode insulation and Telfon as side insulation (see Figure 3.5). The cathode is recessed by 1.5 mm from the front end to limit the amount of the liquid droplets escaping and potentially contaminating the spacecraft. However, this will also limit the amount of useful thrust produced by the VAT. The arc is now triggered using the HV flashover technique which removes the need to apply an trigger-enhancing conduction layer on the insulation between the electrodes. It is possible for a spring feed mechanism to be installed behind the cathode. However, a spring mechanism was omitted for the design as cathode erosion would be very small during tests, making feeding unnecessary. Detailed design drawings of the thruster are presented in Appendix C.

The final power circuit design is made up of a capacitive discharge circuit/driver powered by a standard laboratory 40V DC Power supply (see Figure 3.6). An ignition coil is used to transform the supply voltage up to 25 kV. A NTE517 rectifier diode (15 kV, 550 mA max current) rectifies the voltage input. A normally open IRF840 transistor switch is used to provide pulsed charging of the capacitor.

HV capacitors (6.3 kV, 100 nF total) provides the high arc current once voltage breakdown across the gap occurs. Bleeder resistors (0.5 W series resistors of 33 kΩ total resistance) are also provided to protect the diode in the event of a thruster short circuit. A Topward 8140 Function Generator provides a 8 V square wave of desired frequency to the transistor switch, allowing control of the pulse discharge rate. The transistor switch has a on-off-on switching limit of 2 μs.

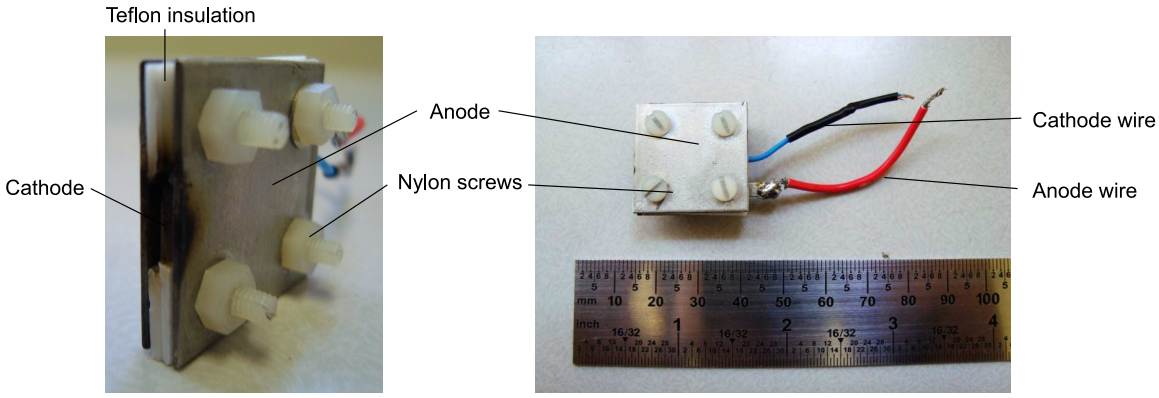

Figure 3.5: Final VAT design

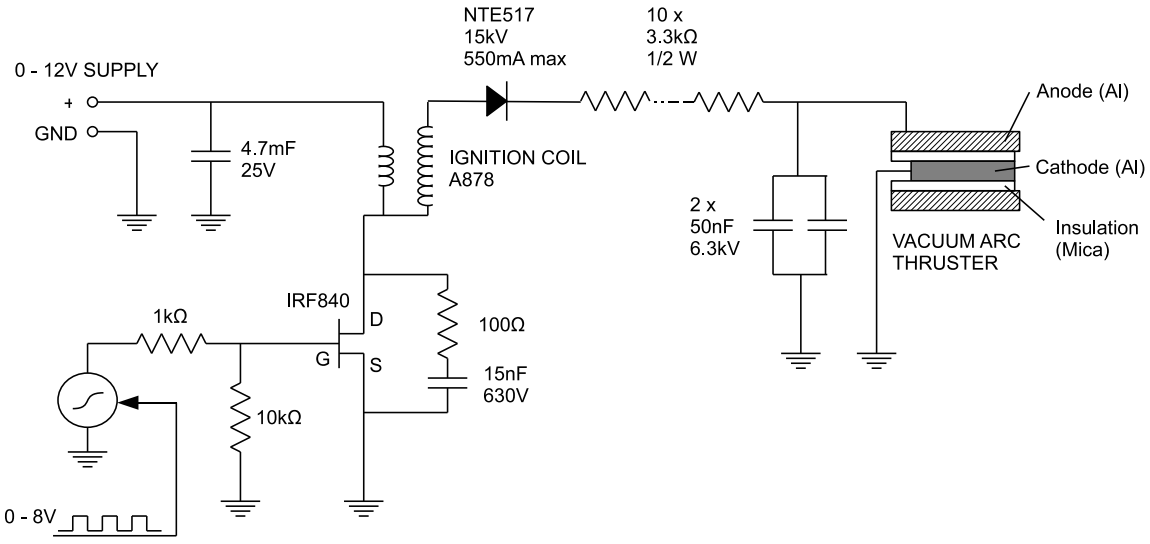

Figure 3.6: Final VAT capacitive power circuit

3.4 Thruster Operation

Figure 3.7 shows the typical voltage across the thruster over time. The capacitor charge rate is controlled by the transistor switch to gradually charge in an exponential fashion, eventually reaching the gap's breakdown point. At that point, an arc discharge occurs and the capacitors release all their energy into the thruster arc. The process then repeats for the next discharge. The user is able to manually adjust the transistor switching frequency and DC voltage input to control the thruster charging rate (or pulse rate). Fluctuating breakdown voltages are often observed during thruster operation. There are a number of possible reasons: (1) small amounts of macroparticles deposit back onto the thruster in the cathode-insulation region, which reduces the electrode gap and makes the subsequent arc easier to arc at a lower breakdown voltage; (2) tall microstructures (possibly formed also by condensed macroparticles) on the cathode surface are melted down, so the next arc has to occur at the next highest microprotrusion, thereby increasing the gap; and (3) it is also observed that operating the thruster at higher pulse rates tends to result in lower breakdown voltages. This occurs because the cathode surface is still hot from the previous arc event, making it easier for the next arc to occur. Also, ionised vapour from the previous arc event may still be in the cathode region, providing a conducting medium for the next arc initiation. This means that the breakdown voltage cannot at this point, be controlled by the user, other than with the pulse rate. Even then, the breakdown voltage remains relatively 'constant' beyond a pulse rate of 20–30 Hz. An important consequence of this effect is that the arc current discharged by the capacitors is entirely dependent on the breakdown voltage. Therefore, a relationship between the breakdown voltage and the average arc current must be formulated in order to make a comparison of experimental data with theory (see Section 4.1).

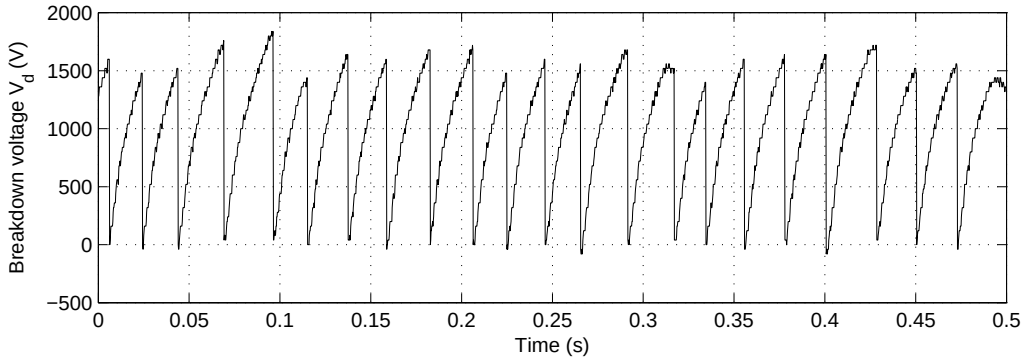

Figure 3.7: Typical thruster discharge voltage over time

Initial tests showed the voltage profile (Figure 3.8) of a single discharge contains prominent oscillatory portion. This behaviour is due to the inductance of the wire leads between the capacitors and the thruster. Thus, whenever possible, the capacitors were connected as close as possible to the thruster to reduce this oscillatory effect. The voltage and current signals were filtered with first- and second-order low pass Butterworth filters, with cut-off frequencies of 25 MHz and 12.5 MHz respectively. The induction-causing oscillations after the discharge occurred were ignored in determining the arc current.

The arc current is obtained by measuring the voltage V across a capacitor C and using basic circuit theory,

$$I(t) = -C\frac{dV(t)}{dt} \tag{3.2}$$

and the arc power is

$$P(t) = I(t)V(t) \tag{3.3}$$

Figure 3.8 is an example of typical arc discharge profiles (breakdown voltage V_d = 1800 V). Note that in the capacitively powered circuit, the breakdown voltage profile becomes the arc voltage [1].

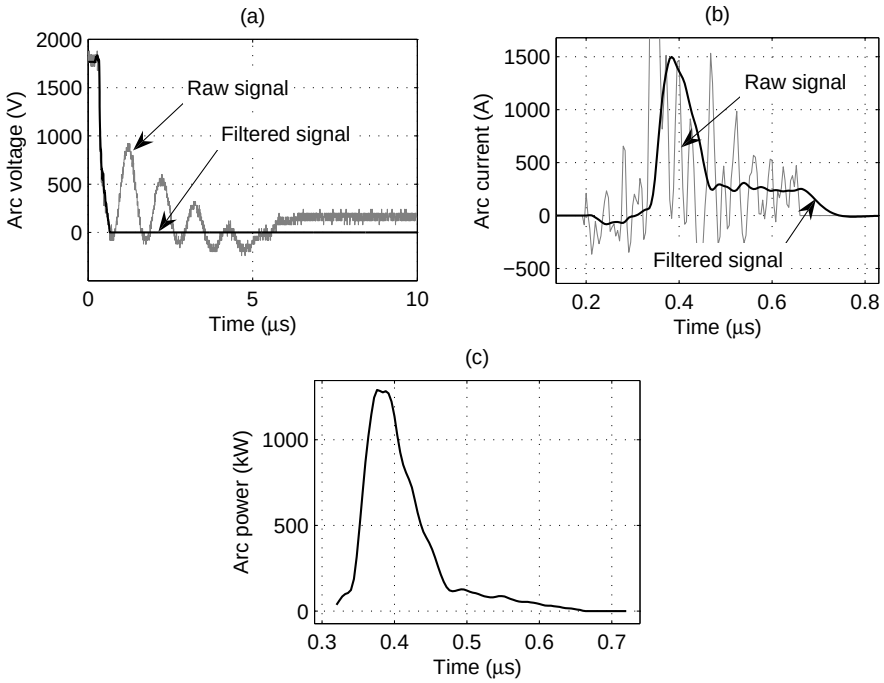

Figure 3.8: Typical (a) arc voltage, (b) current and (c) power profiles

3.5 Summary

A vacuum arc thruster was successfully designed using a planar design. The anode and cathode is made of aluminium and the insulation layer made of micanite sheets. A HV flashover technique was used to initiate the arc and a pure capacitive driver was built to deliver high current to the thruster. The thruster pulse rate can be partially controlled with a transistor switch and DC voltage supply, but the arc current depends on the breakdown voltage of the thruster gap. The power circuit is capable of delivering up to 800 A of average arc current per pulse at pulse rates between 10–100 Hz depending on the breakdown voltage.

[1] This report uses these two terms interchangeably. However, a distinction must be made for other types of pulse circuits, which may use a different breakdown voltage from the arc voltage to initiate the arc.

Chapter 4

Experimental Work

Experimental work was performed to study the thruster's behaviour and verify its operation and performance. This chapter explains the experimental design, setup, analysis and test procedures. The quantities to be measured are the thrust, ion velocity, ion current and erosion rate of the VAT. A thruster and pulse circuit was built (see Chapter 3) and tested in high vacuum (all tests were done between 1×10^{-4} and 2×10^{-5} Torr). Direct and indirect methods of thrust measurement were designed and used. All experiments were performed in an Edwards Model E12E Bell jar vacuum chamber in the Superconducting Lab, Electrical and Electronic Engineering Department (Figure 4.1). A roughing and diffusion pump allows the chamber to achieve pressures of up to 10^{-6} Torr. A high voltage probe (15 kV, $1000\times$ attenuation) was connected to a Tektronics TDS 1012B two channel digital storage oscilloscope to read the voltage drop across the capacitors. The chamber contains electrodes for supplying power to the thruster as well as earth ground electrodes. An additional chamber leadthrough was built to allow electrical cabling from experimental test equipment within the chamber to pass though to the outside environment.

4.1 Arc Current, Voltage and Power

An average arc current and arc power was calculated from their respective discharge profiles to enable practical comparison between experimental tests and the analytical model of the VAT. This was performed for a range of breakdown voltages to establish a convenient relationship between arc voltage, arc current and arc power (See Figures 4.2 and 4.3) as follows:

$$I_d = 0.24V_d + 4 \tag{4.1}$$

$$P_d = 0.0013I_d^2 - 0.0093I_d + 14 \tag{4.2}$$

where the units of V_d, I_d and P_d are V, A and kW respectively. When studying the discharge profiles, it was observed that the discharge time for the arc was approximately $t_d \approx 400$ ns for a wide range of

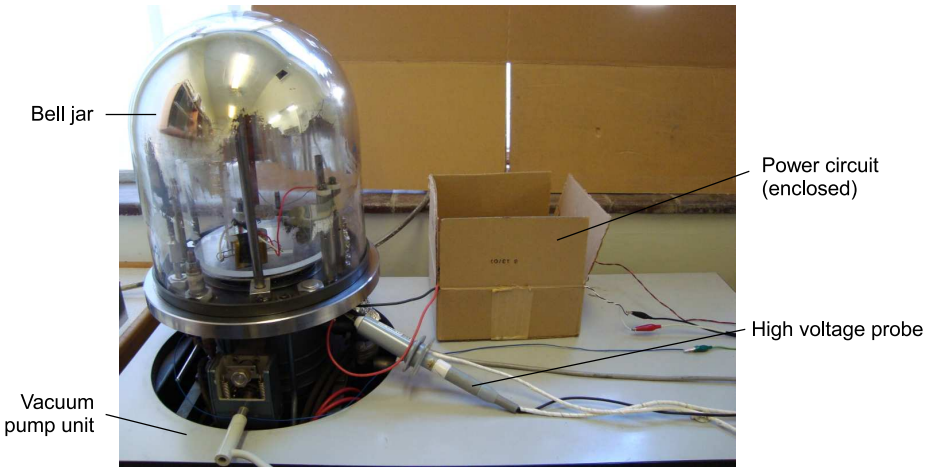

Figure 4.1: Vacuum chamber setup

breakdown voltages. This is evident in the linear relationship between arc voltage and (average) arc current. A consequence of the linear relationship is that arc power has an exponential relationship to (average) arc current and arc voltage.

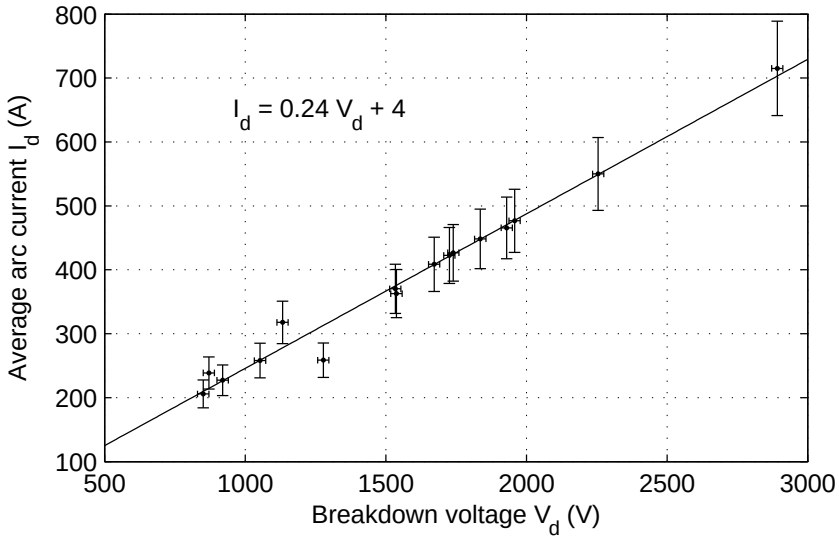

Figure 4.2: Average arc current against arc voltage

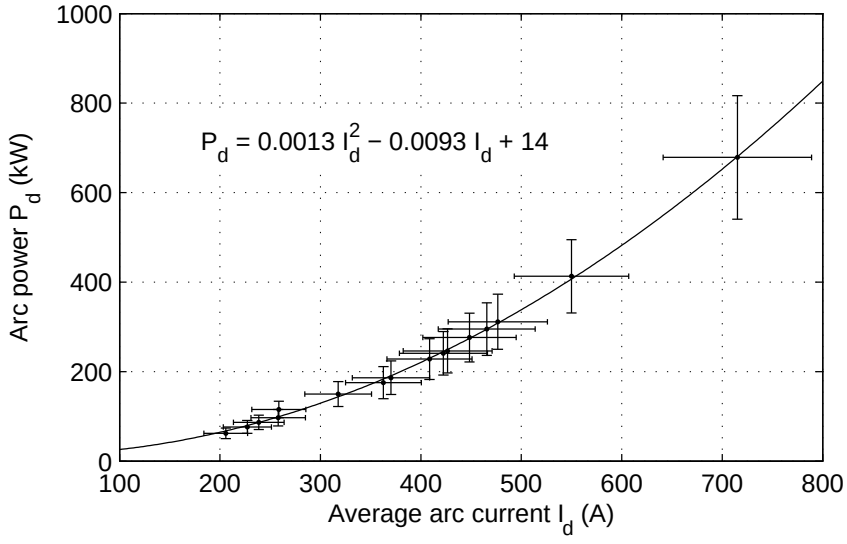

Figure 4.3: Average arc power against average arc current

4.2 Direct Thrust Measurement

4.2.1 Design of the DTMS

A product requirement specification was created (Table 4.1) as an objective basis for choosing a suitable thrust measurement system. Three concepts for a direct method of thrust measurement were created and evaluated against Table 4.1 and a preliminary designs for the DTMS was developed.

Table 4.1: Thrust measurement system requirements

Functional Requirements	**Priority**
Not significantly interfere, mechanically or electrically, with the ability to measure thrust	High
Operate in vacuum	High
Not introduce significant friction against the direction of the thrust vector	High
Be able to measure thrust (average or pulsed) as a function of time	High
Have a minimal amount of moving parts	Medium
Non-functional Requirements	**Priority**
The measurement system must fit inside the available vacuum chamber	High
Use as much locally available materials and components as possible	Low
Use as much easily accessible materials and components as possible	Medium
No maintenance required during a vacuum test	High
Use minimal number of electrical leadthroughs to the vacuum chamber	Low
Provide sufficient electromagnetic interference (EMI) protection to the signal cables	High
Must be able to be calibrated	High
Low cost	Medium
Short manufacturing and development time	Medium
Minimal material outgassing	Low

Generation and Evaluation of DTMS Concepts

The first design concept is the use of a cantilever beam (Figure 4.4 (a)). The displacement or strain of a thin beam fixed at one end is measured and the steady state thrust inferred. Numerous methods of strain/displacement measurement include: laser deflection, optical interferometry, strain gauges and linear displacement sensors. Calibration can be done with small mass loads.

The second concept is the use of a swinging arm (Figure 4.4 (b)). A thin pivoting beam is disturbed by the thrust and the end displacement measured. Two types of pivoting mechanisms may be used. One method is to fix one end of a pendulum to a frictionless bearing for support and swiveling. The sensors used for steady state thrust measurement are similar to the cantilever beam. A second method is to build a neutrally stable pendulum with equal mass on either end (the thruster and a counterweight) and supported at the center of mass of the pendulum system. This concept was used by Lafleur (2007). Calibration can be done with small mass loads.

The third concept is a rotating balance (Figure 4.4 (c)). The thrust produces a torque which rotates a swing through a measurable angle. The rotation angle can be measured visually or even movement of a laser point reflected off a mirror. A frictionless bearing is required to support and swivel the swing. A counterweight is placed at the opposite end of the swing to balance the thruster. The balance may be calibrated electrostatically (Gamero-Castaño 2003).

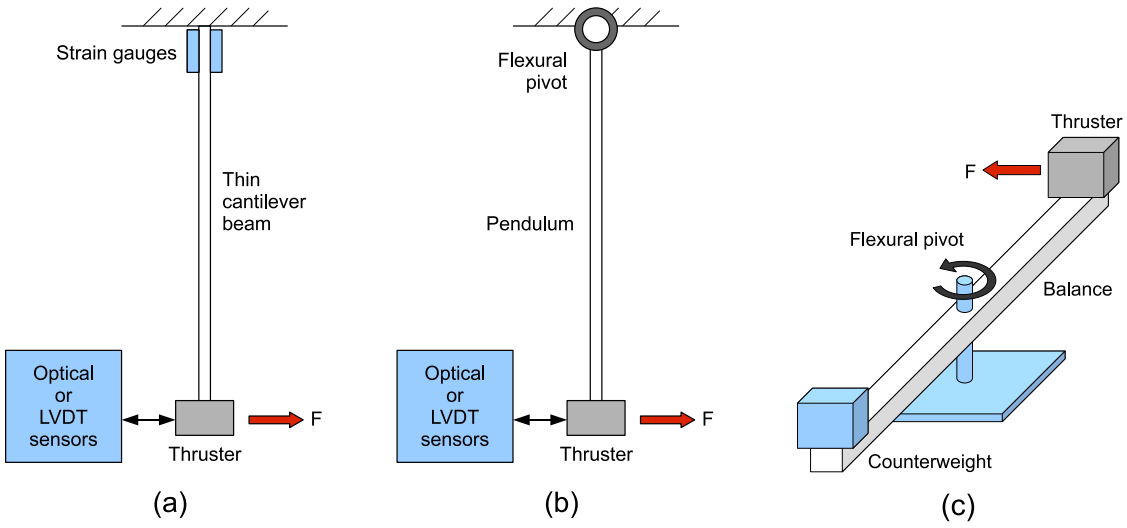

Figure 4.4: DTMS concepts (a) 1, (b) 2 and (c) 3

Although similar in function to the cantilever beam, the pivoting balance is more suited to constant thrust since it is a heavier system and will respond much slower to short thrust pulses. The rotating swing will only be able to measure average thrust levels from a set thruster operation time. This method is also conceptually elegant and simple and the accumulated rotation angle can be measured reliably if a long test time is used. The greatest difficulty lies in obtaining a frictionless bearing and its ability to handle axial loads from the swing and thruster. The cantilever beam is relatively

easy to manufacture out of metal, available in sheets as thin as 0.1 mm. The thrust stand can be easily designed to fit inside a vacuum chamber. No complex components are required other than the displacement/strain sensors. The cantilever beam is also capable of measuring an individual thrust pulse. Weaknesses with the cantilever method are that the beam may experience strain hardening over time and that any connecting leads and strain gauge sensors will increase beam stiffness.

Optical interferometry and laser deflection is probably the most accurate form of measuring displacement since it does not, in this case, interfere mechanically or electrically with the thrust measurement. Also, the measured signal can be amplified outside the vacuum chamber. However, space limitations in the test room and vacuum chamber make this difficult. For example, the beam must reflect over at least a few meters to allow a discernible visual measurement of laser beam movement. Also, calibration of the system would be difficult to achieve, since it would need to be done *in situ*. Equipment such as lasers, mirrors and photonic sensors also have a high cost and expected long design/development time. Proximity sensors that use capacitance, inductance or magnetic fields to measure deflection were not seen as suitable because they would need to be placed very close to the thruster and it's leads, which emit large amounts of disruptive electric fields. This would be expected to adversely affect sensor functioning or even damage sensors. In addition, sensors such as LVDTs (with a suitable sensitivity and accuracy for this project) have a high cost. Strain gauges have low cost and can be positioned some proximity away from the thruster. However, strain gauges may require shielding from electromagnetic interference (EMI). It was eventually decided to use the cantilever beam with strain gauges for reasons of low cost, ease of theoretical modeling and ease of manufacture. A metal beam was used for obtaining linear behaviour.

Preliminary Designs

To measure a quasi-static force on a cantilever beam, one may use the well-known Euler-Bernoulli thin beam theory

$$\sigma_x = E_b \epsilon_x \tag{4.3}$$

$$\sigma_x = \frac{F_b L h}{2 I_b} \tag{4.4}$$

$$I_b = \frac{1}{12} b h^3 \tag{4.5}$$

where σ_x is the beam stress, E_b is Young's modulus of the material, ϵ_x is the beam strain, F_b is the applied load, I_b is the beam's inertia about the neutral axis and L, b and h are the beam length, width and thickness respectively. Thus

$$F_b = \frac{2 I_b \sigma_x}{L h} = \frac{E_b \epsilon_x b h^2}{6 L} \tag{4.6}$$

For example, the expected force resolution of a copper cantilever beam (E_b = 130 GPa (Lide 2003)) with dimensions L = 200 mm, b = 20 mm, h = 0.1 mm and a strain gauge resolution of roughly 0.5 μmm/mm is 10.8 μN. The maximum possible average thrust expected based on literature (Schein et al. 2002) is $\sim$20 μN/W, which for a 5 W average input power, becomes $\sim$100 μN average thrust.

Thus, it is theoretically possible to measure quasi-static thrust from the VAT.

The thruster was mounted at the free end of a thin beam and electrically insulated from it. The beam was made of thin (0.1 mm) copper sheet metal, the dimensions of which are limited by the size of the vacuum chamber and thruster (200 $\times$ 20 mm). A perspex thrust stand was made to fix and support the copper beam vertically and to ensure pure bending at the fixed end. The beam was extended away from the stand such that two Vishay 120 Ω Gauge factor 2.075 strain gauges could be placed on either side to form a half-bridge configuration. This ensures temperature compensation and increased sensitivity to beam strain. The electrical cabling from the strain gauges are shielded with wire mesh to earth ground and travel through a chamber leadthrough to the external environment for signal capture. The strain gauge (SG) signals were amplified by a HBM Scout 55 bridge amplifier. Twelve Vishay ICTE-5 (1N6373) transient voltage suppressors (TVR) were installed on the signal line to prevent any possible bi-directional HV signal damaging the Scout 55 by directing any voltage higher than 10 V to earth ground. The cantilever beam was also grounded to earth for additional safety. Figure 4.5 is an illustration of a preliminary DTMS design and Figure 4.6 below is a schematic of the electrical connections of the DTMS.

Initial tests showed that measured beam strains from a thrust pulse were too small to be sufficiently detected by the strain gauges. To improve sensitivity, several modifications were made to the beam: (1) a large portion of the free end of the beam was stiffened with aluminium sheet to augment deflection at the beam base; (2) the strain gauges were rotated 180 degrees to reduce the stiffness contribution of the strain gauge connecting wires and soldered contact points (the strain gauge leads were initially installed on the beam itself); and (3) the beam width was narrowed to 9 mm at the fixed beam end to further reduce stiffness.

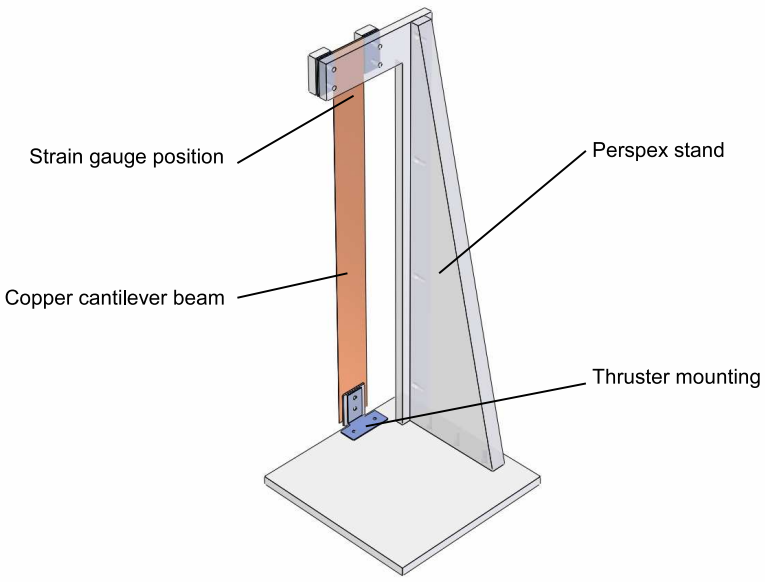

Figure 4.5: Schematic of preliminary DTMS design

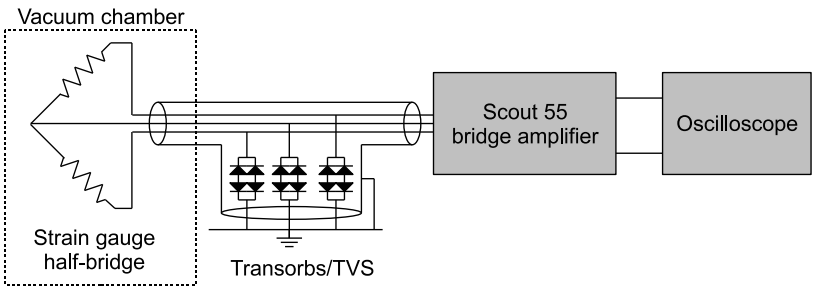

Figure 4.6: Schematic of DTMS setup

Despite these efforts, beam strains were still too small to be sufficiently measured. Reduced and inconsistent strain sensitivity over time due to beam and wire material strain hardening increased measurement difficulties. It was also found that increasing thruster pulse rates caused increasing signal corruption from EMI despite shielding efforts. This was due to the thruster and its leads emitting large electric fields upon the metal beam and strain gauges. This meant that measurement of an average constant thrust was not possible with the current setup. Thus, only a single thrust pulse could be studied, since EMI does not disturb the strain gauge signal after the pulse has occurred. It was identified that the DTMS, with all the additional structural modifications, would be very complex to describe analytically in order to find the deflection of the beam due to a thrust impulse. The simplest approximation would be to assume a *single-degree-of-freedom* (SDOF) vibrating system with a heavy thruster mass and light beam. In reality, however, the beam has appreciable mass, making the DTMS a *continuous* vibrating system. Even if a SDOF could be justified, repeated testing showed that the thruster's inertia was too great to be overcome by a single thrust pulse. Thus a different approach to measuring the thrust was needed.

Final Design

All the above limitations were overcome by measuring the thrust acting upon the beam instead of from it. The thruster was fixed at a small distance d_2 from the beam and pulsed at the beam end. The entire beam width was narrowed to 9 mm and the stiffened aluminium plates removed. Consequently, the greatly reduced mass of the beam allowed for a measurable beam deflection. A flat 45 $\times$ 25 mm deflector made of thin aluminium foil was attached to the beam end to receive a large portion of the exhaust plume exiting the thruster. An additional advantage of the final design is that the discharging capacitors can be placed close to the thruster, thereby reducing inductance oscillations in the arc voltage signal, which was not possible with the DTMS design described earlier. Consequently, a new theoretical approach was used to analyse the beam's response to an impulse (see Section 4.2.3). Figures 4.7 and 4.8 highlight features of the final design.

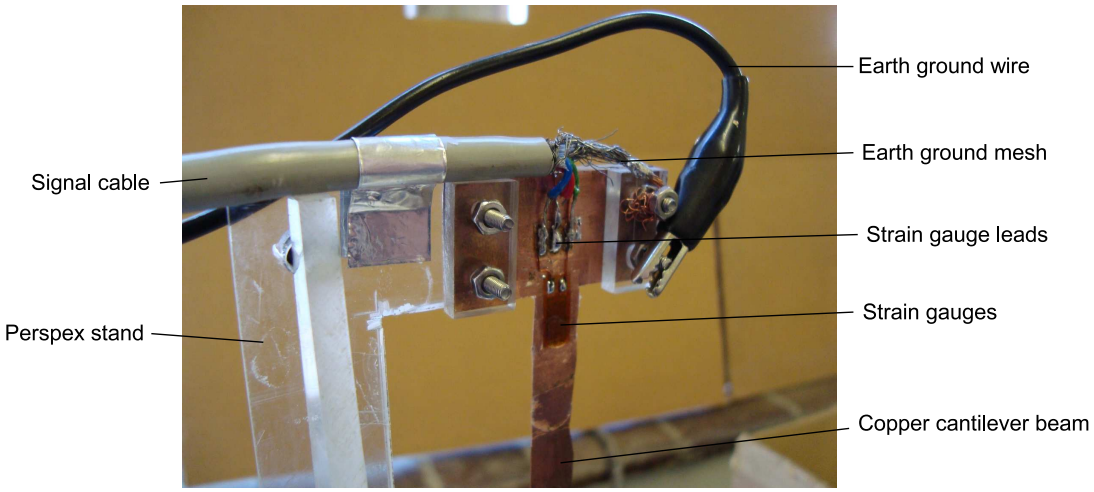

Figure 4.7: Closeup of the strain gauges and cantilever beam

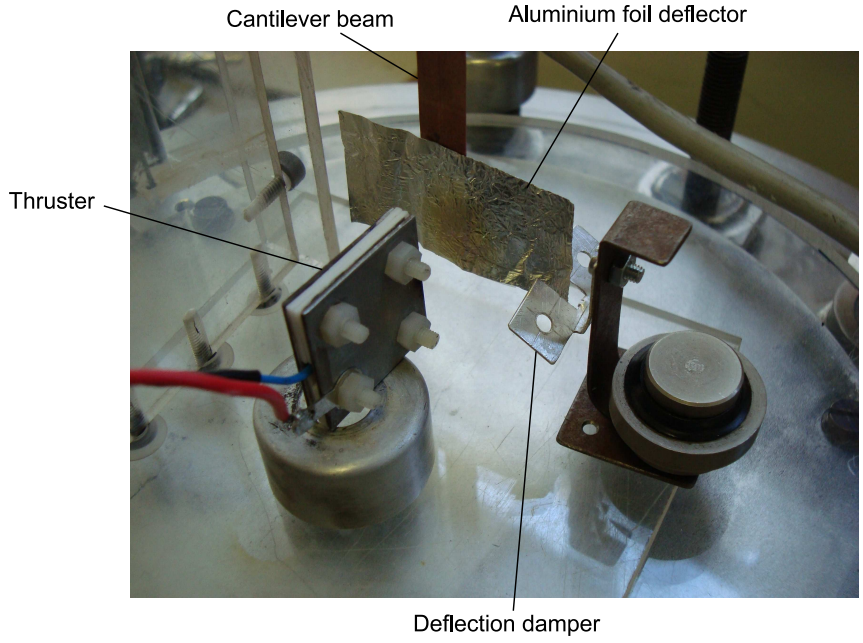

Figure 4.8: Closeup of the deflector

Care was made to place the thruster sufficient distance from the beam (d_2 >10 mm) to avoid significant electrostatic attraction from the thruster electrode during thruster charge-up, thus producing incorrect initial conditions for the beam, which is meant to be at rest. If the beam is too close when the thruster pulse causes the electric field to break down, the attracted beam is released at an initial displacement in the thrust direction, augmenting beam deflection.

The DTMS could only measure thrust once the vacuum pump had been switched off, since vibrations from the pump produced significant beam vibration. Thus, a waiting period of at least a few minutes is required for the beam to settled from the vacuum pump's vibrations to a stable signal indiscernible from random noise. However, a gradual increase in chamber pressure above 10^{-4} Torr

from pressure leaks usually occurred before the beam had sufficiently settled (the beam possessed very low damping). Thus, a deflection damper was added to help settle the beam more quickly by limiting the deflections caused by the vacuum pump running (see Figure 4.8). However, the beam is still made to vibrate freely.

In conclusion, a suitable DTMS that is capable of measuring a single thrust pulse was successfully designed and shown to measure the correct beam deflection. The final design is comprised of two strain gauges that measure the dynamic strain of a 200 $\times$ 9 $\times$ 0.1 mm copper cantilever beam subjected to a thrust pulse. A 45 $\times$ 25 mm aluminium foil deflector on the beam end captures the ions emitted from the thruster. Non-thrust disturbances such as EMI and electrostatic attraction were noted and eliminated.

4.2.2 Test Setup Description

The thrust stand was placed inside the vacuum chamber as shown in Figure 4.10. A circular perspex base plate insulated the chamber base from the entire test setup. The VAT was supported roughly 10–20 mm away from the beam facing the center of the foil deflector face. For convenience, 9 pin connectors are used to carry the SG signals between the strain gauges, vacuum lead-through and the bridge amplifier. A Scout 55 bridge amplifier was set to 4 mV/V sensitivity and provided a 2.5 V half-bridge voltage source. The Scout 55 amplified the SG half-bridge voltage signals and sent them to an oscilloscope for display and data storage (Figure 4.9).

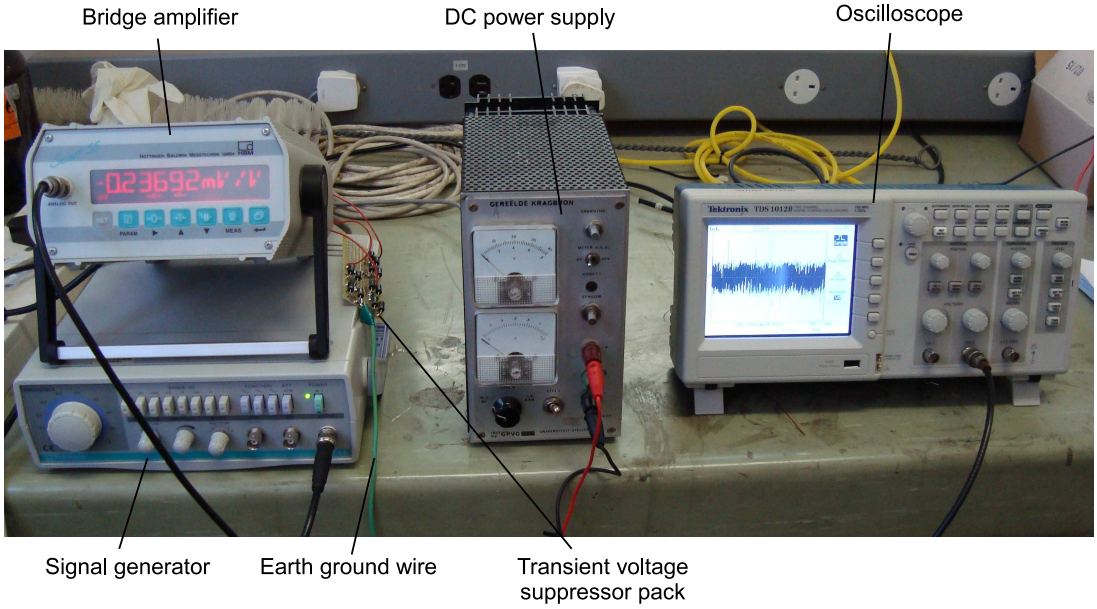

Figure 4.9: Photograph of DTMS test equipment

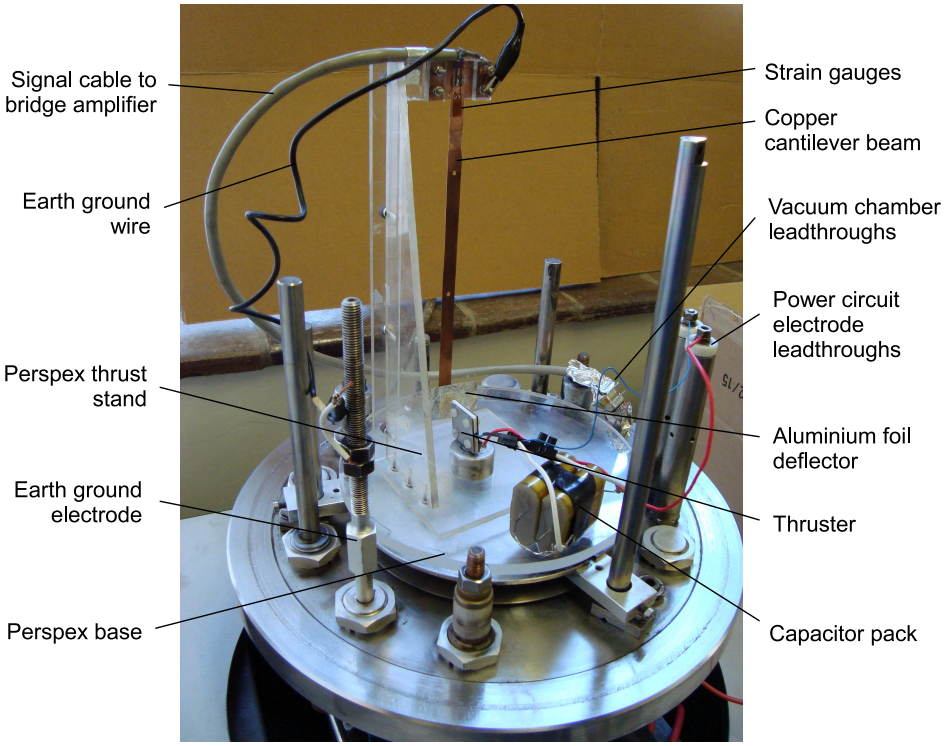

Figure 4.10: Photograph of the DTMS setup in the vacuum chamber

4.2.3 Experimental Analysis

The cantilever beam is classified as a *continuous* vibrating system, that is, a system with an infinite number of degrees-of-freedom. The thruster will provide a single thrust pulse on a much smaller time scale than the resonance frequency of the beam (sub-microsecond compared to sub-seconds). Thus, the system will respond as if to an impulse disturbance. After the impulse, the system will undergo free vibration. Rao (2004) presents a general treatise on the solution of the beam's response. A numerical solution to the beam's response is made available online by the University of Wyoming (Jacquot 2008) and is described as follows:

The steady state response of a uniform cantilever beam to an impulse load can be approximated by a generalised Fourier series of the orthogonal beam functions

$$Y(x,t) = \sum_{t=0}^{t} \sum_{x=0}^{L} \frac{\phi_n(a)\phi_n(x)}{\gamma_n} \sin(\gamma_n \omega_1 t) \tag{4.7}$$

where x is a position along the beam, $x = a$ is the impact point of an impulse I_0, L is the beam length, ω_1 is the first modal frequency, ϕ_n is the nth mode shape, ratio γ_n is defined as

$$\gamma_n = \left(\frac{\beta_n L}{\beta_1 L}\right)^2 \tag{4.8}$$

and the dimensionless deflection parameter Y is defined as

$$Y(x,t) = \frac{y(x,t)\mu L \omega_1}{I_0} \tag{4.9}$$

where $y(x,t)$ is the beam deflection and μ is the beam mass per unit length. The nth normal mode function at position x is

$$\phi_n(x) = \left[\cosh \beta_n Lx - \cos \beta_n Lx - \alpha_n \left(\sinh \beta_n Lx - \sin \beta_n Lx\right)\right], \quad n = 1, 2, ...5 \tag{4.10}$$

where $\beta_n L$ is, and α_n is a trigonometric function of, the nth root of the frequency equation relating to the boundary conditions for a cantilever beam (Rao 2004)

$$\begin{aligned}
\beta_1 L &= 1.8751041 \\
\beta_2 L &= 4.69409113 \\
\beta_3 L &= 7.85475743 \\
\beta_4 L &= 10.99554074 \\
\beta_5 L &= 14.13716839
\end{aligned}$$

$$\begin{aligned}
\alpha_1 &= 0.7340995 \\
\alpha_2 &= 1.0184664 \\
\alpha_3 &= 0.9992245 \\
\alpha_4 &= 1.000033553 \\
\alpha_5 &= 0.9999985501
\end{aligned}$$

Thus, the deflection response can be described for any point along the beam. For example, the transient beam response at a position $x/L = 0.17$ due to an impact at $a/L = 0.94$ is described in Figure 4.11 below. The theoretical, dimensionless, generalised *peak* deflection was measured on average to be Y_{max} = 0.3261 over the first four oscillations, i.e. averaged over the first eight peaks.

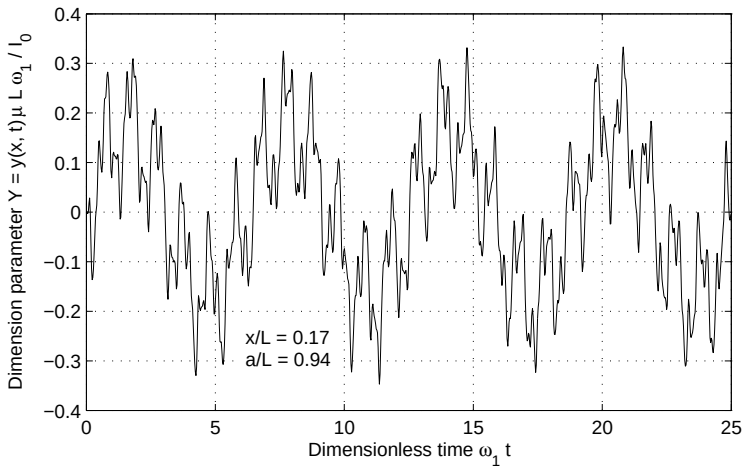

Figure 4.11: Theoretical, dimensionless, generalised beam response to a unit impulse

By substituting the experimentally measured *peak* deflection y_{max} into Equation 4.9, the analytical and experimental responses can be compared and the impulse load inferred from the difference

in the response peaks Y_{max} and y_{max} (Equation 4.11). The peak deflections are used to minimise comparison error. Thus

$$I_0 = \frac{y_{max}}{Y_{max}} \mu L \omega_1 \tag{4.11}$$

It is assumed that the ions experience elastic collisions when impacting the beam. This means that the beam will receive twice as much momentum from the ions to obey momentum conservation (Lafleur 2008). However, it is possible that some ions condense onto the deflector surface. Quantifying the fraction of ions that collide elastically and the fraction of ions that condense on the deflector surface is not a trivial task. One possibility to avoid this issue is to cover the deflector surface with some type of ultra-low density material, such as 'aerogel', which will capture the all ions colliding with it (Lafleur 2008). However, access to such exotic material could not be obtained for this work. Thus, assuming elastic ion collision, the average thrust experienced by the beam is

$$F_b = \frac{I_0}{2t_d} = \frac{y_{max}}{Y_{max}} \frac{\mu L \omega_1}{2t_d} \tag{4.12}$$

Finally, since the foil deflector on the beam is of finite size and distance from the thruster ($x = \pm c_1/2$ = ± 22.5 mm, $y = \pm c_2/2 = \pm$ 12.5 mm and $z = d_2$ as defined in Figure 4.12), only a fraction of the emitted ions will collide with the deflector. To confirm correct modeling and ensure that electrostatic attraction of the beam did not affect results, two sets of thrust tests at different deflector distances from the thruster (d_2 = 12 mm and 18 mm) were performed. Assuming an exponential ion current density distribution, the ratio between the ion current captured by the finitely-sized deflector and an imaginary large deflector (assumed to capture all the ions ejected by the VAT) is calculated. This ratio, otherwise known as the deflector intercepting correction factor D_{Ta}, represents the fraction of ions, and hence thrust, that the deflector can measure from the VAT. Also, a plume distribution correction factor D_{Tb} is required to account for the contribution of ejected ions to normal thrust. A detailed theoretical analysis of thrust correction factors is presented in Section 5.2.11. Note that the thruster's anode will limit the escape angle of the ions as shown in Figure 4.12 below.

Angles θ_1 and θ_3 are the angles at which the anode surface intercepts the ion's trajectory from the cathode center. Angles θ_2 and θ_4 are the angles at which the deflector intercepts the ion's trajectory. Thus

$$\theta_1 = \arctan\left(\frac{w_3}{w_2/2}\right) \tag{4.13}$$

$$\theta_2 = \arctan\left(\frac{w_3 + d_2}{c_1/2}\right) \tag{4.14}$$

$$\theta_3 = \arctan\left(\frac{w_3}{w_1/2}\right) \tag{4.15}$$

$$\theta_4 = \arctan\left(\frac{w_3 + d_2}{c_2/2}\right) \tag{4.16}$$

Note that if $\theta_2 < \theta_1$ or $\theta_4 < \theta_3$, the deflector surface will capture all the ejected ions within the corresponding co-ordinate plane. For the deflector size used in this work, this is true for the X plane, but not for the Y plane (see Figure 4.12). Thus, the large imaginary deflector surface used to find D_{Ta}, is appropriately sized to capture *only the ions that are ejected by the VAT and not those created by it*.

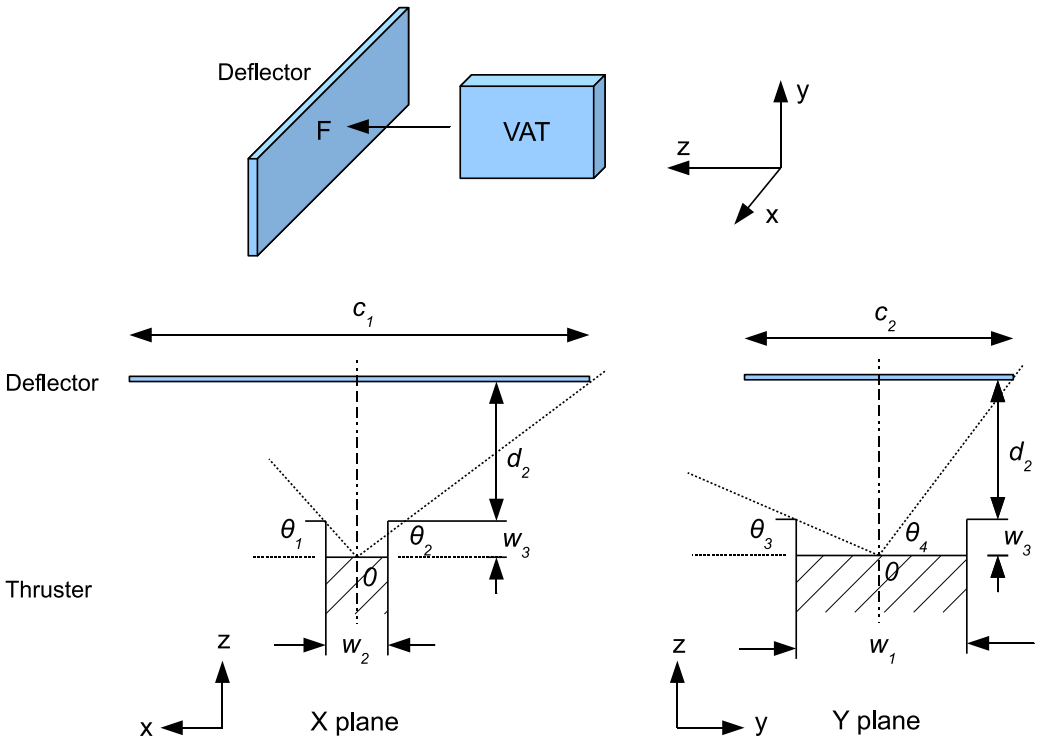

Figure 4.12: Co-ordinate system and defined parameters of the deflector surface and VAT

The ion current density distribution (ICDD) for the large imaginary deflector and the actual deflector (Figure 4.13) was determined and numerically integrated across the large surface area and the results compared in a ratio to give a deflector intercepting correction factor D_{Ta}. In addition, a plume distribution correction factor D_{Tb} was also determined (see Figure 4.14). Thus, the final deflector correction factor is $D_T = D_{Ta}D_{Tb}$. Correction factors D_T = 0.62 and 0.51 were found for test setups with deflector distances d_2 = 12 mm and 18 mm respectively. This means that only 62 % and 51 % of the ions emitted by the thruster will impact the deflector as a normally applied impulsive load. Therefore the true thrust generated by the thruster is

$$F = \frac{F_b}{D_T} = \left(\frac{y_{max}}{Y_{max}}\right)\frac{\mu L \omega_1}{2t_d D_T} \tag{4.17}$$

4.2.4 Calibration of the Cantilever Beam

The strain experienced by the strain gauges at the fixed beam end *cannot* be directly related to the free end deflection as is usually assumed in a steady state deflection. This is because the beam response is wave-like in nature as illustrated is Figure 4.15. This means that the strain along the beam is non-linear with multiple beam bending points. Thus, from the strain gauges' point of view, it cannot "see" beyond the first inflection point in the beam.

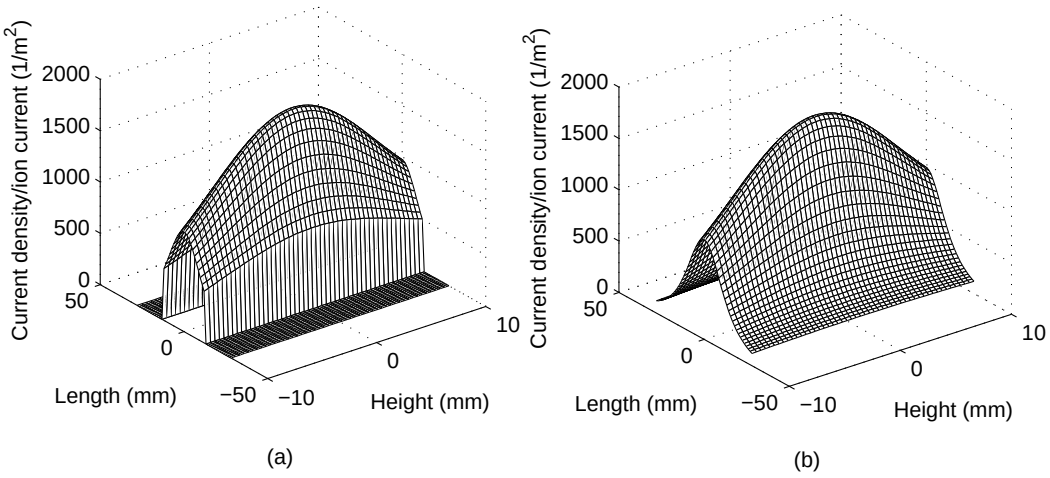

Figure 4.13: Ion current density distribution over the (a) actual deflector area and (b) a large imaginary deflector

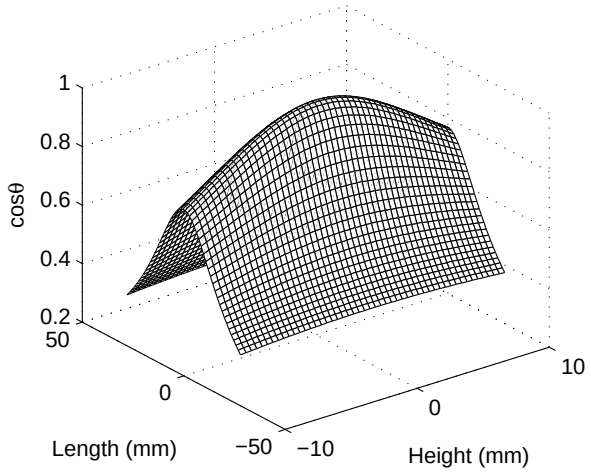

Figure 4.14: Normal component of the ejected ion current density distribution

To overcome this behaviour, the beam must be calibrated by measuring deflection close to the fixed end, where a direct linear relationship between strain and deflection can be made. Observing a simulation of the transient beam response, it was seen that the first inflection point was in the region of x/L = 0.2–0.4. Thus, a calibration point at x/L = 0.17 was chosen. The cantilever beam was calibrated by manually applying a beam deflection with the translating rod of a traveling microscope (See Figure 4.16). The traveling microscope (which is basically a large micrometer) was horizontally aligned with a water level rod and a measurement for zero deflection was recorded. A metal enclosure surrounded the beam to minimise local disturbances from air movement during the measurement process. The beam was then deflected at intervals of 5 μm from 0–25 μm. The measurement was repeated to ensure a reliable correlation between the SG voltage and deflection and performed above the expected range of deflections produced by the thruster. Figure 4.17 shows the calibration curve for the measured SG voltage signal against the applied beam deflection. No significant hysteresis

behaviour was observed and the beam was shown to deflect linearly. Based on a linear fitting of the results, an approximate calibration equation was found to be:

$$y = 2.1720\Delta V - 0.1681 \tag{4.18}$$

where y is in μm and ΔV is in mV.

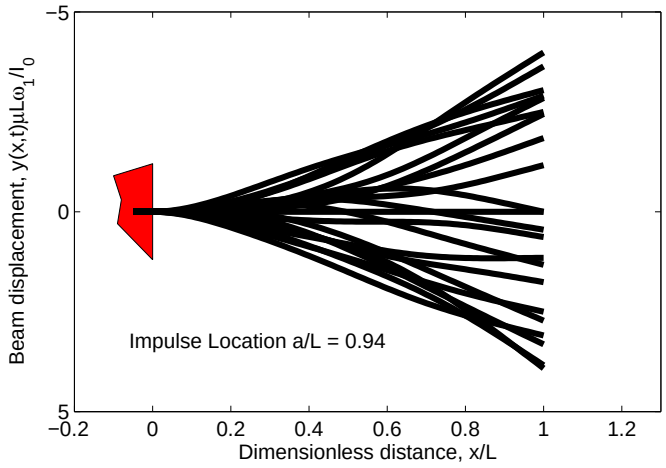

Figure 4.15: Non-linear transient beam response (adapted from Jacquot (2008))

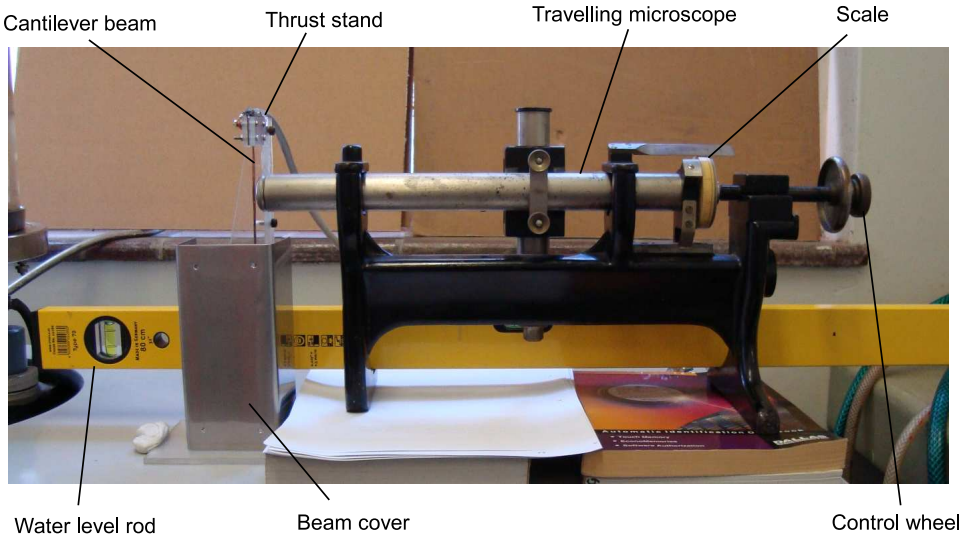

Figure 4.16: Calibration setup

4.2.5 Experimental Test Method

To reduce signal noise, the SG signals were filtered by the Scout 55 amplifier at 10 Hz. The signal was then further filtered with a second-order Butterworth filter at no less than 10 Hz to avoid Nyquist frequency problems (sample rate must be at least twice the measured frequency). Finally, the SG voltage signal was translated to a deflection using Equation 4.18.

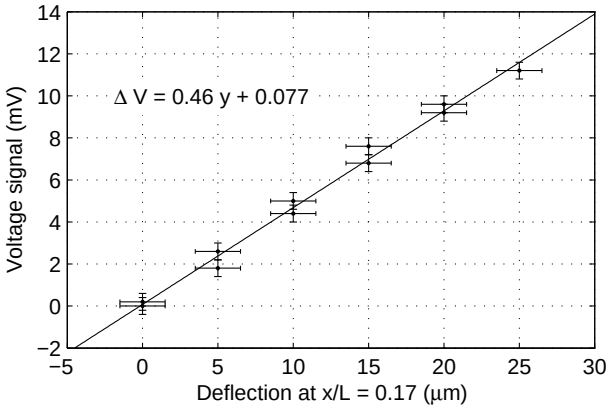

Figure 4.17: Calibration curve of SG voltage signal against beam deflection

The beam's first modal or natural frequency was found by deflecting the beam a small distance and measuring the oscillatory response. In the illustration below (see Figure 4.18), an integer number of n complete cycles was chosen using the oscillation peaks and the time difference between the first and last peaks was measured. For example, a time difference of $4.136 - 0.536 = 3.6$ s over n = 9 complete cycles gave a natural frequency of $\omega_1 = 9/3.6 = 2.5$ Hz.

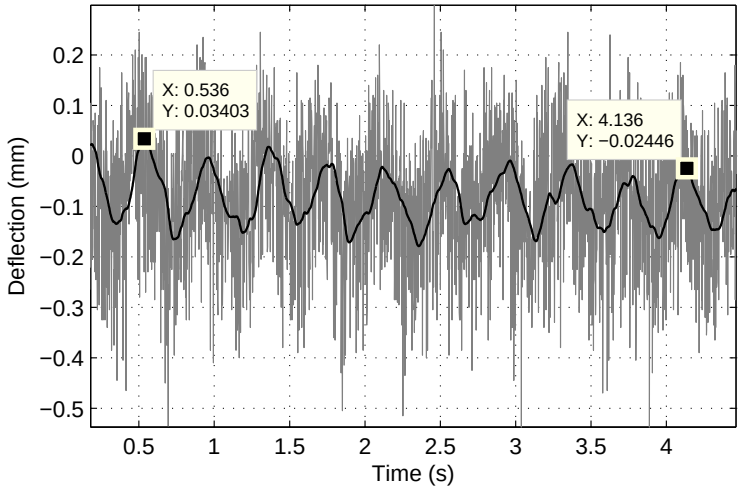

Figure 4.18: Determining the beam's natural frequency

Thrust tests were performed after the thruster had undergone at least a few hundred pulses prior to the tests to remove any surface contaminants and ensure reliable and consistent thruster operation. Each test was performed after waiting for the beam to settle until signal oscillations could no longer be distinguished from sensor noise (2–3 minutes). For a single thrust pulse, the peak beam deflection at x/L = 0.17 was measured for the first usable oscillation cycle recorded. The peak thrust was assumed, on average, to act at the center of the foil deflector. Thus, the bulk of the plasma cloud will act upon the center of the deflector surface, i.e. a/L = 0.94. Figure 4.19 shows a test sample taken at V_d = 1335 V (∼317 A, based on Equation 4.1). To ensure consistency, a total of nineteen samples were taken over a two day period at different times (at least 15 minutes apart), with seven samples taken

on the first day and the rest on the second day. Two additional samples taken at $V_d \approx 3000$ V, but were discarded due to electrostatic attraction effects. Each sample was taken at random breakdown voltages and for as wide a breakdown voltage range as possible. Some signal distortion was caused by electromagnetic interference from the arc discharge as shown by the large data spike in Figure 4.19. However, this does not significantly affect the resulting data thereafter. The oscillations must be measured as soon as possible after the pulse to minimise error from system damping that will decay the oscillations over a period of time, giving an underestimated maximum deflection.

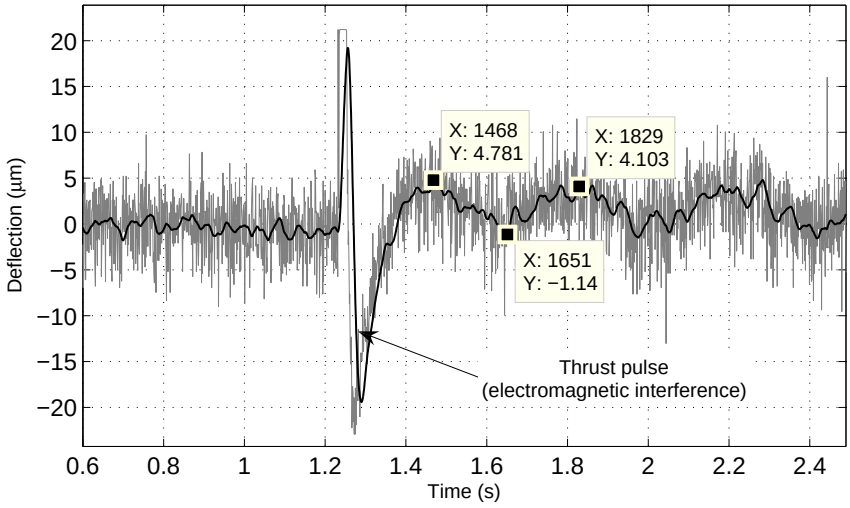

Figure 4.19: Measuring peak beam deflections

The difference between the deflection peaks is calculated, halved, and averaged over two samples to estimate the absolute peak beam deflection y_{max}. This approach eliminates the need to zero the voltage signal. Using the example of Figure 4.19, peak measurements of 4.781, -1.14 and 4.103 μm gave an estimated peak beam deflection of

$$y_{max} = \frac{1}{2}\left[\frac{4.781-(-1.14)}{2} + \frac{4.103-(-1.14)}{2}\right] = 2.791\ \mu\text{m}$$

Appendix D contains tabulated data of y_{max}. Substituting y_{max} into Equation 4.12 gives the force experienced by the beam. For example, for $L = 200$ mm, ω_1 = 2.5 Hz, $\mu = 8.0640 \times 10^{-4}$ kg/m (9 mm wide, 0.1 mm thick, ρ = 8.96 g/cm^3 (Lide 2003)), Y_{max} = 0.3261, t_d = 400 ns and y_{max} = 2.791 μm, an approximate thrust pulse of 27.1 mN was generated by a 317 A arc pulse.

Taking into account the deflector correction factor (d_2 = 12 mm), the true thrust generated by the thruster as described by Equation 4.17 is $F = F_b/D_T = 27.1/0.62 = 43.7$ mN for I_d = 317 A. Comparison of the example theoretical and experimental deflection response as demonstrated in Figure 4.20 confirms correct modeling of the beam.

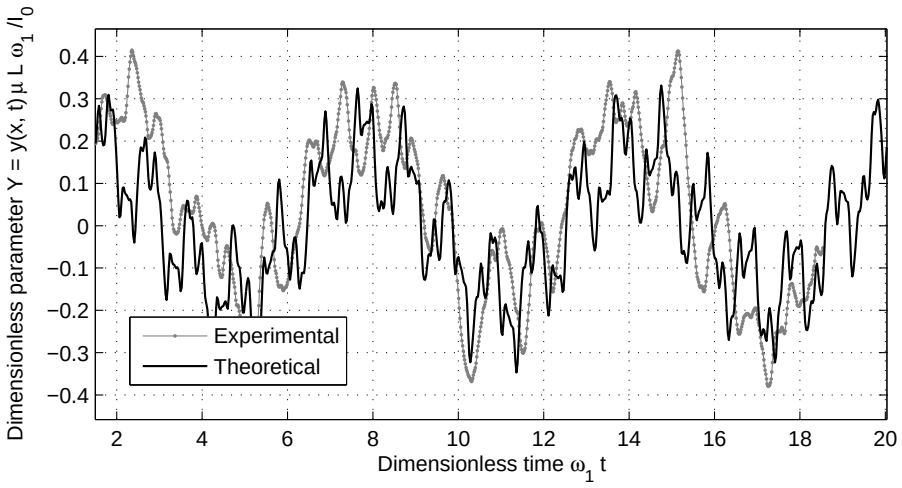

Figure 4.20: Comparison example of the non-dimensionalised theoretical and experimental beam response

4.3 Indirect Thrust Measurement

4.3.1 Design of the ITMS

The ITMS concept developed to measure ion velocity and current was the TOF measuring system based on the design of Byon & Anders (2003) and Anders & Yushkov (2002). Due to vacuum chamber space limitations, a drift length of d_1 = 150 mm was used. An aluminium 40 mm square tunnel was used to: (1) direct ions to an ion collector made of 30 mm square copper sheet; (2) absorb incoming plasma electrons; and (3) protect the collector from EMI not originating from the VAT itself. The thruster was placed at one end of the tunnel, whilst the collector was fixed to the other end, insulated from the tunnel walls with 0.5 mm micanite sheet lining. The collector was negatively biased to $\sim$90 V with a battery pack of ten 9 V batteries. A 10 kΩ terminating resistor was used to infer the ion current using Ohm's law, i.e. the voltage across the resistor is measured during a thrust pulse. The voltage is then divided by the resistor's resistance to get the current flowing through the resistor. This current represents the current induced by the collision of ions on the ion collector plate. The entire measurement system was electrically shielded by means of coaxial cabling and a metal enclosure for the battery pack. Exposed portions of the circuit to the outside environment were sealed up with aluminium foil. The ion collector system is arranged as shown in Figures 4.21 and 4.22.

4.3.2 Verifying the Ion Collector Circuit

The effect of the collector circuit on the measured ion current was identified. Figure 4.23 shows an ion current test sample taken during a thrust pulse of V_d = 1500 V and its corresponding arc voltage profile. Oscillations present in the measured discharge voltage are credited to inductance effects

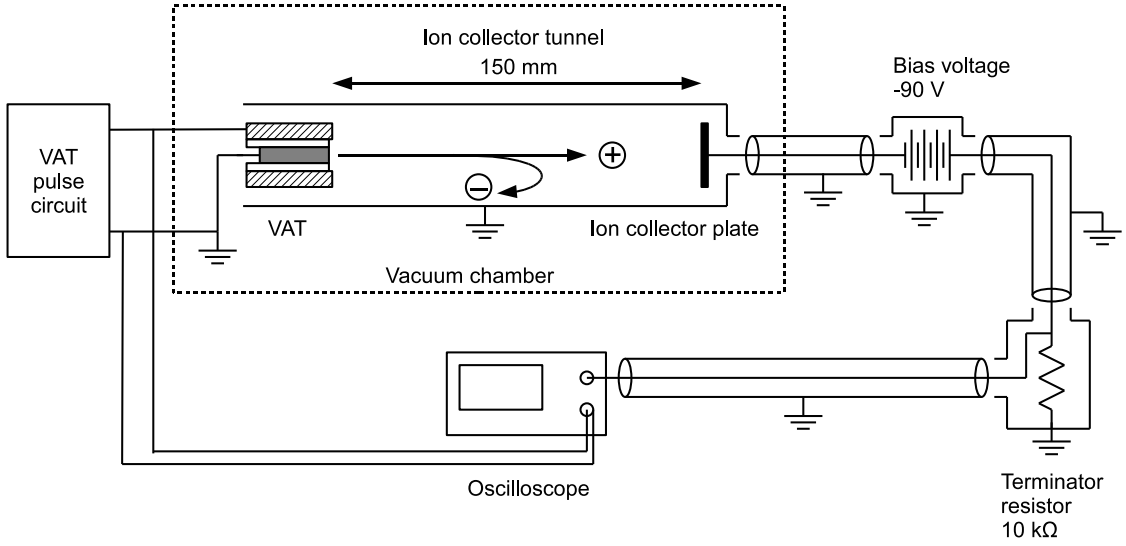

Figure 4.21: Schematic of ITMS setup

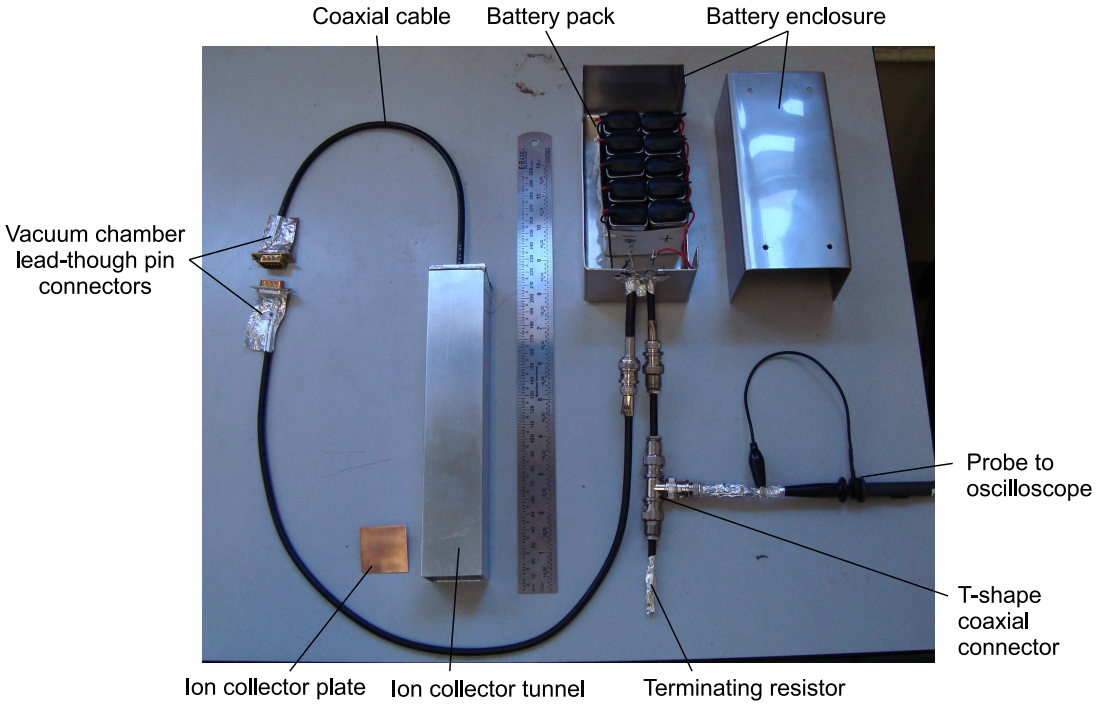

Figure 4.22: Layout of ITMS design

caused by the thruster leads and possibly within the thruster itself. This was verified by shortening the capacitor leads where practically possible and measuring correspondingly smaller oscillations. Figure 4.23 clearly shows that the oscillations are picked up by the ion collector circuit. Fortunately, the oscillations usually cease just as the majority of the ion current is detected, as indicated by the sharp spike in current levels (∼12 mA).

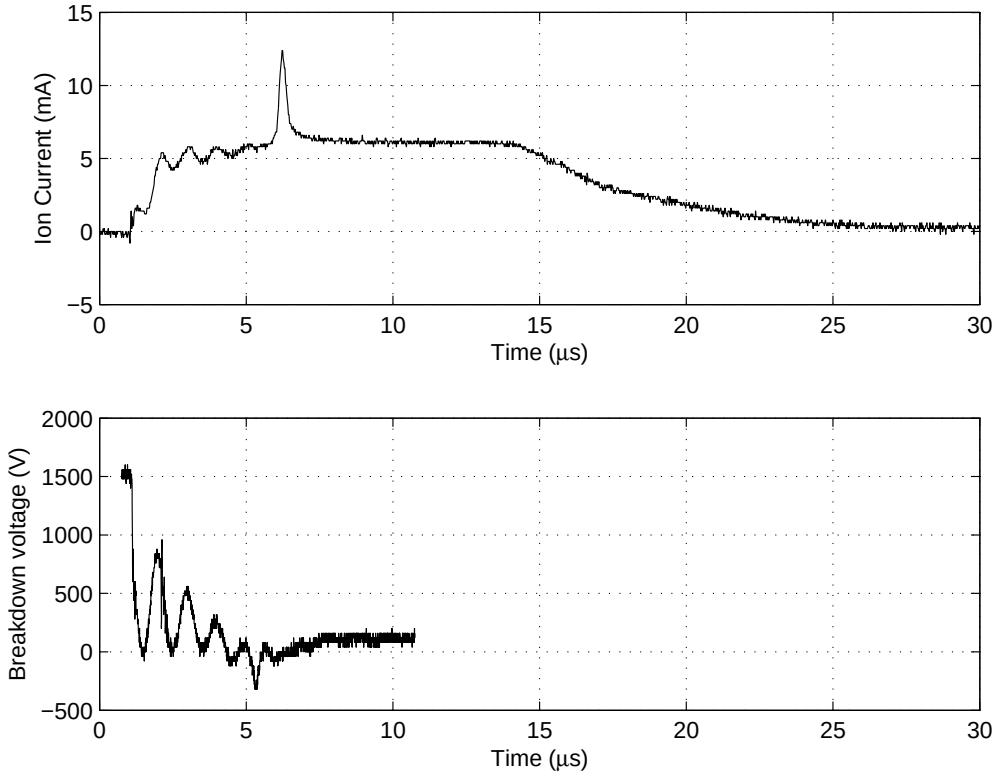

Figure 4.23: Sample graph of the ion current and breakdown voltage for a 1500 V thrust pulse

Figure 4.23 shows the ion current increasing soon (< 6 μs) after the arc pulse. This implies that some ion travel as high as 40–60 km/s. Experiments by Byon & Anders (2003) show that this is indeed possible. After the current spike, the ion current approaches a steady state offset value, then slowly decays. This was ascribed to capacitive effects in the cabling and/or battery pack and some of the plasma in the tunnel eventually diffusing into the plate. The resistor also plays a role in the rise time (time constant in an resistor-capacitor circuit is RC). This effect is seen in Figure 4.23 where the ion current signal decays after a long period of time compared to the thruster pulse (by about 2 orders of magnitude). Shortening the coaxial cable was shown to reduce the rise and decay time of the ion current. A rough estimate of the time constant can be found by assuming the total decay time (five times the circuit time constant $5\tau = RC$) is roughly 15 μs and the terminating resistance R = 10 kΩ to give a total circuit capacitance C of the order of 0.3 nF. The RC nature of the circuit does not appear to affect the portion of the ion current profile where most of the ions collide, since the sharp peak in the signal consistently occurs during the steady state region with rise and fall times lower than that seen in other parts of the waveform. Possible capacitive or plasma effects between the collector plate

and tunnel were eliminated with the addition of micanite lining to isolate the two components.

Interestingly, the steady state value in the ion current signal was shown to be directly proportional to the negative bias voltage applied to the collector. This means that the battery pack had an effect on ion current results. The ion current peak is usually seen near the point where the current signal has risen to a relatively steady value. In addition, the magnitude of the current peaks alone did not appear to be affected by the offset.

Additional tests were performed by removing the collector plate and leaving a bare coaxial lead. The expected result is that very little or no ions will be absorbed by the coaxial lead, inducing no current. However, if a current signal is measured (and there was), then it is *not* due to ion collision, but some other effect in the circuit. The results from these tests showed the same "hill" profile as for the ion collector tests, but at a much lower current (typically 1.5–2.5 mA) and without any signal peaks (Figure 4.24). This confirmed that the current peaks observed previously are due to the presence of ions. In addition, the ion current peaks occurred within the expected time delay of 3–10 μs, which also confirms that the greatest concentration of ions collide at the expected velocity of around 20–30 km/s. The magnitude of the ion current also appears to be proportional to the discharge voltage, which corresponds to a large arc current and therefore ion current emitted. Now that the effect of the collector circuit has been identified, its profile can be subtracted from the ion collector waveform, conceivably leaving just the true ion current. Details of this technique are explained in Section 4.3.5.

When one measures the magnitude of the peak ion current, it is over an order of magnitude lower than what is expected. This may be a result of the current signal being "spread out" as indicated by the long decay time ($\sim$20 μs) of the current signal. To overcome this problem, the total amount of charge received by the collector was calculated by integrating the ion current over the current collection time. This collected charge represents the total amount of charge released by the thruster in a single pulse. Thus, the true ion current was estimated by dividing the total collected charge over the discharge time (more details in Section 4.3.6).

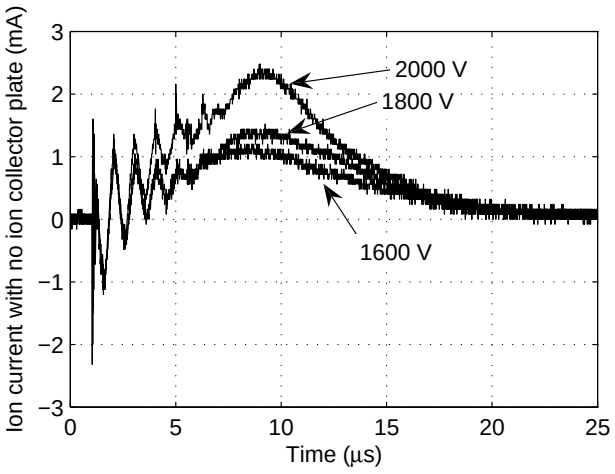

Figure 4.24: Example of circuit response without an ion collector plate at -93.6 V bias voltage

The effect of the biased ion collector on the ion velocity was assessed. A number of possible effects were surmised: (a) the negatively charged plate will induce an electric field across the tunnel, significantly accelerating the ions through the tunnel. The result is that the measured ion velocity will be overestimated; (b) the plate will only induce a local disturbance of the plasma, forming a space charge sheath and blinding the rest of the incoming plasma to the charged plate; and (c) the electric field is much smaller than the field at the thruster, accelerating the ions only slightly. To test these hypotheses, a series of tests of measuring the ion velocity with varying bias voltage was done. Fifteen test samples for each bias voltage at roughly 10 V increments were taken at random breakdown voltages, resulting in a large scatter of results (implications of the scatter are discussed in Section 6.3.1). A linear fit of the ion velocity samples in Figure 4.25 revealed that a small increase in average ion velocity with increasing bias voltage was present. A -93.6 V bias voltage increased the average ion velocity by about 10% when compared to the average ion velocity obtained for a 0 V bias. Thus, the bias voltage only weakly attracted the ions electrostatically. Nevertheless, the effect was compensated for by reducing the measured ion velocity by 10 %.

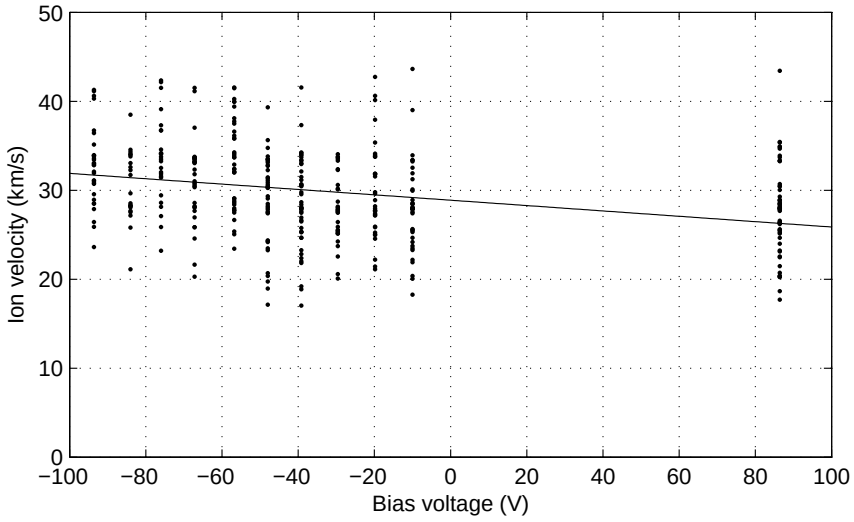

Figure 4.25: Effect of bias voltage on average ion velocity

When the ions collide with the collector surface, the kinetic energy of the ion may be high enough to displace electrons from the surface, producing what is known as secondary electron emission. The effect of these secondary electrons on the measured ion current needs to be known. These electrons will overestimate the ion current measured because they will generally flow in the opposite direction to the ions, producing a current flow in the same direction as if ions had been collected. The quantity of secondary electrons produced in a collision is quantified by the secondary (electron) emission coefficient γ_{se}, which is the ratio of emitted electrons per particle impacts. To determine if secondary electron emission is significant, the kinetic energy of an ion is determined by

$$E_{k,i} = \frac{1}{2} m_i v_i^2 \tag{4.19}$$

For example, an aluminium ion ($m_i = 4.4803 \times 10^{-26}$ kg) traveling at an average velocity of 30 km/s has a kinetic energy of 126 eV. Several sources (Chutopa et al. 2003, Fridman & Kennedy 2004, Lieber-

man & Lichtenberg 2005) show that γ_{se} is only significant for ion particle energies ≥ 1 keV. For ion energies of 100–200 eV, however, γ_{se} will be less than a few percent. Byon & Anders (2003) neglected secondary electron emission in their vacuum arc plasma TOF tests due to the low energy of the ions impacting the collector. Anders et al. (2004) used a -200 V bias voltage to repel plasma electrons and yet not produce significant secondary electrons. Thus, the effect of secondary electrons can likewise be neglected for simplicity.

In conclusion, the ion current was proved to be physically measurable. The effect of the collector circuit was identified and the effect of secondary electron emission shown to be negligible. Ion velocity measurements were also shown to be reliable. The use of ion optics (i.e. charged potential grids) was found to be unnecessary and the roughly -90 V bias voltage is indeed suitable for use. Thus, an ion collection and TOF measurement system was successfully developed to "indirectly" measure the thrust.

4.3.3 Test Setup Description

The ion collector tunnel was placed inside the vacuum chamber and fixed to a perspex base (see Figure 4.26). The VAT was placed at the open end of the tunnel aimed at the collector center. Coaxial cables connected the collector plate, vacuum lead-through, battery pack, terminator resistor, and voltage probe. All connection points were sealed with aluminium foil tape to shield the setup from background EMI noise. An oscilloscope was used to measure the resistor voltage and arc voltage. The coaxial cable shield and collector tunnel were earthed.

4.3.4 Experimental Analysis

This section describes the analysis needed to obtain the thrust based on the experimental results from the indirect thrust measurement method (See Section 4.3). The TOF method employed in this project makes use of the time difference between arc initiation and peak ion current collected to find the average ion velocity. Calculation of the mean ion velocity, ion-to-arc current ratio, thrust and erosion rate are described below. Thruster performance parameters are then derived from these quantities.

The mean ion velocity is simply described as

$$\bar{v}_i = \frac{d_1}{t_i} \tag{4.20}$$

where d_1 is the ion collector tunnel drift length as before and t_i is the time difference between the peak collected ion current and arc initiation.

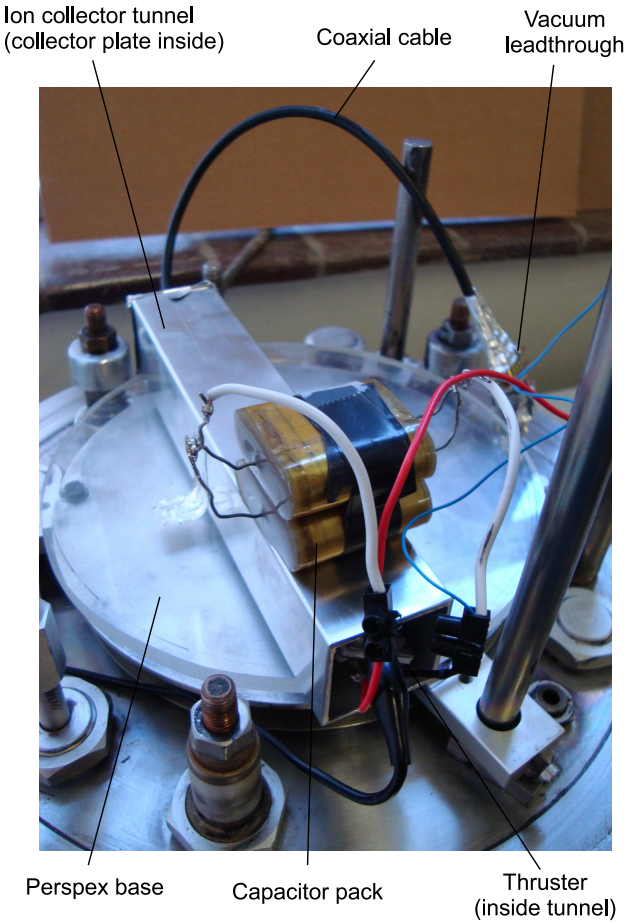

Figure 4.26: Photograph of the ITMS setup in the vacuum chamber

A correction factor was determined, as was for the DTMS, since only a small portion of the ions will be detected by the collector plate (see Section 5.2.11 for the theoretical analysis). A large imaginary collector surface was defined such that it was able to collect all the ions ejected by the VAT (based on the same analysis that found the imaginary deflector size in Section 4.2.3). The current density distributions for the imaginary collector and the actual square collector ($x = y = \pm c_3/2 = \pm 15$ mm) were determined and numerically integrated across the imaginary collector area to produce an ion collector correction factor B_T (see Figure 4.27). For a collector distance of $z = d_1$ = 150 mm, a correction factor of B_T = 0.0145 was calculated, i.e only 1.45 % of the emitted ion current is collected.

The amount of charge the ions give to the collector over the collection time t_c is

$$Q_{i,p,f} = \int_0^{t_c} I_{i,c}(t)\, dt \tag{4.21}$$

The total ion charge emitted from the thruster can be estimated as

$$Q_{i,t} = \frac{Q_{i,p,f}}{B_T} \tag{4.22}$$

Thus, the average ion current emitted from the thruster is

$$\bar{I}_{i,t} = \frac{Q_{i,t}}{t_d} \tag{4.23}$$

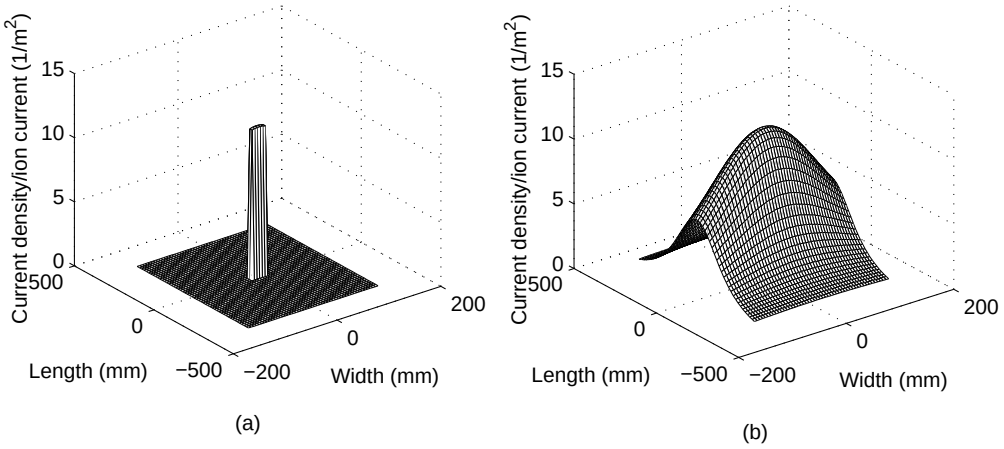

Figure 4.27: Ion current density distribution over the (a) actual collector surface and (b) a large imaginary collector surface

Thus, the ion-to-arc current ratio (that is, the ratio of the ion current created in the cathode region to arc current) can be found with

$$\zeta = \frac{I_{i,p}}{I_d} = \frac{I_{i,t}}{I_d C_{Ta}} = \frac{Q_{i,p,f}}{B_T C_{Ta} I_d t_d} \tag{4.24}$$

Based on Equation 5.46, the average ion mass flow rate from the thruster can be approximated by

$$\dot{m}_{i,t} \approx \frac{m_{i,t}}{t_c} = m_i \frac{I_{i,t}}{e\bar{Z}} \tag{4.25}$$

It is assumed that there is no angular variation in the ion charge state distribution (Polk et al. 2001). In conclusion, based on Equation 5.48 and taking into account the thruster plume distribution correction factor, the resultant thrust produced is

$$F = C_{Tb}\dot{m}_{i,t}\bar{v}_i = C_{Tb}\left(m_i \frac{I_{i,t}}{e\bar{Z}}\right)\bar{v}_i \tag{4.26}$$

4.3.5 Calibration of the Ion Collector System

The ion current was recorded for the case of an absent collector in order to identify the response of the collector circuit alone as argued in Section 4.3.2. This was performed over a range of V_d = 1000–3000 V at random breakdown voltages. A fitting function was designed to approximate the collector circuit response for any ion current sample's breakdown voltage by producing a linear fitting across all the collector circuit responses, resulting in Figure 4.28. Thus, an ion current sample can be made for any breakdown voltage. The fitting function will then generate an approximate collector circuit response correlated to that breakdown voltage level. The true ion current can then be found by subtracting the collector circuit response from the measured ion current as Figure 4.29 illustrates. Curve 1 is the measured ion current, curve 2 is the approximated collector circuit current and curve 3 is the difference between curves 1 and 2, resulting in the true ion current.

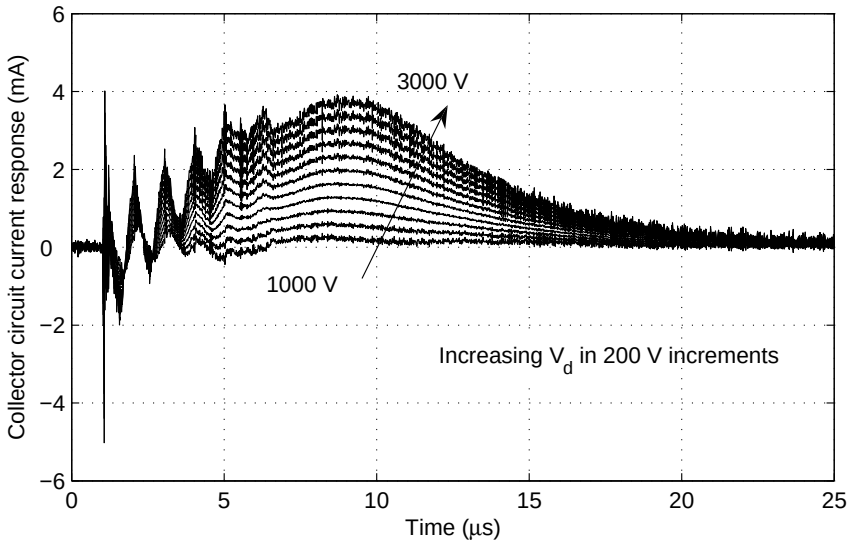

Figure 4.28: Approximated collector circuit response for V_d = 1000–3000 V

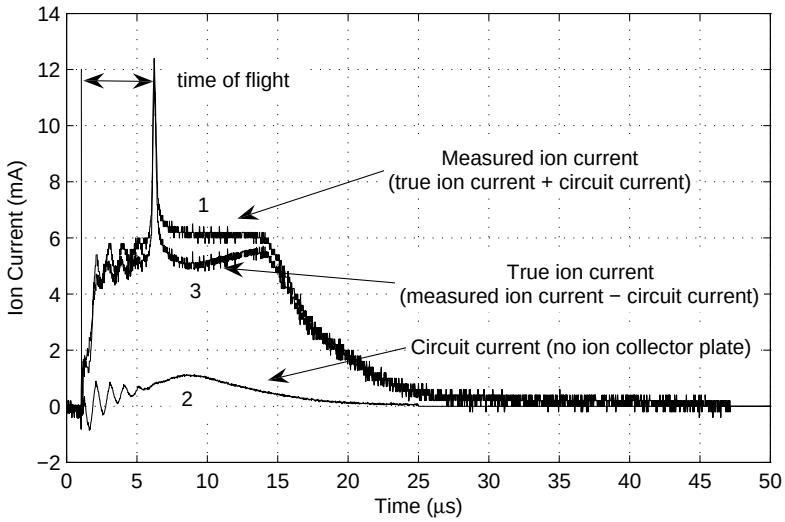

Figure 4.29: Sample ion collector response at V_d = 1500 V

4.3.6 Experimental Test Method

Ion current tests were performed, as for the direct thrust tests, after running the thruster for at least a few hundred pulses prior to measurements to remove surface contaminants, etc. The thruster was randomly pulsed between 1–20 Hz and eighteen samples measurements of the voltage across the terminating resistor were taken over a randomised range of arc voltages (1000–3000 V) roughly every 1–30 seconds. The random breakdown voltages are a result of the ever-changing size of the electrode gap due to cathode droplets, atoms and ions condensing at the cathode-insulator interface as described in Section 3.4. The signals were interpreted as induced ion current by dividing the voltage signal across the terminating resistor by its resistance (10 kΩ). Since the thruster was not guaran-

teed to fire plasma consistently in the collector's centerline of sight, the observed signals were quite scattered. Thus only the samples of greatest magnitude and typical signal profile were recorded.

The true ion current was found by subtracting the effect of the collector circuit as described in the previous section. Then using Equation 4.21, the true ion current signal was integrated over the collection time (that is, until no more ion current is measured) to find the collected charge. Tabulated charge data is in Appendix D. For example, a sample test at V_d = 1500 V (I_d = 356 A, based on Equation 4.1) as shown in Figure 4.29 gave a collected charge of $Q_{i,pf} = 8.7360 \times 10^{-8}$ C over a collection time of about 45 μs.

Taking into account the ion current distribution over the tunnel distance (Equation 4.22), the average ion current is found by dividing by the discharge time (Equation 4.23). The ion-to-arc current ratio is found by simply dividing the measured ion current by the arc current at which the sample was taken at (also taking into account anode electrode interference). Thus

$$\begin{aligned} Q_{i,t} &= \frac{Q_{i,pf}}{B_T} = \frac{8.7360 \times 10^{-8}}{0.0145} = 6.0248 \times 10^{-6}\ \text{C} \\ \bar{I}_{i,t} &= \frac{Q_{i,t}}{t_d} = \frac{6.0248 \times 10^{-6}}{400 \times 10^{-9}} = 15.062\ \text{A} \\ \zeta &= \frac{I_{i,t}}{I_d C_{Ta}} = \frac{15.062}{356(0.43)} = 0.098 \end{aligned}$$

For a TOF/drift length of d = 150 mm and a measured time delay of t_i = 4.3 μs, an average ion velocity of $\bar{v}_i = 34.88$ km/s is obtained, which is re-adjusted for the 10% speed increase caused by the collector plate's bias voltage (see Section 4.3.2). The thrust can then be found with Equation 4.26, for example,

$$F = C_{Tb}\left(m_i \frac{I_{i,t}}{e\bar{Z}}\right)\bar{v}_i = 0.76\left(4.4803 \times 10^{-26}\frac{15.062}{1.6 \times 10^{-19}(2.679)}\right)0.9(34884) = 37.71\ \text{mN}$$

4.4 Erosion Rate Measurement

4.4.1 Experimental Analysis

Measurement of the cathode erosion rate was done by measuring the weight difference of the cathode after a set operating time. This erosion rate, however, will be much higher than the erosion rate calculated by Equation 5.35, due to macroparticle ejection. The mass flow rate at any given time t during thruster operation is

$$\dot{m}_s(t) = E_r I_d(t) t_d S(t) \tag{4.27}$$

Since the pulse frequency and arc current are dependent on V_d, which fluctuates over time due to the nature of the discharge mechanism of the power circuit, I_d and S were measured over the operating time. Thus, integrating $\dot{m}_s(t)$ over the thruster operating period t_o gives the change in cathode mass

$$\Delta m_s = \int_0^{t_o} \dot{m}_s(t)dt = E_r t_d \int_0^{t_o} I_d(t)S(t)dt \tag{4.28}$$

Rearranging gives the erosion rate

$$E_r = \frac{\Delta m_s}{t_d \int_0^{t_o} I_d(t) S(t) dt} \tag{4.29}$$

The number of pulses that the thruster experiences can likewise be found by integrating the frequency over the operating time

$$N_s = \int_0^{t_o} S(t) dt \tag{4.30}$$

4.4.2 Experimental Test Method

Before each test, the cathode was prepared by cleaning its surface with a fine file to remove oxides and contaminants. Measurement of the thruster was done with a Precisa 40SM-200A digital mass measurement scale with a resolution of 0.1 mg. The scale was calibrated by taring the empty scale to zero and then weighing the cathode three times to determine the uncertainty in measurement. After weighing the cathode, the VAT was tested for a total of 9 hours over a period of two days (4 hours for the first day, 5 hours for the second day). The thruster was maintained at an average DC circuit power input of $\sim$10 W and samples of the arc discharge voltage were manually recorded at t_m = 20–60 minutes. Figure 4.30 is an example of such a test sample. Observations show that the arc voltage and pulse frequency fluctuate a lot during thruster operation. Thus, to improve sampling accuracy, a real-time monitoring system was built where voltage data would be sampled over the entire operating period. However, the vast amount of data that needed to be captured would be on the order of gigabytes and was impractical to process. Thus, the accuracy of the weight loss method in this work is not very accurate due to sampling limits.

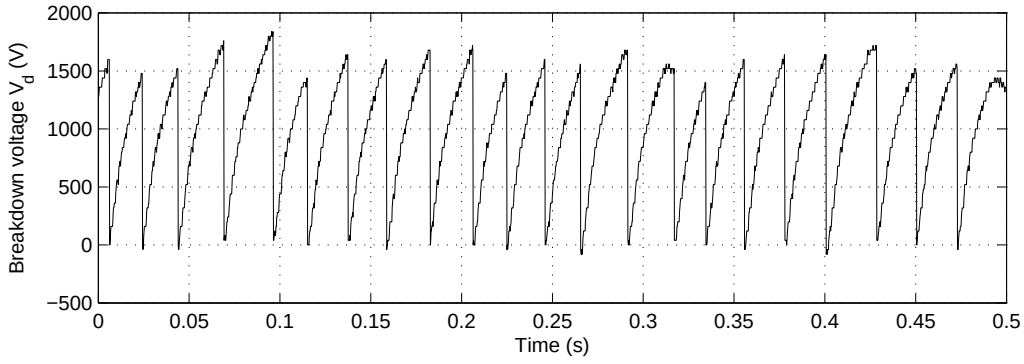

Figure 4.30: Test sample of breakdown voltages

Once the test was complete, the chamber was slowly filled with air again and the cathode removed from the thruster, weighed again and the mass difference recorded. The data samples were processed by calculating the average breakdown voltage and frequency in each sample. A MATLAB program was created to identify the arc discharge in each sample by analysing the gradient of the voltage sample. A very large negative gradient 'spike' indicates the presence of a discharge. The example in Figure 4.31 shows that 22 pulses are present for the test sample in Figure 4.30. The voltage and time

of each discharge event is stored and used to calculated $\bar{V}_d$ and $\bar{S}$ (Table 4.2). The pulse frequency of two adjacent discharges separated by time t_D is found by

$$S = \frac{1}{t_D} \tag{4.31}$$

Using the Equation 4.1, the resulting arc currents were found (an example of which is shown in Figure 4.32). Figure 4.33 shows an example of frequency plotted over the test time. Plotting I_d against S, Figure 4.34 shows the indirect proportional relationship between the arc voltage and pulse frequency (due to the charging nature of the capacitor circuit). Substituting the measured values of I_d, S and the measured cathode mass loss Δm_s into Equation 4.29 and numerically integrating gives the final erosion rate E_r. A second-order curve fit of the integrand in Equation 4.29 needed to be made to correctly integrate over the operating time. Substituting values into Equation 4.28 also gives the resultant cathode mass flow rate Δm_s. Thus, the measured erosion rate in this work is time- and current-averaged.

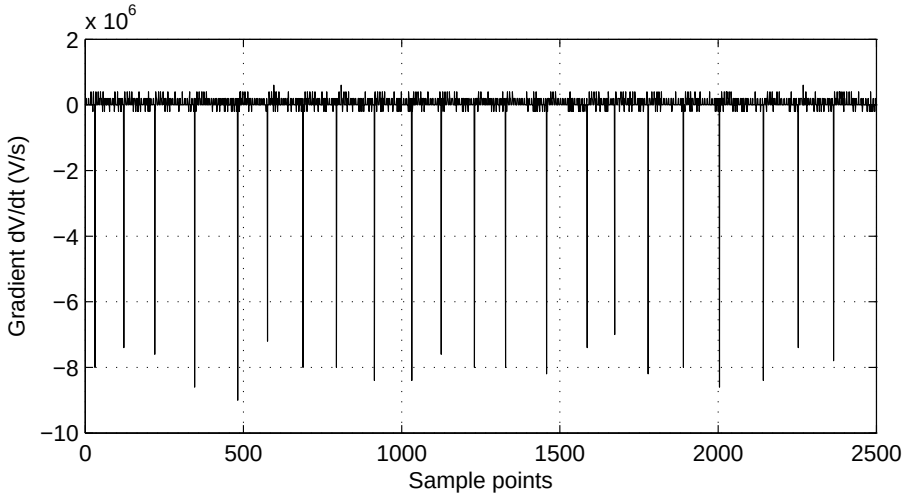

Figure 4.31: Test sample V_d gradient with respect to time

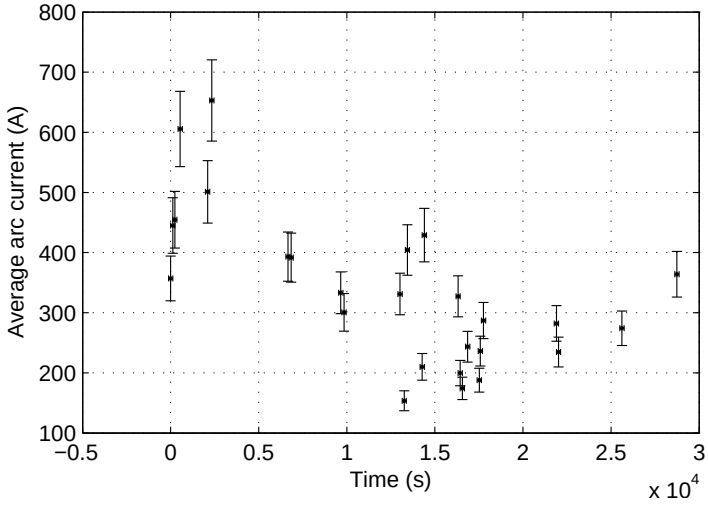

Figure 4.32: Change of I_d over test time

Table 4.2: Average voltage and frequency data for voltage test sample

Pulse	V_d (V)	t_D (s)	S (Hz)
1	1600	0.0182	54.9451
2	1480	0.0196	51.0204
3	1520	0.0252	39.6825
4	1720	0.0272	36.7647
5	1800	0.0188	53.1915
...	...	...	...
19	1600	0.0278	35.9712
20	1720	0.022	45.4545
21	1480	0.0224	44.6429
22	1560	-	-
Avg.	**1587**	**-**	**45.7618**

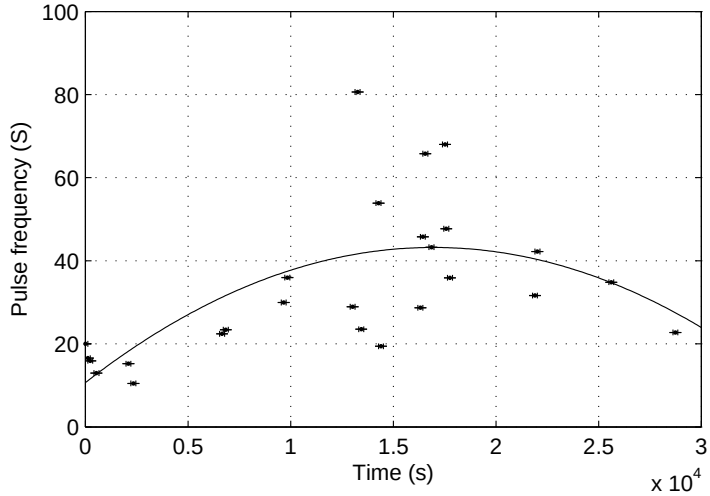

Figure 4.33: Change of S over test time

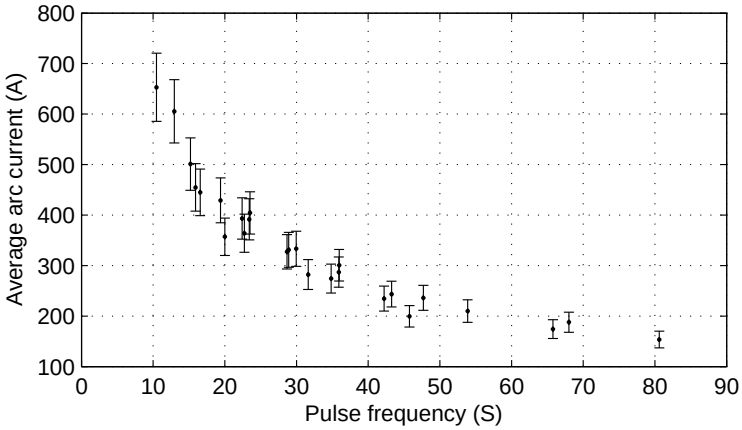

Figure 4.34: Change of I_d with S

4.5 Error Analysis

The error bars for all test results are found using the following analysis:

$$\delta D = \sqrt{\left(\frac{\partial D}{\partial X_1}\right)^2 \delta X_1^2 + \left(\frac{\partial D}{\partial X_2}\right)^2 \delta X_2^2 + \ ...} \tag{4.32}$$

where the resulting parameter D is a function of independent variables X_1, X_2, etc. δD is the total error and δX_1, δX_2, etc., are the uncertainties of each independent variable. Appendix E contains the derivatives used in the error analysis and the final parameter errors for this work.

The uncertainties of all the experimental parameters are presented below in Table 4.3, whilst y_{max} uncertainties are in Tables D.1 and D.2 in Appendix D. The uncertainty of variable Y_{max} was approximated by using the largest error produced with $\delta(x/L)$ and $\delta(a/L)$. Some uncertainties such as C, C_{Ta}, C_{Tb}, D_{Ta}, D_{Tb}, $\bar{Z}$, μ and $Q_{i,p,f}$ could be not be calculated in a straightforward manner and were estimated. The greatest uncertainties were those of t_m at 100 %, Y_{max} at 20 % and y_{max} at an average of 42 %.

For example, to calculate the error of an average arc current of 300 A ($V_d \approx 1260$ V),

$$I_d \approx -C\frac{V_d}{t_d}$$

The derivatives are

$$\begin{aligned} \frac{\partial I_d}{\partial t_d} &= -\frac{I_d}{2t_d} \\ \frac{\partial I_d}{\partial V_d} &= \frac{I_d}{V_d} \\ \frac{\partial I_d}{\partial C} &= \frac{I_d}{C} \end{aligned}$$

Thus the final error is

$$\frac{\delta I_d}{I_d} = \sqrt{\frac{1}{4}\left(\frac{\delta t_d}{t_d}\right)^2 + \left(\frac{\delta V_d}{V_d}\right)^2 + \left(\frac{\delta C}{C}\right)^2} = \sqrt{\frac{1}{4}\left(\frac{20\times10^{-9}}{400\times10^{-9}}\right)^2 + \left(\frac{20}{1260}\right)^2 + (0.1)^2} = 10.43\ \%$$

Table 4.3: Uncertainties of independent variables

Independent variable	Uncertainty
a/L	$\pm$0.02
B_T	$\pm$10 %
C	$\pm$10 %
C_{Ta}	$\pm$10 %
C_{Tb}	$\pm$10 %
D_T	$\pm$14 %
D_{Ta}	$\pm$10 %
D_{Tb}	$\pm$10 %
d_1	$\pm$2.5 mm
d_2	$\pm$1 mm
L	$\pm$0.5 mm
$Q_{i,p,f}$	$\pm$10 %
t_D	$\pm$0.1 ms
t_d	$\pm$20 ns
t_i	$\pm$0.1 μs
t_o	$\pm$120 s
t_m	$\pm$100 %
V_d	$\pm$20 V
Y_{max}	$\pm$20 %
x/L	$\pm$0.005
$\bar{Z}$	$\pm$10 %
Δm_s	$\pm$0.2 mg
μ	$\pm$5 %
ω_1	$\pm$3 %

4.6 Summary

A DTMS and ITMS was successfully designed and used for VAT thrust measurements over a range of arc currents [1]. A time- and current-averaged erosion rate was also obtained. A correlation between the breakdown voltage and average arc current and arc power was made to allow comparison between theoretical and experimental results. Analysis work on test results was identified and sample calculations are provided throughout the chapter where practical. An error analysis of the test data was also performed. Experimental results are presented in Chapter 6 alongside theoretical predictions.

[1] All future references to "arc current" refers to the average arc current per pulse.

Chapter 5

Thruster Theory and Analytical Thruster Model

This chapter presents the theory developed to predict VAT performance and operation. A one-dimensional model of the vacuum arc is formulated and the solution of the model explained. The model is based on the work of a number of authors such as Riemann (1989), Rethfeld et al. (1996), Coulombe (1997), Rossignol et al. (2003) and Messaad et al. (2006). The *Zero Order Model* is used to estimate the plasma jet (Boxman et al. 1995). VAT performance parameters defined by Polk et al. (2001) are also used. The analytical model may be used to solve a wide arc current range of a few amperes to hundreds of amperes (or at least up to the point where anode phenomena become influential to vacuum arc processes and other assumptions no longer hold true). The model, in its current form, is designed for analysing non-refractory metals such as aluminium and copper. The model concentrates primarily on solving the mass and energy conservation equations at the surface, sheath and plasma boundaries. A mathematically closed solution would be very difficult to achieve, given the complexities of the vacuum arc region. Therefore, a number of experimentally-obtained values are used to supplement the characteristic equations, although effort was made to use as little of these 'free parameters' as possible. Many of the equations presented in the following sections may be derived from plasma physics textbooks such as Lieberman & Lichtenberg (2005) and Boxman et al. (1995), but are presented in their final form here for conciseness.

5.1 Assumptions and Simplifications

The following simplifications are used (Hantzsche 1983, Coulombe 1997):

1. One dimensional model along a line normal to the cathode surface plane.
2. Steady state arc processes (start-up and shut-down transient of the arc is ignored)
3. Singular, stationary, circular, independent cathode spots on a large, cold body surface
4. Uniform cathode spot temperature distribution
5. Energy flux processes are limited within the confines of the cathode spot
6. Maxwellian distributions of ions and electrons
7. Collisionless, uniformly thick sheath region
8. Quasi-neutral plasma in Local Thermal Equilibrium (LTE)
9. Uniform plasma region with constant densities, particle temperatures and ion charges according to the Zero-Order model (Boxman et al. 1995)
10. Negligible external or internal magnetic field influence on the plasma

The model also ignores feedback effects that involve complex study beyond the scope of this work or that play a weak role in vacuum arc operation such as the effect of the plasma on cathode surface properties or on itself. Macroparticle/liquid droplet ejection has also not been accounted for.

5.2 Vacuum Arc Thruster Theory

5.2.1 Emitted Atoms

The equilibrium vapour pressure p_{vap} is the pressure of the gas atoms at the cathode surface temperature T_s such that the rate of atom condensation and vapourisation are equal. Roth (1976) approximates the vapour pressure as

$$\log\left(p_{vap}\right) = K_1 - \frac{K_2}{T_s} \tag{5.1}$$

where K_1 and K_2 are material-dependent constants.

The evaporating atom flux density is determined by the Hertz-Knudsen formula as (Mitterauer & Till 1987, Coulombe 1997, Messaad et al. 2006):

$$\Gamma_{vap} = \frac{p_{vap}}{4}\left(\frac{m_n K_b T_s}{3}\right)^{-1/2} \tag{5.2}$$

where m_n is the cathode atom mass and K_b is the Boltzmann constant.

5.2.2 Ion Charge State Distribution

Measurement of ion charge states reveal that they are often multiply-charged (Rysanek & Burton 2003). The ion charge state distribution (CSD) may be characterised as

$$\sum_k f_k = 1 \tag{5.3}$$

where f_k is the fraction that each ion species k contributes to the overall plasma charge state. The ion CSD is assumed independent of arc current (Polk et al. 2001). The CSD is usually determined experimentally (see Anders (2001) and Oks et al. (2006)) due the limited understanding of complex particle dynamics in the vacuum arc. The number of ion species created by the arc is found to be material-dependent. For example, aluminium contains a maximum ion species charge of 3^+ ($k = 3$), that is, ionised by the loss of 3 electrons from the atom's outer orbital cloud.

The mean ion charge of the plasma is thus

$$\bar{Z} = \sum_k f_k Z_k \tag{5.4}$$

where Z_k is the charge state corresponding to ion species k, i.e. $Z_1 = 1$, etc.

5.2.3 Ion Bombardment

Ions formed above the cathode spot are attracted back to the cathode surface because of the electric field and bombard it, causing a significant portion of the heat generated there (see Figure 2.11). The current density of the returning ions is determined by (Hantzsche 1983, Kutzner & Miller 1989, Messaad et al. 2006):

$$J_i = \sum_k J_{i,k} = \sum_k \alpha\gamma f_k Z_k e\Gamma_{vap} \tag{5.5}$$

where $J_{i,k}$ is the portion of the ion current corresponding to ion species k, α is the backflow coefficient (estimated), γ is the degree of ionisation and e is electron charge.

The ion velocity at the sheath edge is determined by application of the Bohm sheath criterion, which states that the ions must have a minimum velocity toward the cathode to maintain a stable sheath zone. The Bohm criterion is commonly used as a boundary condition between the sheath and ionisation zone (Riemann 1989, Rethfeld et al. 1996, Coulombe 1997, Rossignol et al. 2003, Messaad et al. 2006):

$$v_{i,sh} = \sqrt{\frac{K_b(T_{i,sh} + T_e)}{m_i}} \tag{5.6}$$

where $T_{i,sh}$ and T_e are the ion and electron temperatures at the sheath edge (both estimated) and m_i is the ion mass.

The ion density at the sheath is therefore

$$n_{i,sh} = \frac{J_i}{ev_{i,sh}} \tag{5.7}$$

5.2.4 Electric Field

The electric field at the cathode surface may be described by a simplified form of the Mackeown equation (Mitterauer & Till 1987, Riemann 1989, Bolotov et al. 1995, Messaad et al. 2006):

$$E = \beta \left(\frac{8 \bar{Z} m_i J_i^2 V_{cs}}{e \epsilon_o^2} \right)^{1/4} \tag{5.8}$$

where β is a local field-enhancement factor due to surface roughness and other factors (Lafferty 1980), V_{cs} is the sheath potential drop or 'potential hump' (estimated from literature) and ϵ_o is the permittivity of free space.

The electric field reduces the cathode material work function (the amount of energy electrons need to escape the material surface), resulting in an effective field-enhanced work function (Lafferty 1980, Coulombe 1997, Messaad et al. 2006), otherwise known as the Schottky effect:

$$\phi_{eff} = \phi - \sqrt{\frac{eE}{4\pi\epsilon_o}} \tag{5.9}$$

5.2.5 Emitted Electrons

The current density of emitted electrons is described by the thermo-field emission equation (Murphy & Good 1956) as

$$J_{em} = -e \int_{-W_e}^{\infty} D(W, E) N(W, T_s) dW \tag{5.10}$$

where W is defined as the energy potential level, W_e represents the electron potential energy in the metal, $D(W, E)$ is the probability of electron escape due to the quantum tunneling effect and $N(W, T_s)$ is the electron flux. For simplicity, Rossignol et al.'s (2003) approximation of the original Murphy & Good equation may be used, which is valid for the ranges $E \in [10^8, 10^{10}]$ V/m and $T_s \in [300, 4000]$ K:

$$J_{em} \sim \frac{4\pi m_e K_b T_s}{h^3} e \int_{W_1}^{W_2} \ln \left\{ 1 + \exp \left[-\frac{e(W + \phi)}{K_b T_s} \right] \right\} dW \tag{5.11}$$

where the integration limits are $W_1 = -\sqrt{\frac{eE}{4\pi\epsilon_o}}$ and $W_2 = 5$ eV.

Thus, the emitted electron density at the sheath edge is (Rethfeld et al. 1996, Coulombe 1997):

$$n_{em,sh} = \frac{J_{em}}{e} \left(\frac{m_e}{2} \right)^{1/2} (2 K_b T_s + e V_{cs})^{-1/2} \tag{5.12}$$

where m_e is the electron mass.

5.2.6 Returning Electrons

From the quasi-neutral plasma assumption, the total electron density at the sheath edge is

$$n_{e,sh} = \bar{Z} n_{i,sh} \tag{5.13}$$

The back-diffused/returning electron density is found by a density balance at the sheath edge (see Figure 5.1):

$$n_{er,sh} = n_{e,sh} - n_{em,sh} \tag{5.14}$$

Consequently, the current density of the returning electrons may be described by (Bolotov et al. 1995, Rethfeld et al. 1996, Coulombe & Meunier 1997, Rossignol et al. 2003):

$$J_{er} = \frac{1}{4} e n_{er,sh} \sqrt{\frac{8K_bT_e}{\pi m_e}} \exp\left(-\frac{eV_{cs}}{K_bT_e}\right) \tag{5.15}$$

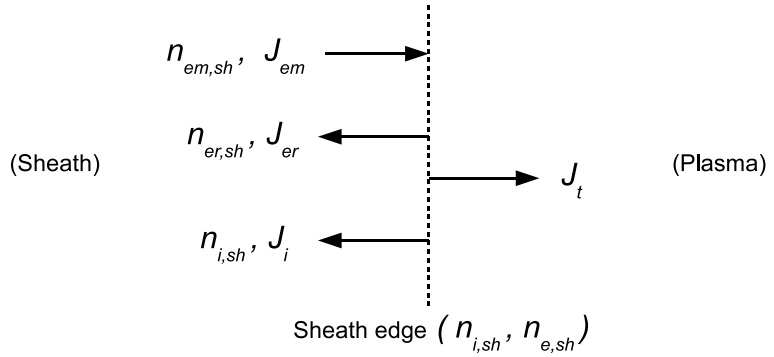

Figure 5.1: Current and particle density balance at the sheath edge

5.2.7 Arc Current

Consolidating the calculated current densities from Sections 5.2.3, 5.2.5 and 5.2.6 and applying a current density balance at the sheath edge (see Figure 5.1) gives the total current density for the cathode spot:

$$J_t = J_{em} - (-J_i) - J_{er} = J_{em} + J_i - J_{er} \tag{5.16}$$

The arc current for a cathode spot is thus

$$I_t = J_t A_s \tag{5.17}$$

where cathode spot area $A_s = \pi r_s^2$ and r_s is the cathode spot radius.

The total arc current from the cathode is

$$I_d = N I_t \tag{5.18}$$

where N is the number of cathode spots present on the surface. Larger arc currents generate a proportionally greater number of cathode spots. Experimental values obtained by Djakov and Holmes were used to approximate the average current contained in a single spot I^*, which is material-dependent (Lafferty 1980).

5.2.8 Cathode Energy Flux Balance

The energy flux components that heat and cool the cathode surface respectively are grouped as follows (see Figure 5.2):

$$q_{heat} = q_i + q_{er} + q_J \tag{5.19}$$

$$q_{cool} = q_{em} + q_{vap} + q_{rad} + q_{cond} \tag{5.20}$$

which are equated to obey energy conservation at the cathode surface, i.e.

$$q_{heat} = q_{cool} \tag{5.21}$$

The current densities within the sheath region (including the cathode surface) are constant due to the assumption of a collisionless sheath (no ions are created or destroyed in this region). This allows the energy fluxes at the surface to be determined using the current densities determined previously.

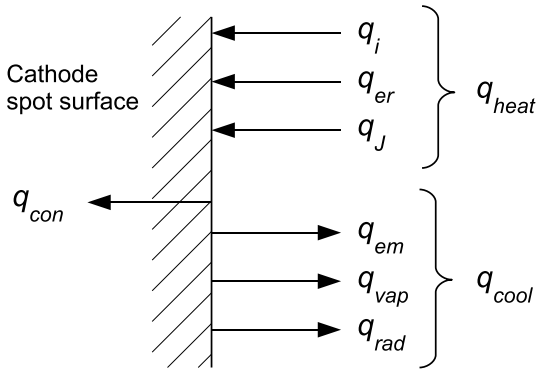

Figure 5.2: Energy flux balance at the cathode surface

The ion bombardment energy flux is described as (Hantzsche 1983, Coulombe 1997, Coulombe & Meunier 1997, Rossignol et al. 2003):

$$q_i = \sum_k \frac{J_{i,k}}{Z_k} \left(U_{i,k} + Z_k V_{cs} - Z_k \phi_{eff} + \frac{5 K_b T_{i,sh}}{2e} + W_{vap} \right) \tag{5.22}$$

where $U_{i,k}$ is the ionisation potential of species k and W_{vap} is the evaporation potential of the cathode atoms.

Joule heating is approximated by Boxman et al. (1995) and Rossignol et al. (2003) as

$$q_J \approx \frac{1}{2} \frac{J_t^2 r_s}{\sigma} \tag{5.23}$$

where the electric conductivity of the cathode material σ is determined by means of the Wiedmann-Franz Law

$$\sigma = \frac{\lambda}{L T_s} \tag{5.24}$$

and λ is the thermal conductivity of the cathode material (assumed constant with temperature) at its molten temperature point and L is the Lorentz number.

The emitted and returning electron energy flux respectively is determined by (Bolotov et al. 1995, Coulombe 1997, Messaad et al. 2006):

$$q_{em} = J_{em}\left(\phi_{eff} + \frac{5K_bT_s}{2e}\right) \tag{5.25}$$

$$q_{er} = J_{er}\left(\phi_{eff} + \frac{5K_bT_e}{2e}\right) \tag{5.26}$$

Vapourised atom energy flux is (Hantzsche 1983, Mitterauer & Till 1987, Coulombe 1997):

$$q_{vap} = eW_{vap}\Gamma_{vap} \tag{5.27}$$

Radiation energy flux is simply (Mitterauer & Till 1987, Coulombe 1997, Messaad et al. 2006):

$$q_{rad} = \sigma_{sb}T_s^4 \tag{5.28}$$

where σ_{sb} is the Stefan-Boltzmann constant.

Heat conduction energy flux is approximated by assuming the crater depth is equal to the spot radius and that all the material becomes liquid within the crater (Boxman et al. 1995):

$$q_{con} = \lambda\nabla T \approx \lambda\left(\frac{T_s - T_b}{r_s}\right) \tag{5.29}$$

5.2.9 Plasma Jet

Since ion mass is much larger than electron mass, it is assumed that thrust is mainly due to ion flow only. Assuming no ion loss or recombination in the ionisation zone, the current density of the ions flowing away from the cathode as the plasma jet can described as

$$J_{i,p} = J_i\left(\frac{1-\alpha}{\alpha}\right) \tag{5.30}$$

The fraction of the ion current to the arc current is therefore

$$\zeta = \frac{J_{i,p}}{J_t} = \frac{I_{i,p}}{I_d} \tag{5.31}$$

where $I_{i,p}$ is the total ion current emitted from the cathode.

Rossignol et al. (2003) approximates the plasma electron and ion densities by means of the *Zero Order Model* (Boxman et al. 1995):

$$n_{e,p} = n_{e,sh}\exp\left(\frac{1}{2}\right) \tag{5.32}$$

$$n_{i,p} = n_{e,p}/\bar{Z} \tag{5.33}$$

Yushkov et al. (2001) approximates the mean ion velocity as

$$\bar{v}_i \approx \left(\frac{20\bar{Z}K_bT_e}{m_i}\right)^{1/2} \tag{5.34}$$

5.2.10 Erosion Rate

Coulombe (1997) estimated the cathode erosion rate by applying a mass flux balance at the cathode surface, where atoms are evaporated and returning ions condense (neutralise and become part of the bulk material again). Assuming all the returning ions condense on the surface, the approximate erosion rate is

$$E_r = \left(\Gamma_{vap} - \sum_k \frac{J_{i,k}}{Z_k e} \right) \frac{m_n}{J_t} \tag{5.35}$$

Note that this erosion rate equation does not consider macroparticle production.

5.2.11 Ion Current Density Distribution

Polk et al. (2001) found that the ion density follows an exponential function. In a polar coordinate system, the ion current density at a radius r and angle θ from the cathode area A_d, which is the sum of all spot areas A_s, is described by

$$J_{i,p,f} = \frac{2 J_{i,p} A_d}{\sqrt{\pi} r^2 k \, \text{erf}\left(2\pi/k\right)} \exp\left(\frac{-\left[2\pi\left(1-\cos\theta\right)\right]^2}{k^2} \right) \tag{5.36}$$

where the ion current from the cathode discharge region is $I_{i,p} = J_{i,p} A_d$. The spread factor of the distribution is taken as $k = 4.5$ based on observations by Polk et al. (2001). The ICDD is used to determine the influence of anode electrode interference on ion emission and exhaust plume distribution, both of which limit the effective thrust in the z direction. Polk et al. (2001) derived a single thrust correction factor that accounts for both effects for a cylindrical thruster geometry by integrating the ion momentum flux through the anode exit plane. This work only made use of the ejected ion current due to its direct proportional relationship to thrust/momentum (see Equations 5.46 and 5.48). In addition, the distribution was modified for a planar geometry for application to the thruster design of Section 3.3. It was also found to be more useful to define separate anode interference and plume distribution correction factors separately for analysing experimental data (see Sections 4.2.3 and 4.3.4).

To convert polar coordinates into planar coordinates,

$$r = \sqrt{x^2 + y^2 + z^2} \tag{5.37}$$

$$\cos\theta = z/r \tag{5.38}$$

where x and y are the Cartesian coordinates on a plane normal to the cathode at a distance z away and r is re-defined as the ion trajectory vector arm. The cathode spot is taken as the origin. Re-writing Equation 5.36 results in the ICDD on a flat plane per unit of cathode ion current ($J_{i,p} A_d = 1$)

$$J'_{i,p,f} = \frac{2}{\sqrt{\pi} r^2 k \, \text{erf}\left(2\pi/k\right)} \exp\left(\frac{-\left[2\pi\left(1-z/r\right)\right]^2}{k^2} \right) \tag{5.39}$$

Anode Interference Correction Factor

It is necessary to determine what fraction of produced ions are ejected from the thruster. Firstly, it is assumed that ions which contact the anode walls will neutralise and be absorbed, contributing no thrust. Secondly, the recessed cathode will, on average, produce ions from a cathode spot at the cathode center. Figure 5.3 outlines the parameters in the generalised planar thruster geometry, where the cathode surface is recessed into the exit plane of the thruster. The anode electrode (or possibly insulation) walls surrounds the recessed cathode. A Cartesian co-ordinate system is defined on the cathode surface with the origin at the cathode center. Variables w_1, w_2 and w_3 are the cathode length, width and recession depth respectively.

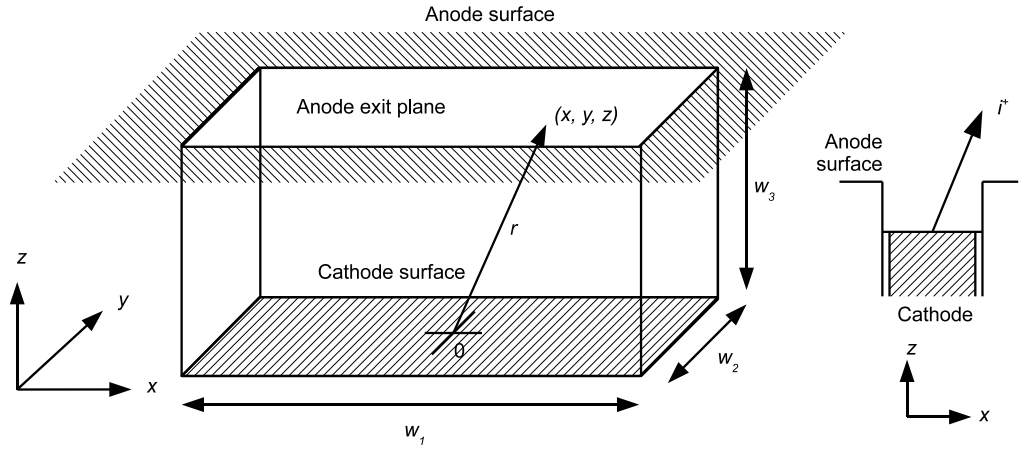

Figure 5.3: Co-ordinate system and geometry of the VAT's frontal face

An exponential ICDD $J'_{i,p,f,\infty}$ is characterised over an imaginary large surface area on the exit plane as if all the ions were intercepted by that surface ($z = w_3$). A second ICDD $J'_{i,p,f}$ is identified for the anode exit plane, which has the same profile as the first distribution, but is limited by the boundaries of the anode exit plane ($x = \pm w_2/2$, $y = \pm w_1/2$). Beyond those boundaries, no current density is present. Figure 5.4 below illustrates these two distributions.

Both distributions are integrated over the large surface area numerically (by summation) by discretising the areas to form a large grid where each grid block is of area dA and then multiplying by the current density distribution. Assuming an imaginary surface of 20 mm square width,

$$I'_{i,p,f} = \int J'_{i,p,f}\, dA_{exit} \approx \sum_{x=-0.01}^{0.01} \sum_{y=-0.01}^{0.01} J'_{i,p,f} xy \tag{5.40}$$

$$I'_{i,p,f,\infty} = \int J'_{i,p,f,\infty}\, dA_{\infty} \approx \sum_{x=-0.01}^{0.01} \sum_{y=-0.01}^{0.01} J'_{i,p,f,\infty} xy \tag{5.41}$$

where $I'_{i,p,f}$ and $I'_{i,p,f,\infty}$ are the ion current per unit of cathode ion current collected by the anode exit plane and imaginary plane respectively.

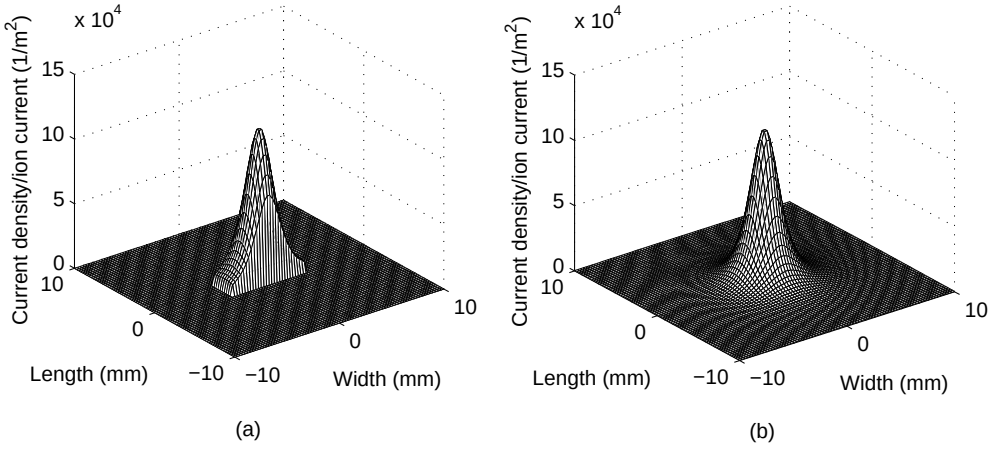

Figure 5.4: ICDD over the (a) anode exit area and (b) an imaginary large surface

The ratio of these two quantities gives the anode interference correction factor

$$C_{Ta} = \frac{I'_{i,p,f}}{I'_{i,p,f,\infty}} \tag{5.42}$$

Plume Divergence Correction Factor

The plume divergence correction factor C_{Tb} takes into account the z component of the ion trajectory vector arm r that produces useful thrust, i.e. the normal thrust component. Using the anode exit plane's ICDD calculated earlier, and defining the angle between the z axis and the plane vector arm r as

$$\theta = \arctan\left(\frac{\sqrt{x^2+y^2}}{z}\right) \tag{5.43}$$

The normal component of the ejected ion current flowing through the anode exit plane is thus

$$I'_{i,p,f,z} \approx \sum_{x=-0.01}^{0.01} \sum_{y=-0.01}^{0.01} J'_{i,p,f} xy \cos\theta \tag{5.44}$$

Thus

$$C_{Tb} = \frac{I'_{i,p,f,z}}{I'_{i,p,f}} \tag{5.45}$$

Correction Factor Results

Thruster geometry values were measured to be $w_1 = 7$ mm, $w_2 = 2.5$ mm, $w_3 = 1.5$ mm and a large imaginary exit plane surface of 20 mm square width was assumed. The anode interference and the plume divergence factors were calculated to be $C_{Ta} = 0.43$ and $C_{Tb} = 0.76$ respectively. The final correction factor of $C_T = (0.43)(0.76) = 0.33$ was verified to be roughly close in value to the

correction factors calculated by Polk et al. (2001) for a cylindrical geometry of similar interference effects.

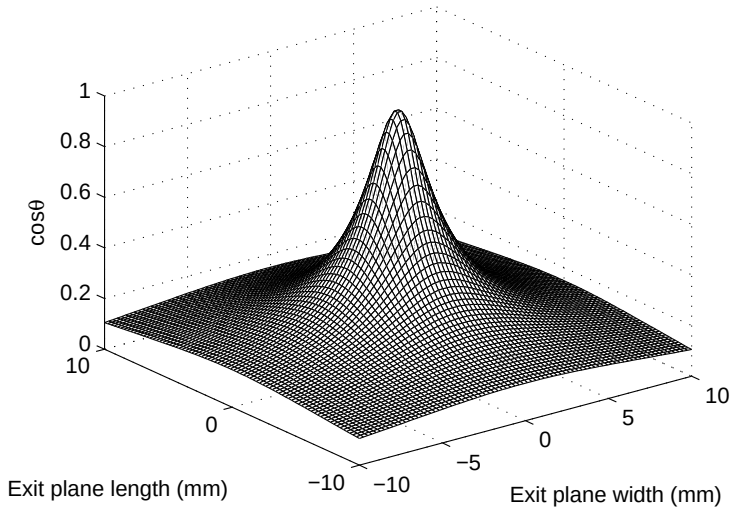

Figure 5.5: Normal component of the ejected ICDD

5.2.12 Theoretical Thruster Performance

The following expressions are based on the thruster performance parameters defined by Polk et al. (2001).

The ion mass flow rate is defined as

$$\dot{m}_{i,p} = m_i \left(\frac{J_{i,p} N A_s}{e \bar{Z}} \right) \tag{5.46}$$

The portion of eroded cathode mass converted into ion mass is known as the ion mass fraction

$$M_f = \frac{\dot{m}_{i,p}}{I_d E_r} \tag{5.47}$$

The thrust due to ion ejection in the direction normal to the cathode surface is

$$F = C_T \dot{m}_{i,p} \bar{v}_i = C_T m_i \left(\frac{J_{i,p} N A_s}{e \bar{Z}} \right) \bar{v}_i \tag{5.48}$$

where the thrust correction factor C_T consolidates the exhaust plume and anode interference into a single parameter, i.e.

$$C_T = C_{Ta} C_{Tb} \tag{5.49}$$

The analytical thrust has been assumed constant during the arc pulse, which results in the thruster pulse signature behaving as a square wave. Although ion charge states and ion velocities may vary across different pulses, they can only be applied as approximated average quantities in this analysis.

The thruster impulse bit is defined as

$$I_T = \int_0^{t_d} F dt \approx F t_d \tag{5.50}$$

and the average thrust is approximately

$$\bar{F} = I_T S = F(t_d S) \tag{5.51}$$

where t_d is the pulse duration and S is the pulse frequency. The product $t_d S$ is the duty cycle.

The arc power is

$$P_d = I(t)V(t) \tag{5.52}$$

where I and V are the arc current and voltage over the discharge time. For practical reasons, the arc power was made a function of the average arc current (see Section 3.4). The average input power to the thruster circuit is

$$\bar{P_d} = P_d(t_d S) \tag{5.53}$$

The thrust-to-power ratio is therefore

$$H = \frac{F}{P_d} \tag{5.54}$$

Specific impulse is defined as

$$I_{sp} = \frac{F}{g I_d E_r} \tag{5.55}$$

Finally, the thruster efficiency is the ratio of thrust power to input power

$$\eta_T = \frac{F^2}{2 P_d I_d E_r} \tag{5.56}$$

Note that the thrust is proportionally related to the ion flux, whilst the specific impulse and efficiency is inversely proportional to the cathode erosion rate. Thus, two conclusions may be stated: factors that (i) maximise the ionisation of vapourising cathode material, and (ii) minimise macroparticle ejection will improve thruster performance.

5.3 Choice of Free Parameters

The choice of free parameters was initially based on typical values found in literature. This provided a basis for validating the analytical model's results and confirming order-of-magnitude parameter values, especially the current, particle and power densities. Once the model could be verified, the free parameters were refined by means of a sensitivity analysis (Section 6.2).

5.3.1 Backflow Coefficient

Whilst most literature assumes that nearly all the ions fall back to the cathode surface, i.e. $\alpha \approx 1$, the assumption is dependent on the electrode setup studied. Most vacuum arc models characterise the

scenario of the cathode and anode electrodes facing one another at opposite ends. In these scenarios, it is observed that anode phenomena is limited to electron absorption. Thus, the only explanation is that the ions must return to the cathode or be absorbed into the surrounding walls. In the case of the electrodes placed adjacent to one another, exposing both their surfaces to the surrounding vacuum, one cannot use that assumption since one views thrust from ion acceleration away from the cathode. As a crude one-dimensional approximation, it appears reasonable to assume a uniform expansion of the plasma from the cathode region such that one half of the ions return to the cathode and the other half expands into the vacuum i.e. $\alpha \approx 0.5$. Unfortunately, the ion backflow currently remains the most ambiguous variable to quantify since one cannot directly measure the portion of ions returning to the surface due to the small sheath size.

5.3.2 Field-Enhancement Factor

The enhancement factor β was introduced by the RSA (Rough Surface Spot with Average Structure Effects) model to represent the overall effect surface protrusions have on cathode spot operation. Literature has mainly focused on its effect on the electric field, which is currently assumed dominant over other effects (Lafferty 1980). The total spot area is assumed to be very much smaller than the total cathode area, and consequently, the protrusion profiles are expected to play a weak role in influencing β. Also, the crater-forming behaviour of the arc 'flattens' the surface, removing the protrusion and reducing the field-enhancing effect (Boxman et al. 1995). However, Lafferty (1980) warns that fluctuations in β may be high, given the uncertainty and changing conditions of the cathode surface due to arcing. The field-enhancement factor β was assumed to be ~2, based on the definition by Lafferty (1980).

5.3.3 Electron Temperature

Messaad et al. (2006) studied the effects of varying electron temperature and found that it played a significant role in dictating arc properties. This makes the choice of the electron temperature relatively important. However, very little is known about the electron temperature since it can only be measured with probes outside the spot region. Hantzsche (1991), Rethfeld et al. (1996) and Coulombe (1997) used electron temperatures of roughly 2 eV for their theoretical models, which is within the lower-temperature (0)-mode existence region of the vacuum arc (Lafferty 1980). Anders et al. (2001) compiled literature sources which indicated an electron temperature of up to 3 eV for aluminium at arc currents of about 300 A. As an initial guess, T_e was assumed to be in the region of 2 eV (23 200 K). However, this caused Equation 5.34 to predict an ion velocity of 19.6 km/s, which is much smaller than its experimentally measured value of 30 km/s (Polk et al. 2001). Setting T_e = 3 eV gives a better result of about 24 km/s. Also, Beilis (2001a) found that larger electron temperatures were present for short pulses with large current rise rates. Thus, T_e = 3 eV was eventually chosen.

5.3.4 Ion Temperature

Messaad et al. (2006) assumed the ion temperature at the sheath edge to be approximately equal to the surface temperature, i.e. $T_i \approx T_s$ ($\sim$ 3500 K). Alternatively, Keidar et al. (2005) assumed an ion temperature of 0.5 eV (5800 K). In Chapter 6.2, a sensitivity analysis will show that the ion temperature has a weak effect on the vacuum arc model, avoiding the need to accurately specify the ion temperature. Thus, this work shall assume $T_i \approx T_s$.

5.3.5 Sheath Potential Drop

There has been some debate on the determination of the sheath potential drop, with results with a range of $\sim$10–20 V. For simplification, some authors such as Mitterauer & Till (1987), Coulombe (1997) and Messaad et al. (2006) specify a constant potential drop $V_{cs} = 15$V, whilst others such as Bolotov et al. (1995) and Rethfeld et al. (1996) prefer to determine it through the system of vacuum arc equations, indicating the potential drop's dependence on the type of cathode material and other factors such as surface temperature. Lafferty (1980) presented an analysis supporting the constant potential drop assumption within the arc existence region of mode (0). For simplicity, this work initially used a constant potential drop V_{cs} = 15 V.

5.3.6 Cathode Spot Number

The number of cathode spots present was based on studies by Djakov and Holmes (Lafferty 1980, Boxman et al. 1995). For aluminium, a single operating cathode spot (i.e. N = 1) is observed for currents $<$ 30–50 A, whilst higher currents will spawn a proportionally larger number of spots. Thus, $I^* \approx 30$ A.

5.3.7 Cathode Spot Radius

The cathode spot radius was a difficult parameter to identify, mainly because of the extreme and rapid conditions in which they are formed. As an initial guess, the most probable spot radii observed ($r_s \approx$ 1–10 μm) was chosen as a free parameter based on studies from Daalder (see Lafferty (1980)), who plotted a direct proportional relationship between cathode spot size and arc current. However, due to the direct (and therefore critical) role of the cathode spot size on the amount of thrust produced, the model was modified to include calculation of the cathode spot radius by means of an energy flux balance at the cathode surface, removing it's status as a free parameter. A detailed explanation of this approach is described in the next section.

5.3.8 Degree of Ionisation

The degree to which the evaporated atoms are singly ionised is generally assumed in literature to be in the upper region of roughly 0.8–1 for simplicity (Kutzner & Miller 1989, Messaad et al. 2006). The main reason for this assumption is that multiply charged ions are often present, suggesting that, on average, nearly all the ions must have been ionised at least to the first degree. Studying Equations 5.5, 5.30, 5.46 and 5.48 will show that thruster performance is directly related to γ. A further complication is that γ is difficult to physically measure/confirm experimentally. Thus, the Saha equation was used to find γ more accurately within the analytical model, no longer making it a free parameter. However, the assumption of single ionisation is still used to reduce complexity (see Appendix F).

5.3.9 Ion Charge State Distribution

The ion charge state distribution has been found to be time-dependent such that average ion charge states are higher at short pulse durations (Anders 2001, Anders 1998). For longer pulses, the ion CSD settles to relatively constant values. As an assumption, ion CSD data was taken from experimental work by Anders (2001), performed specifically for aluminium and short vacuum arc pulses (3 μs, 300 A) and initiated with the "triggerless" arcing method.

5.4 Method of Solving the Analytical Thruster Model

In earlier versions of the model, arc properties were solved as functions of temperature. However, it was later realized that an iterative approach was needed since the surface temperature is dependent on the cathode spot size, which is governed by the balance of energy flowing in and out of the spot region.

To begin, an arc current is prescribed and the spot number and spot current is found (Equation 5.18). An assumed spot radius is specified to determine the total current density J_t (Equation 5.17). A surface temperature T_s is assumed within an appropriate range (2800–8000 K) and used to solve various properties of the arc (Equations 5.1, 5.2, 5.5–5.15). To solve γ more accurately, the Saha equation is used as discussed in Section 5.3. An initial plasma density n_p is assumed to find γ, which is substituted into Equation 5.5. From the sequence of Equations 5.5–5.14 (which includes the particle density balance), 5.32 and 5.33, a new plasma density n_p' is calculated and fed back into the sequence of equations for iteration until a convergence criterion is reached, namely

$$\left| \frac{n_p' - n_p}{n_p} \right| \leq 10^{-6} \tag{5.57}$$

Once the plasma density is found, the total current density J_t' can be found with Equation 5.16 and compared to the "specified" J_t (Figure 5.6). Using a modified *Bisection Method*, a closer approxima-

tion of T_s is iterated until the "specified" and calculated total current densities are suitably close in value (negligible improvement in accuracy of T_s is observed, < 0.1 K), resulting in the convergence criterion

$$\left| \frac{J_t' - J_t}{J_t} \right| \leq 10^{-3} \tag{5.58}$$

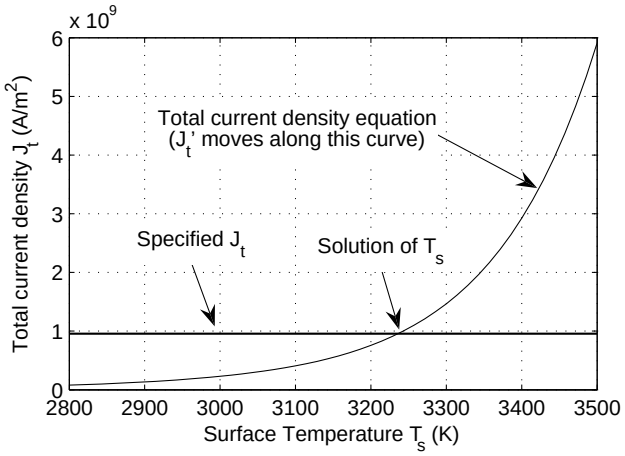

Figure 5.6: Example of the intersection of calculated and specified total current densities to solve for the surface temperature

At this point, the surface temperature and subsequent arc properties are found (using the current density balance) for the assumed spot radius. However, the energy flux balance (Equation 5.21) must also be solved for completeness and may be used to calculate the spot radius, since r_s plays a direct role in Joule heating and heat conduction. Calculation of the energy flux terms (Equations 5.22–5.29) results in a comparison of the conduction energy flux q_{con} from Equation 5.29 and re-arrangement of the terms in Equation 5.20, i.e. $\Delta = |q'_{con} - q_{con}|$. The principle of using the energy flux balance to solve for the cathode spot size was also used by Benilov (Jüttner 2001) and Messaad et al. (2006). The entire solution process was repeated for a range of radii, starting at 0.2 μm and increasing in 0.05 μm increments until the smallest difference between the conduction terms was found (typically 6–8 orders of magnitude smaller than the peak difference). Surprisingly, there are actually *two* solutions that emerge from the energy flux balance (See Figure 5.7). However, the result of two apparent solutions immediately brings to mind Ecker's concept of two arc existence regions, namely mode (0) and mode (1) mentioned in Section 2.3.2. Recalling that mode (1) is characterised by larger values of T_s, E, J_t, etc. compared to mode (0), suggests that mode (1) should have a smaller spot radius than mode (0) to account for the larger current density and other arc properties. In the convergence graph, the first convergence point occurs around 1–2 μm and the second at around 10 μm, which produces the expected order of magnitude difference in arc properties. Non-refractory metals usually prefer operating at mode (0) due to the lower arc voltage requirement and greater arc stability than mode (1) (Lafferty 1980). Hence, the larger spot radius is chosen.

The final result is a predicted cathode spot radius, surface temperature and other arc properties that obey the defined particle density and cathode surface energy balances. The erosion rate is found

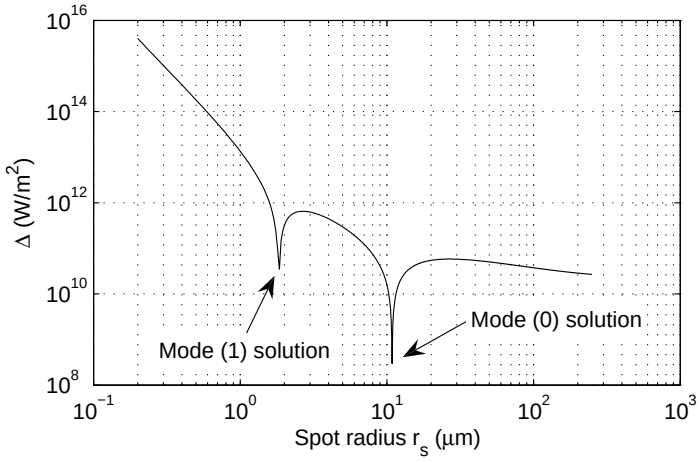

Figure 5.7: Convergence of energy flux balance showing possible mode (0) and (1) solutions

with Equation 5.35. The ion velocity is found with Equation 5.34. Finally, thruster performance parameters may be determined from Equations 5.31, 5.46–5.56. The solution process is summarised in Figure 5.8 below. Figure 5.9 presents a more detailed illustration of the interaction between major variables.

5.5 Summary

A theoretical model of the VAT was successfully formulated and a numerical method of solution made possible by solution of a current and particle density balance at the sheath edge and an energy flux balance at the cathode surface. The choice of free parameters for an aluminium cathode were approximated and, to some extent, justified. The presence of two arc modes was observed to emerge from the model's solution. Mode (0) (according to Ecker's definition) was chosen as the arc operating point and thrust performance parameters determined hence. Sample calculations of the analytical model are presented in Appendix G. Theoretical results are presented and discussed in the next chapter.

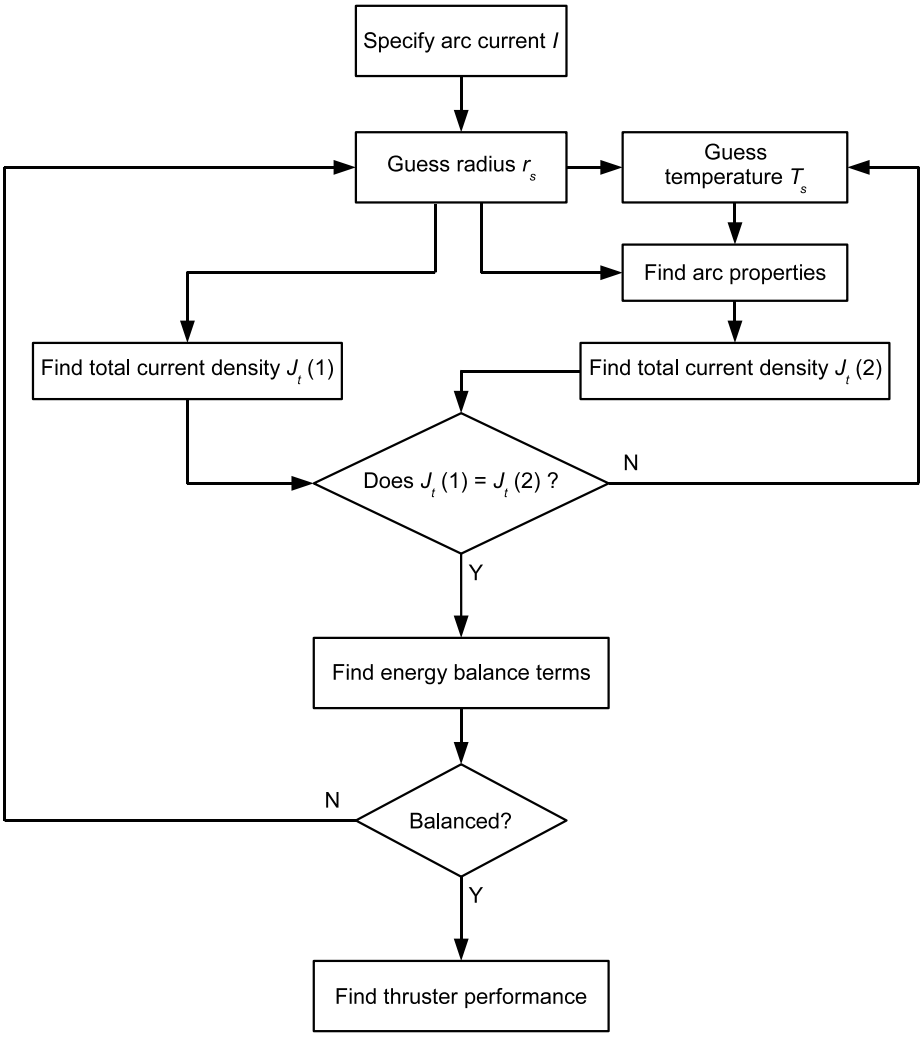

Figure 5.8: Solution flow diagram

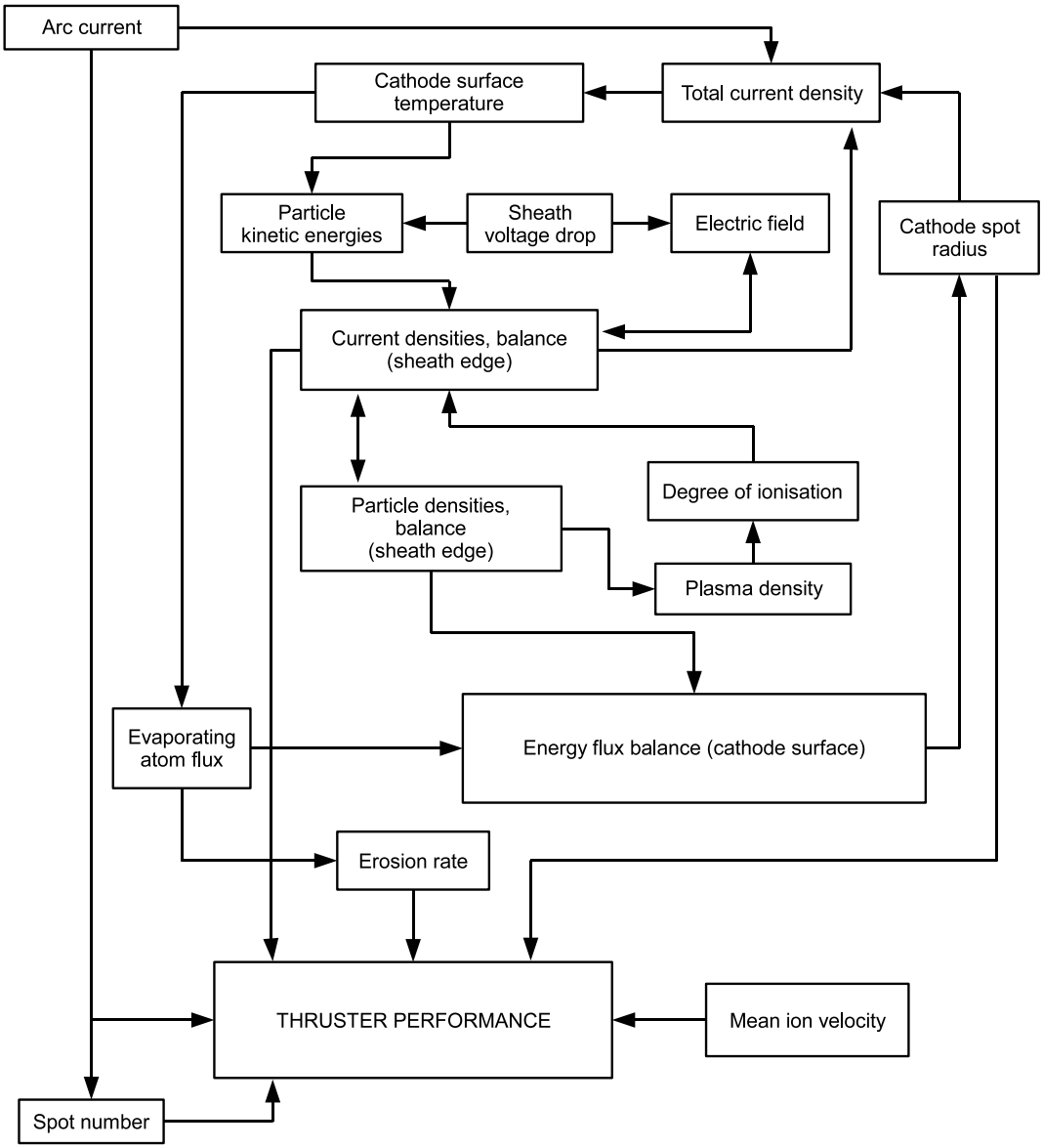

Figure 5.9: Variable interaction flow diagram

Chapter 6

Results and Discussion

This chapter presents detailed analytical model results and a sensitivity analysis on the analytical model's dependence on the free parameters chosen for the vacuum arc model. General trends are observed and explained where possible. Predicted and measured results of ion velocity, ion-to-arc current ratio, erosion rate, thrust and thruster performance are also presented and compared with literature. Observations of the cathode surface were made and notable thruster behaviour is explained.

6.1 Detailed Results of the Analytical Model

Table 6.1 is detailed summary of results obtained by the analytical model for an arc current of I_d = 300 A. Order of magnitude particle, current and energy flux densities compare well with literature such as Riemann (1989), Rethfeld et al. (1996), Coulombe (1997), Rossignol et al. (2003), Lafferty (1980), Boxman et al. (1995), Anders & Yushkov (2002), Hantzsche (1983) and Beilis (2001b). Note that the use of the approximate thermo-field electron emission mechanism (Equation 5.11) is verified since T_s and E are within the valid temperature and electric field range of the approximation. The predicted surface temperature is close to the expected value found in literature ($\sim$3500 K) and the spot radius is also within general literature bounds (1–20 μm). Table 6.1 also shows that the heat conduction energy flux is almost negligible compared to other energy flux terms ($> 10^4$ magnitude difference). Other model results are discussed more thoroughly in following sections.

Table 6.1: Analytical model results for I_d = 300 A

Result	**Symbol**	**Value**
Spot radius	r_s	10.9 μm
Surface temperature	T_s	3553.1 K
Evaporating atom flux density	Γ_{ev}	2.47$\times^{28}$ m^{-2}s^{-1}
Electric field	E	4.76$\times 10^9$ V/m
Degree of ionisation	γ	0.9937
Ion current density	J_i	5.27$\times 10^9$ A/m^2
Emitted electron current density	J_{em}	8.31$\times 10^{10}$ A/m^2
Returning electron current density	J_{er}	7.99$\times 10^9$ A/m^2
Total current density	J_t	8.04$\times 10^{10}$ A/m^2
Ion particle density (sheath)	n_{is}	9.58$\times 10^{24}$ m^{-3}
Total electron particle density (sheath)	n_{es}	2.57$\times 10^{25}$ m^{-3}
Emitted electron particle density (sheath)	n_{ems}	2.22$\times 10^{23}$ m^{-3}
Returning electron particle density (sheath)	n_{ers}	2.54$\times 10^{25}$ m^{-3}
Ion particle density (plasma)	n_{ip}	1.58$\times 10^{25}$ m^{-3}
Electron particle density (plasma)	n_{ep}	4.23$\times 10^{25}$ m^{-3}
Plasma particle density (plasma)	n_p	5.81$\times 10^{25}$ m^{-3}
Mean ion velocity	$\bar{v}_i$	23.97 km/s
Ion bombardment energy flux	q_i	1.29$\times 10^{11}$ W/m^2
Emitted electron energy flux	q_{em}	1.86$\times 10^{11}$ W/m^2
Returning electron energy flux	q_{er}	7.17$\times 10^{10}$ W/m^2
Joule heating	q_J	1.40$\times 10^{10}$ W/m^2
Vapourised atom energy flux	q_{vap}	1.38$\times 10^{10}$ W/m^2
Radiation energy flux	q_{rad}	9.03$\times 10^6$ W/m^2
Heat conduction energy flux	q_c	1.58$\times 10^{10}$ W/m^2
Ion-to-arc current ratio	ζ	0.0653
Erosion rate	E_r	6.91 μg/C
Thrust	F	16.22 mN
Specific impulse	I_{sp}	797.5 s

6.2 Sensitivity Analysis for the Analytical Model

A sensitivity analysis was performed to ascertain the behavioural response of the model structure to the free parameters (as defined by Chapter 5) and to determine the confidence in quantifying these parameters. Their range of values were based on typical literature results. 'Nominal' values of the free parameters, as discussed in Section 5.3, are defined in Table 6.2. Several key vacuum arc thruster results, namely, the cathode spot radius r_s, cathode surface temperature T_s, electric field E, degree of ionisation γ, ion-to-arc current ratio ζ, erosion rate by vapourisation E_r, thrust F and specific impulse I_{sp} were studied. For convenience, these results are normalised with respect to their values obtained for a 'nominal' model solution at I_d = 300 A (see Table 6.1 in the previous section). An arc current of 300 A was used since all model results are independent of arc current as long as $I_d \geq I^*$.

Table 6.2: List of free parameters

Free parameter	Symbol	Units	Nominal	Range of study
Backflow coefficient	α	-	0.5	0.3–0.7
Field-enhancement factor	β	-	2	1–5
Electron temperature	T_e	eV	3	1–4
Ion temperature	T_i	eV	$T_s \approx 0.3$	0.2–2
Sheath potential drop	V_{cs}	V	15	12–50
Average spot current	I^*	A	30	30–50

6.2.1 Backflow Coefficient

The backflow coefficient α dictates how much ion bombardment occurs at the cathode surface. This has several effects: a slight linear decrease (2 %) of T_s in either direction from nominal over α = 0.3–0.7 is observed in Figure 6.1 (b). r_s shows an exponential decay with increasing α (30 % above and 15 % below nominal for α = 0.3 and 0.7 respectively (Figure 6.1 (a)). Less ion bombardment means that the spot radius must increase dramatically to maintain plasma densities. Figure 6.1 (c) shows a gradual exponential increase in the electric field with increasing α ($\pm$10–15 % above and below nominal within α range). E increases due to larger ion backflow as expected. Figure 6.1 (d) shows a very small linear decrease ($\pm$0.02 % from nominal) in γ across the entire range of α. Figure 6.1 (e) shows a strong exponential decay of ζ with increasing α (280 % above and 40 % below nominal for α = 0.3 and 0.7 respectively). The behaviour of the ion-to-arc current ratio emphasises the direct control α has on the amount of ions escaping the cathode region. α also has an identical effect on the erosion rate and thrust, which are direct derivatives of ζ (Figures 6.1 (f) and (g)). Greater ion bombardment means more ion condensation on the cathode surface and thus a lower E_r. Likewise, higher α means less ions available for thrust. α has little effect on specific impulse with < 1 % change from nominal because I_{sp} is a function of both F and E_r, and the effect of α cancels out. (Figure 6.1 (h)). The fluctations observed are likely due to rounding error in the analytical model.

In summary, the backflow coefficient has little effect on the surface temperature, degree of ionisation and specific impulse. It has a medium effect on the electric field and a large effect on the spot radius and, most importantly, the amount of ions available for thrust. Thus, α has a significant impact on thruster performance as witnessed by large changes in erosion rate and thrust.

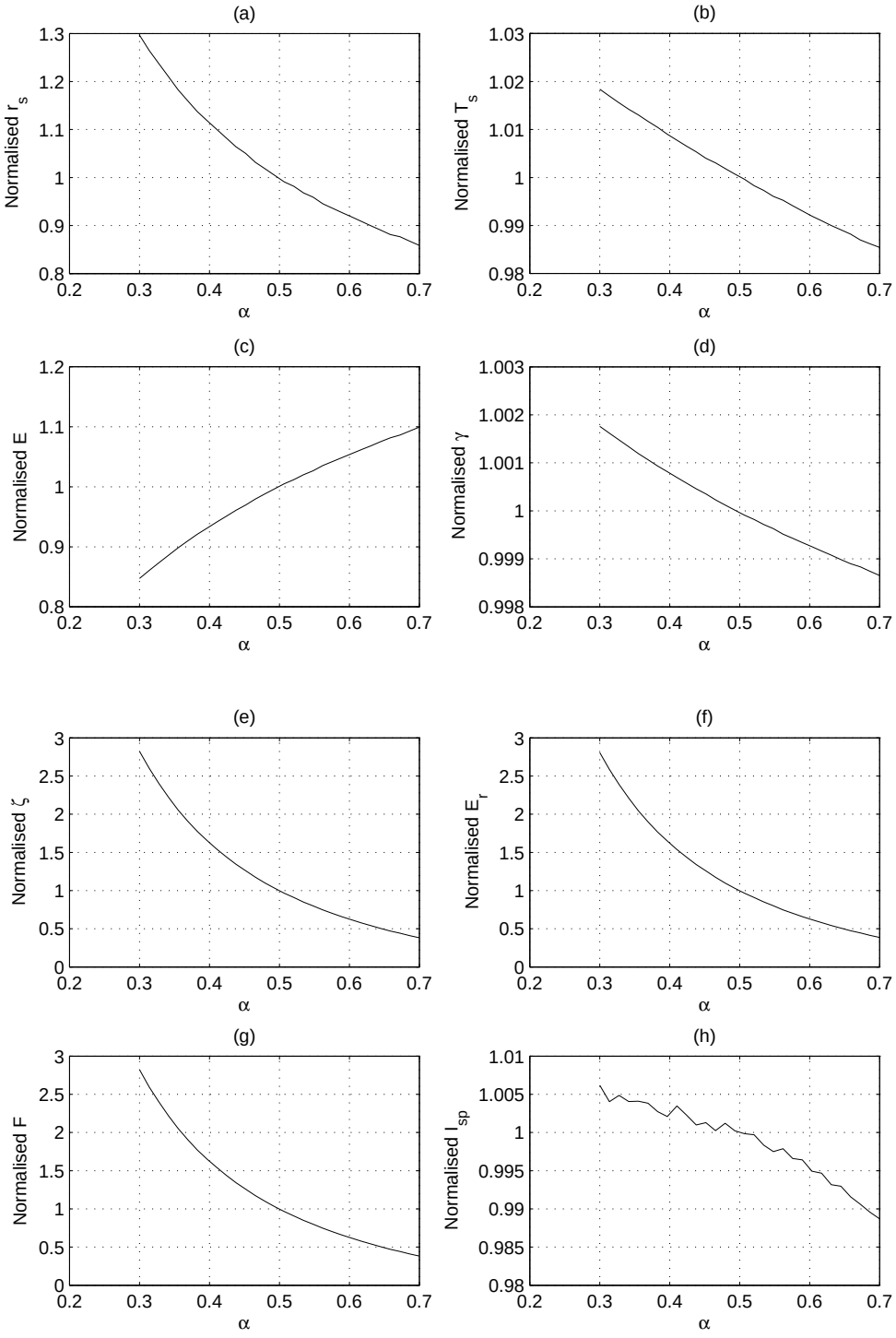

Figure 6.1: Effect of α on (a) r_s, (b) T_s, (c) E, (d) γ, (e) ζ, (f) E_r, (g) F and (h) I_{sp}

6.2.2 Field-Enhancement Factor

Figure 6.2 (a) shows a linearly increasing spot radius with increasing β by as much as 300 % above nominal for β = 5. At higher values of β, more electron flux is created. Thus, r_s can be larger because sufficient electron flux density is created. The effect of β on T_s is the opposite: electrons are more easily created by field emission, which means lower thermionic emission and hence a lower T_s. Also, greater electron emission will cool the cathode, resulting in a lower T_s. The surface temperature exponentially decays from 30 % above to 17 % below nominal for β = 1 and 5 respectively (Figure 6.2 (b)). Interestingly, the electric field shows similar behaviour to T_s even though E is directly proportional to β (Figure 6.2 (c)). It seems that the effect of β on T_s influences the ion current density, which has a greater effect on E for $\beta < 2$ (30 % above nominal at β = 1). Larger values of β have more influence on E as shown by the near linear decrease in E. E decreases somewhat (15 % below nominal at β = 5) because less effort is required to extract the electrons from the rougher cathode surface. E is seen to approach a steady value with increasing β (15 % below nominal). Another effect of increased field emission is that more electrons are available to collide with atoms, increasing the degree of ionisation (Figure 6.2 (d)). γ rapidly approaches unity (full ionisation) with increasing β and differs only by 3 % below nominal at the extreme condition of β = 1 (clean smooth surface). Figures 6.2 (e)–(g) show identical behaviour in that ζ, E_r and F rapidly increase (starting at 30 % below nominal) with increasing β settling at stable values (5 % above nominal) for $\beta > 3$. Specific impulse also quickly increases to about 1 % from nominal (Figures 6.2 (h)).

In summary, the surface temperature and electric field possess decreasing medium sensitivity (20–30 % from nominal) to increasing values of the field-enhancement factor. Most results were highly sensitive to values of $\beta < 3$ and insensitive beyond. The exception is the spot radius, which increases linearly with increasing β regardless. However, it is expected that r_s will also approach a steady value as T_s approaches the limit of the boiling point of the cathode material.

6.2.3 Electron Temperature

The effect of the electron temperature on results is more subtle and complex due to non-linear behaviour. A comparison of the behaviour of r_s, T_s, E and E_r against varying T_e was done with Messaad et al.'s (2006) work and confirmed general trends. Figure 6.3 (a) shows a large decrease of r_s with increasing T_e (220 % above and 60 % below nominal for T_e = 1 and 4 eV respectively). Figure 6.3 (b) shows a relatively steady T_s (5 % below nominal) at T_e = 1–2 eV, but an exponential increase for greater T_e values (7 % above nominal at T_e = 4 eV). Figure 6.3 (c) shows a relatively increasing E with increasing T_e (30 % below and 40 % above nominal for T_e = 1 and 4 eV respectively). The electric field increases because more energetic electrons are present in the sheath. Figure 6.3 (d) shows a low value of γ (45 % below nominal) at T_e = 1 eV, which rapidly approaches unity for $T_e > 2$ eV. Greater ionisation occurs because at higher electron temperatures, the electrons have more energy and can collide with more atoms. Figure 6.3 (e) shows a large decrease of ζ with increasing T_e (200 %

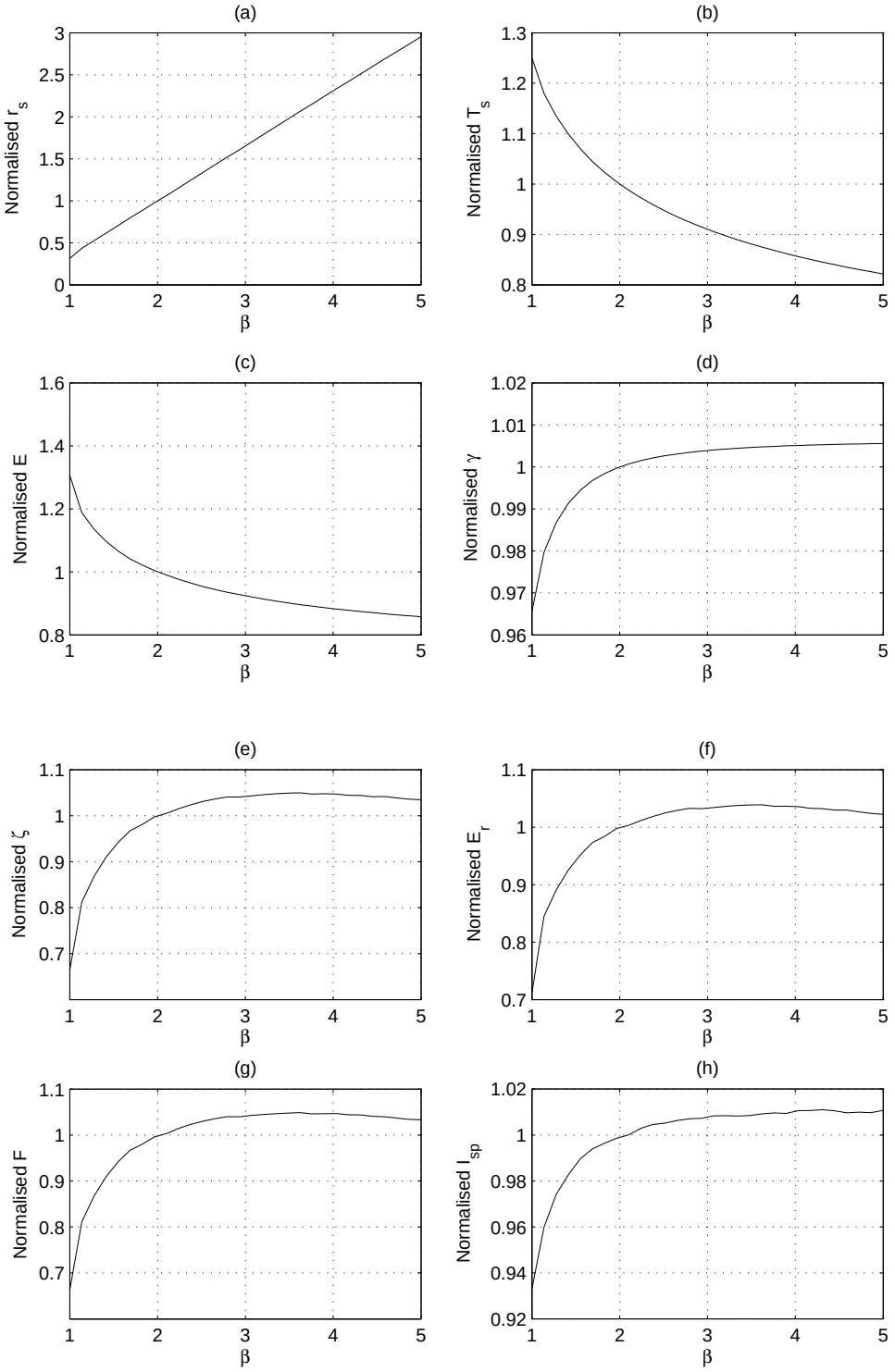

Figure 6.2: Effect of β on (a) r_s, (b) T_s, (c) E, (d) γ, (e) ζ, (f) E_r, (g) F and (h) I_{sp}

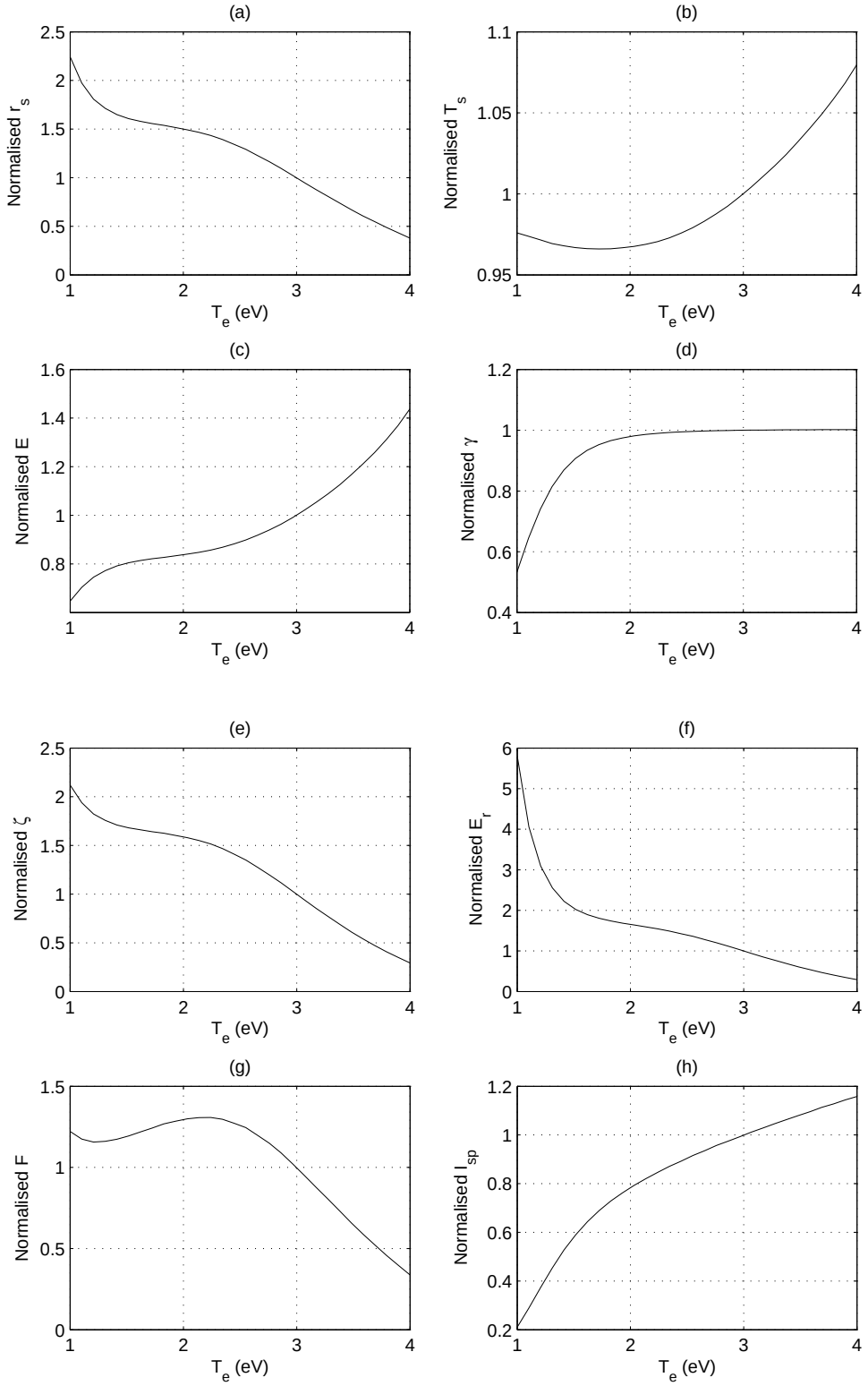

Figure 6.3: Effect of T_e on (a) r_s, (b) T_s, (c) E, (d) γ, (e) ζ, (f) E_r, (g) F and (h) I_{sp}

above and 70 % below nominal for T_e = 1 and 4 eV respectively). Interestingly, less ions are created at higher electron temperatures even though more ions are ionised. This is attributed to the fact that a high electron temperature reduces the number of plasma particles in general, reducing the amount of ions present. Figure 6.3 (f) shows a rapid decrease of E_r from 600 % above nominal at T_e = 1 eV to 200 % above nominal at T_e = 1.5 eV. Thereafter, E_r decreases linearly with increasing T_e to 70 % below nominal at T_e = 4 eV. Figure 6.3 (g) shows an oscillating value of F ($\pm$15–25 % above nominal) for $T_e < 2$ eV. For $T_e > 2$ eV, F rapidly decreases linearly to 65 % above nominal at T_e = 4 eV. The effect of less ions present is seen in a lower erosion rate and thrust. Figure 6.3 (h) shows a gradual increase of I_{sp} from 80 % below to 115 % above nominal over T_e = 1–4 eV. Another interesting observation is that most of the graphs show inflection points at T_e = 1.5 eV and 2.3 eV. Also, F peaks at 2.3 eV, caused by the same inflection point occurring in r_s and ζ.

In summary, the electron temperature has a highly non-linear effect on most results, which cannot be fully explained. T_e has a small effect on the surface temperature and the degree of ionisation (only for $T_e > 2$ eV). T_e has a generally large effect on the spot radius, electric field, ion current, erosion rate, thrust and specific impulse.

6.2.4 Ion Temperature

Figures 6.4 (a)–(h) show that the ion temperature has very little effect on all results (2 % from nominal over an order of magnitude change in T_i). Fluctuations in graphs are probably due to numerical and rounding error. However, the general trend of a gradual increase for all results with increasing T_i (except for T_s and E, which show a decrease) is observed. It is interesting to note that T_i was also observed to produce parameter trends opposite to those of α (except for T_s). It is not possible at this point to say exactly how the ion temperature affects arc conditions and further study is needed.

6.2.5 Sheath Potential Drop

Figure 6.5 (a) shows that r_s increases with increasing V_{cs} from 40 % below nominal at V_{cs} = 12 V and reaches a peak of 25 % above nominal at V_{cs} = 20 V. r_s then decreases to 12 % below nominal at V_{cs} = 50 V. Figure 6.5 (b) shows T_s decrease from 5 % above to 4 % below nominal from V_{cs} = 12–25 V. Thereafter, T_s remains constant across higher values of V_{cs}. The effect of a smaller sheath potential means that less backflow of particles to the surface occur, requiring the need for a smaller r_s and larger T_s to sustain the arc. However, the effect of larger values of V_{cs} on r_s and T_s is uncertain. Figure 6.5 (c) shows the electric field with a "valley" type behaviour starting at 20 % above nominal at V_{cs} = 12 V down to a minimum of 7 % below nominal at V_{cs} = 20 V, and then increasing to 10 % above nominal at V_{cs} = 50 V. A smaller V_{cs} means a smaller sheath region, hence producing a larger electric field and vice versa. Figure 6.5 (d) shows γ increase from just under nominal to just over nominal between V_{cs} = 12–20 V. Thereafter, γ remains constant near unity. Figures 6.5 (e)–(g) exhibit

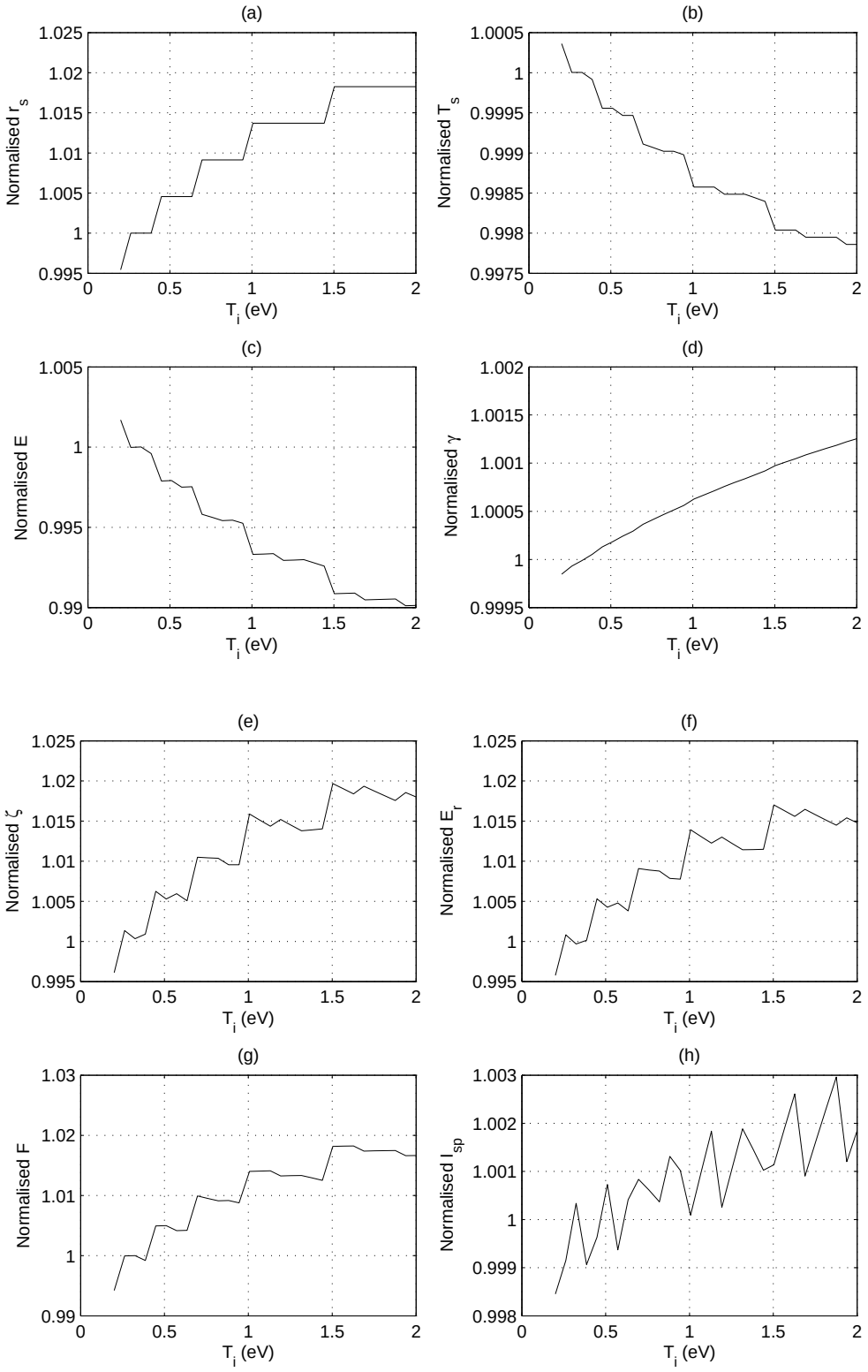

Figure 6.4: Effect of T_i on (a) r_s, (b) T_s, (c) E, (d) γ, (e) ζ, (f) E_r, (g) F and (h) I_{sp}

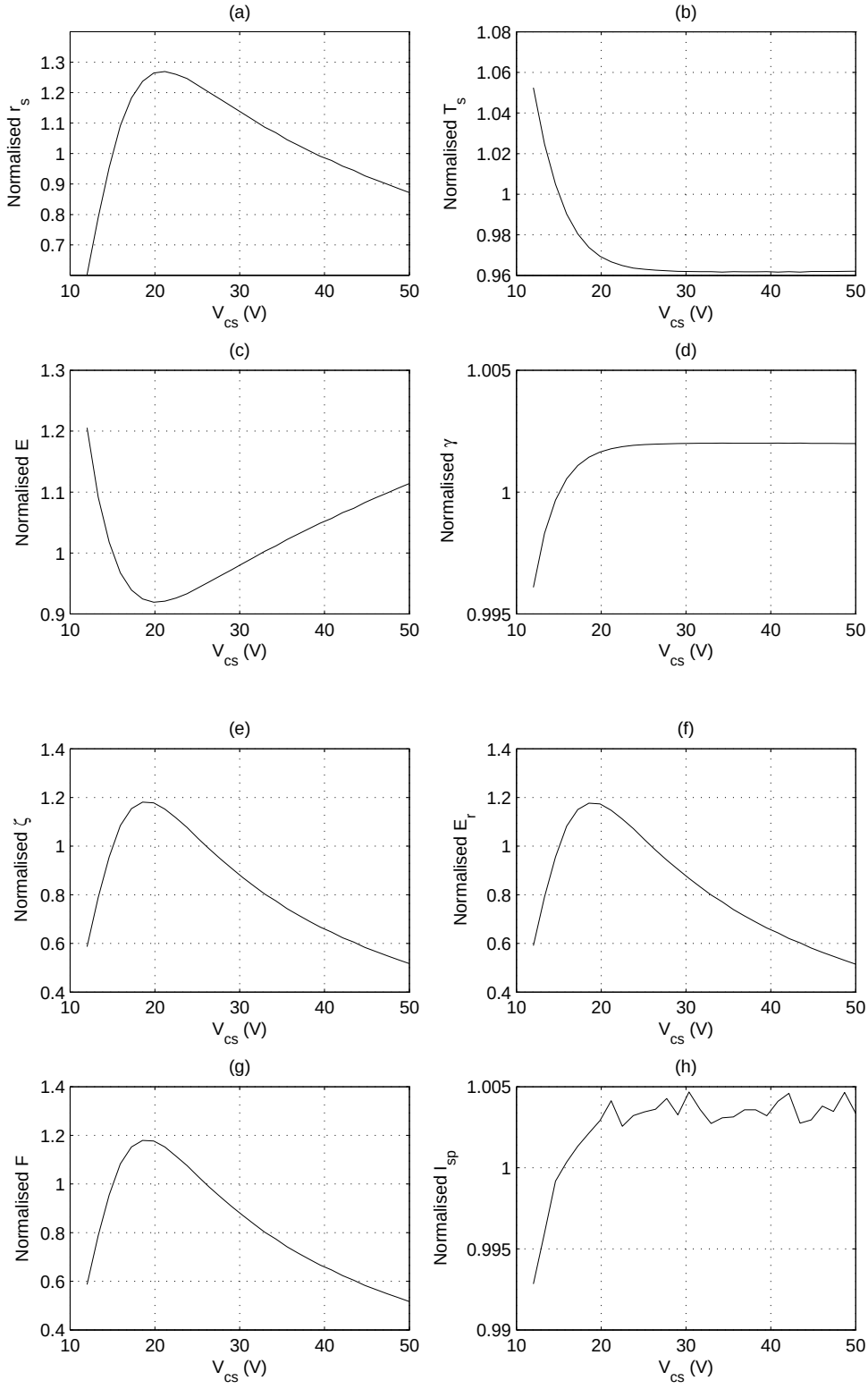

Figure 6.5: Effect of V_{cs} on (a) r_s, (b) T_s, (c) E, (d) γ, (e) ζ, (f) E_r, (g) F and (h) I_{sp}

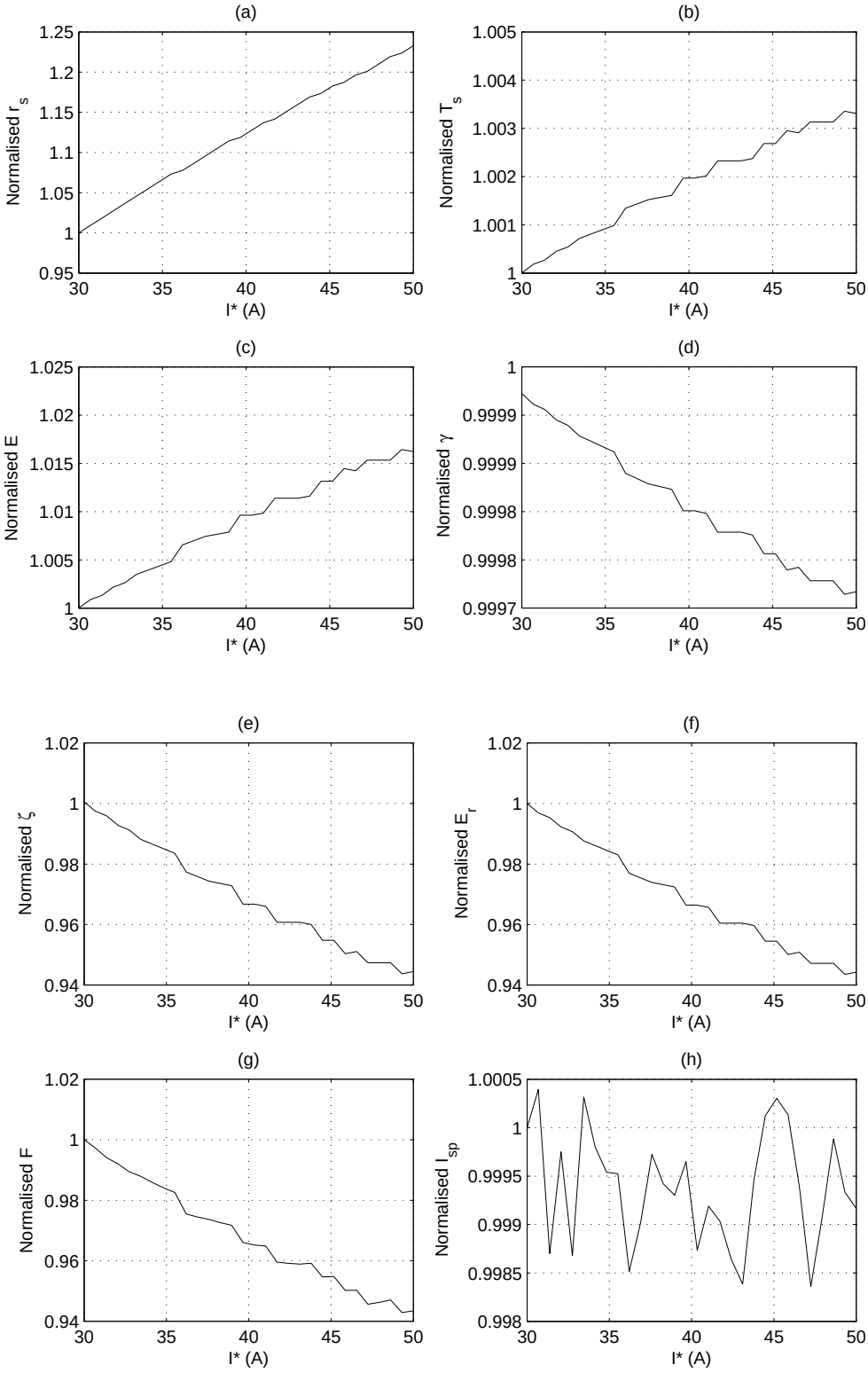

Figure 6.6: Effect of I^* on (a) r_s, (b) T_s, (c) E, (d) γ, (e) ζ, (f) E_r, (g) F and (h) I_{sp}

the same "hill" profile, with 40 % below nominal at V_{cs} = 12 V, peaking at 20 % above nominal around V_{cs} = 20 V and decreasing to 50 % below nominal at V_{cs} = 50 V. Too large a V_{cs} means particles, especially ions, are attracted back to the surface due to the larger 'potential hump', reducing the erosion rate and thrust. Figure 6.5 (h) shows similar behaviour to γ in magnitude and shape (slight change and increase to a steady value). Fluctuations are likely due to rounding error.

In summary, the potential sheath drop has a small effect on the surface temperature, degree of ionisation and specific impulse. It has a non-linear medium effect on the spot radius, electric field, ion current, erosion rate and thrust.

6.2.6 Average Spot Current

Figures 6.6 (a) shows r_s increasing linearly to 23 % above nominal at I^* = 50 A. This is because a higher spot current present requires a larger spot radius to achieve the same current density. In Figures 6.6 (b)–(h), the average spot current has a small effect on T_s, E, ζ, E_r and F and virtually no effect on γ and I_{sp}. At I^* = 50 A, T_s and E slowly increase about 3 % and 1.5 % above nominal respectively. ζ, F and E_r decrease about 6 % below nominal at I^* = 50 A, which is contrary to the expected performance increase from a larger r_s. In summary, the average spot current has a weak effect on most results (except for r_s as expected). However, a negative performance hit of a few percent is seen at higher I^*.

6.2.7 Conclusions

Discussion on the Choice of Free Parameters

Results show highly non-linear behaviour with all free parameters, emphasising the complexity of vacuum arc models. The free parameters that had the greatest effect on results were α, T_e and V_{cs}. Parameters with the least effect were T_i and I^*. Therefore, an opportunity exists to verify or refine the choice of free parameters.

The sensitivity analysis shows that the initial choice of a backflow coefficient of $\alpha = 0.5$ is reasonable, since a value of ζ = 6.6 % is only slightly below the literature's range of 0.07–0.1. The high sensitivity of α is problematic, since a 10 % adjustment of α produces a 50 % change in ion current. Thus, the choice of α remains intuitive until further study can be done.

The field-enhancement factor has a negative effect on performance for low values of β. It is interesting to note that for surface roughness beyond β = 3, little gains in performance are obtained. This means that making the surface more rough will not increase performance. Initially, the cathode surface will contain many microprotrusions and surface defects which act to enhance field emission.

However, during arcing, the formation of craters and melted metal will change the structure of the surface 'landscape' and eventually smooth the surface out. Thus, the surface roughness will change significantly over time, but is then likely to settle upon an average value. Thus, surface roughness is maintained at $\beta = 2$ since it gives a reasonably correct prediction of $T_s \approx 3500$ K, which is consistent with literature and high values of β will not remain valid for a heavily eroded surface.

The sensitivity analysis shows that T_e = 1–2 eV produces unrealistic values of γ, ζ and E_r. However, higher values of T_e severely affect the amount of ejected ions. A notable problem is that measurements of the electron temperature Boxman et al. (1995) indicate a much higher value (> 5 eV) than those obtained from model predictions (2–3 eV). However, Boxman et al. notes that the Zero-Order model underestimates the plasma electron density by a factor of 2–4. A higher T_e would result in a correspondingly smaller plasma ion density and hence less ions current. Thus, the choice of T_e = 2–3 eV at the sheath would appear to produce plasma densities in good agreement with reality even though the actual electron temperatures in the plasma are much higher. Another observation is that model results are relatively stable near the inflection point of T_e = 2.3 eV, but the significance of this is unclear. Therefore, there is no choice but to maintain T_e at approximately 3 eV.

The weak effect of the ion temperature on free parameter variation justifies the loose assumption of T_i. It should be noted, however, that the ion temperature was ignored when using the Saha equation (Appendix F) to approximate the LTE plasma temperature. This would make γ more sensitive to T_i, so the analysis is not entirely accurate for the whole range of T_i studied. However, the analysis is still valid for this model ($T_i < 0.7$ eV), since values of T_i = 1–2 eV are nevertheless inconsistent with reported results in literature (Keidar et al. 2005). The effect of the average spot current is also relatively weak, allowing for a more flexible choice of I^*. The choice of I^* was maintained at 30 A, since its effect on the model's results was only of a few percent.

The sensitivity analysis for V_{cs} highlighted an interesting effect, with all results (except for γ and I_{sp}) being insensitive within the narrow range of V_{cs} = 18–20 V. On either end of that region; results all diverge away from their peak or minimum value at V_{cs} = 18–20 V, producing "hill" and "valley" profiles. This pattern is striking enough to suggest that a suitable sheath potential drop has emerged from the results for stable vacuum arc conditions in the cathode spot region. Further evidence is that the 'insensitive' region (V_{cs} = 18–20 V) occurs near the assumed sheath potentials commonly reported and estimated in literature of 15–20 V (Boxman et al. 1995). Thus, the sheath potential drop was adjusted to 18 V to slightly improve the predicted erosion rate and ion-to-arc current ratio, both of which are underestimated.

A sensitivity analysis for $\bar{Z}$ could not be performed because knowledge of how the ion charge state distribution changes with increasing average charge state could not be obtained. The ion CSD is needed because it is used in the calculation of the ion current density (Equation 5.5) and ion bombardment energy flux (Equation 5.22). It is expected that more energetic ions would travel faster (Equation 5.34) and create more intense conditions within the arc, thereby improving thrust. On the other hand, more energetic ions also mean less of them, which will reduce thrust (Equation 5.46).

Therefore, the thrust is likely to have a non-linear relationship with $\bar{Z}$, as the sensitivity analysis has demonstrated for a number of other free parameters.

The Effect of Model Results on Thrust

The degree of ionisation was observed to be very close to unity in all cases, indicating that nearly all atoms are ionised in the ionisation zone, which is consistent with literature. The use of the Saha equation had proved useful in confirming the degree of ionisation, since literature had given a very wide range of γ to choose from (0.8–1). The sensitivity analysis also found that the electric field had an adverse effect on thrust. It was observed that every time the electric field increased when varying a free parameter, the thrust decreased proportionately (and *vice versa*), revealing an approximately inverse linear relationship between E and F. This effect can be explained by the fact that in the sheath region, a very strong electric field will encourage electron acceleration away from the cathode, but accelerate ions *toward* the cathode. This means that the ions flowing away from the cathode are reduced and even decelerated, resulting in a lower thrust. This conclusion suggests that E may affect the value of α in some way. As discussed earlier, the cathode spot and ion-to-arc current ratio play a significant and direct role in determining the amount of thrust produced. Thus, accurate prediction of these quantities is of considerable importance, especially ζ.

6.3 Experimental and Theoretical Results

This section presents and compares results from the predictive analytical model and measured experimental data for ion velocity, ion-to-arc current ratio, erosion rate, and thrust. Thruster performance parameters (thrust-to-power ratio, specific impulse and efficiency) are also presented. A description of each result is given, trends and behaviour explained and conclusions made. The *refined* analytical model uses the nominal free parameters, with V_{cs} changed to 18 V as discussed in the previous section and its results are presented here.

6.3.1 Ion Velocity

Figure 6.7 compares the ion velocity samples measured by the ITMS and predicted by the refined analytical model. An initial glance shows that the predicted result is slightly less than the average measured ion velocity. However, a relatively large scatter of experimental results is seen (17–37 km/s). Results for individual pulse are quite scattered because of the non-uniform nature of plasma generation (Polk et al. 2001, Anders et al. 2001). A reason for less scatter at higher voltages is suggested in Section 6.3.3. However, more sample data is required to determine if this effect is random scatter or a data trend. The comparison of results with literature in Table 6.3 shows that the experimental re-

sults are well within literature bounds. However, this is only because a large discrepancy of reported mean ion velocities exists. One possible reason is that the ion velocity depends on the pulse duration. Anders & Yushkov (2002) reports that ion velocity was measured to be highest at the beginning of each arc pulse and approached lower steady-state values after about 150 μs. This work's higher velocity results are consistent with this explanation, since a pulse duration of 400 ns was used and literature reported results for pulse durations > 150 μs.

The measured ion velocity also appears to be decreasing with increasing breakdown voltage and average values drop below the predicted value after V_d = 2000 V ($I_d \approx 500$ A). This is inconsistent with literature, which report velocities independent of arc current. A possible explanation is that a much higher arc voltage was used, as opposed to the usual 20–30 V arc voltage. The effect of a high voltage on the ion velocity was hinted at earlier in the sensitivity analysis of the previous section. It was explained previously in Section 6.2.7 that a high electric field and sheath potential drop may have the effect of slowing down ion flow away from the cathode region, which would explain a decreasing ion velocity with increasing V_d. The effect of high arc currents is also discussed in Section 6.3.3.

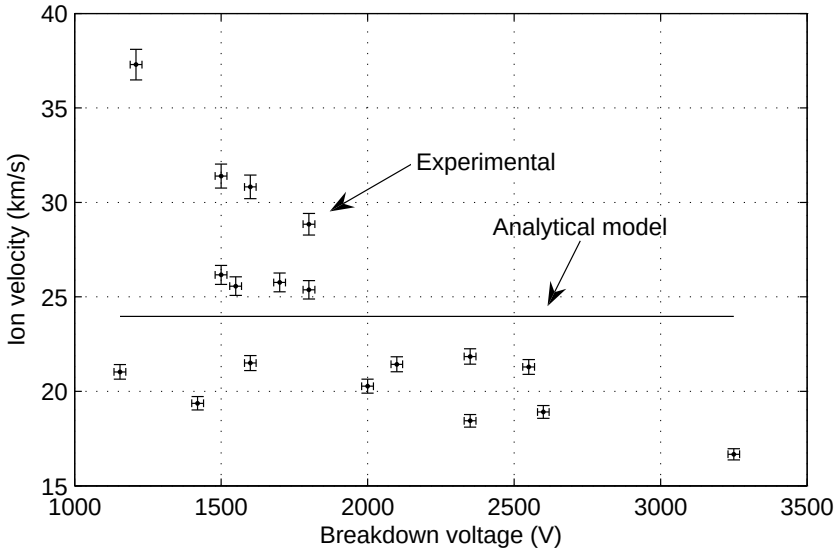

Figure 6.7: Comparison of predicted and measured ion velocities

Table 6.3: Comparison of mean ion velocity results

Source	**Type**	**Value (km/s)**
This work	Refined analytical model	23.97
	Experiment ($V_d \leq 2000$ V)	26.12
Polk et al. (2001)	Semi-empirical model	29.9
Anders & Yushkov (2002)	Experiment (100–300 A)	15.4
Boxman et al. (1995)	Experiment (100 A)	~20.7
Lafferty (1980)	Experiment (50–100 A)	~16.9

6.3.2 Ion-to-Arc Current Ratio

Figure 6.8 compares measured ion-to-arc current ratios against arc voltage with the refined analytical model. Experimental results are also fairly scattered as with the ion velocity, but are generally larger than the predicted value. The reason for decreased scatter of ζ, as with $\bar{v}_i$, at higher arc voltages is presented in Section 6.3.3. Some samples are seen to be about 20–30 % higher than the literature upper bound, which suggests that the measured ion current may be overestimated overall. Most samples, however, are comfortably within the general literature range of 0.07–0.1. Table 6.4 indicates that the averaged measured ζ is within reported literature values. The predicted value of ζ is lower compared to literature and measured values (this may due to the 'loose' choice of the backflow coefficient α).

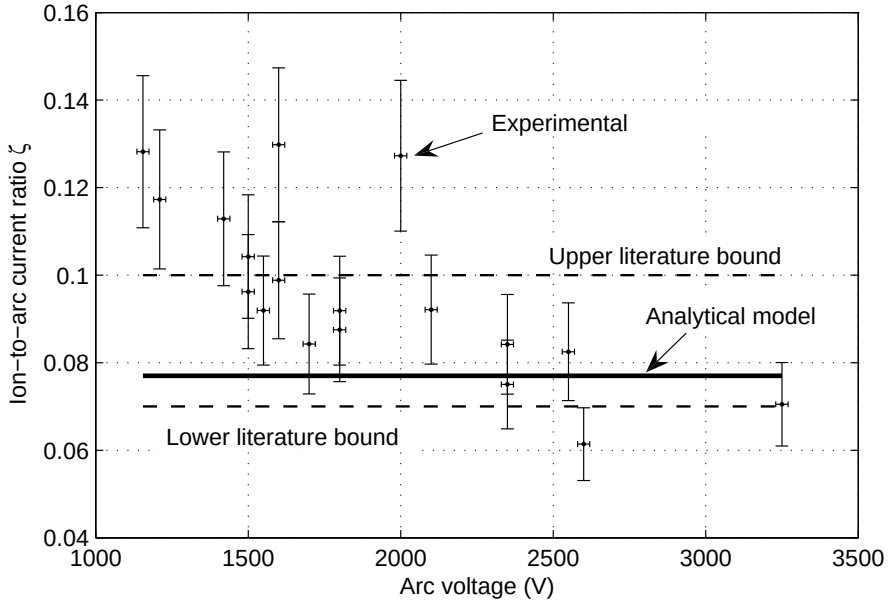

Figure 6.8: Comparison of predicted and measured ion-to-arc current ratios

Measured samples of ion-to-arc current ratio also show a decreasing trend as with measured ion velocities, with a noticeable drop in value beyond V_d = 2000 V. This can also be related to the high arc voltages applied in the arc. It is possible that ion flow is not only decreased, but also *reduced* as an ever increasing amount of electrons are emitted by the higher electric field. The effect of high arc currents is also discussed in Section 6.3.3. The ion current may be slightly overestimated as not all the EMI effects on the ion current signal could be eliminated, leaving a residual signal. Another effect is that secondary electron emission may have also played a role, but that is likely to be small. The most likely cause of a higher ion current is that the collector tunnel walls would have directed much of the expanding plasma 'cloud' in the direction of the collector plate. Some of it would have reached the collector and diffused into it, giving the impression of a larger amount of charge emitted in the direction of the plate.

Table 6.4: Comparison of mean ion-to-arc current ratio results

Source	Type	Value
This work	Refined analytical model	0.077
	Experiment ($V_d \leq 2000$ V)	0.106
Polk et al. (2001)	Semi-empirical model	0.1
Oks et al. (2006)	Experiment (50–500 A)	$\sim$0.112
Anders et al. (2004)	Experiment (100 A)	0.083

6.3.3 Erosion Rate and Cathode Microstructure

Table 6.5 compares predicted, measured and reported values of cathode erosion rate. The predicted erosion rate, which only considers atom vapourisation and ion condensation, is over an order of magnitude less than that measured and reported. This shows that macroparticle ejection makes up the majority of cathode erosion. The measured erosion rate is in very good agreement with literature tests at short pulses. However, some sources report erosion rates as low as a factor of five. This is because the erosion rate is highly dependent on interrelated factors such the surface temperature, pulse duration, arc current, cathode specimen size, etc. A higher pulse rate was found to increase erosion rate due to the increase in average surface temperature (Shalev et al. 1985). Also, the erosion rate increases rapidly with longer pulses and higher arc currents from gross melting. Another interesting effect is that very short pulses (in the nanosecond range) also produce higher erosion rates (Boxman et al. 1995). This is because arc initiation is a violent event, with rapid Joule heating, which causes micro-explosions on the cathode surface. Thus, many liquid droplets are formed and ejected every time the arc forms (Coulombe 1997). Thus, the high value of the measured erosion rate in this work is to due to the use of high currents, relatively high pulse rates, a very short pulse duration and a small specimen size, which impedes heat dissipation. Boxman et al. (1995) discussed the possible effect that ejected macroparticles have on ion flow. They proposed that these large droplets impede ion flow and even absorb ions and neutralize them, becoming charged in the process. This means that when the ion flux is reduced, the measured overall ion energy is reduced, which may be interpreted as a lower average ion velocity. This could also explain why ion current and ion velocity measurements in Figures 6.7 and 6.8 appear less scattered at higher voltages/high arc current (2000 V/500 A) because fewer of the high energetic ions are able to reach the collector plate. Thus, high arc voltages and high arc currents produce additional macroparticles, which absorb ions and impede ion flow.

There may have also been a slight possibility of outgassing with the cathode specimen during the erosion rate test, since a piece of electrical wire was attached to it. However, the specimen had been used in vacuum over a period of a few months and it was assumed that outgassing was no longer an issue. The relatively good result of measured erosion rate compared with literature confirms that outgassing was not a problem. Figure 6.9 shows the final estimated mass flow rate estimated with a second-order curve fit, which ranges roughly between 0.3–0.5 μg/s. The very large uncer-

tainty bounds is due to the sampling limit of erosion rate test, where samples were only taken every 20–60 minutes.

Table 6.5: Comparison of erosion rate results

Source	**Type**	**Value (μg/C)**
This work	Refined analytical model	8.1
	Experiment	110
As cited by	Experiment (Juttner, 10–500 ns)	100
Boxman et al. (1995)	Experiment (Plyutto)	120
	Experiment (Brown)	28
	Experiment (Daalder, Eckhardt)	19

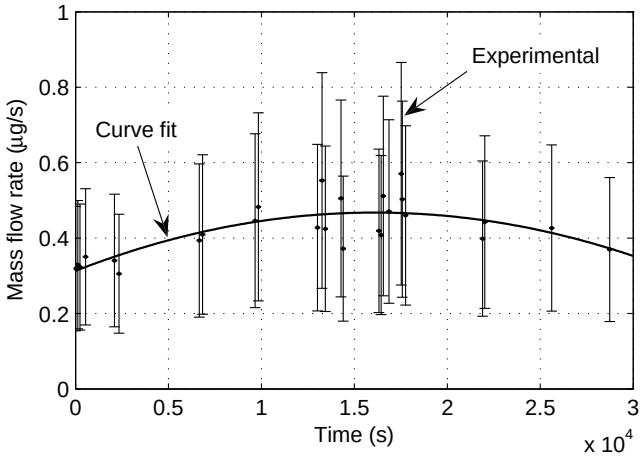

Figure 6.9: Estimated mass flow rate $\dot{m}_s(t)$ over the time of the erosion rate test

Microscopic pictures of the cathode specimen were taken at various resolutions to reveal the presence of craters caused by cathode spots (Figure 6.10). At $\times$3 and $\times$470 magnification, Figures 6.10 (a) and (b) show gross melting and large structures are clearly seen on the specimen edge. At $\times$2660 magnification, Figure 6.10 (c) reveals crater diameters as large as 50 μm. However, these are often comprised of smaller craters with diameters on the order of 15–20 μm, which is not far off from the predicted spot diameter of the refined analytical model (26.7 μm). However, many large craters indicate heavy and violent erosion occurred. All craters are relatively deep and spherical in profile and their rims smooth.

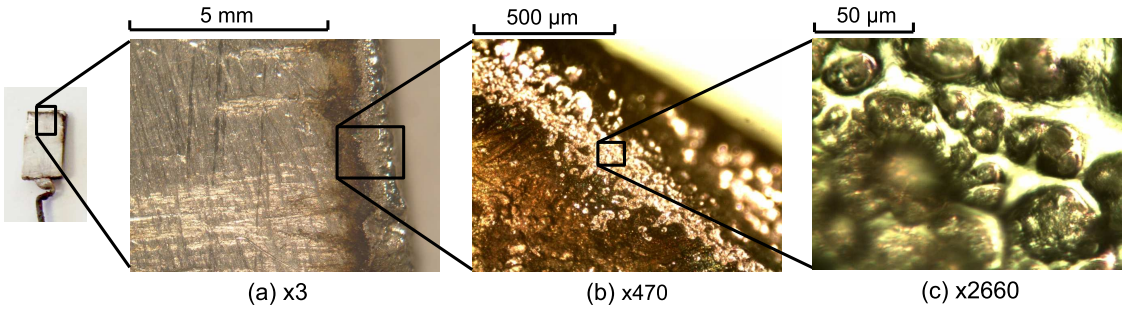

Figure 6.10: Microscopic view of cathode surface at (a) ×3, (b) ×470, and (c) ×2660 magnification

6.3.4 Thrust

For general comparison, an estimated VAT model was made to produce upper and lower bounds of possible VAT thrust. Table 6.6 shows the list of parameters based on typical reported quantities in literature, to roughly estimate the thrust based on a modified form of Equations 4.26 and 5.48:

$$F = C_T \left(m_i \frac{\zeta I_d}{e\bar{Z}} \right) \bar{v}_i \tag{6.1}$$

Table 6.6: Upper and lower bound parameters to be used in Equation 6.1

Parameter	Symbol	Upper bound	Lower bound
Thrust correction factor	C_T	0.33	0.33
Ion-to-arc current ratio	ζ	0.1	0.07
Average ion charge	$\bar{Z}$	1.5	2.5
Average ion velocity	$\bar{v}_i$	30 km/s	15 km/s

Figure 6.11 shows a comparison between analytical thrust, directly and indirectly measured thrust, predicted thrust by Polk et al. (2001) and boundaries of the estimated thrust from Equation 6.1. Figure 6.12 shows the relative percentage difference between measured and predicted thrust values. The basic VAT model estimation shows a very wide range in which thrust is possible. The predicted thrust is relatively close to the lower estimation bound with a linear dependency on arc current at roughly 63 μN/A of average arc current. Polk et al.'s (2001) model predicts a relatively large thrust close to the upper estimation bound. Polk et al. credits this to high ion current mass fraction. Their model also uses a higher measured ion velocity (∼30 km/s) and lower average ion charge state (due to longer pulse durations) than this work. Thus, a lower average ion charge state tends to improve thrust (see Equation 6.1). The average directly measured thrust is about 120 % larger than the predicted thrust (Figure 6.12), but shows a generally linear increase with arc current. This places directly measured thrust at roughly 140 μN/A of average arc current ($<$ 400 A). A comparison of DTMS thrust results taken at 12 and 18 mm deflector distances shows that electrostatic attraction

was successfully reduced to negligible effect. However, thrust levels for arc currents above 500 A could not be obtained due to electrostatic attraction problems. Large uncertainty bounds are mainly due to large sensor noise when measuring deflection. Possible reasons for much larger direct thrust measurements are thrust contributions from liquid droplets and burnt Teflon insulation particulates being ejected. However, it is likely that macroparticle thrust will be small because of the recessed cathode design used. Evidence of ejected Teflon particulates is shown in Figure 6.13, where a thin burnt layer as well as small black particles deposited onto the perspex plate after a long thruster operation. Also, burn marks were also seen on the Teflon area exposed to expanding plasma. So, in a sense, the VAT is also acting like a pulsed plasma thruster (PPT), which ablates Teflon material for thrust (see Appendix A for a brief description of the PPT).

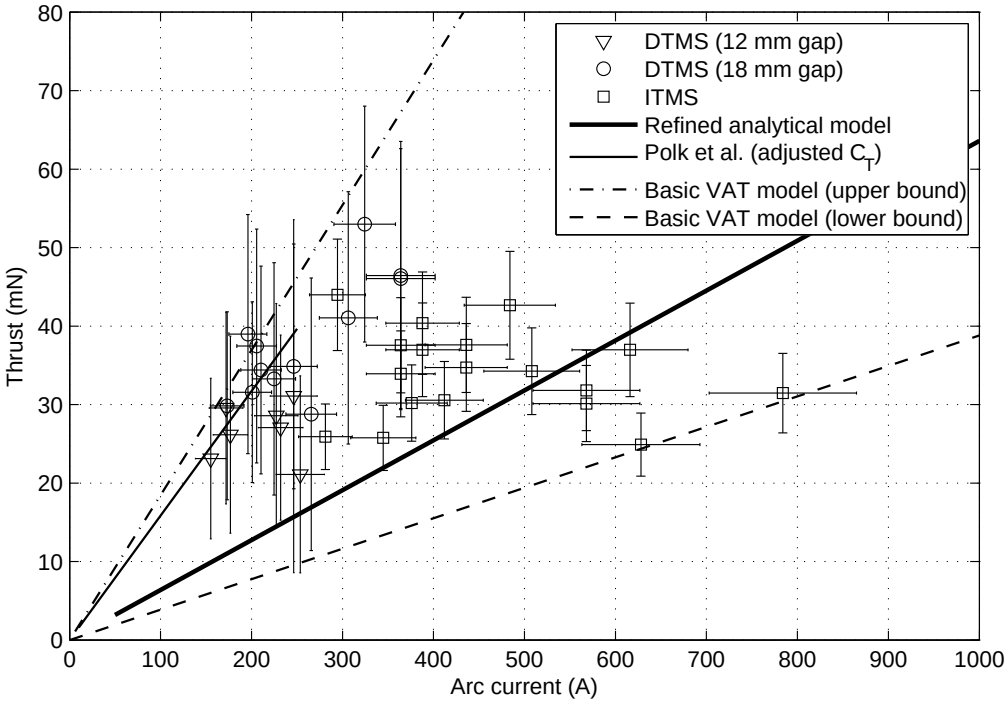

Figure 6.11: Comparison of predicted, measured and estimated thrust

Average ITMS thrust results are approximately 30 % larger than the predicted thrust at roughly 82 μN/A of average arc current ($<$ 500 A). This confirms DTMS results of thrust sources in addition to ion flow. Thus, it appears that ablated Teflon accounts for almost as much thrust as ion flow. As stated before in Section 6.3.2, the ion current may be slightly overestimated from the higher ion-to-arc current ratio measured. Taking this into account places ITMS thrust results reasonably close to predicted values of thrust. Beyond arc currents of 500 A, ITMS thrust declines significantly by more than 30 % below predicted thrust (Figure 6.12). The lower thrust at $I_d > 500$ A is as a result of the combination of a high arc voltage and current to produce a lower ion velocity and ion current discussed previously. The large scatter seen in DTMS and ITMS results is due to non-uniform plasma formation as explained before in Section 6.3.1.

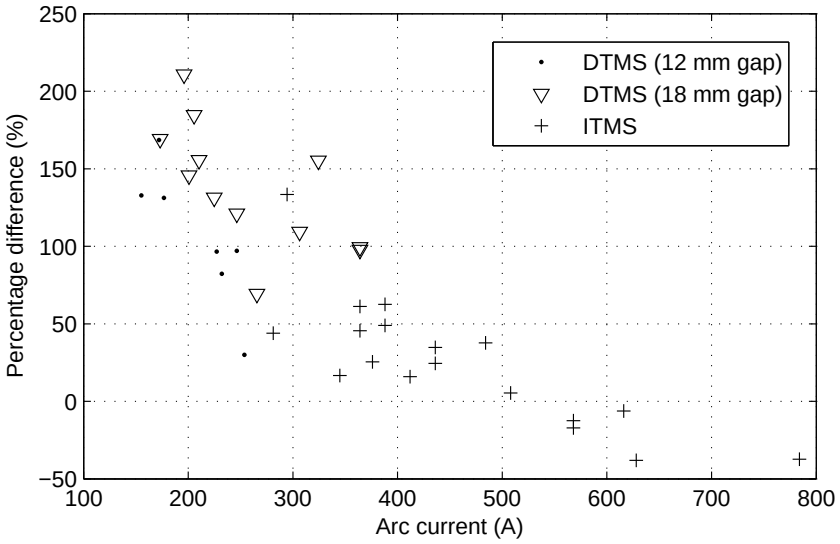

Figure 6.12: Relative difference between predict and measured thrust (error bars omitted for clarity)

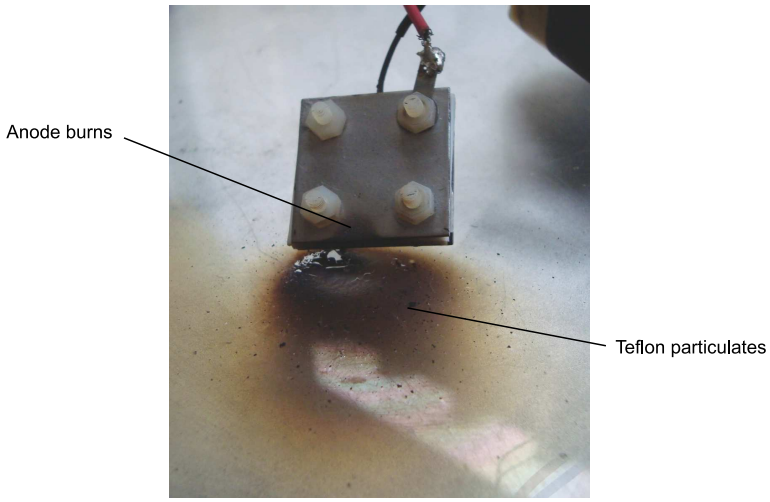

Figure 6.13: Evidence of ejected Teflon particulates

Figure 6.14 illustrates how strongly the backflow coefficient and mean ion velocity affects the under-predicted thrust. Nominal free parameter values were based on the findings of the sensitivity analysis. Reducing α to 0.4 increases predicted thrust significantly ($\sim$50 %), whilst employing a mean ion velocity similar to Polk et al. would improve thrust by $\sim$20 %. For example, adjusting α to 0.43 would predict ζ and thrust per arc current at 0.1023 and 84.6 μN/A respectively, which matches the ITMS results. Thus, the refined analytical model's accuracy relies heavily on the 'loose' choice of these parameters, which cannot be avoided at this present time.

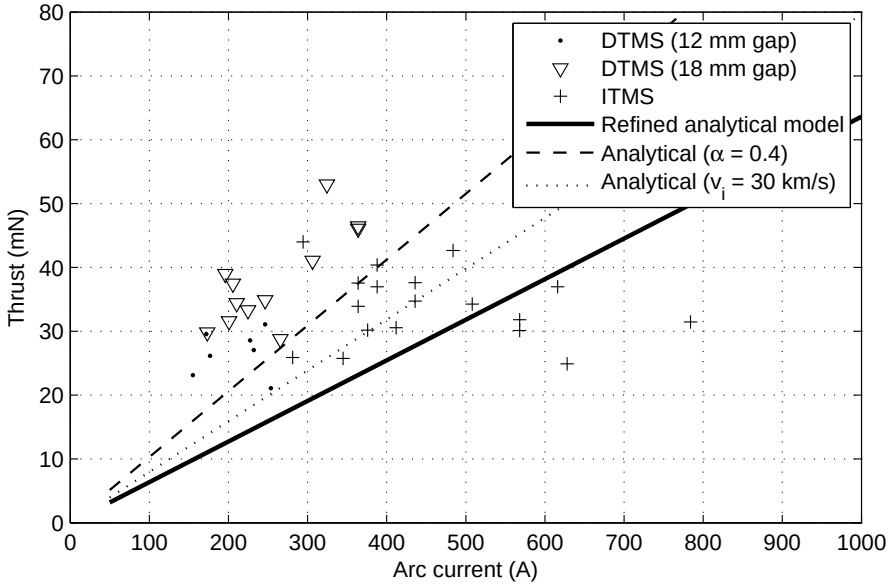

Figure 6.14: Illustration of the effect of α and $\bar{v}_i$ on thrust (error bars omitted from measured data for clarity)

6.3.5 Thrust-to-Power Ratio, Specific Impulse and Efficiency

Figures 6.15–6.17 present calculated values of H, I_{sp} and η_T based on the measured values of thrust, erosion rate and arc power. Peak values of H, I_{sp} and η_T were 0.6 μN/W, 160 s and 0.05 % respectively at I_d = 200 A. All values are significantly lower than those predicted by Polk et al. (2001) and reported by Schein et al. (2002) and Schein et al. (2007) by more an order of magnitude. This is due to a number of reasons: (1) a very high arc voltage (1–2 kV) was used for the arc pulse, which results in a high arc power (1–2 kV), whereas other VAT designs have used arc voltages of around 30 V; (2) a high erosion rate was measured in this work, which employed very short pulses and high arc currents; (3) a higher average ion charge state is present at short arc pulses, which reduces thrust; and (4) the cathode surface was recessed into the thruster, reducing the thrust correction factor to about half that of a design with a flush surface (Polk et al. 2001). All performance parameters show exponentially decreasing values with increasing arc current. This is due to less and slower ion flow at high arc currents as well as the exponential relationship of arc power with arc current. Thus, the thruster performs best at currents less than 200 A.

6.4 The Presence of Anode Spots

It was observed that a diffuse and unstable anode spot had sometimes formed during thruster operation. This is because the peak instantaneous arc current during the single pulse is much higher than the average arc current used. Thus, instantaneous arc currents could reach levels greater than 1–2

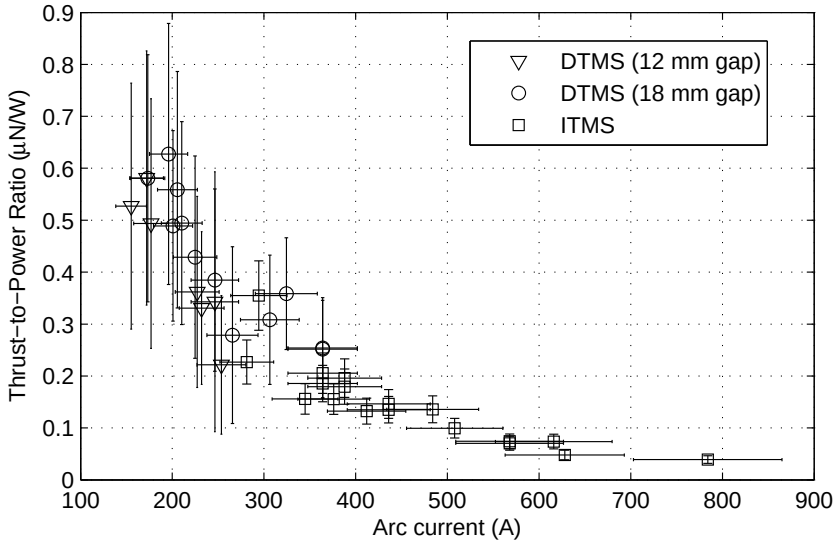

Figure 6.15: Thrust-to-power ratio results

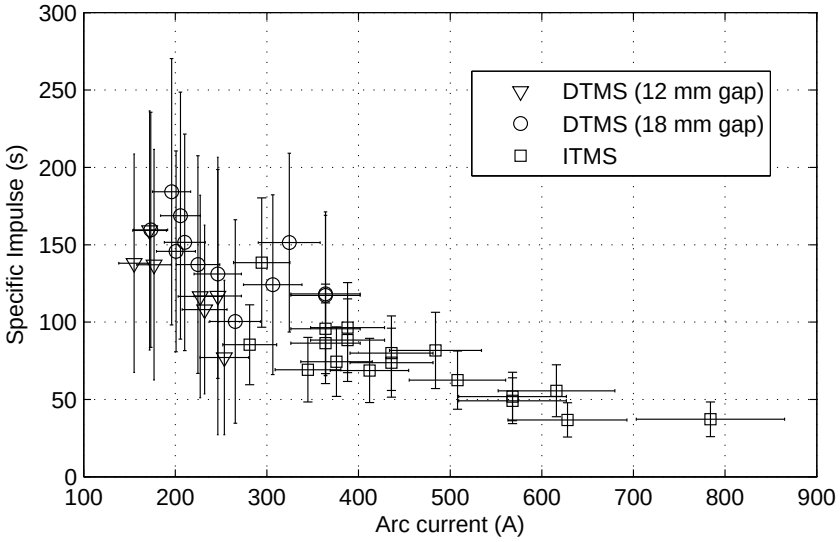

Figure 6.16: Specific impulse results

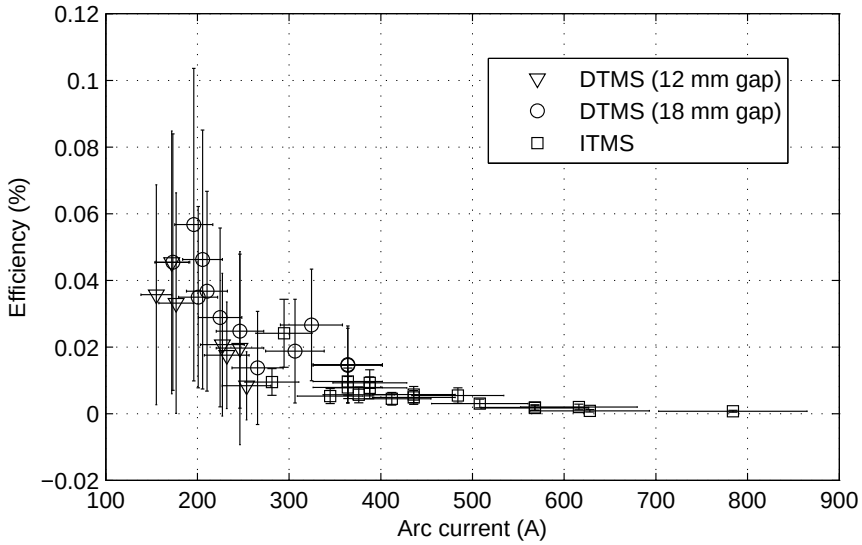

Figure 6.17: Efficiency results

kA during arcing, thus forming anode spots. These spots were characterised by a different colour (purple) to the cathode region plasma (blue). Figure 6.18 indicates the presence of an anode spot on the top electrode. It appears that some plasma formation has also occurred there due to the high density of the electron flux. Further inspection of the anode electrode after a test shows the presence of pitting and possible anode craters formed on the surface (Figure 6.19). This indicates that some material has been removed by melting and possibly ionisation. This would likely deliver a small thrust contribution apart from the cathode ions. Another interesting effect has been a black burn mark, apart from the craters, on the anode surface, also seen in Figure 6.13. The mark is similar to the one observed on the perspex plate, making it likely that this burn layer originated from ablated Teflon near the cathode, which was carried by the plasma and deposited onto the anode. The anode spot is seen to play a weak role in vacuum arc phenomena (Lafferty 1980).

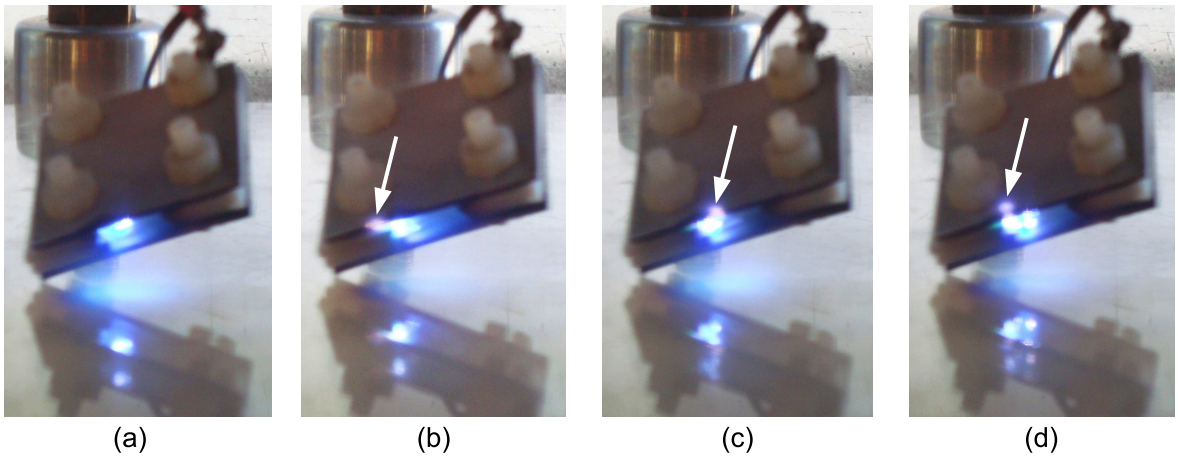

Figure 6.18: Presence of anode spots: (a) no spot, (b)–(d) diffuse spot (indicated by arrow)

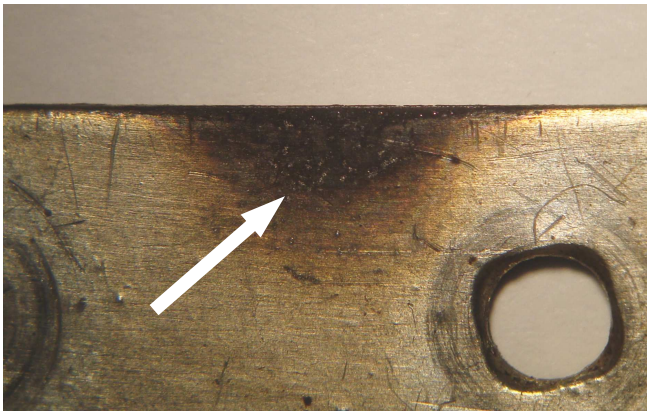

Figure 6.19: Presence of anode craters/pitting

6.5 VAT Design and Operation

A number of observations were made of the VAT's design and operation. Firstly, the position of the screw holes to fix the electrodes together were placed quite close to the cathode. Since Teflon has a lower dielectric strength compared to micanite and vacuum, internal arcing through the screw holes could easily occur if the cathode was not aligned correctly. This is evident in Figure 6.20. Secondly, only one anode could be used because linking both anode plates would cause eddy currents to flow around the anode, heating up the thruster significantly. Thirdly, the arc tended to remain near the corners of the cathode where the curvature was highest and thus electric field concentrations largest. However, cathode spots were still seen to form over most of the cathode surface, giving a fairly uniform plasma jet. Recessing the cathode helped to direct the plasma and greatly reduced the amount of macroparticles emitted.

An endurance test of the thruster was performed simultaneously with the erosion rate measurement test, where the VAT was operated until short-circuiting between the electrodes occurred. Using Equation 4.30, the thruster was estimated to have operated for up to 8×10^5 pulses, which is comparable with other VAT designs (Anders et al. 1998). Figure 6.20 shows evidence of degradation of various thruster components after the endurance test. Figure 6.20 (a) reveals that many large liquid droplets were formed and had deposited onto the anode's inner walls. Figure 6.20 (b) confirms Teflon ablation and Figure 6.20 (c) reveals failure of the micanite insulator at the thruster edge. Burn marks are credited to Teflon ablation. All pictures were taken at $\times$ 3 magnification.

A thruster performance analysis and specification was undertaken to study the suitability of a single or group of VATs to achieve specific tasks such as a satellite separation manoeuvre or a satellite rotation (Appendix H). Estimates show that the VAT is certainly capable of achieve such tasks within possible time frames, power limits and mass loss, even at poor specific impulse and thrust to power ratio. Each VAT can use ≤ 3 W of constant average power during manoeuvres.

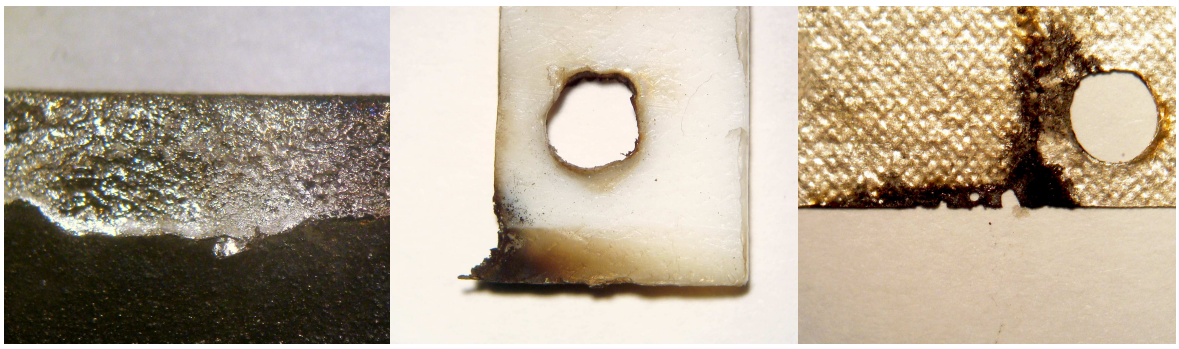

Figure 6.20: Degradation of VAT after endurance test: (a) deposition of molten aluminium onto inner anode surface, and burning of (b) Teflon and (c) micanite insulation edges and screw holes

Chapter 7

Conclusions and Recommendations

A small vacuum arc thruster was successfully developed, tested and shown to be a potential low-thrust propulsion system for a low mass, low power nanosatellite. The thruster was successfully tested with both direct and indirect means of thrust measurement. A one-dimensional steady state vacuum arc model was developed to predict thruster performance. The model is remarkably capable of describing general vacuum arc conditions, despite many simplifications. A number of VAT design changes, improved test methods and analytical model refinements is suggested for further work.

7.1 VAT and Circuit Design

The planar design of the VAT and the use of an aluminium cathode allowed for easy component manufacture and modification. The use of thin ($\sim$0.1 mm) micanite sheets was found to be very suitable for inter-electrode insulation due to its high dielectric strength. To achieve reliable arc initiation, a high voltage pulse (typically 1–2 kV) was used. A HV capacitive circuit was used to apply a 400 ns high current pulse between 150–800 A at pulse rates between 10–100 Hz. A recessed cathode specimen also reduced much surface contamination from liquid metal droplets. The VAT was proved to endure up to 8 $\times 10^5$ pulses over a 9 hour total testing period and was capable of operating below an average power of 5 W. Peak measured values of thrust-to-power ratio, specific impulse and efficiency were 0.6 μN/W, 160 s and 0.05 % respectively at an average arc current of 200 A.

During testing, it was observed that the small size of the VAT made it susceptible to internal arcing. Also, ablation of the Teflon insulation occurred, damaging the thruster. On the other hand, this also created additional thrust from the ejection of Teflon particulates, effectively producing a hybrid VAT-PPT thruster. It is recommended that other VAT geometries such as the ring geometry be tested to achieve increased VAT performance and reliability. The cause of eddy currents in the anode should also be eliminated. Other cathode materials should be used to evaluate their feasibility in VATs,

especially refractory metals (e.g. tungsten, magnesium), since their higher boiling point temperature means that these materials can sustain intense arc conditions without large erosion rates (Coulombe 1997). Composite and alloy cathodes are also possible candidates for study as well as the use of a magnetic field to direct the plasma (Keidar et al. 2005).

The VAT did not perform well at higher arc voltages and currents. High average arc currents ($>$ 500 A) and a short pulse duration caused a high erosion rate by increased production of liquid metal droplets, which also impeded ion flow. Thus, it is recommended to separate the pulse circuit into two circuits (similar to Rysanek (2007b)): one trigger circuit is used to deliver a high voltage ($>$ 3 kV), low current (milli-Amperes), short pulse (nanoseconds) to initiate the arc; and a second PFN arc circuit to deliver a low voltage (30 V), medium current ($\sim$100 A), long pulse (10–300 μs) for the vacuum arc itself.

The benefits of a two-stage arc pulse circuit is that: (1) a lower arc voltage and lower arc current will reduce the arc power significantly; (2) a lower arc current will reduce the cathode erosion rate; (3) a longer pulse will reduce the average ion charge state for increased thrust, reduce the frequency of violent liquid droplet formation events and still provide a larger amount of average thrust. Based on direct thrust results, if (1) the arc power decreased by a factor of $\sim$9 ($P_d = I_d V_d = 30 \times 100 = 3$ kW versus 26 kW), (2) the erosion rate could be decreased by a factor of 3 ($\sim$36 μg/C) and (3) the pulse duration increased to 200 μs ($\bar{Z} \approx 1.7$, for $\sim$60 % increase in thrust), according to Equations 5.54–5.56, the VAT's thrust-to-power ratio, specific impulse and efficiency would increase by a factor of 14.5 (8.7 μN/W), 5 (800 s) and 70 (3.5 %) respectively. These estimated performance results are comparable to other VAT designs.

A thruster performance specification on the VAT was undertaken in Appendix H and showed that the VAT holds much potential for being used on-board a low power ($\sim$5 W) nanosatellite and is capable of performing satellite orbital changes and slew manoeuvres. This makes an improved VAT design even more attractive as a propulsion system, possibly achieving $<$ 1 W of average constant power and a multiple factor of improvement for the specific impulse and efficiency if implemented with the aforementioned design changes.

7.2 Experimental Approach

The simple design of the DTMS was successful in measuring very small thrust impulses in the order of nNs. Directly measured thrust levels were approximately 140 μN/A of average arc current ($<$ 400 A). The cantilever beam was also shown to be successfully modeled analytically. The strain gauge sensor system was capable of detecting beam deflections at the calibrated point as small as 1.5 μm. However, the sensor system suffered from EMI interference and a low signal-to-noise ratio at the range of deflections measured. These were overcome by measuring single thrust pulses and data filtering. The use of 'aerogel' should be considered for ion capture by the deflector to ensure

accurate momentum transfer to the beam by the ions. It is also recommended to employ an optical system, where (for example) beam deflection can be measured by reflection of a laser beam. This eliminates the issue of EMI and is likely to improve the signal-to-noise ratio. Quasi-steady-state thrust could also be measured with such a system, which was not possible with the DTMS. A refined direct thrust measurement system could thus have application as a general thrust measurement system for microthrusters.

The relatively simple design of the ITMS proved to be successful in simultaneously measuring the ion current emitted by the thruster as well as the ion velocity by using the TOF technique. Indirect thrust measurements of thrust were approximately 82 μN/A of average arc current ($<$ 500 A). However, the ITMS could not accurately capture the true ion current over the discharge time. This was overcome by measuring the total charge produced by the colliding ions instead. The effect of the collector plate's bias voltage on the measured ion velocity was also shown to be small. ITMS results also showed that the presence of a large electric field due to a high arc voltage impedes and decelerates ion flow such that lower thrust was observed at arc voltages higher than 2000 V and high arc currents ($>$ 500 A). Measurements of average ion current (ζ = 0.106) and ion velocity ($\bar{v}_i$ = 26.12 km/s) below the 500 A current limit show reasonable correlation with literature. It is recommended that a Faraday cup probe be used for future tests to verify this work's averaged results. Testing should occur in a larger vacuum chamber so that a longer TOF length can be used. This will also remove the effect of EMI from the VAT on ion current results. The total ion current should be measured more accurately by trying to capture as many ions as possible to reduce the uncertainty in assuming a thrust correction factor.

The use of both direct and indirect thrust measurement methods demonstrated that not all the VAT's thrust was due to ion flux. Teflon ablation was credited as the main cause of the higher total thrust seen in the DTMS's results. A collection of 18–19 samples for each thrust measurement method was taken over a wide range of arc voltages/currents. A much larger sample collection (50) should have been made to minimise variability from non-uniform plasma formation. Also, the dependency of arc current to arc voltage in a capacitive circuit caused arc current levels to change with the fluctuating breakdown voltage over time. This made testing at specific arc currents difficult and average arc currents per pulse had to be used for comparison of experimental and analytical results. Finally, a time- and current-averaged erosion rate was found using the cathode weight loss method. A result of E_r = 110 μg/C shows good correlation to literature results for short pulses. However, sampling limits reduced measurement accuracy.

7.3 Analytical Model

The one-dimensional model gave order-of-magnitude results of particle, current and energy flux densities in the cathode spot region that were consistent with literature. The predicted cathode surface

temperature and spot radius were also within literature bounds. Despite the use of free parameters and simplified assumptions such as stationary, steady-state, independent cathode spots and a uniform plasma region, the refined analytical model (α = 0.5) was able to predict an ion-to-arc current ratio of ζ = 0.077, which is fairly close to the literature result of roughly 0.08–0.1. This meant that the ion current density and cathode spot size was fairly close to actual quantities. A visual observation of crater diameters (15–20 μm) also confirmed the reasonably good prediction of spot size (26.7 μm). A predicted mean ion velocity of $\sim$24 km/s also was in good agreement with literature. The emergence of two arc modes in the model solution was consistent with reported literature and mode (0) was chosen as the arc operating condition.

A sensitivity analysis for the nominal model's free parameters was successfully performed. The analysis justified the choice of values for these free parameters and revealed their non-linear effect on model results. The spot radius was found to be the most sensitive of all the results showing large changes typically between 30–200 %. In general, the spot radius is indirectly proportional to particle densities and energies, indicating that the smaller the spot is, the more intense the environmental conditions are inside of it. The cathode surface temperature is most sensitive to β and T_e ($\sim$15 %), but least sensitive to other free parameters. Results also indicate that increasing electron flow from the surface increases cooling of the surface, but increasing electron energies has the opposite effect. The electric field generally behaves in an opposite manner to the spot radius, indicating that a higher electric field is present during more intense arc conditions. The electric field shows the most sensitivity to α, β, T_e, V_{cs}, which confirms the role that ion and electron movement have on the electric field. The degree of ionisation is quite insensitive to all free parameters, differing by no more than 2 % during any given point in the study. The ion-to-arc current ratio has a direct effect effect on the thrust and erosion rate since all three results displayed similar or identical responses to free parameter variation. ζ, E_r and F show greatest sensitivity to α, T_e and V_{cs} ($\sim$ 50–200 %). T_e had the greatest effect on the specific impulse (50–100 %). An important finding was that an increase in electric field was found to have a proportionate decrease in thrust, which was confirmed experimentally.

A theoretical analysis on the effect of anode interference and plume distribution on the current density distribution and effective thrust was successfully developed for a planar thruster geometry and correctly applied to experimental results. Predicted thrust correction factors appear reasonably well with those of Polk et al.'s (2001). However, the ICDD could not be verified experimentally. Thus, one should experimentally measure the ion current density distribution in future studies.

The refined analytical model also predicted a much lower thrust ($\sim$63 μN/A) than what was experimentally measured by the DTMS and ITMS. This was due to thrust sources other than ion flux as discussed previously in Sections 7.1 and 7.2. The loose choice of the backflow coefficient (which influences ζ) and the simplified calculation of the ion velocity also appear to be the main causes of discrepancy as illustrated in Figure 6.14. A more detailed analysis of the plasma region is recommended to refine these parameters. This may be achieved by means of a more complex model of the plasma region above the cathode surface (Boxman et al. 1995, Keidar et al. 2005). A plasma model

would also be able to determine, and hence, reduce the use of, free parameters such as the the ion, electron, and plasma temperatures (Hantzsche 1983).

It would be interesting to see if the analytical model is capable of modeling the vacuum arc process for a refractory metal such as tungsten. The model should indicate only one possible mode (or converged solution) at which the arc can exist. Some modifications to the model equations would be required. For example, the emitted electron current density equation (Equation 5.11) was approximated by Equation 5.10, which is only valid for the ranges $E \in [10^8, 10^{10}]$ V/m and $T_s \in [300, 4000]$ K as stated in Section 5.2.5. A tungsten cathode is expected to operate at or above this electric field range limit and more importantly, at a surface temperature of $\sim$5000 K. Thus, a model that is able to correctly predict thrust for refractory *and* non-refractory cathode materials would be useful indeed, especially if refractory metals are to be considered for cathode material in VATs as discussed in Section 7.1. Coulombe (1997) hints at the possibility of such a model for high pressure arcs, which show many similarities with vacuum arcs. However, it has been reported that simplified vacuum arc models like the one presented in this work show no existing solution for refractory metals depending on model assumptions and simplifications (Lafferty 1980, Boxman et al. 1995). Further investigation into the causes of this are needed.

The vacuum arc model may also be improved in a number of ways: (1) develop a transient model of the cathode region; (2) consider a more detailed analysis of rough surface effects; (3) expand the Saha equation to include multiple ionisation, and thus calculate the ion CSD (Hantzsche 1983); (4) perform a sensitivity analysis for the average ion charge state; (5) improve modeling of the thermodynamics at the cathode spot surface with more refined heat conduction and Joule heating equations; (6) modeling the multi-phase metal flow out of the crater; (7) consider the thrust contribution from liquid metal droplets; and (8) consider two- or even three-dimensional vacuum arc models. Implementing these approaches will go far into understanding the VAT, given the vast amount of knowledge that has yet to be discovered about the vacuum arc.

Appendix A

Thruster Survey for the ESL Nanosat Project

This appendix describes various micropropulsion techniques currently employed in the small satellite class, specifically micro- and nanosatellites. Below is a description of each propulsion technique and brief design characteristics associated with each thruster. A comparison of the performance of each thruster type is presented to aid the decision choice for a suitable thruster (See Table A.1 below). Suitable thrusters are evaluated as to which performs the task of provide suitable thrust levels and other thruster performance qualities for a nanosatellite formation flying demonstration as prescribed by Steyn (2007). Guideline specifications to consider in the conceptual nanosatellite mission are a velocity change of 5 m/s and a maximum average power usage of 5 W.

Schein (2006) provides an extensive overview and comparison of various micropropulsion thrusters in the 10 W range. Whilst many other papers reviewed (as of yet) described various thruster systems, none provided data on a sub-10 W thruster system. This makes it difficult to evaluate the performance of ultra-low powered thrusters based purely on empirical and numerical data. Lack of physical understanding and accurate scaling laws prevent reasonable prediction of the performance of thrusters without direct experimentation. Thus, whilst copious amounts of information of how these propulsion systems operate are available, only Schein (2006) could be used as a basis for choice of micropropulsion in the sub-10 W range.

A.1 Thruster Descriptions

It should be noted that only some thrusters are presented here, as not all have been tested and developed on a micropropulsion level as of yet. This may be due to impractical reasons such as scaling

problems, power constraints and unknown physics.

A.1.1 Electric Propulsion

μPPT (Micro Pulse Plasma Thruster)

Thrust is produced by ablating and accelerating a solid insulator by applying a high voltage through the material.

- High voltages (> 1 kV)
- Repetition cycles less than 10 Hz
- Low total system mass due to minimal power processing electronics and lighter lower-voltage components
- Quasi-neutral plasma, no neutraliser required

μVAT (Micro Vacuum Arc Thruster)

Similar to the μPPT, except metallic cathode is the propellant

- Any conducting material can be used as propellant
- Low system mass
- Quasi-neutral plasma
- Possible spacecraft contamination
- Simple thruster design

FEEP (Field Emission Electric Propulsion)

Metal atoms are employed through a needle. A local electric field ionises the atoms and accelerates them.

- High thrust-power ratio (> 100 μN/W)
- High specific impulse (10000 s)

- Large capability (continuous thrust throttling, small impulse bit, instant on/off, mechanical/electrical simplicity and thruster clustering)
- Small thrust noise and stable operation
- High efficiency
- High voltages – bulky DC/DC converters may be necessary
- Neutraliser required
- Possible contamination

μLAT (Micro Laser Ablation Thruster)

A laser heats a coating placed on a transparent substrate to produce a small ablation jet. Thrust is formed from pressure within the plasma.

- High versatility – adjustable specific impulse
- Quasi-neutral plasma, non-metallic

μIT (Micro Ion Thruster)

Ion plasma is created by a cathode or microwaves and is then accelerated electrostatically.

- Well-proven technology
- Difficulty in scaling thruster for small satellites – limit on discharge chamber size
- Magnets are a mass liability.
- Neutraliser required
- Grid erosion

μR/VLT (Micro Resistojet/Vaporizing Liquid Thruster)

Heats passing propellant to increase pressure and produces thrust through a Laval nozzle.

- Well-proven technology
- Simple to implement

- Low system mass
- No contamination problems
- No large power conversion units needed
- Use of vapourising liquid technique increases system reliability

A.1.2 Chemical Propulsion

Cold Gas

Simplest propulsion system. Pressurised gas passing through a Laval nozzle.

- Well-proven technology
- Low specific impulse
- Low efficiency
- Large drag forces from miniaturisation
- Gas leakage
- Low power requirements

Monopropellant Thruster

Catalytic reaction causes liquid to become hot gas, which is exhausted through a nozzle.

- Large residual propellant
- Leakage problems
- Well-proven technology

Radioisotope Propulsion

Radiated alpha particles are used for thrust. A shutter valve controls thrust.

- Simple operation
- Minimal shielding mass

A.2 Thruster Evaluation

A comparison of the various thrusters are shown in Table A.1 below. Data was obtained from Schein (2006).

Table A.1: Comparison of nanosatellite thrusters

Performance Parameters	**Electrical**						**Chemical**		**Radio-isotope**
	μPPT	μVAT	FEEP	μLAT	μIT	μR/VLT	Cold Gas	Mono-prop.	
Isp (s)	500	1000–3000	8000–12000	430	3184	100–150	65	130	3.9×10^{6}
I-bit (μNs)	15	0.01–30	DC	0.01	DC		550	1	1.55×10^{-4}
Rep Rate (Hz)	2	1000	DC	100	DC				1000
Power (W)	10	10–30	0.5–10	8.6	43	1–3		1	0.001
Thrust (μN)	30	0.1–3000	100	635	1500	250-500	55	1000	0.155
Thrust/Power (μN/W)	10	0.01–300	20	74	35	200		1000	155
Impulse/Prop (Ns/g)	5	10	5	4.2		1		1	1.58×10^{-5}
Feed Mech	N	Y	Y	Y	Y	Y		N	
Mass (g)	600	500	500	750		50		100	2

Nearly all electric-based micropropulsion technologies developed have thrust-to-power ratios of 10–300 μN/W. This means that for a 5 W power supply, a thrust of at most 1.5 mN may be possible with some electric propulsion technologies such as the resistojet or arc thruster (In reality, the power available for propulsion will be much less depending on the simultaneous use of other systems).

Despite the high specific impulse of EP thrusters, a lower thrust and higher power requirement offsets its attractive use. Currently, chemical designs are popular for their practical, relatively easy-to-implement designs in the nanosat class. However, there also lies opportunity for improving electric micropropulsion (for the mid-to-long term) despite the popularity of a chemical propulsion design. Also, EP systems consume less fuel and therefore allow potentially significant mass savings over chemical systems. This is the main priority in the nanosatellite project.

Only the FEEP and microresistojet have been found to be developed in the 1–5 W power range. It is currently unknown if other propulsion technologies are scalable or being tested at that power level. The power restriction limits many of the electric propulsion types such as the electrostatic ion engine and magnetoplasmadynamic engine.

The most promising propulsion types in terms of simplicity, thrust-to-power ratios and scalability are the FEEP, VAT, Resistojet and Laser ablation thruster. The desired throttling capability and high specific impulse single out FEEP and VAT. Also, previous studies such as those done by Leach & Neal

(2002) and Rysanek et al. (2002) on FEEP and μVAT respectively promote the use of such systems. These thrusters are therefore provisionally the propulsion of choice for the nanosatellite concept. Table A.2 below compares these two systems for final evaluation.

Table A.2: Comparison of FEEP and VAT propulsion systems

FEEP		**VAT**	
Pros	**Cons**	**Pros**	**Cons**
Low noise	Heating propellant	Any propellant	High noise
High Efficiency	Accurate Machining	Simple design	Ionisation energy loss
Low mass	Propellant deposition	Low mass	Propellant deposition
Throttle feature	Neutraliser	Throttle feature	Lower thrust accuracy
Very High I_{sp}	Charged plasma	High I_{sp}	Power conditioning
Accurate thrust	Power conditioning	No neutraliser	Less thrust uniformity
Instant on/off		Simple operation	
Small impulse bit		Quasi-neutral plasma	
Uniform thrust		Small Impulse bit	

FEEP has high efficiency, accurate thrusting and simple operation, whilst VAT does not require a neutraliser and as accurate manufacturing as FEEP. Both provide reasonable thrust and high specific impulse. Leach & Neal (2002) mention that FEEP may pose a problem for small satellites due to the high voltages required for operation. Also, most thruster types suffer from the limited lifetime of the cathode emitter. The problem is made superfluous in the VAT system. Based on lower mass, long lifetime, simplicity and throttling capability, the μVAT thruster was chosen for study in the context of a nanosatellite performing formation flying.

Appendix B

Vacuum Arc Thruster Product Requirement Specification

The criteria used in Tables B.1–B.3 were based on propulsion selection criteria published by Loh (1968).

Table B.1: VAT purpose, constraints and economic criteria

Purpose	
The thruster must be able to perform orbital manoeuvres and/or attitude control for a LEO nanosatellite	
Constraints	
Engine weight	$<$ 100 g
Propulsion system weight, including PPU (% total spacecraft mass)	$<$ 500 g (10%)
Operating temperature limits	$\sim$ 1000 °C
Operating environment pressure (space vacuum)	$\sim 10^{-9}$ Torr
Vehicle-supplied engine inputs (regulated power)	max. 4–5 W avg.
Vehicle-supplied engine inputs (voltage bus)	12–14 V DC
Economic Criteria	
Cost of engine/vehicle integration	minimal
Cost of engine unit in production	$\sim$R5000
Availability of engine	on request
Manufacturing tolerance	$\sim$ 0.5 mm
Manufacturing and test facilities	local
Lead time for key component manufacture	$<$ 1 month

Table B.2: VAT functional requirements

Engine Performance	
Should be comparable to other vacuum arc thrusters developed in research	-
Thrust magnitude in 10's of μN's for 1–5 W range	$\sim$10–20 μN/W
Single thrust pulse magnitude accuracy	$\sim$20%
Thrust vector accuracy	$\sim$10 deg
Specific impulse	$\sim$1100–3000 s
Total impulse	$\sim$0.2 Ns
Thruster start-up/shut-down transient	$<$ 10 μs
Pulse rate	$<$50 Hz
Residual propellant (% of total propellant)	$\sim$5%
Volume of engine/propulsion system	$\sim$25 cc
Operation capability should range from single pulse to long term firing	-
Number of operating cycles	$\sim 10^6$ pulses
Propellant should eroded as uniformly as possible	-
Insulator and anode erosion over thruster lifetime	minimal
Thruster lifetime (non-operational in space environment)	5 years
Reliability	
Number of moving parts	minimal
Degree of built-in redundancy	none
Demonstrated reliability of engine	95–99%
Ability to check out engine or critical components prior to use	yes
No internal arcing	yes
Failure sensing and safe shut-down devices	yes
Prior flight history – none (launch failure of Illinois Observing Satellite in July 2006)	-

Table B.3: VAT non-functional requirements

Storability and Environment	
Storage life	10 years
Storage temp limitations	20–50 °C
Low humidity to minimise electrode oxidation	-
Must be able to perform engine checkout during storage	yes
Must withstand launch environment, including vibrations, pressure, temperature	
Must withstand thermal cycling, atomic erosion, space radiation during mission	
Operating Parameters	
EMI emissions must not prevent functioning of other subsystems such as observation, communications, attitude control systems, etc	yes
Spacecraft contamination from exhaust plume	minimal
The propulsion system must not fail thermally or cause other satellite subsystems to experience thermal failure	yes
Engine controls: input power, input voltage, burn time, direction	-
Measurements/indicators during engine operation: arc voltage, arc current, avg. power, thrust	-
Operating environmental limitation: space vacuum, power availability in orbit	-
Readiness for use	always
Safety	
Non-corrosive propellant	yes
Non-toxic propellant and/or exhaust products	when possible
Comply with required national/international safety procedures	yes
Supply and Logistics	
Ease of checking and replacing or fixing critical components while engine is installed in vehicle	yes
Non-permanent mounting for easy removal	yes
Flexibility	
Power scalable	yes
Cluster or stacked configuration for greater thrust	yes
Size expansion for more propellant	yes
Any propellant type	yes
Mount in multiple locations on spacecraft	yes

Appendix C

Design Drawings

This appendix contains design drawings of the VAT (Figures C.1–C.5), the initial DTMS design (Figures C.6–C.14) and the ITMS tunnel (Figures C.15–C.18).

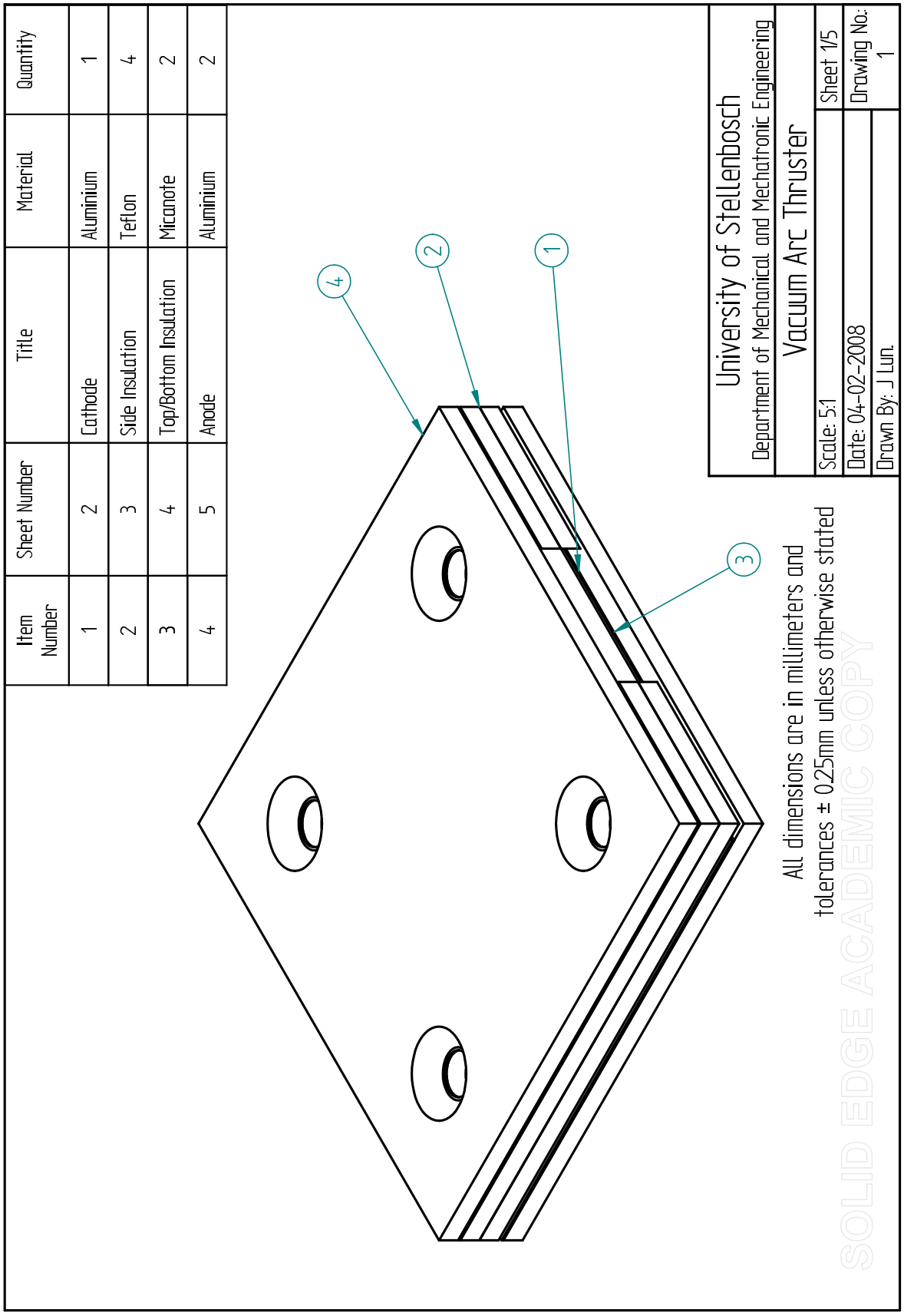

Figure C.1: Design drawing of VAT overview

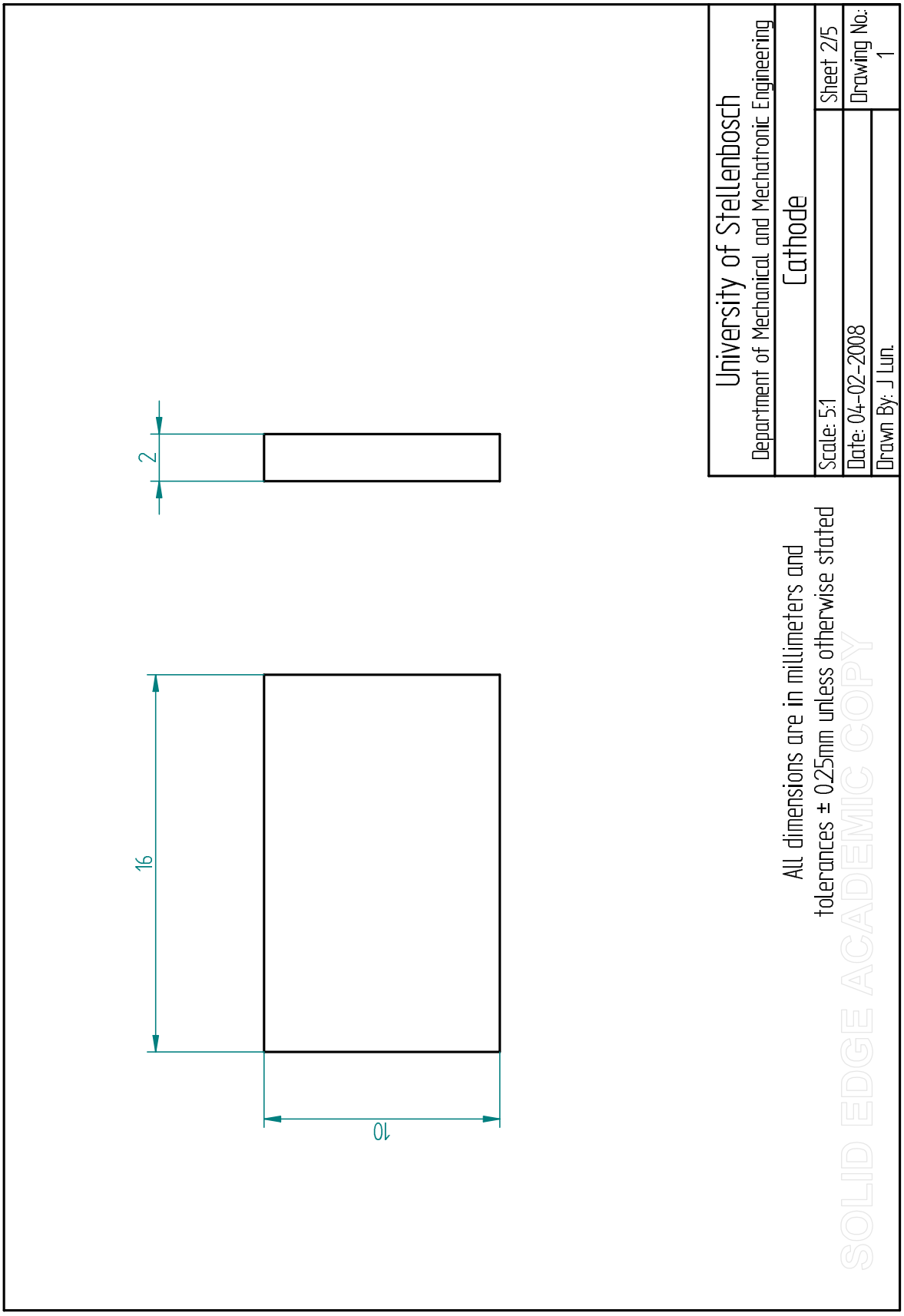

Figure C.2: Design drawing of VAT cathode electrode

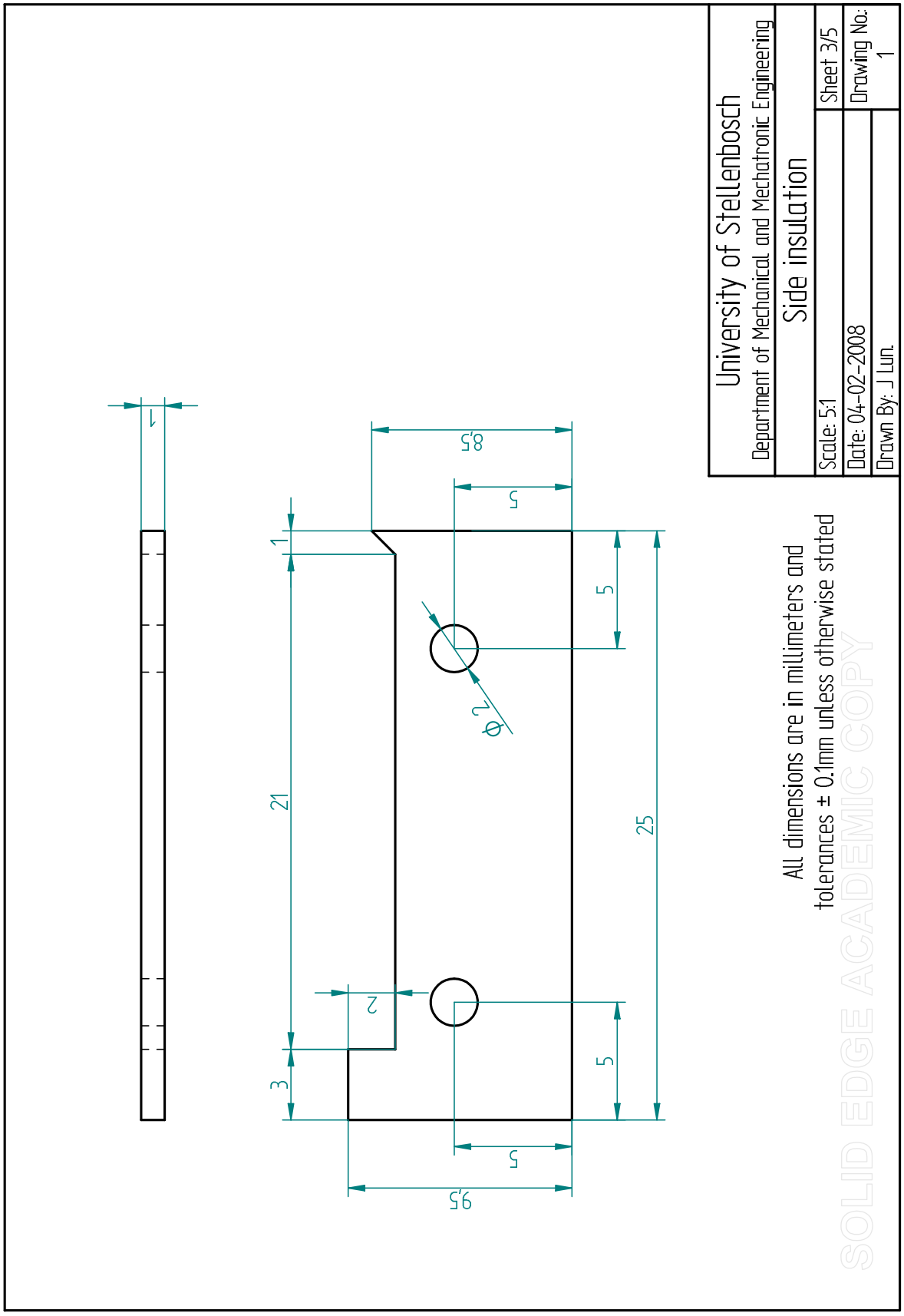

Figure C.3: Design drawing of VAT Teflon side insulation

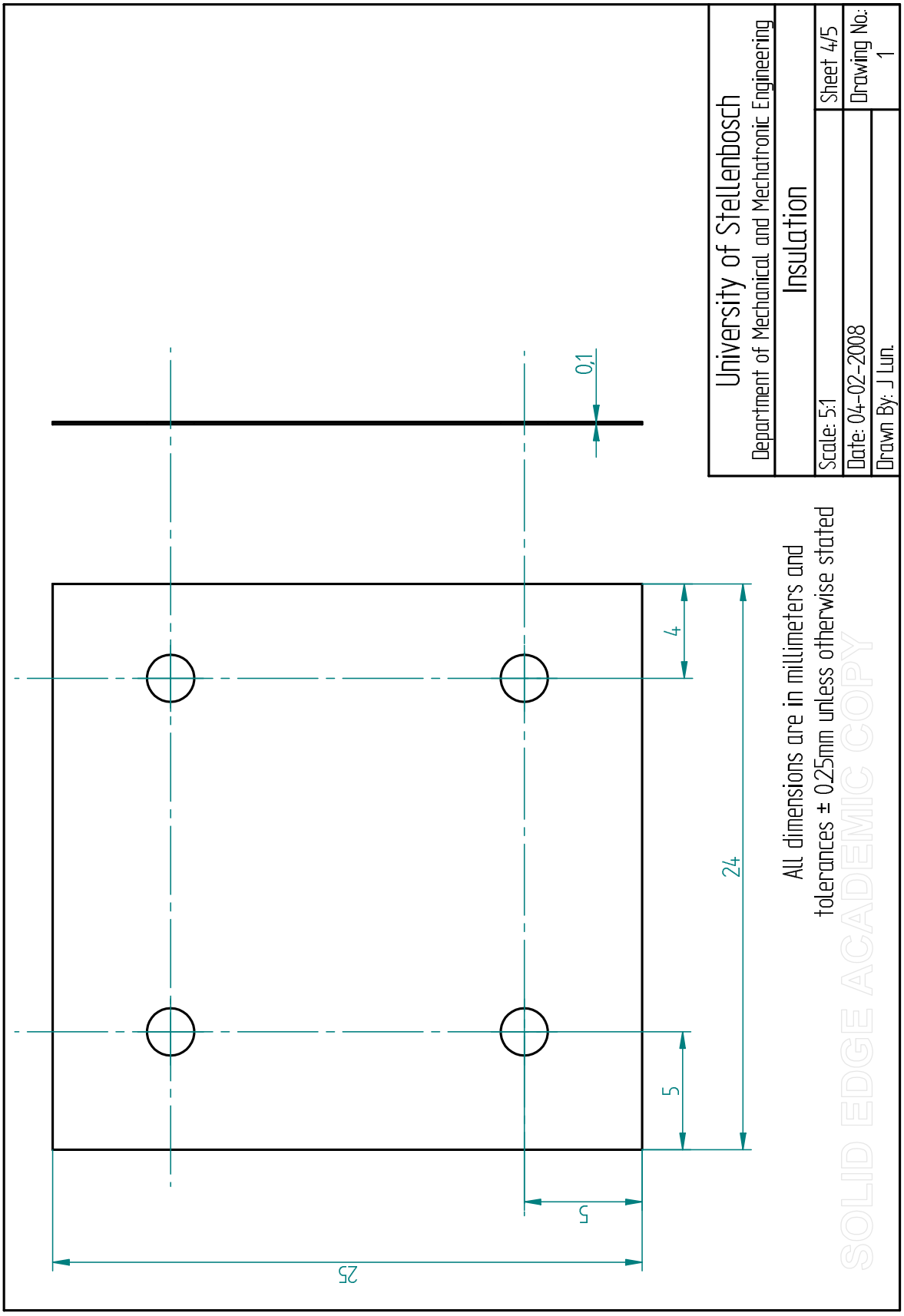

Figure C.4: Design drawing of VAT main electrode insulation

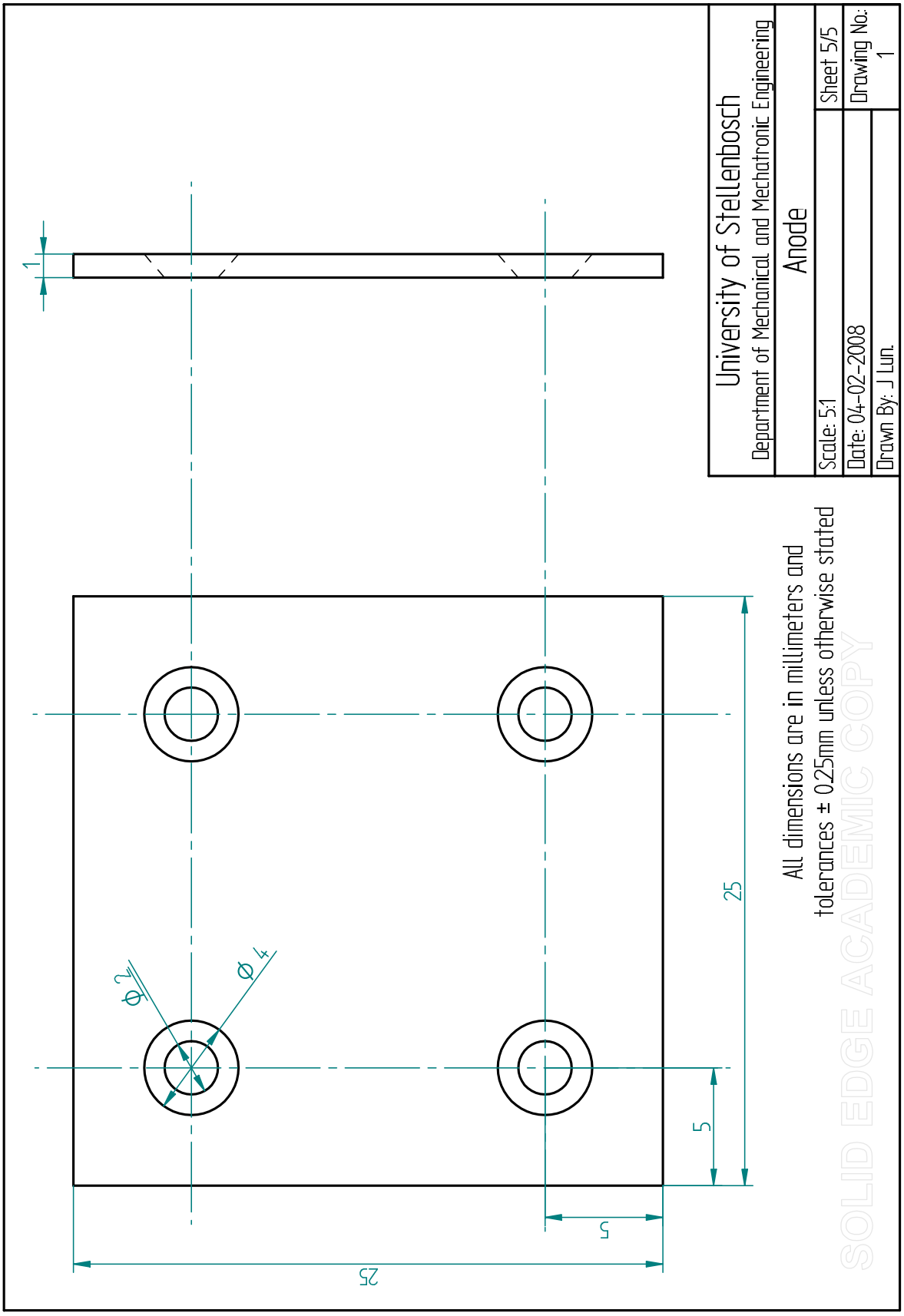

Figure C.5: Design drawing of VAT anode electrode

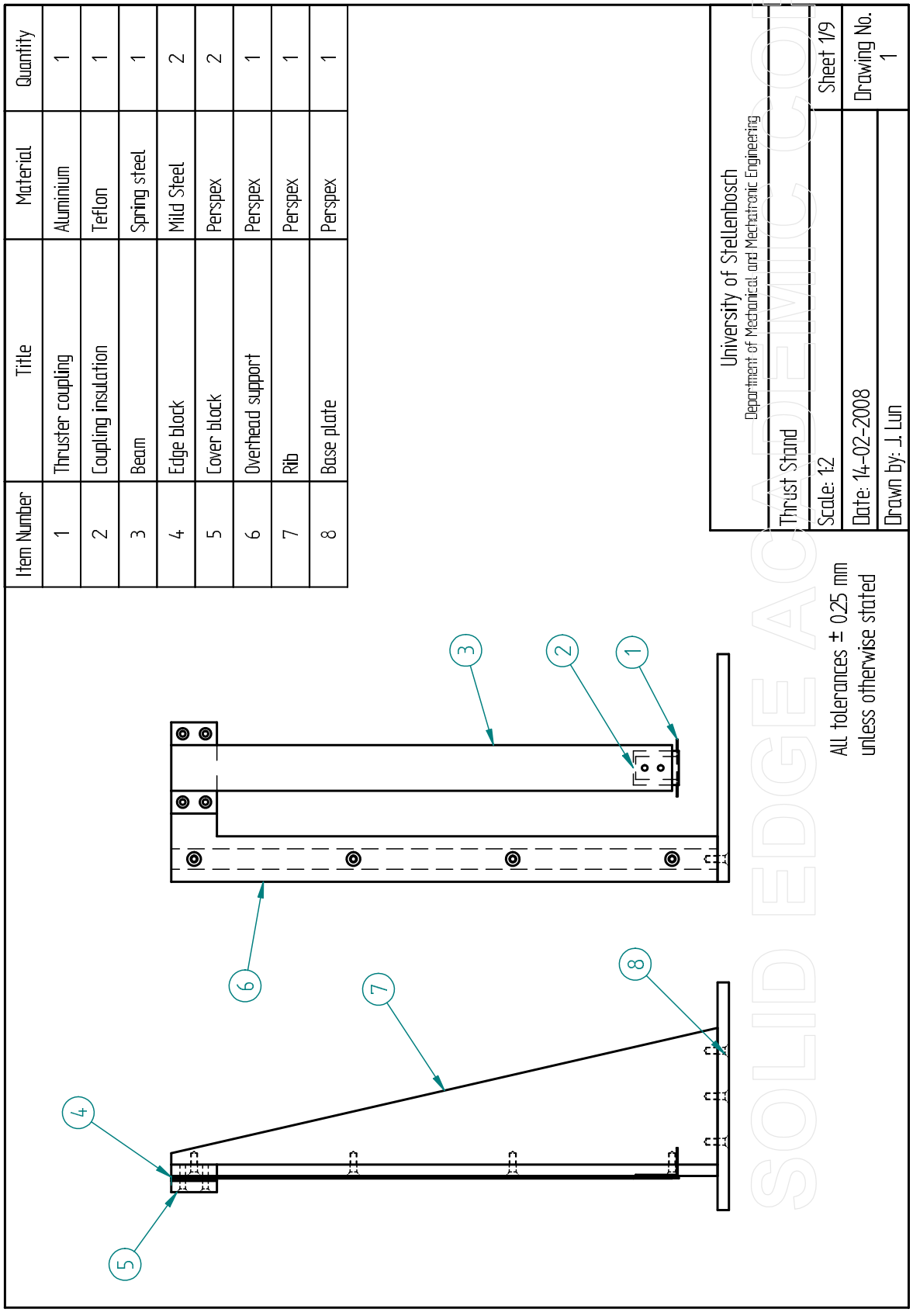

Figure C.6: Design drawing of initial DTMS overview

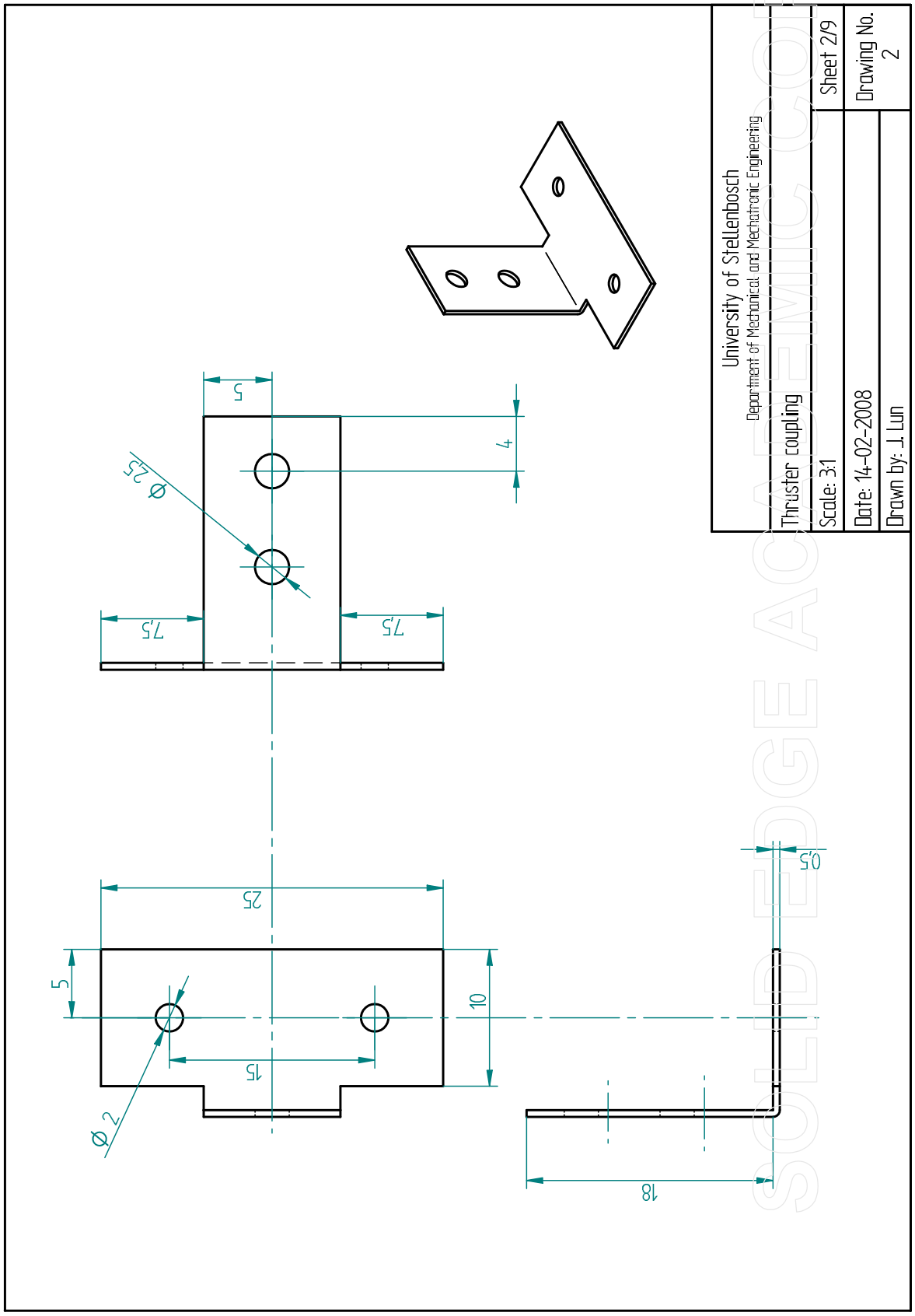

Figure C.7: Design drawing of initial DTMS thruster coupling

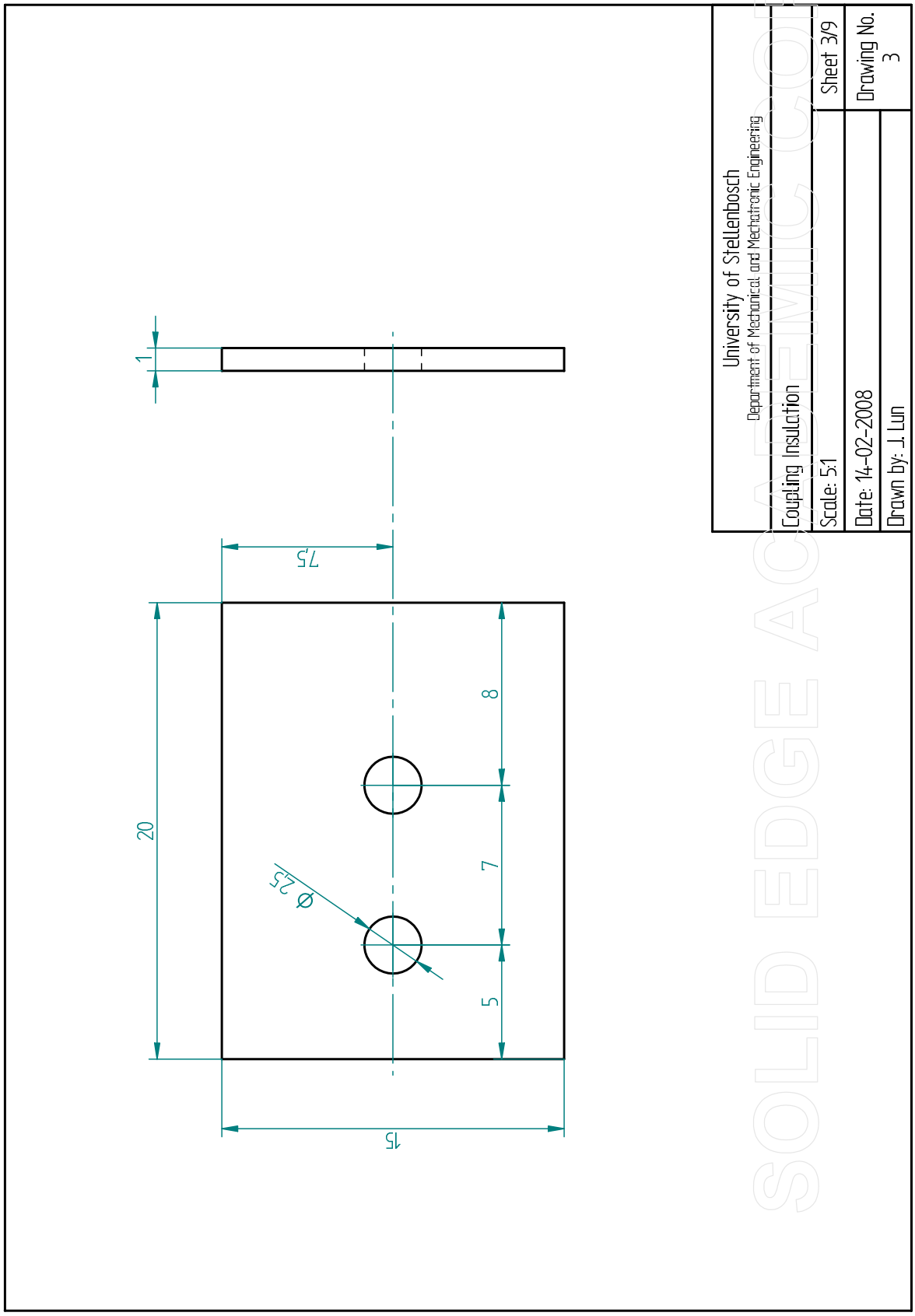

Figure C.8: Design drawing of initial DTMS coupling insulation

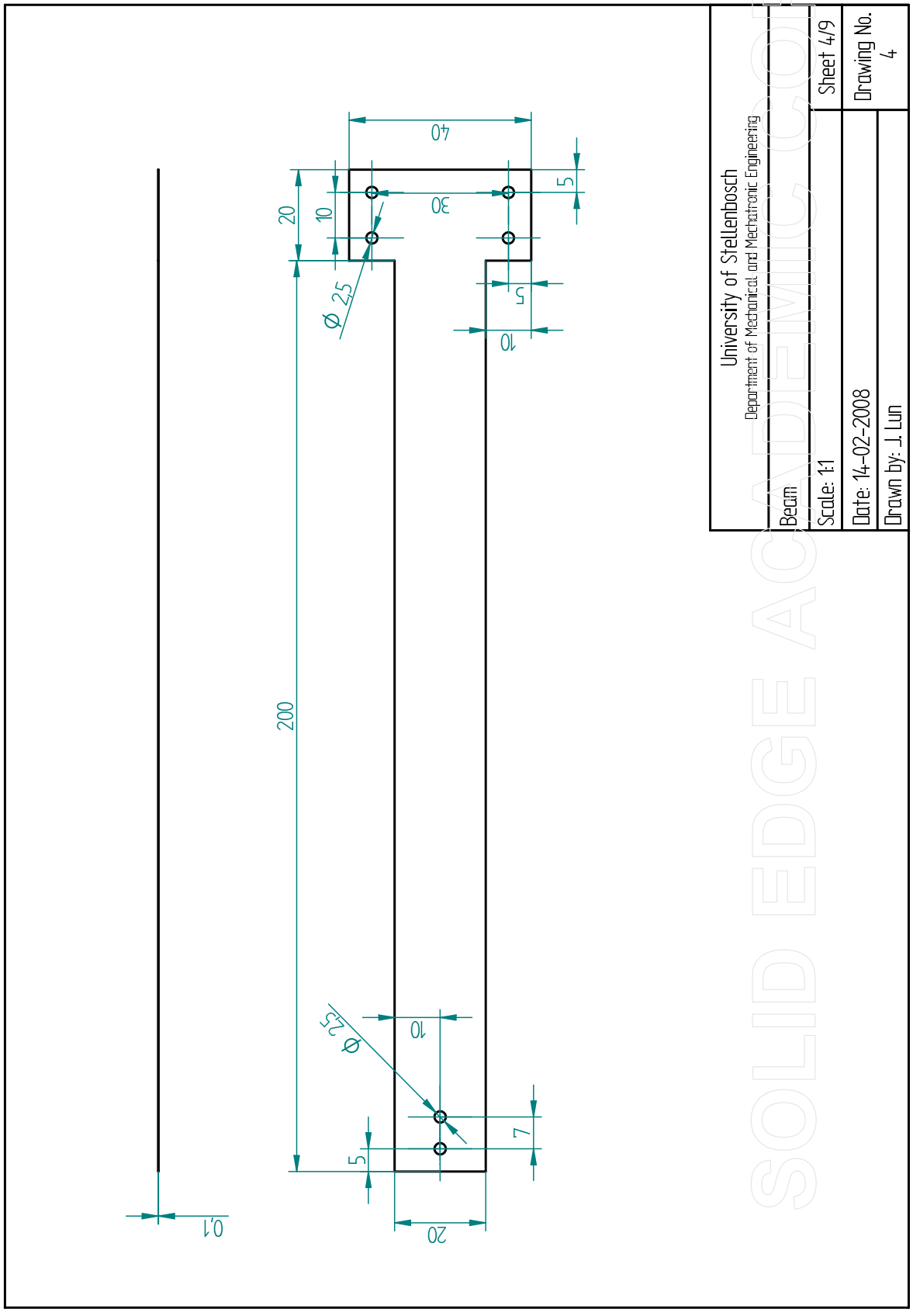

Figure C.9: Design drawing of initial DTMS cantilever beam

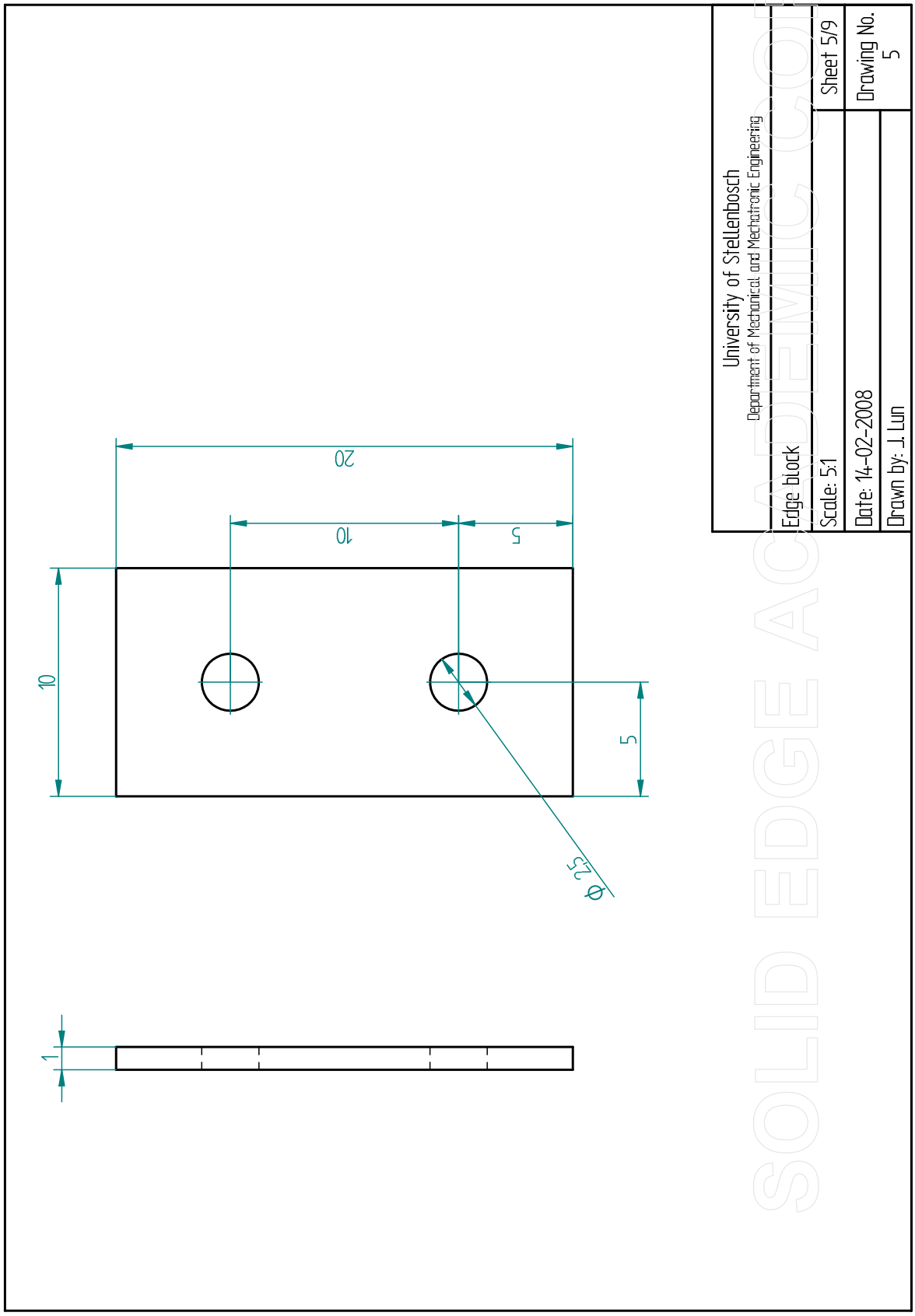

Figure C.10: Design drawing of initial DTMS supporting edge blocks

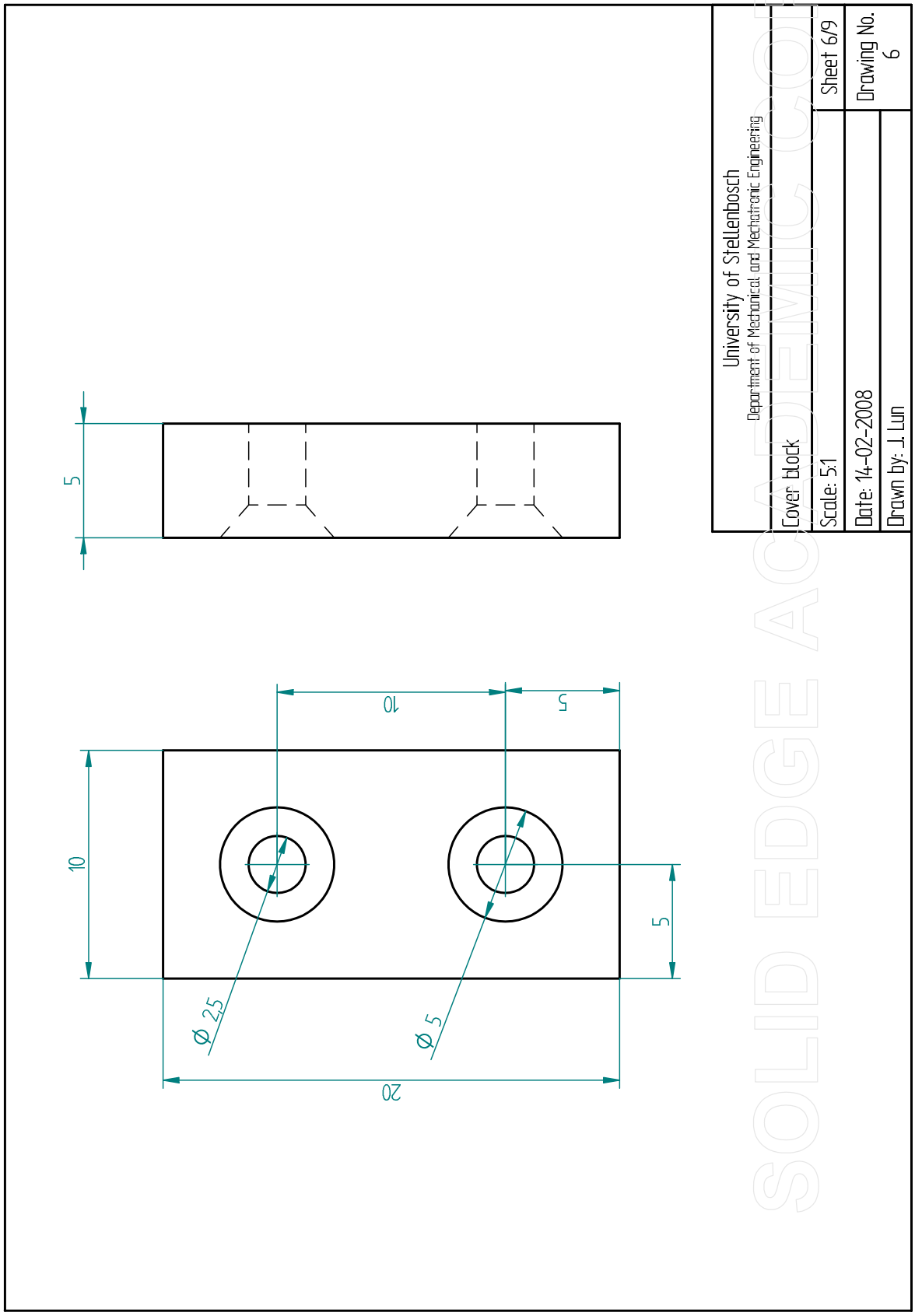

Figure C.11: Design drawing of initial DTMS supporting cover blocks

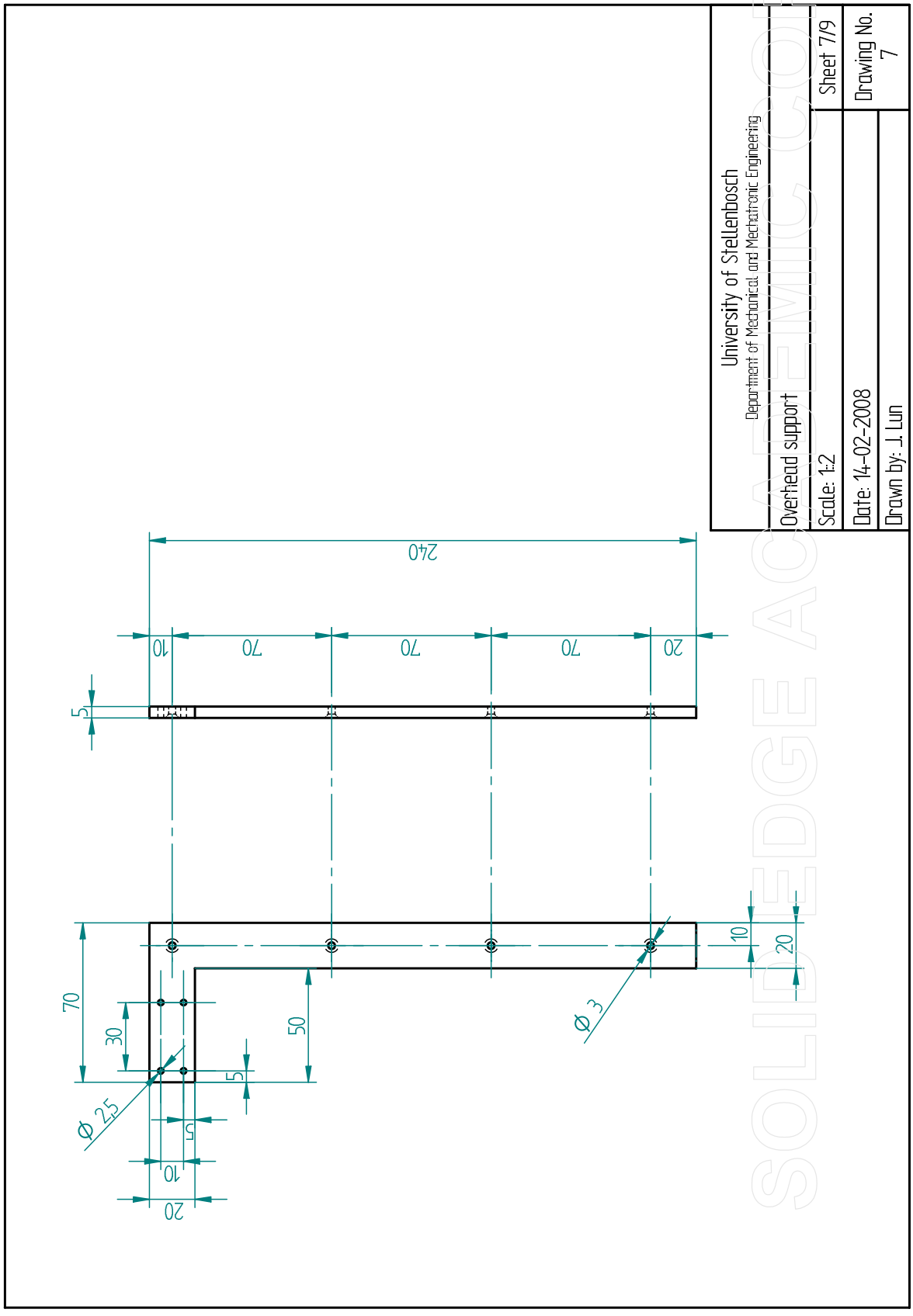

Figure C.12: Design drawing of initial DTMS overhead support stand

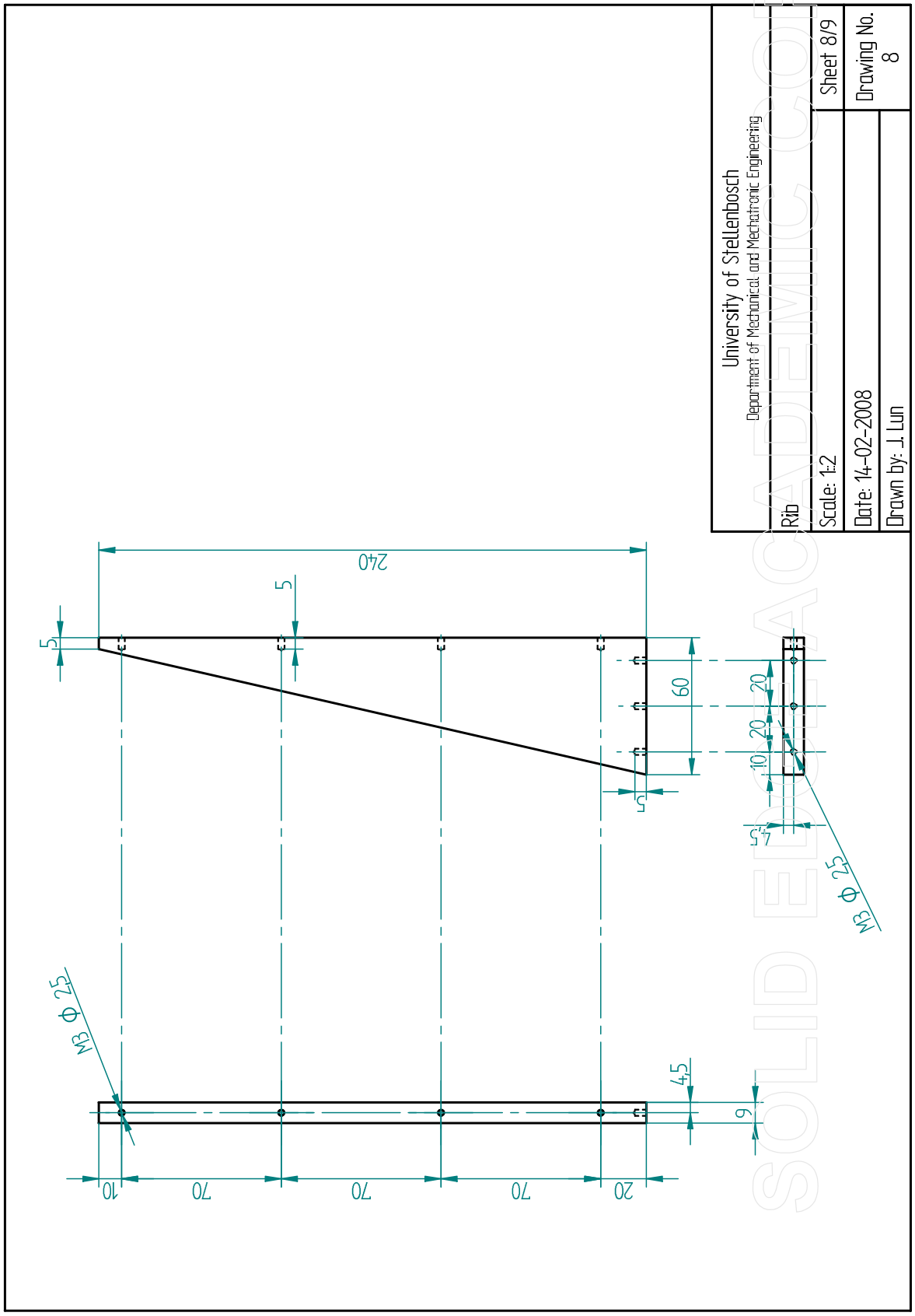

Figure C.13: Design drawing of initial DTMS support stand rib

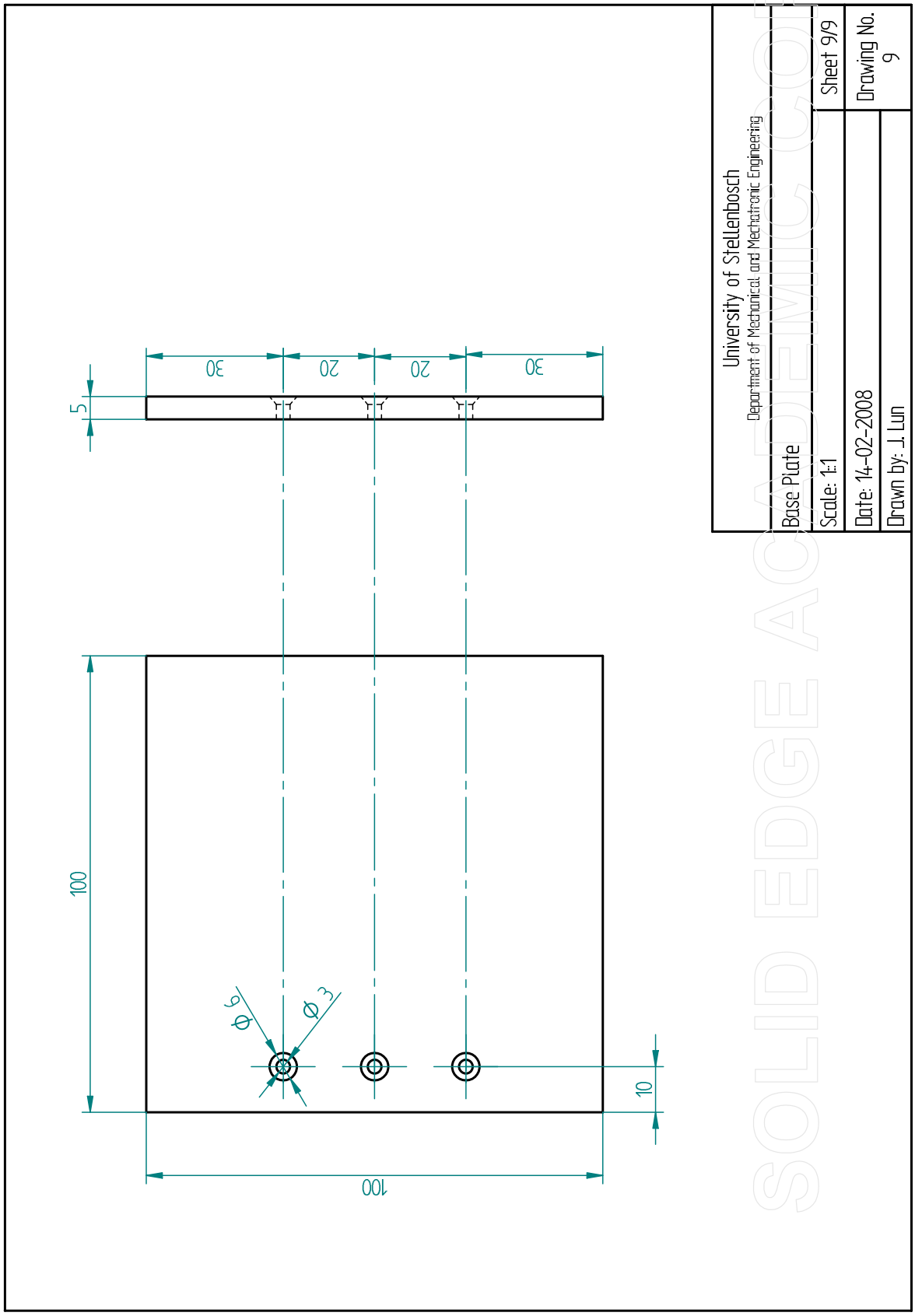

Figure C.14: Design drawing of initial DTMS support stand base

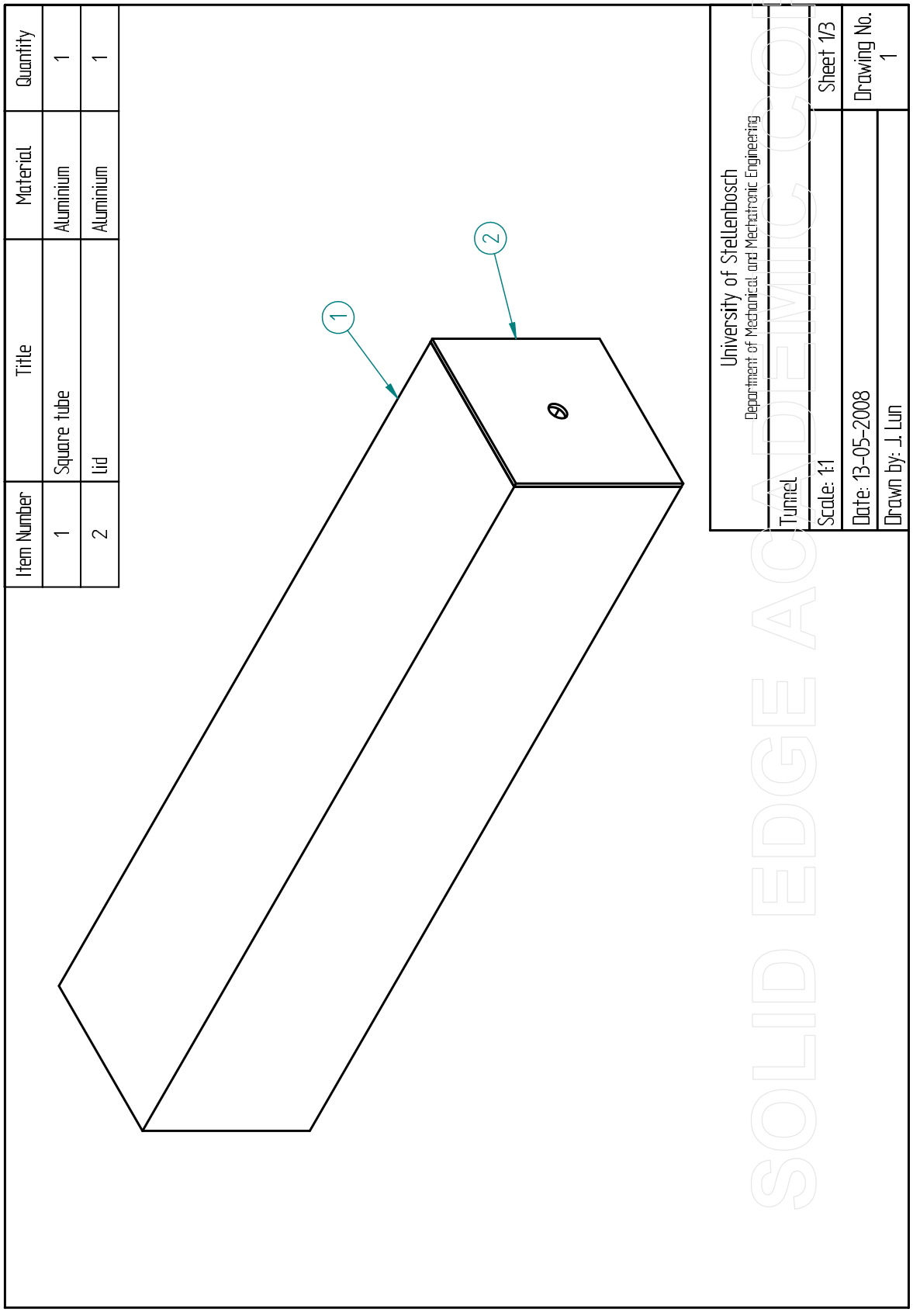

Figure C.15: Design drawing of ITMS overview

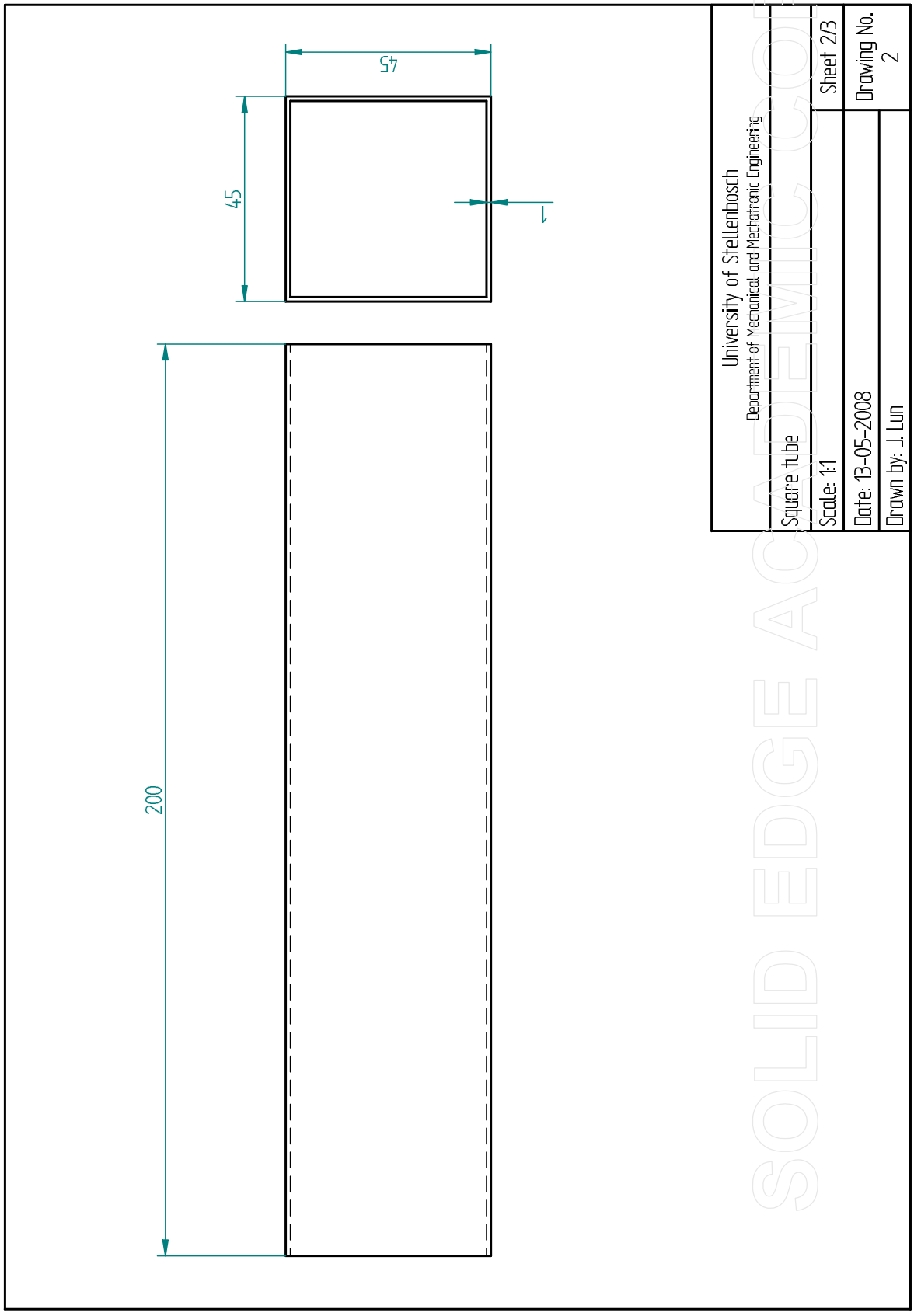

Figure C.16: Design drawing of ITMS tunnel

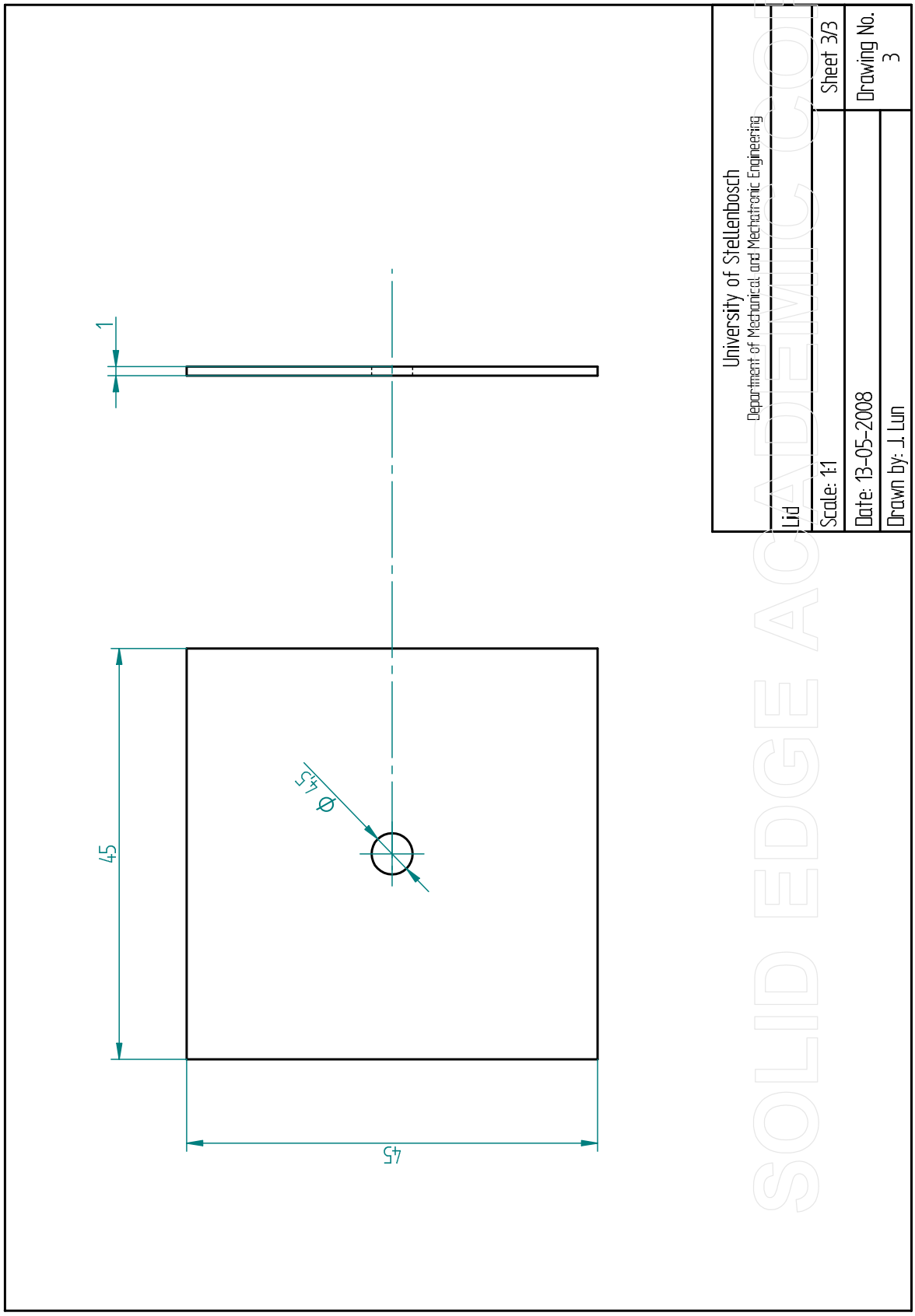

Figure C.17: Design drawing of ITMS lid

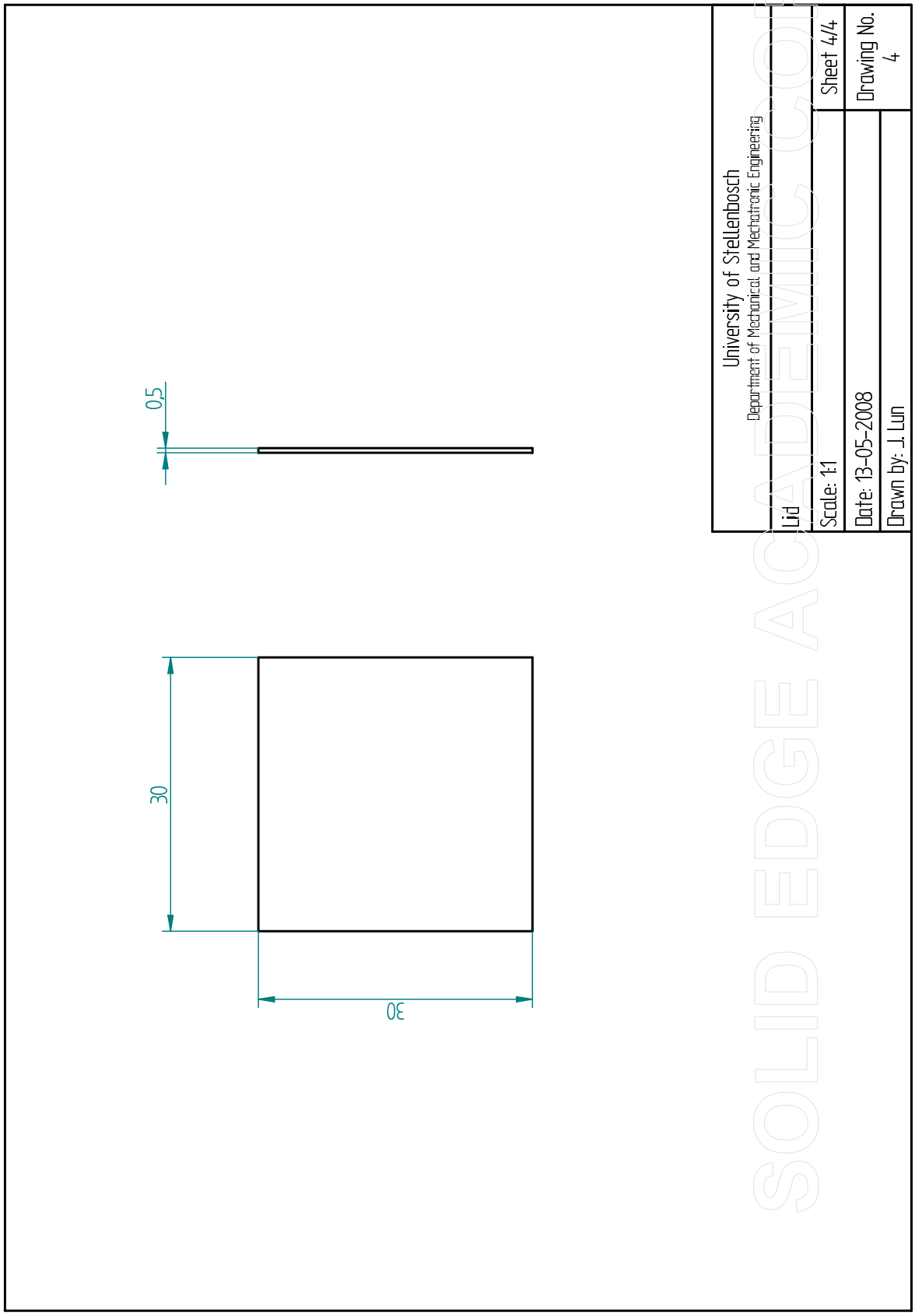

Figure C.18: Design drawing of ITMS collector

Appendix D

Experimental Data

Deflection data is given in Tables D.1 and Tables D.2 below. The uncertainty of y_{max} for each sample was determined by calculating the standard deviation of the measured SG signal of the beam at rest just before the thrust pulse was applied. Collected charge and average ion velocity data is given in Table D.3 below.

Table D.1: Deflection data for d_2 = 12 mm

Sample	V_d (V)	y_{max} (μm)	Uncertainty (μm)
1	630	1.476	$\pm$0.62
2	700	1.887	$\pm$0.73
3	720	1.670	$\pm$0.77
4	930	1.825	$\pm$0.88
5	950	1.728	$\pm$0.71
6	1010	1.984	$\pm$1.41
7	1040	1.347	$\pm$0.78

Table D.2: Deflection data for d_2 = 18 mm

Sample	V_d (V)	y_{max} (μm)	Uncertainty (μm)
1	705	1.567	$\pm$0.60
2	800	2.047	$\pm$0.75
3	820	1.658	$\pm$0.56
4	840	1.967	$\pm$0.73
5	860	1.807	$\pm$0.65
6	920	1.748	$\pm$0.74
7	1010	1.831	$\pm$0.77
8	1090	1.511	$\pm$0.89
9	1260	2.156	$\pm$0.79
10	1335	2.783	$\pm$0.69
11	1500	2.439	$\pm$0.83
12	1500	2.419	$\pm$0.80

Table D.3: Collected charge and average ion velocity data

Sample	V_d (V)	$Q_{i,pf}$ (μC)	$\bar{v}_i$ (km/s)
1	1155	0.0899	21.0280
2	1210	0.0861	37.2928
3	1420	0.0971	19.3687
4	1500	0.0946	26.1628
5	1500	0.0874	31.3953
6	1550	0.0862	25.5682
7	1600	0.1256	21.4968
8	1600	0.0956	30.8219
9	1700	0.0866	25.7634
10	1800	0.0999	25.3759
11	1800	0.0952	28.8462
12	2000	0.1536	20.2703
13	2100	0.1167	21.4286
14	2350	0.1193	18.4426
15	2350	0.1063	21.8447
16	2550	0.1268	21.2934
17	2600	0.0962	18.9076
18	3250	0.1378	16.6667

Appendix E

Detailed Error Analysis

This appendix contains all the derivatives and final calculated error equations for all model results based on the error analysis in Section 4.5.

E.1 Arc Current

Recalling Equation 4.1,

$$I_d = M_1 V_d + M_2 \approx -C\frac{V_d}{t_d}$$

where M_1 = 0.24 and M_2 = 4.

The derivatives are

$$\begin{aligned}\frac{\partial I_d}{\partial t_d} &= -\frac{I_d}{2t_d}\\ \frac{\partial I_d}{\partial V_d} &= \frac{I_d}{V_d}\\ \frac{\partial I_d}{\partial C} &= \frac{I_d}{C}\end{aligned}$$

Thus the final error is

$$\frac{\delta I_d}{I_d} = \sqrt{\frac{1}{4}\left(\frac{\delta t_d}{t_d}\right)^2 + \left(\frac{\delta V_d}{V_d}\right)^2 + \left(\frac{\delta C}{C}\right)^2} \tag{E.1}$$

E.2 Arc Power

Recalling Equation 4.2,

$$P_d = M_3 I_d^2 + M_4 I_d + M_5$$

where M_3 = 0.0013, M_4 = -0.0093 and M_5 = 14.

The derivatives are

$$\frac{\partial P_d}{\partial I_d} = 2M_3 I_d + M_4$$

Thus the final error is

$$\frac{\delta P_d}{P_d} = \frac{(2M_3 I_d + M_4)\delta I_d}{P_d} \tag{E.2}$$

E.3 Erosion Rate

Recalling Equation 4.29,

$$E_r = \frac{\Delta m_s}{t_d \int_0^{t_o} I_d(t)S(t)dt} \approx \frac{\Delta m_s}{t_d \sum_0^{t_o} I_d(t_m)S(t_m)t_m}$$

The derivatives are

$$\begin{aligned}
\frac{\partial S}{\partial t_D} &= -\frac{S}{2t_D} \\
\frac{\partial E_r}{\partial S} &= -\frac{E_r}{2S} \\
\frac{\partial E_r}{\partial \Delta m_s} &= \frac{E_r}{\Delta m_s} \\
\frac{\partial E_r}{\partial t_d} &= -\frac{E_r}{2t_d} \\
\frac{\partial E_r}{\partial t_o} &= -\frac{E_r}{2t_o} \\
\frac{\partial E_r}{\partial I_d} &= -\frac{E_r}{2I_d} \\
\frac{\partial E_r}{\partial t_m} &= -\frac{E_r}{2t_m}
\end{aligned}$$

Thus the final error is

$$\frac{\delta E_r}{E_r} = \sqrt{\left(\frac{\delta \Delta m_s}{\Delta m_s}\right)^2 + \frac{1}{4}\left(\frac{\delta t_d}{t_d}\right)^2 + \frac{1}{4}\left(\frac{\delta I_d}{I_d}\right)^2 + \frac{1}{4}\left(\frac{\delta t_o}{t_o}\right)^2 + \frac{1}{4}\left(\frac{\delta S}{S}\right)^2 + \frac{1}{4}\left(\frac{\delta t_m}{t_m}\right)^2} \tag{E.3}$$

where $\delta S/S = \delta t_D S/2$.

E.4 Cathode Mass Flow Rate

Recalling Equation 4.27,

$$\dot{m}_s(t) = E_r I_d(t) t_d S(t)$$

The derivatives are

$$\begin{aligned}\frac{\partial \dot{m}_s}{\partial E_r} &= \frac{\dot{m}_s}{E_r} \\ \frac{\partial \dot{m}_s}{\partial I_d} &= \frac{\dot{m}_s}{I_d} \\ \frac{\partial \dot{m}_s}{\partial t_d} &= \frac{\dot{m}_s}{t_d} \\ \frac{\partial \dot{m}_s}{\partial S} &= \frac{\dot{m}_s}{S}\end{aligned}$$

Thus the final error is

$$\frac{\delta \dot{m}_s}{\dot{m}_s} = \sqrt{\left(\frac{\delta \Delta E_r}{\Delta E_r}\right)^2 + \left(\frac{\delta I_d}{I_d}\right)^2 + \left(\frac{\delta t_d}{t_d}\right)^2 + \left(\frac{\delta S}{S}\right)^2} \tag{E.4}$$

where $\delta S/S = \delta t_D S/2$.

E.5 Ion Velocity

Recalling Equation 4.20,

$$\bar{v}_i = \frac{d_1}{t_i}$$

The derivatives are

$$\begin{aligned}\frac{\partial \bar{v}_i}{\partial d_1} &= \frac{1}{t_i} \\ \frac{\partial \bar{v}_i}{\partial t_i} &= -\frac{\bar{v}_i}{2t_i}\end{aligned}$$

Thus the final error is

$$\frac{\delta \bar{v}_i}{\bar{v}_i} = \sqrt{\left(\frac{\delta d_1}{d_1}\right)^2 + \frac{1}{4}\left(\frac{\delta t_i}{t_i}\right)^2}$$

E.6 Ejected Ion Current

Recalling Equation 4.23,

$$\bar{I}_{i,t} = \frac{Q_{i,t}}{t_d} = \frac{Q_{i,p,f}}{B_T t_d}$$

The derivatives are

$$\begin{aligned}\frac{\partial \bar{I}_{i,t}}{\partial Q_{i,p,f}} &= \frac{\bar{I}_{i,t}}{Q_{i,p,f}} \\ \frac{\partial \bar{I}_{i,t}}{\partial B_T} &= -\frac{\bar{I}_{i,t}}{2B_T} \\ \frac{\partial \bar{I}_{i,t}}{\partial t_d} &= -\frac{\bar{I}_{i,t}}{2t_d}\end{aligned}$$

Thus the final error is

$$\frac{\delta \bar{I}_{i,t}}{\bar{I}_{i,t}} = \sqrt{\left(\frac{\delta Q_{i,p,f}}{Q_{i,p,f}}\right)^2 + \frac{1}{4}\left(\frac{\delta B_T}{B_T}\right)^2 + \frac{1}{4}\left(\frac{\delta t_d}{t_d}\right)^2} \tag{E.5}$$

E.7 Ion-to-Arc Current Ratio

Recalling Equation 4.24,

$$\zeta = \frac{I_{i,t}}{I_d C_{Ta}}$$

The derivatives are

$$\begin{aligned} \frac{\partial \zeta}{\partial \bar{I}_{i,t}} &= \frac{\zeta}{\bar{I}_{i,t}} \\ \frac{\partial \zeta}{\partial C_{Ta}} &= -\frac{\zeta}{2C_{Ta}} \\ \frac{\partial \zeta}{\partial I_d} &= -\frac{\zeta}{2I_d} \end{aligned}$$

Thus the final error is

$$\frac{\delta \zeta}{\zeta} = \sqrt{\left(\frac{\delta \bar{I}_{i,t}}{\bar{I}_{i,t}}\right)^2 + \frac{1}{4}\left(\frac{\delta C_{Ta}}{C_{Ta}}\right)^2 + \frac{1}{4}\left(\frac{\delta I_d}{I_d}\right)^2} \tag{E.6}$$

E.8 Indirect Thrust

Recalling Equation 4.26,

$$F = C_{Tb}\left(m_i \frac{I_{i,t}}{e\bar{Z}}\right)\bar{v}_i$$

The derivatives are

$$\begin{aligned} \frac{\partial F}{\partial \bar{I}_{i,t}} &= \frac{F}{\bar{I}_{i,t}} \\ \frac{\partial F}{\partial C_{Tb}} &= \frac{F}{C_{Ta}} \\ \frac{\partial F}{\partial \bar{v}_i} &= \frac{F}{\bar{v}_i} \\ \frac{\partial F}{\partial \bar{Z}} &= -\frac{F}{2\bar{Z}} \end{aligned}$$

Thus the final error is

$$\frac{\delta F}{F} = \sqrt{\left(\frac{\delta \bar{I}_{i,t}}{\bar{I}_{i,t}}\right)^2 + \left(\frac{\delta C_{Tb}}{C_{Tb}}\right)^2 + \left(\frac{\delta \bar{v}_i}{\bar{v}_i}\right)^2 + \frac{1}{4}\left(\frac{\delta \bar{Z}}{\bar{Z}}\right)^2} \tag{E.7}$$

E.9 Direct Thrust

Recalling Equation 4.17,

$$F = \left(\frac{y_{max}}{Y_{max}}\right)\frac{\mu L \omega_1}{2 t_d D_T}$$

The derivatives are

$$\begin{aligned}
\frac{\partial F}{\partial y_{max}} &= \frac{F}{y_{max}} \\
\frac{\partial F}{\partial \mu} &= \frac{F}{\mu} \\
\frac{\partial F}{\partial t_d} &= -\frac{F}{2t_d} \\
\frac{\partial F}{\partial L} &= \frac{F}{L} \\
\frac{\partial F}{\partial \omega_1} &= \frac{F}{\omega_1} \\
\frac{\partial F}{\partial D_T} &= -\frac{F}{2D_T} \\
\frac{\partial F}{\partial Y_{max}} &= -\frac{F}{2Y_{max}}
\end{aligned}$$

Thus the final error is

$$\frac{\delta F}{F} = \sqrt{\left(\frac{\delta y_{max}}{y_{max}}\right)^2 + \frac{1}{4}\left(\frac{\delta t_d}{t_d}\right)^2 + \left(\frac{\delta L}{L}\right)^2 + \left(\frac{\delta \mu}{\mu}\right)^2 + \left(\frac{\delta \omega_1}{\omega_1}\right)^2 + \frac{1}{4}\left(\frac{\delta D_T}{D_T}\right)^2 + \frac{1}{4}\left(\frac{\delta Y_{max}}{Y_{max}}\right)^2} \tag{E.8}$$

E.10 Thrust-to-Power Ratio

Recalling Equation 5.54,

$$H = \frac{F}{P}$$

The derivatives are

$$\begin{aligned}
\frac{\partial H}{\partial F} &= \frac{H}{F} \\
\frac{\partial H}{\partial P} &= -\frac{F}{2P}
\end{aligned}$$

Thus the final error is

$$\frac{\delta H}{H} = \sqrt{\left(\frac{\delta F}{F}\right)^2 + \frac{1}{4}\left(\frac{\delta P}{P}\right)^2} \tag{E.9}$$

E.11 Specific Impulse

Recalling Equation 5.55,

$$I_{sp} = \frac{F}{gI_dE_r}$$

The derivatives are

$$\begin{aligned}
\frac{\partial I_{isp}}{\partial F} &= \frac{I_{isp}}{F} \\
\frac{\partial I_{isp}}{\partial g} &= -\frac{I_{isp}}{2g} \\
\frac{\partial I_{isp}}{\partial I_d} &= -\frac{I_{isp}}{2I_d} \\
\frac{\partial I_{isp}}{\partial E_r} &= -\frac{I_{isp}}{2E_r}
\end{aligned}$$

Thus the final error is

$$\frac{\delta I_{isp}}{I_{isp}} = \sqrt{\left(\frac{\delta F}{F}\right)^2 + \frac{1}{4}\left(\frac{\delta g}{g}\right)^2 + \frac{1}{4}\left(\frac{\delta I_d}{I_d}\right)^2 + \frac{1}{4}\left(\frac{\delta E_r}{E_r}\right)^2} \tag{E.10}$$

E.12 Efficiency

Recalling Equation 5.56,

$$\eta_T = \frac{F^2}{2PI_dE_r}$$

The derivatives are

$$\begin{aligned}
\frac{\partial \eta_T}{\partial F} &= \frac{2\eta_T}{F} \\
\frac{\partial \eta_T}{\partial P} &= -\frac{\eta_T}{2P} \\
\frac{\partial \eta_T}{\partial I_d} &= -\frac{\eta_T}{2I_d} \\
\frac{\partial \eta_T}{\partial E_r} &= -\frac{\eta_T}{2E_r}
\end{aligned}$$

Thus the final error is

$$\frac{\delta \eta_T}{\eta_T} = \sqrt{4\left(\frac{\delta F}{F}\right)^2 + \frac{1}{4}\left(\frac{\delta P}{P}\right)^2 + \frac{1}{4}\left(\frac{\delta I_d}{I_d}\right)^2 + \frac{1}{4}\left(\frac{\delta E_r}{E_r}\right)^2} \tag{E.11}$$

Appendix F

Finding the Degree of Ionisation using the Saha Equation

F.1 Assumptions

For simplicity, assume an ideal gas that is ionised into singly-ionised atom species to produce LTE plasma. Thus, only the first ionisation state is considered. Based on the discussions of Pfender (1978) and Cambel (1963), and adopting the approaches of Coulombe (1997), Rethfeld et al. (1996) and Riemann (1989), the LTE plasma temperature T_p is assumed to be approximately equal to the electron temperature T_e, i.e.

$$T_p \approx T_e \tag{F.1}$$

This is because the electron temperature is much higher than the ion temperature (20 000 K versus 4000 K). Therefore, T_p will be much closer in value to T_e than T_i.

F.2 Saha Equation

Due to the quasi-neutral plasma assumption, the degree of ionisation may be defined as the ratio of the electron density n_e, p or ion density n_i, p to the total plasma density n_p

$$\gamma = \frac{n_{e,p}}{n_p} = \frac{n_{i,p}}{n_p} \tag{F.2}$$

where the plasma density is assumed $n_p = n_{e,p} + n_{i,p}$ (singly ionised). Densities $n_{e,p}$ and $n_{i,p}$ are calculated in Section 5.2.9.

The degree of ionisation for a singly ionised species may be found by applying the Saha equation

(only valid for LTE plasma) (Cambel 1963)

$$\frac{\gamma^2}{1-\gamma^2} = \left(\frac{2\pi m_e}{h^2}\right)^{3/2} \frac{(K_b T_p)^{5/2}}{p} \frac{2\Lambda_1}{\Lambda_0} \exp\left(\frac{-eU_{i,1}}{K_b T_p}\right) \tag{F.3}$$

where h is Planck's constant, Λ_0, Λ_1 are the partition functions for the neutral atom and singly ionised ion respectively (see next section below) and

$$p = \sum_{k=i,e} n_k K_b T_k \tag{F.4}$$

which is the ideal gas equation to describe the plasma pressure.

F.3 Partition Functions

According to Cambel (1963), the partition function of a particle is defined as

$$\Lambda_k = \sum_Y G_Y \exp\left(\frac{-eU_{i,k}}{K_b T_p}\right) \tag{F.5}$$

where $U_{i,k}$ is the ionisation energy of ion species k and G_Y is the degeneracy or statistical weight of energy level Y within that species. The degeneracy may be found from $G_Y = 2S_Y + 1$ where S_Y is the particle's corresponding spin number.

Thus

$$\Lambda_0 = G_0 \tag{F.6}$$

$$\Lambda_1 = G_0 + G_1 \exp\left(\frac{-eU_{i,1}}{K_b T_p}\right) \tag{F.7}$$

Appendix G

Sample Calculations of the Analytical Thruster Model

G.1 Constants, Free Parameters and Material Properties

Table G.1: Material characteristics of commercially pure aluminium

Parameter	Symbol	Units	Value	Reference
Average spot current	I^*	A	∼30	Boxman et al. (1995)
Boiling point	T_b	K	2792	Lide (2003)
Atom spin number	S_0	-	$1/2$	Martin et al. (1999b)
Ion spin number	S_1	-	0	Martin et al. (1999b)
Vapour pressure constant	K_1	-	11.79	Roth (1976)
Vapour pressure constant	K_2	-	1.594×10^4	Roth (1976)
Cathode atom mass	m_n	amu	$26.981u$	Wieser (2006)
Cathode ion mass (= m_n)	m_i	kg	4.4803×10^{-26}	Wieser (2006)
First ionisation potential	$U_{i,1}$	eV	5.99	Lide (2003)
Second ionisation potential	$U_{i,2}$	eV	18.83	Lide (2003)
Third ionisation potential	$U_{i,3}$	eV	28.45	Lide (2003)
Condensation potential	W_{vap}	eV/atom	∼3.49	Anders & Yushkov (2002)
Work function	ϕ	eV	4.08	Tipler & Llewellyn (1999)
Thermal conductivity	λ	W/mK	∼218	Hatch (1984)
Ion fraction (1^+)	f_1	-	0.026	Anders (2001)
Ion fraction (2^+)	f_2	-	0.272	Anders (2001)
Ion fraction (3^+)	f_3	-	0.703	Anders (2001)

Note: The thermal conductivity was taken at a molten temperature of 1073 K.

Table G.2: Constants

Parameter	Symbol	Units	Value	Reference
Electron charge	e	C	1.6×10^{-19}	Quinn & S. Leschiutta (2000)
Gravitational acceleration	g	m/s^2	9.81	
Planck's constant	h	Js	6.626×10^{-34}	Quinn & S. Leschiutta (2000)
Lorentz number	L	$W\Omega K^{-2}$	2.44×10^{-8}	Rajagopal (2004)
Boltzmann constant	K_b	J/K	$1.3806504 \times 10^{-23}$	Quinn & S. Leschiutta (2000)
Electron mass	m_e	kg	0.91×10^{-30}	Quinn & S. Leschiutta (2000)
Permittivity of free space	ϵ_o	C^2/Nm^2	$8.8541878176 \times 10^{-12}$	Quinn & S. Leschiutta (2000)
Stefan-Boltzmann constant	σ_{sb}	W/m^2K^4	5.6704×10^{-8}	Mohr et al. (2008)
Atomic mass unit	u	kg	$1.660538782 \times 10^{-27}$	Quinn & S. Leschiutta (2000)

Table G.3: Thruster operating condition and free parameters

Parameter	Symbol	Units	Value
Backflow coefficient	α	-	0.5
Field-enhancement factor	β	-	2
Anode interference correction factor	C_T	-	0.33
Pulse frequency	S	Hz	100
Electron temperature	T_e	eV	2
Pulse duration	t_d	ns	400
Sheath potential drop	V_{cs}	V	15

G.2 Detailed Calculations

For $I_d = 100$ A (Equation 5.18),

$$\begin{aligned} N &= \frac{I_d}{I^*} = \frac{100}{30} = 3.333 \\ I_t &= \frac{I_d}{N} = I^* = 30 \text{ A} \end{aligned}$$

Assume $r_s = 0.5$ μm (Equation 5.17),

$$\begin{aligned} A_s &= \pi r_s^2 = (3.1415927)(0.5 \times 10^{-6})^2 = 7.854 \times 10^{-13} \text{ m}^2 \\ J_t &= \frac{I_t}{A_s} = \frac{30}{7.854 \times 10^{-13}} = 3.820 \times 10^{13} \text{ A/m}^2 \end{aligned}$$

Let T_s be within the range $T_s \in [2800, 8000]$ K. Using a modified *Bisection Method*, initially assume $T_s = \frac{1}{2}(2800 + 8000) = 5400$ K.

Finding the evaporating atom flux density (Equations 5.1 and 5.2),

$$\begin{aligned}\log(p_{vap}) &= K_1 - \frac{K_2}{T_s} = 11.79 - \frac{1.594\times10^4}{5400} = 8.838\\ \Rightarrow p_{vap} &= 10^{8.838} = 688.9\times10^6 \text{ Torr} \equiv 91.84 \text{ MPa}\end{aligned}$$

$$\begin{aligned}\Gamma_{vap} &= \frac{p_{vap}}{4}\left(\frac{m_n K_b T_s}{3}\right)^{-1/2}\\ &= \frac{91.84\times10^6}{4}\left[\frac{(4.4803\times10^{-26})(1.3806504\times10^{-23})(5400)}{3}\right]^{-1/2}\\ &= 6.881\times10^{29}\ 1/\text{m}^2\text{s}\end{aligned}$$

Assuming $T_p \approx T_e = 2$ eV $\equiv 23200$ K (Equations F.5–F.7),

$$\begin{aligned}G_0 &= 2S_0 + 1 = 2(1/2) + 1 = 2\\ G_1 &= 2S_1 + 1 = 2(0) + 1 = 1\\ \Lambda_0 &= G_0 = 2\\ \Lambda_1 &= G_0 + G_1 \exp\left(\frac{-eU_{i,1}}{K_b T_p}\right)\\ &= 2 + (1)\exp\left[\frac{(-1.6\times10^{-19})(5.99)}{(1.3806504\times10^{-23})(23200)}\right] = 21.927\end{aligned}$$

Assuming $n_p \approx 10^{26}\ 1/\text{m}^3$ (Equation F.4),

$$p = \sum_{k=i,e} n_k K_b T_k \approx n_p K_b T_p = (10^{26})(1.3806504\times10^{-23})(23200) = 32.167 \text{ MPa}$$

Use the Saha equation to find γ (Equation F.3),

$$\frac{\gamma^2}{1-\gamma^2} = \left(\frac{2\pi m_e}{h^2}\right)^{3/2}\frac{(K_b T_p)^{5/2}}{p}\frac{2\Lambda_1}{\Lambda_0}\exp\left(\frac{-eU_{i,1}}{K_b T_p}\right)$$

Re-arranging the above equation gives

$$\gamma = \sqrt{\frac{\chi}{1+\chi}}$$

where

$$\begin{aligned}\chi &= \left(\frac{2\pi m_e}{h^2}\right)^{3/2}\frac{(K_b T_p)^{5/2}}{p}\frac{2\Lambda_1}{\Lambda_0}\exp\left(\frac{-eU_{i,1}}{K_b T_p}\right)\\ &= \left[\frac{(2)(3.1415927)(0.91\times10^{-30})}{(6.626\times10^{-34})^2}\right]^{3/2}\left[\frac{\left[(1.3806504\times10^{-23})(23200)\right]^{5/2}}{32.167\times10^6}\right]\left[\frac{(2)(21.927)}{2}\right]\\ &\quad \exp\left[\frac{(-1.6\times10^{-19})(5.99)}{(1.3806504\times10^{-23})(23200)}\right] = 93.354\end{aligned}$$

Thus

$$\gamma = \sqrt{\frac{\chi}{1+\chi}} = \sqrt{\frac{93.354}{1+93.354}} = 0.995$$

Finding the ion current density (Equation 5.5),

$$J_i = \sum_k J_{i,k} = \sum_k \alpha\gamma f_k Z_k e \Gamma_{vap}$$

Thus

$$\begin{aligned} J_{i,1} &= \alpha\gamma f_1 Z_1 e\Gamma_{vap} = (0.5)(0.995)(0.026)(1)(1.6\times10^{-19})(6.881\times10^{29}) \\ &= 1.424\times10^{9}\ \mathrm{A/m^2} \\ J_{i,2} &= \alpha\gamma f_2 Z_2 e\Gamma_{vap} = (0.5)(0.995)(0.272)(2)(1.6\times10^{-19})(6.881\times10^{29}) \\ &= 29.796\times10^{9}\ \mathrm{A/m^2} \\ J_{i,3} &= \alpha\gamma f_3 Z_3 e\Gamma_{vap} = (0.5)(0.995)(0.703)(3)(1.6\times10^{-19})(6.881\times10^{29}) \\ &= 115.516\times10^{9}\ \mathrm{A/m^2} \end{aligned}$$

And

$$J_i = \sum_k J_{i,k} = J_{i,1} + J_{i,2} + J_{i,3} = (1.424 + 29.796 + 115.516)\times10^9 = 146.736\times10^9\ \mathrm{A/m^2}$$

Assuming $T_{i,sh} \approx T_s$, the ion sheath velocity is (Equation 5.6),

$$v_{i,sh} = \sqrt{\frac{K_b(T_{i,sh}+T_e)}{m_i}} = \sqrt{\frac{(1.3806504\times10^{-23})(5400+23200)}{4.4803\times10^{-26}}} = 2968.73\ \mathrm{m/s}$$

The ion density at the sheath edge is (Equation 5.7),

$$n_{i,sh} = \frac{J_i}{ev_{i,sh}} = \frac{146.736\times10^9}{(1.6\times10^{-19})(2968.73)} = 3.089\times10^{26}\ 1/\mathrm{m^3}$$

Finding the average ion charge state (Equation 5.4),

$$\bar{Z} = \sum_k f_k Z_k = f_1 Z_1 + f_2 Z_2 + f_3 Z_3 = (1)(0.026) + (2)(0.272) + (3)(0.703) = 2.68$$

The electric field is (Equation 5.8),

$$\begin{aligned} E &= \beta\left(\frac{8\bar{Z}m_i J_i^2 V_{cs}}{e\epsilon_o^2}\right)^{1/4} = 2\left[\frac{(8)(2.68)(4.4803\times10^{-26})(146.736\times10^9)^2(15)}{(1.6\times10^{-19})(8.8541878176\times10^{-12})^2}\right]^{1/4} \\ &= 25.081\times10^9\ \mathrm{V/m} \end{aligned}$$

Electron emission is approximated by Equation 5.11,

$$J_{em} \sim \frac{4\pi m_e K_b T_s}{h^3} e\int_{W_1}^{W_2} \ln\left\{1+\exp\left[-\frac{e(W+\phi)}{K_b T_s}\right]\right\} dW$$

where

$$\begin{aligned} W_1 &= -\sqrt{\frac{eE}{4\pi\epsilon_o}} = -\sqrt{\frac{(1.6\times10^{-19})(25.081\times10^9)}{(4)(3.1415927)(8.8541878176\times10^{-12})}} = -6.006\ \mathrm{eV} \\ W_2 &= 5\ \mathrm{eV} \end{aligned}$$

Use Simpson's rule to approximate the integrand (101 integration steps).

$$J_{em} \approx 1.5232\times10^{14}\ \mathrm{A/m^2}$$

Thus, using Equations 5.12–5.14, 5.32, 5.33 and the fact that the sum of plasma electrons and plasma ions gives the total number of plasma particles,

$$n_{em,sh} = \frac{J_{em}}{e}\left(\frac{m_e}{2}\right)^{1/2}(2K_bT_s + eV_{cs})^{-1/2}$$

$$
\begin{aligned}
&= \frac{1.5232 \times 10^{14}}{(1.6 \times 10^{-19})} \sqrt{\frac{(0.5)(0.91 \times 10^{-30})}{(2)(1.3806504 \times 10^{-23})(5400) + (1.6 \times 10^{-19})(15)}} \\
&= 4.022 \times 10^{26}\ 1/\mathrm{m}^3 \\
n_{e,sh} &= \bar{Z} n_{i,sh} = (2.68)(3.089 \times 10^{26}) = 8.279 \times 10^{26}\ 1/\mathrm{m}^3 \\
n_{er,sh} &= n_{e,sh} - n_{em,sh} = 8.279 \times 10^{26} - 4.022 \times 10^{26} = 4.257 \times 10^{26}\ 1/\mathrm{m}^3 \\
n_{e,p} &= n_{e,sh} \exp\left(\frac{1}{2}\right) = 8.279 \times 10^{26} \exp\left(\frac{1}{2}\right) = 13.650 \times 10^{26}\ 1/\mathrm{m}^3 \\
n_{i,p} &= n_{e,p}/\bar{Z} = 13.650 \times 10^{26}/2.68 = 5.093 \times 10^{26}\ 1/\mathrm{m}^3 \\
n'_p &= n_{e,p} + n_{i,p} = 13.650 \times 10^{26} + 5.093 \times 10^{26} = 18.743 \times 10^{26}\ 1/\mathrm{m}^3
\end{aligned}
$$

Comparing with n_p (Equation 5.57) gives

$$\left|\frac{n'_p - n_p}{n_p}\right| = \left|\frac{18.743 \times 10^{26} - 10^{26}}{10^{26}}\right| = 17.743 \gg 10^{-6}$$

Let $n_p = n'_p$ and iterate to find a new p, γ, J_i, etc. until convergence is achieved.

After convergence

$$
\begin{aligned}
J_i &= 9.5398 \times 10^{10}\ \mathrm{A/m}^2 \\
J_{em} &= 9.3391 \times 10^{13}\ \mathrm{A/m}^2 \\
n_{er,sh} &= 2.9144 \times 10^{26}\ 1/\mathrm{m}^3
\end{aligned}
$$

From Equations 5.15,

$$
\begin{aligned}
J_{er} &= \frac{1}{4} e n_{er,sh} \sqrt{\frac{8 K_b T_e}{\pi m_e}} \exp\left(-\frac{e V_{cs}}{K_b T_e}\right) \\
&= \frac{1}{4}(1.6 \times 10^{-19})(2.9144 \times 10^{26}) \sqrt{\frac{(8)(1.3806504 \times 10^{-23})(23200)}{(3.1415927)(0.91 \times 10^{-30})}} \\
&\quad \exp\left[-\frac{(1.6 \times 10^{-19})(15)}{(1.3806504 \times 10^{-23})(23200)}\right] = 6.1490 \times 10^{9}\ \mathrm{A/m}^2
\end{aligned}
$$

Therefore (Equation 5.16),

$$
\begin{aligned}
J'_t &= J_{em} + J_i - J_{er} = (9.3391 \times 10^{13}) + (9.5398 \times 10^{10}) - (6.1490 \times 10^{9}) \\
&= 9.3480 \times 10^{13}\ \mathrm{A/m}^2
\end{aligned}
$$

Comparing with J_t (Equation 5.58) gives

$$\left|\frac{J'_t - J_t}{J_t}\right| = \left|\frac{9.3480 \times 10^{13} - 3.820 \times 10^{13}}{3.820 \times 10^{13}}\right| = 1.447 \gg 10^{-3}$$

Using the modified *Bisection Method* and the fact that $J'_t > J_t$, the temperature range is now reduced to $T_s \in [2800, 5400]$ K and a new temperature is assumed at $T_s = \frac{1}{2}(2800 + 5400) = 4100$ K. Iterate T_s to find a new p_{vap}, Γ_{vap}, p, γ, etc. until convergence is reached.

After convergence

$$T_s = 4884.6\ \mathrm{K}$$

$$
\begin{aligned}
T_{i,sh} &= 4884.6\,\mathrm{K} \\
\Gamma_{vap} &= 3.5315 \times 10^{29}\ 1/\mathrm{m^2 s} \\
E &= 1.5499 \times 10^{10}\ \mathrm{V/m} \\
J_{i,1} &= 5.4390 \times 10^{8}\ \mathrm{A/m^2} \\
J_{i,2} &= 1.1380 \times 10^{10}\ \mathrm{A/m^2} \\
J_{i,3} &= 4.4118 \times 10^{10}\ \mathrm{A/m^2} \\
J_{i} &= 5.6042 \times 10^{10}\ \mathrm{A/m^2} \\
J_{em} &= 3.8157 \times 10^{13}\ \mathrm{A/m^2} \\
J_{er} &= 4.5980 \times 10^{9}\ \mathrm{A/m^2} \\
J_{t} &= 3.8208 \times 10^{13}\ \mathrm{A/m^2}
\end{aligned}
$$

Finding the field-enhanced work function (Equation 5.9),

$$
\begin{aligned}
\phi_{eff} &= \phi - \sqrt{\frac{eE}{4\pi\epsilon_o}} = 4.08 - \sqrt{\frac{(1.6\times10^{-19})(1.5499\times10^{10})}{(4)(3.1415927)(8.8541878176\times10^{-12})}} \\
&= -0.641\ \mathrm{eV}
\end{aligned}
$$

Solving the energy flux balance terms (Equations 5.20–5.29),

$$
\begin{aligned}
\mu &= \frac{5K_bT_{i,sh}}{2e} = \left[\frac{(5)(1.3806504\times10^{-23})(4884.6)}{(2)(1.6\times10^{-19})}\right] = 1.0537 \\
q_i &= \sum_k \frac{J_{i,k}}{Z_k}\left(U_{i,k} + Z_kV_{cs} - Z_k\phi_{eff} + \mu + W_{vap}\right) \\
&= \frac{5.4390\times10^{8}}{1}(5.99 + (1)(15) - (1)(-0.641) + 1.0537 + 3.49) \\
&\quad + \frac{1.1380\times10^{10}}{2}(18.83 + (2)(15) - (2)(-0.641) + 1.0537 + 3.49) \\
&\quad + \frac{4.4118\times10^{10}}{3}(28.45 + (3)(15) - (3)(-0.641) + 1.0537 + 3.49) \\
&= (14.236\times10^{9}) + (310.99\times10^{9}) + (1.1753\times10^{12}) = 1.501\times10^{12}\ \mathrm{W/m^2}
\end{aligned}
$$

$$
\begin{aligned}
\sigma &= \frac{\lambda}{LT_s} = \frac{218}{(2.44\times10^{-8})(4884.6)} = 1.829\times10^{6}\ \mathrm{S/m} \\
q_J &\approx \frac{1}{2}\frac{J_t^2 r_s}{\sigma} = \frac{1}{2}\left[\frac{(3.8208\times10^{13})^2(0.5\times10^{-6})}{1.829\times10^{6}}\right] = 1.995\times10^{14}\ \mathrm{W/m^2} \\
q_{em} &= J_{em}\left(\phi_{eff} + \frac{5K_bT_s}{2e}\right) = 3.8157\times10^{13}\left[-0.641 + \frac{(5)(1.3806504\times10^{-23})(4884.6)}{(2)(1.6\times10^{-19})}\right] \\
&= 1.592\times10^{13}\ \mathrm{W/m^2} \\
q_{er} &= J_{er}\left(\phi_{eff} + \frac{(5K_bT_e}{2e}\right) = 4.5980\times10^{9}\left[-0.641 + \frac{(5)(1.3806504\times10^{-23})(23200)}{(2)(1.6\times10^{-19})}\right] \\
&= 20.065\times10^{9}\ \mathrm{W/m^2} \\
q_{vap} &= eW_{vap}\Gamma_{vap} = (1.6\times10^{-19})(3.49)(3.5315\times10^{29}) = 197.200\times10^{9}\ \mathrm{W/m^2} \\
q_{rad} &= \sigma_{sb}T_s^4 = (5.6704\times10^{-8})(4884.6)^4 = 32.280\times10^{6}\ \mathrm{W/m^2} \\
q_{con} &= \lambda\left(\frac{T_s - T_b}{r_s}\right) = 218\left(\frac{4884.6 - 2792}{0.5\times10^{-6}}\right) = 2.130\times10^{12}\ \mathrm{W/m^2} \\
q'_{con} &= q_i + q_{er} + q_J - q_{em} - q_{vap} - q_{rad}
\end{aligned}
$$

$$= (1.501 \times 10^{12}) + (20.065 \times 10^{9}) + (1.995 \times 10^{14}) - (1.592 \times 10^{13})$$
$$-(197.200 \times 10^{9}) - (32.280 \times 10^{6}) = 1.849 \times 10^{14}\ \mathrm{W/m^2}$$

Comparing conduction terms gives

$$\Delta = |q'_{con} - q_{con}| = \left|1.849 \times 10^{14} - 2.130 \times 10^{12}\right| = 1.828 \times 10^{14}\ \mathrm{W/m^2}$$

Since the energy flux terms are not balanced, iterate by increasing r_s in 0.05 μm steps until a minimal difference between the conduction terms is reached, upon which the iteration process ceases. The two possible solutions possibly represent mode (0) and (1) operation of the vacuum arc (Figure G.1).

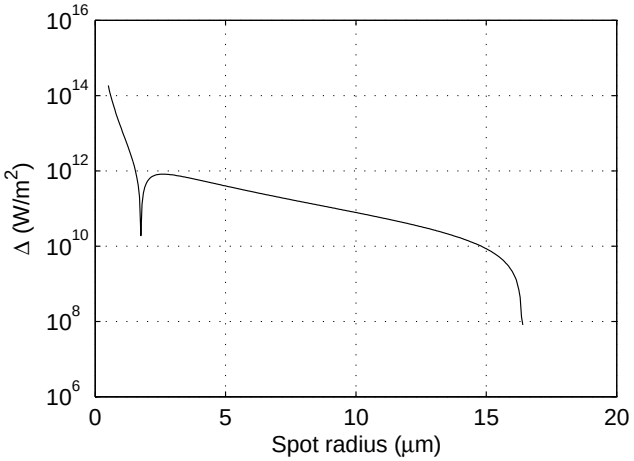

Figure G.1: Convergence of conductions to solve energy flux balance

As discussed in Section 5.4, the model shall resume calculations assuming mode (0) operation. Hence, the larger radius is chosen by means of a subroutine that ignores and passes the first root and stops iterations at the second root (See Figure G.1). The energy flux terms are approximately balanced at r_s = 16.5 μm.

Finally, the correct arc properties are

$$\begin{aligned} T_s &= 3434.3\ \mathrm{K} \\ \Gamma_{vap} &= 1.7634 \times 10^{28}\ 1/\mathrm{m^2 s} \\ J_{i,1} &= 3.5702 \times 10^{7}\ \mathrm{A/m^2} \\ J_{i,2} &= 7.4699 \times 10^{8}\ \mathrm{A/m^2} \\ J_{i,3} &= 2.8960 \times 10^{9}\ \mathrm{A/m^2} \\ J_i &= 3.6787 \times 10^{9}\ \mathrm{A/m^2} \\ J_t &= 3.5080 \times 10^{10}\ \mathrm{A/m^2} \end{aligned}$$

The ion jet current density is (Equation 5.30),

$$J_{i,p} = J_i \left(\frac{1-\alpha}{\alpha}\right) = 3.6787 \times 10^{9} \left(\frac{1-0.5}{0.5}\right) = 3.6787 \times 10^{9}\ \mathrm{A/m^2}$$

Thus, from Equation 5.31,

$$\zeta = \frac{J_{i,p}}{J_t} = \frac{3.6787 \times 10^9}{3.5080 \times 10^{10}} = 0.1049$$

Solving for the average ion velocity (Equation 5.34),

$$\bar{v}_i \approx \left(\frac{20\bar{Z}K_bT_e}{m_i}\right)^{1/2} = \left(\frac{20(2.68)(1.3806504 \times 10^{-23})(23200)}{4.4803 \times 10^{-26}}\right)^{1/2} = 19.575\,\text{km/s}$$

Solving for the erosion rate (Equation 5.35),

$$\begin{aligned}
\nu &= \sum_{k=1}^{3} \frac{J_{i,k}}{Z_k e} = \frac{1}{e}\left(\frac{J_{i,1}}{Z_1} + \frac{J_{i,2}}{Z_2} + \frac{J_{i,3}}{Z_3}\right) \\
&= \frac{1}{1.6 \times 10^{-19}}\left(\frac{3.5702 \times 10^7}{1} + \frac{7.4699 \times 10^8}{2} + \frac{2.8960 \times 10^9}{3}\right) = 8.591 \times 10^{27}\ 1/\text{m}^2\text{s} \\
E_r &= (\Gamma_{vap} - \nu)\frac{m_n}{J_t} \\
&= \left(1.7634 \times 10^{28} - 8.591 \times 10^{27}\right)\left(\frac{4.4803 \times 10^{-26}}{3.5080 \times 10^{10}}\right) = 11.549\ \mu\text{g/C}
\end{aligned}$$

Hence, the resulting thruster performance is (Equations 5.46–5.56),

$$\begin{aligned}
\dot{m}_i &= m_i\left(\frac{J_{i,p}NA_s}{e\bar{Z}}\right) \\
&= 4.4803 \times 10^{-26}\left[\frac{(3.6787 \times 10^9)(3.333)(3.1415927)(16.5 \times 10^{-6})^2}{(1.6 \times 10^{-19})(2.68)}\right] \\
&= 1.096\ \text{mg/s} \\
M_f &= \frac{\dot{m}_i}{I_d E_r} = \frac{1.096}{1.155} = 0.949 \\
F &= C_T\dot{m}_i\bar{v} = (0.33)(1.096 \times 10^{-6})(19.575 \times 10^3) = 7.080\ \text{mN} \\
I_T &= \int_0^{t_d} F dt \approx Ft_d = (7.080 \times 10^{-3})(400 \times 10^{-9}) = 2.832\ \text{nNs} \\
\bar{F} &= I_T t_d = (100)(2.832 \times 10^{-9}) = 0.2832\ \mu\text{N} \\
P &= 0.0013I_d^2 - 0.0093I_d + 14 = 26.07\ \text{kW} \\
\bar{P} &= P(t_d S) = (26.07 \times 10^3)(400 \times 10^{-9})(100) = 1.043\ \text{W} \\
H &= \frac{F}{P} = \frac{7.080 \times 10^{-3}}{26.07 \times 10^3} = 0.272\ \mu\text{N/W} \\
I_{sp} &= \frac{F}{gI_d E_r} = \frac{7.080 \times 10^{-3}}{(9.81)(100)(11.549 \times 10^{-9})} = 624.9\ \text{s} \\
\eta_T &= \frac{F^2}{2PI_d E_r} = \frac{(7.080 \times 10^{-3})^2}{(2)(26.07 \times 10^3)(100)(11.549 \times 10^{-9})} = 0.0832\ \%
\end{aligned}$$

Appendix H

Thruster Performance Analysis and Specification

This appendix determines the capability of the VAT designed in this work to achieve specific manoeuvres for a conceptual nanosatellite mission. Two simple case studies were made on the ability of the VAT to perform a specific orbital and attitude control manoeuvre. Based on VAT performance results in Chapter 6, operational parameters in Table H.1 were assumed. The relationship between arc current and pulse frequency was based on a measured sample of the VAT's pulse operating condition occurring between 3–5 W of average constant thruster power (see Figure H.1).

Table H.1: Assumed VAT operating parameters

Parameter	**Symbol**	**Value**
Arc current	I_d	200 A
Pulse frequency	S	115 Hz
Erosion rate	E_r	110 μg/C
Specific impulse	I_{sp}	160 s
Pulse duration	t_d	400 ns

H.1 Case Study 1: Satellite Separating Manoeuvre (1 km)

In achieving a 1 km separating distance between a 5 kg nanosatellite and say, a mother satellite, a manoeuvre similar to a high thrust Hohmann transfer was used since the radius ratios between the drift orbit and original orbit is very close to unity (Martinez-Sanchez 2004). Continuous low thrust is assumed to be applied to move the nanosatellite into the drift orbit and back into the original

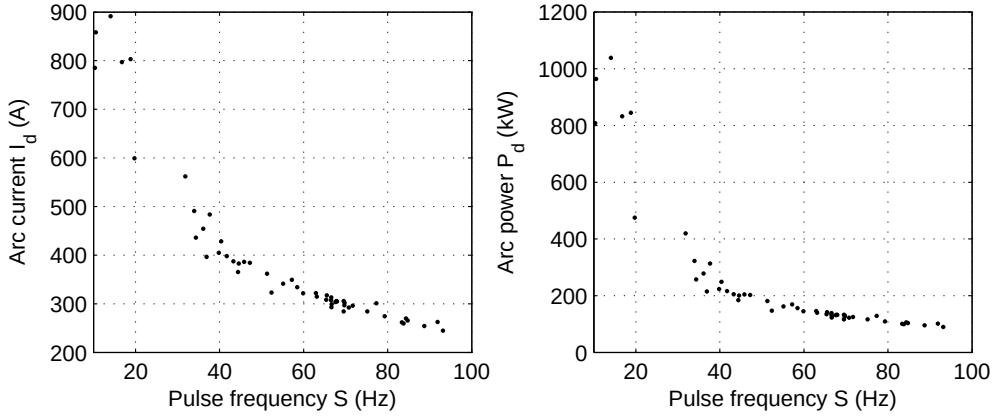

Figure H.1: Measured VAT I_d and P_d against S for $\bar{P}$ = 3–5 W

orbit. The radial velocity component picked up during the spiral flight is ignored here. The aim of the analysis is to determine the burn times, total manoeuvre time and velocity change required. Martinez-Sanchez (2004) derived an expression for determining the Δv needed for each burn to separate two satellites in the same orbit by means of low thrust (this analysis includes the time needed to accelerate *and* decelerate the satellite during the manoeuvre):

$$\Delta v = \frac{2}{3}\frac{r_o \Delta\theta}{(\Delta t - t_o)} \tag{H.1}$$

where r_o is the orbit altitude, $\Delta\theta$ is the final separating angle between the two satellites, t_o is the operating or burn time and Δt is the manoeuvre time (including burns). The burn time t_o is assumed to be the same for the start burn and stop burn. The classical rocket equation is as follows:

$$\frac{\Delta m_p}{m_o} = 1 - \exp\left(-\frac{\Delta v}{c}\right) \tag{H.2}$$

where Δm_p is the propellant mass used for the manoeuvre, m_o is the satellite total mass and c is the system's exhaust velocity. The exhaust velocity is defined as $c = I_{sp}g$, where I_{sp} is the specific impulse and g is the gravitational acceleration constant. The Equations H.1 and H.2 can be combined by equating the velocity change to produce

$$\Delta v = -c \ln\left(1 - \frac{\dot{m}_p t_o}{m_o}\right) = \frac{2}{3}\frac{r_o \Delta\theta}{(\Delta t - t_o)} \tag{H.3}$$

where $\Delta m_p = \dot{m}_p t_o$ assuming a constant mass flow rate for each burn. Rearranging Equation H.3 gives

$$\Delta t = -\frac{2}{3} r_o \Delta\theta \left[c \ln\left(1 - \frac{\dot{m}_p t_o}{m_o}\right)\right]^{-1} + t_o \tag{H.4}$$

It is now possible to describe Δt as a function of the propulsion system's performance and t_o. The corresponding velocity change Δv can also be determined. The burn time has an upper limit of $\frac{\Delta t}{2}$ and a lower limit of $\frac{\pi}{\Omega}$ (Hohmann transfer time of half an orbit), where the orbital angular velocity is defined as

$$\Omega = \sqrt{\frac{\mu_o}{r^3}} \tag{H.5}$$

where standard gravitational parameter $\mu_o = 3.986 \times 10^5$ km^3 s^{-2} and orbit radius $r \approx r_o$. Figure H.2 illustrates an example of the range of manoeuvre times and velocity changes that can be made by a

single-thruster nanosatellite to achieve a 1 km separation manoeuvre (the separation distance is $r\Delta\theta$). VAT operating parameters in Table H.1 are assumed constant throughout the burn time for simplicity and the satellite it assumed to be in LEO (300 km above the earth's surface). The graphs show that a burn time as large as possible should be specified to maximise the velocity change and minimise the manoeuvre time. Table H.2 provides performances results for various number of thrusters that could be used for the manoeuvre and maximum and minimum burn times. The average power for each thruster is calculated using Equations 4.2 and 5.53:

$$\bar{P} = P_d S t_d = 10^3 \left(0.0013(200)^2 - 0.0093(200) + 14\right)(115)(400 \times 10^{-9}) = 2.95 \text{ W} \tag{H.6}$$

Total cathode mass loss is

$$\Delta m_p = \Delta m_s = n E_r I_d t_d S t_o \tag{H.7}$$

where n is the number of thrusters and the pulse number is merely $N_s = S t_o$.

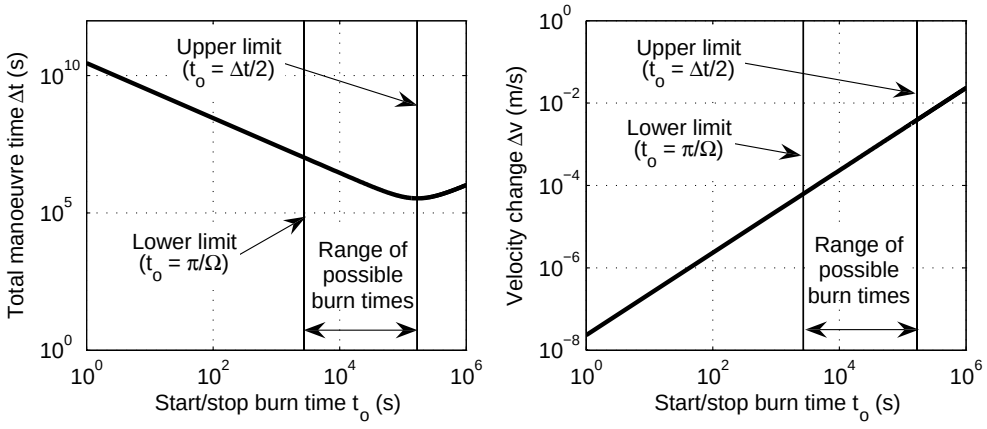

Figure H.2: Manoeuvre and burn times for 1 km separation using a single thruster

Table H.2: Results of case study 1: satellite separating manoeuvre (1 km)

Number of thrusters used	**1**		**2**		**4**	
Burn time	**Max**	**Min**	**Max**	**Min**	**Max**	**Min**
Tot. avg. thruster power $\bar{P}n$ (W)	2.95	2.95	5.90	5.90	11.80	11.80
Manoeuvre time Δt (days)	122.32	3.92	61.18	2.77	30.60	1.96
Velocity change Δv (mm/s)	0.063	3.9	0.126	5.6	0.252	7.9
Cathode mass loss/thruster Δm_p (mg)	2.75	171.42	5.50	242.42	10.99	342.84
Pulse number/thruster N_s/n ($\times 10^6$)	0.31	19.5	0.31	13.77	0.31	9.74

Table H.2 shows a factor of 15–30 manoeuvre time difference between the minimum and maximum allowed burns times, emphasising the importance of maximising the burn time. However, this will be limited by other processes that the satellite needs to perform as well as power schedules, i.e. a continuously-supplied thruster power may not be practically possible. A large increase in total mass loss (factor of 30–100) is seen with increasing Δv, but is quite affordable for the current mission

(< 0.5 g at most). Pulse numbers are also limiting factors as the VAT has only been verified for $\sim 10^6$ pulses (which will improve with better designs). For the moment, increasing the number of thrusters used for the manoeuvre will reduce the pulse number that each thruster must undergo, which improves reliability. However, note that a law of diminishing returns for manoeuvre times and pulse numbers per thruster is also seen as additional thrusters are used. As expected, the most critical performance factor is the amount of available power to the thruster (3–12 W average). In conclusion, it is expected that the burn time (and its consequential effect on thruster performance) will lie somewhere between maximum or minimum t_o, but as close to maximum t_o as practically possible.

H.2 Case Study 2: 90 Degree Rotation of Satellite

The time taken to perform a 90° rotation can be estimated by assuming a solid cubic satellite body with a side length of L_m = 20 cm , m_o = 5 kg uniform mass and pairs of opposite-firing thrusters on both sides of the body for performing the manoeuvre as illustrated in Figure H.3.

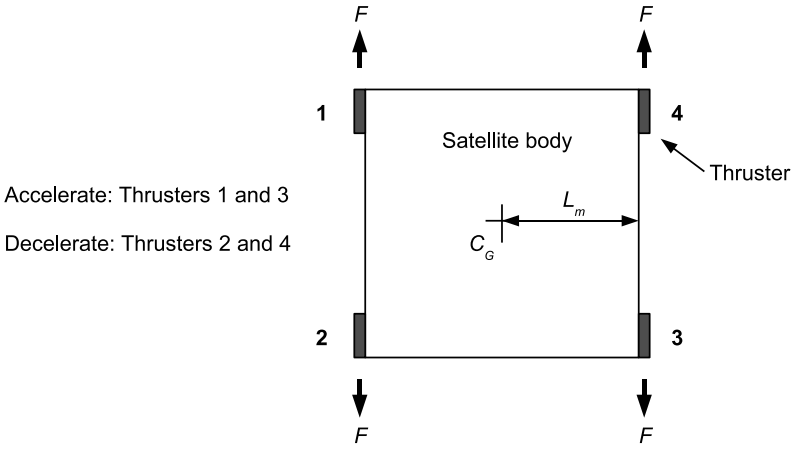

Figure H.3: Thruster configuration for 90 degree rotation manoeuvre

The mass moment of inertia of the satellite body (assuming the rotation occurs about the center of gravity C_G in the x,y or z axis of the satellite body) is

$$I_m = \frac{1}{12} m_o (L_m^2 + L_m^2) = \frac{1}{6} m_o L_m^2 \tag{H.8}$$

Using the equation for accelerating a body with a given torque

$$I_m \ddot{\theta} = 2F \left(\frac{L_m}{2} \right) \tag{H.9}$$

where $L_m/2$ is the moment arm from point C_G, θ is the angle of rotation, and $2F$ is the total amount of force produced by a thruster pair. Rearranging the equation to make θ the subject gives

$$\theta = \int \int \ddot{\theta} dt = \int \int \frac{F L_m}{I_m} dt = \frac{F L_m t^2}{2 I_m} \tag{H.10}$$

Noting that when half the rotation angle is achieved, the thrusters must act in the opposite direction to decelerate the satellite body to bring it to rest again. Thus, the thrusters are assumed to accelerate the satellite for a time t_o until a rotation of 45° reached, after which they decelerate the satellite for an equal time t_o until the 90° rotation is complete. Assuming VAT operating parameters in Table H.1, the average thrust (according to Equations 5.51 and 5.55) is

$$F = I_{sp}E_r I_d g t_d S = 160(110 \times 10^{-9})(200)(9.81)(400 \times 10^{-9})(115) = 1.59\ \mu\text{N} \tag{H.11}$$

Thus, the burn time needed is

$$t_o = \sqrt{\frac{2I_m\theta}{FL_m}} = \sqrt{\frac{m_o L_m \theta}{3F}} = \sqrt{\frac{5(0.2)\pi}{12(1.59 \times 10^{-6})}} = 405.78\ \text{s} \tag{H.12}$$

Thus a total manoeuvre time of $\Delta t = 2t_o$ = 811.5 s = 13.5 minutes, is required to perform a 90° manoeuvre. The total average power needed for the manoeuvre is 2 × 2.95 = 5.90 W (see Equation H.6), which may be reduced by pulsing the thruster at a lower rate for a smaller burn time, hence increasing the manoeuvre time (with a portion of coasting, i.e. no thrust). The total cathode mass loss (including both burns) is $\Delta m_s = 2nE_r I_d t_d S t_o$ = 1.64 mg and the total number of pulses needed for the manoeuvre is ∼93 300.

Appendix I

Additional Material

An accompanying DVD contains material related to this thesis including, but not limited to:

- A digital copy of this thesis,
- MATLAB scripts and figures of all analytical modeling and experimental data processing,
- Raw experimental data,
- Photographs and video footage of the thruster, experimental equipment and some tests,
- Design drawings of the thruster, ITMS and DTMS,
- Material and component data and specification sheets,
- Some slide show presentation material,
- Additional notes on theory, and
- Some referenced material such as journal papers relating to VATs and vacuum arcs in general.

References

Anders, A. (1998). Ion charge state distributions of pulsed vacuum arcs–interpretation of their temporal development, *IEEE Transactions on Plasma Science* **26**(1): 118–119.

Anders, A. (2001). A periodic table of ion charge-state distributions observed in the transition region between vacuum sparks and vacuum arcs, *IEEE Transactions on Plasma Science* **29**(2): 393–398.

Anders, A. & Yushkov, G. Y. (2002). Ion flux from vacuum arc cathode spots in the absence and presence of a magnetic field, *Journal of Applied Physics* **91**(8): 4824–4832.

Anders, A. et al. (1998). 'Triggerless' triggering of vacuum arcs, *Journal of Physics D: Applied Physics* **31**: 584–587.

Anders, A. et al. (2000). Pulsed vacuum-arc ion source operated with a "triggerless" arc initiation method, *Review of Scientific Instruments* **71**(2): 827–829.

Anders, A. et al. (2001). Correlation between cathode properties, burning voltage, and plasma parameters of vacuum arcs, *Journal of Applied Physics* **89**(12): 7764–7771.

Anders, A. et al. (2004). Measurement of total ion flux in vacuum arc discharges, *XXIst International Symposium on Discharges and Electrical Insulation in Vacuum*, Vol. 1, pp. 272–275.

Anders, S. et al. (1993). On the macroparticle flux from vacuum arc cathode spots, *IEEE Transactions on Plasma Science* **21**(5): 440–446.

Baker, A. M. et al. (2005). "You can get there from here":advanced lowcost propulsion concepts for small satellites beyond leo, *Acta Astronautica* **57**: 288–301.

Beilis, I. I. (2001a). A mechanism for nanosecond cathode spot operation in vacuum arcs, *IEEE Transactions on Plasma Science* **29**(5): 844–847.

Beilis, I. I. (2001b). State of the theory of vacuum arcs, *IEEE Transactions on Plasma Science* **29**(5): 657–670.

Bolotov, A. et al. (1995). A physical model of the low-current-density vacuum arc, *IEEE Transactions on Plasma Science* **23**(6): 884–891.

Boxman, R. L. et al. (eds) (1995). *Handbook of Vacuum Arc Science and Technology*, Noyes Publications.

Brown, I. G. et al. (1999). Recent advances in surface processing with metal plasma and ion beams, *Surface and Coatings Technology* **112**: 271–277.

Byon, E. & Anders, A. (2003). Ion energy distribution functions of vacuum arc plasmas, *Journal of Applied Physics* **39**(4): 1899–1906.

Cambel, A. B. (1963). *Plasma Physics and Magnetofluidmechanics*, McGraw-Hill Series in Missile and Space Technology, McGraw-Hill, chapter 6.

Chutopa, Y. et al. (2003). Measurement of secondary electron emission yields, *IEEE Transactions on Plasma Science* **31**(5): 1095–1099.

Coulombe, S. (1997). *A Model of the Electric Arc Attachment on Non-Refractory (Cold) Cathodes*, PhD thesis, Department of Chemical Engineering, McGill University.

Coulombe, S. & Meunier, J.-L. (1997). Importance of high local cathode spot pressure on the attachment of thermal arcs on cold cathodes, *IEEE Transactions on Plasma Science* **25**(5): 913–918.

Cubbin, E. A. et al. (1997). Pulse thrust measurements using laser interferometry, *Review of Scientific Instruments* **68**(6): 2339–2346.

Daalder, J. E. (1976). Components of cathode erosion in vacuum arcs, *Journal of Physics D: Applied Physics* **9**: 2379–2395.

Esper, J. et al. (2003). Nano/micro satellite constellations for earth and space science, *Acta Astronautica* **52**: 785–791.

Fridman, A. A. & Kennedy, L. A. (2004). *Plasma Physics and Engineering*, Taylor & Francis, chapter 8, pp. 510–512.

Gamero-Castaño, M. (2003). A torsional balance for the characterization of micronewton thrusters, *Review of Scientific Instruments* **74**(10): 4509–4514.

Hantzsche, E. (1983). The state of the theory of vacuum arcs, *Contributions from Plasma Physics* **23**(1): 77–94.

Hantzsche, E. (1991). Theory of the expanding plasma of vacuum arcs, *Journal of Physics D: Applied Physics* **24**: 1339–1353.

Hantzsche, E. (2003). Mysteries of the arc cathode spot: A retrospective glance, *IEEE Transactions on Plasma Science* **31**(5): 799–808.

Hantzsche, E. & Jüttner, B. (1985). Current density in arc spots, *IEEE Transactions on Plasma Science* **PS-13**(5): 230–234.

Hatch, J. E. (1984). *Aluminum: Properties and Physical Metallurgy*, ASM International.

Jacquot, R. G. (2008). Matlab program for modelling a cantilever beam response to an impulse, Personal communication. http://wwweng.uwyo.edu/classes/matlabanimate/.

Jilla, C. D. & Miller, D. (1997). Satellite design: Past, present and future, *International Journal of Small Satellite Engineering* **1**.

Jüttner, B. (2001). Cathode spots of electric arcs, *Journal of Physics D: Applied Physics* **34**: 103–123.

Keidar, M. et al. (2005). Magnetically enhanced vacuum arc thruster, *Plasma Sources Science and Technology* **14**: 661–669.

Kutzner, J. & Miller, H. C. (1989). Ion flux from the cathode region of a vacuum arc, *IEEE Transactions on Plasma Science* **17**(5): 688–694.

Lafferty, J. M. (ed.) (1980). *Vacuum Arcs–Theory and Application*, John Wiley & Sons, Inc.

Lafleur, T. (2007). *Corona discharge as an ionization mechanism for electrostatic propulsion applications*, Bsc(physics) honours project, School of Physics, University of the Witwatersrand, Johannesburg.

Lafleur, T. (2008). Personal communication.

Leach, R. & Neal, K. L. (2002). Discussion of micro-newton thruster requirements for a drag-free control system, *16th Annual/USU Conference on Small Satellites*.

Lewin, A. W. (2004). Evaluating the present and potential future impact of small satellites, *18th Annual/USU Conference on Small Satellites*.

Lide, D. R. (ed.) (2003). *CRC Handbook of Chemistry and Physics*, 84 edn, CRC Press, Boca Raton, Florida.

Lieberman, M. A. & Lichtenberg, A. J. (2005). *Principles of Plasma Discharges and Materials Processing*, John Wiley & Sons, Inc.

Loh, W. H. T. (1968). *Jet, Rocket, Nuclear, Ion and Electric Propulsion: Theory and Design*, Spring-Verlag New York, pp. 294–296.

Long, M. et al. (2002). A cubesat derived design for a unique academic research mission in earthquake signature detection, *16th Annual/USU Conference on Small Satellites*.

Mackeown, S. S. (1929). The cathode drop in an electric arc, *Physical Review* **34**: 611–614.

Martin, M. et al. (1999a). University nanosatellite program, *IAF Symposium*.

Martin, W. C. et al. (1999b). Nist atomic spectra database (version 2.0), Available Online. http://physics.nist.gov/asd. National Institute of Standards and Technology.

Martinez-Sanchez, M. (2004). Lecture 4: Re-positioning in orbits, MIT OpencourseWare. Lecture notes on Space Propulsion.

Messaad, M. et al. (2006). Model for a low current vacuum arc cathode region–effect of the electronic temperature, *Acta Electrotechnica et Informatica* **6**(3).

Mitterauer, J. & Till, P. (1987). Computer simulation of the dynamics of plasma-surface interactions in vacuum arc cathode spots, *IEEE Transactions on Plasma Science* **PS-15**(5): 488–501.

Mohr, P. J. et al. (2008). Codata recommended values of the fundamental physical constants: 2006, *Rev. Mod. Phys.* **80**(2): 633–730.

Murphy, E. L. & Good, R. H. (1956). Thermionic emission, field emission, and the transition region, *Physical Review* **102**(6): 1464–1473.

NASA (2007a). Cluster formation of satellites proposed for the techmap21 mission, Public Domain, Wikimedia Commons. http://commons.wikimedia.org/wiki/Image:TechSat21.jpg.

NASA (2007b). Landsat7 and eo-1 trailing, Public Domain, Wikimedia Commons. http://eo1.gsfc.nasa.gov/technology/Images/EO-1formationflying.gif.

Oks, E. M. et al. (2006). Measurement of total ion current from vacuum arc plasma sources, *Review of Scientific Instruments* **77**(03B504).

Optical Energy Technologies Inc. (2008). Spacecraft attitude control systems product page, Internet Webpage. http://www.opticalenergy.com/spacecraft-attitude-control-system-triple-axis/.

Pfender, E. (1978). Electric arcs and arc gas heaters, *in* M. N. Hirsh & H. J. Oskam (eds), *Gaseous Electronics*, Vol. 1 - Electrical Discharges, Academic Press, Inc., chapter 5, pp. 301–304.

Polk, J. E. et al. (2001). A theoretical analysis of vacuum arc thruster performance, *27th International Electric Propulsion Conference*.

Powerkote (2008). Requested company job. E-mail: powerkote@telkomsa.net, Tel: +27 (021) 555 0920, Website: www.powerkote.co.za.

Qi, N. et al. (1998). A pulsed vacuum arc ion thruster for distributed small satellite systems, *34th AIAA/ASME/SAE/ASEE Joint Propulsion Conference*.

Quinn, T. J. & S. Leschiutta, P. T. (2000). Recent advances in metrology and fundamental constants, *Proceedings of the International School of Physics "Enrico Fermi" Course CXLVI*, IOS Press, Varenna on Lake Como, Villa Monastero.

Rajagopal, A. (2004). *Modern Physics*, Prentice Hall of India.

Rankin, D. et al. (2004). The canx-2 nanosatellite: Expanding the science abilities of nanosatellites, *55th International Astronautical Congress*.

Rao, S. S. (2004). *Mechanical Vibrations*, 4 edn, Pearson Education, p. 613.

Rethfeld, B. et al. (1996). A self-consistent model for the cathode fall region of an electric arc, *Journal of Physics D: Applied Physics* **29**: 121–128.

Riemann, K.-U. (1989). Theory of the cathode sheath in a vacuum arc, *IEEE Transactions on Plasma Science* **17**(5): 641–643.

Rossignol, J. et al. (2003). The modelling of the cathode sheath of an electrical arc in vacuum, *Journal of Physics D: Applied Physics* **36**: 1495–1503.

Roth, A. (1976). *Vacuum Technology*, North-Holland Publishing Company, chapter 4, pp. 149–150.

Rysanek, F. (2007a). Personal Communication on 24 August 2007. frysanek@uiuc.edu.

Rysanek, F. (2007b). *Macroparticle charging in the VAT*, PhD thesis, Department of Aerospace Engineering, University of Illinois - Urbana Campaign.

Rysanek, F. & Burton, R. (2003). Acceleration mechanisms in a vacuum arc thruster, *39th AIAA/ASME/SAE/ASEE Joint Propulsion Conference*.

Rysanek, F. et al. (2002). Microvacuum arc thruster design for a cubesat class satellite, *16th Annual/USU Conference on Small Satellites*.

Schein, J. (2006). Micropropulsion technologies, *in* R. Osiander et al. (eds), *MEMS and Microstructures in Aerospace Applications*, CRC Press, Taylor & Francis Group, LLC, chapter 11, pp. 229–267.

Schein, J. et al. (2002). Inductive energy storage driven vacuum arc thruster, *Review of Scientific Instruments* **73**(2): 925–927.

Schein, J. et al. (2007). Vacuum arc plasma thrusters with inductive energy storage driver. US 2007/0045248 A1.

Shalev, S. et al. (1985). Velocities and emission rates of cathode-produced molybdenum macroparticles in a vacuum arc, *Journal of Applied Physics* **58**(7): 2503–2507.

Steyn, W. H. (2007). SSIS inspection nanosatellite. ESL Nanosat Project, University of Stellenbosch.

Tipler, P. A. & Llewellyn, R. A. (1999). *Modern Physics*, 3 edn, W.H. Freeman.

Weickert, C. (1987). A multicomponent theory of the cathodic plasma jet in vacuum arcs, *Contributions from Plasma Physics* **27**(5): 309–330.

Wieser, M. E. (2006). Atomic weights of the elements 2005, *IUPAC Technical Report 11*, International Union of Pure and Applied Chemistry.

William A. Campbell, J. & Scialdone, J. J. (1993). Outgassing data for selecting spacecraft materials, *Reference Publication NASA RP-1124, Revision 3*, NASA Goddard Space Flight Center, Greenbelt, Maryland 20771. Available online at http://outgassing.nasa.gov/index.cgi.

Xiong, J. et al. (2005). Development of a mems based colloid thruster with sandwich structure, *Sensors and Actuators A* **117**: 168–172.

Yushkov, G. Y. et al. (2001). On a mechanism of ion acceleration in vacuum arc-discharge plasma, *Doklady Physics* **46**(5): 307–309.